Doctoral Dissertation
Doctoral Program in Aerospace Engineering (38th cycle)

Pressure and Flow Regulating Valves for Hydrogen Propulsion Systems, in Aerospace Applications

By

Arash Safaei
******

Supervisor(s):
Prof. Paolo Maggiore, Supervisor
Prof. Matteo Davide Lorenzo Dalla Vedova, Co-Supervisor

Doctoral Examination Committee:
Prof. Paolo Maggiore, Referee, Politecnico di Torino
Prof. Matteo Davide Lorenzo Dalla Vedova, Referee, Politecnico di Torino
Prof. Claudio Guarnaccia, Università di Salerno
Prof. Stefano Valvano, University of Derby
Prof. Pier Carlo Berri, APR s.r.l.
Prof. Emma Frosina, Università degli Studi del Sannio

Politecnico di Torino, 2026

Ringraziamenti

Contents

List of Figures IX
List of Tables XV

Abstract XVI

Sommario XVIII

1 Introduction 1
1.1 Motivations and Objectives 1
1.2 Presentation plan 2

2 State of the Art 5
2.1 Handling Cryogenic Liquid Hydrogen 5
2.2 Evaluation of Conventional Valve Types for Cryogenic Hydrogen Service 7
2.2.1 Gate Valves 8
2.2.2 Butterfly Valves 8
2.2.3 Ball Valves 8
2.2.4 Diaphragm Valves 8
2.2.5 Globe Valves 9
2.2.6 Needle, Plug, and Pinch Valves 9
2.3 Pressure-Reducing and Regulating Valves for Cryogenic Hydrogen 10
2.3.1 Thermophysical Properties and their Regulatory Implications 10
2.3.2 Principles and Phenomenology of Pressure Regulation 11
2.3.3 Operational Challenges at Cryogenic Temperatures 11
2.3.4 Design Strategies for Pressure Regulators in LH_2 Service 12
2.3.5 Comparison with Other Cryogens 13
2.4 Material Compatibility with Liquid Hydrogen 13
2.4.1 Hydrogen Embrittlement: Mechanisms and Micro-Physics 13
2.4.2 Variables Governing Hydrogen Embrittlement Severity 15
2.4.3 Material Selection Guidelines for LH_2 Valve Hardware 17
2.4.4 Mitigation Strategies and Research Frontiers 18

3 Innovative Valve Concepts for Liquid Hydrogen Servive 20
3.1 Brief Introduction 20
3.2 The Passive Pressure Reducer (PPR) 20
3.2.1 Design Concept and Motivation 20

3.2.2 Design Heritage 21
3.2.3 PPR Final Architecture: Convergent-Divergent with Annular Chambers 22
3.2.4 Convergent Section with Multi-Stage Annular Chambers 22
3.2.5 Throat and Cavitation Suppression 23
3.2.6 Divergent Section and Outlet Flow Quality 23
3.2.7 Median Throat and Venturi Section 24
3.2.8 Integrated Pressure Monitoring: Transverse Channels and Sensor Ports 24
3.3 The Piston-Based Pressure Regulating Valve 25
3.3.1 Design Concept and Spool Optimization 25
3.3.2 Spool Material: Inconel 718 Selection Rationale 26
3.3.3 Spring and Hydraulic Actuation Mechanism 26
3.4 Comparison with Conventional LH_2 Valve Solutions 28
3.5 Two-Stage System Architecture and Integration 30

4 Mathematical Model 32
4.1 PPR's Lumped-Parameter Analysis 33
4.1.1 Global Discharge Coefficient of the PPR 34
4.1.2 Flow Through a Circular Orifice: Governing Equations 36
4.1.3 Per-Stage Pressure Drop 38
4.2 Preliminary Numerical Model of the Piston Pressure Regulating Valve 40
4.2.1 Introduction and Fluid Dynamic Challenges 40
4.2.2 Problem Setup 42
4.2.3 Spool Geometry Optimization 44
4.2.4 Numerical Model 46
4.2.5 Governing Dynamics: Full Order Model 51
4.2.6 Simulink Implementation 53
4.2.7 Iterative Viscous Coefficient C Identification 55

5 CFD Analysis 63
5.1 CFD Simulation Strategy and Boundary Conditions 63
5.1.1 Overview and Objectives 63
5.1.2 Boundary Layer Modelling and CFD Setup 64
5.2 CFD Analysis of the PPR Multi-Stage Architecture 65
5.2.1 Mesh Topology and Global Settings 65
5.2.2 Boundary Layer Discretization 66
5.2.3 Mesh Independence Study 68
5.2.4 Solver Setting 69

5.2.5 Results and Discussion 69
5.2.6 Stepped Pressure Profile and Cavitation Avoidance 77
5.3 CFD Analysis of the Piston Pressure Regulating Valve 79
5.3.1 Flow Regime and Orifice Sizing 79
5.3.2 Geometry and Meshing 81
5.3.3 Solver Setting 83
5.3.4 Results and Discussion 84
5.3.5 ROM Dynamic Response: Underdamped LH_2 Behaviour 92
5.3.6 Comparison of CFD Results with the Lumped-Parameter Model 98

6 Experimental Setup Design 100
6.1 Experimental Objectives 100
6.2 Additive Manufacturing of the PPR Prototypes 102
6.2.1 Manufacturing Strategy and Prototype Realization 102
6.2.2 Additive Manufacturing Anisotropy and Surface Effects 104
6.2.3 Motivation for the Second Prototype 105
6.2.4 Improved Manufacturing Strategy and Implications 105
6.3 Design of the Experimental Test Bench 107
6.3.1 Experimental Containment Strategy and Test Line Design 107
6.3.2 Measurement Integration, Repeatability, and Boundary Condition Control 109
6.3.3 Valve Containment Armature: Design, Structural Architecture and Measurement Integration 110
6.3.4 Pressure Rating and Safety Margins 115
6.3.5 Sealing Strategy and Leakage Control 115
6.4 Pressure Measurement System 117
6.4.1 Pressure Tap Design Challenges 117
6.4.2 Sensor Configuration and Placement Strategy 119
6.5 Experimental Rig 121
6.5.1 Hydraulic Circuit Architecture, Operating Conditions, and Filling Procedure 123
6.5.2 Experimental Procedure 126

7 Experimental Campaigns: CFD Validation and Results Analysis 129
7.1 Second Prototype and the Need for a Roughness-Aware CFD Model 129
7.1.1 Results Discrepancy Observed on the First Prototype 129
7.1.2 Second Prototype: Print Resolution and Layer Thickness 130
7.1.3 Implications for the Numerical Framework 131
7.2 CFD Model Updates: Geometric Fidelity, Mesh and Near-Wall Treatment 131

7.2.1 Reconstruction of the Assembled Hydraulic Line 131
7.2.2 Computational Mesh 133
7.2.3 Mesh Refinement at the Radial Pressure Tappings 134
7.2.4 Near-Wall Resolution and Inflation Layers 134
7.3 Wall Roughness Modelling 135
7.3.1 Rough-Wall Log-Law and the Standard Model 135
7.3.2 High Roughness (Icing) Model 136
7.3.3 Roughness Height Bracket Adopted 136
7.4 Simulation Matrix and Solver Settings 136
7.4.1 Boundary Conditions, Solver and Convergence 137
7.5 Integrated Experimental Campaign and CFD Validation 138
7.5.1 Sensor Calibration 138
7.5.2 Water-Test Campaigns: Experimental Pressure Profiles 139
7.5.3 CFD Validation at 1 bar 140
7.5.4 CFD Validation at 2 bar 142
7.5.5 CFD Validation at 3 bar 144
7.5.6 CFD Validation at 4 bar 145
7.5.7 Simulations Ranking Across all Operating Points 147
7.6 Pressure Profile Validation: Integrated View 148
7.6.1 Relative Percentage Error Analysis 151
7.6.2 CFD Error Map by Stage and Pressure 154
7.7 CFD Flow Fields and Interpretation of the Pressure-Tapping Readings 155
7.7.1 Overview of the Simulated Flow Fields 155
7.7.2 Static Pressure Field 156
7.7.3 Dynamic Pressure Field and the Central Jet 157
7.7.4 Turbulence Fields 159
7.7.5 Flow Field Inside the Presure Tappings and Deviation from the Experimental Reading 162
7.7.6 The PPR as a Distributed Hydraulic Impedance 165

8 Conclusion and Future Work 167
8.1 Overall Conclusions 167
8.2 Scientific and Technological Contributions 168
8.2.1 Design Innovation 168
8.2.2 Modelling Framework 169
8.2.3 Experimental Infrastructure 169
8.3 Key Numerical Results 170

8.3.1 PPR: CFD-to-Experimental Validation Summary 170
8.3.2 Piston Valve: FOM-to-CFD Consistency 171
8.4 Physical Insights Emerging from the Research 171
8.4.1 Distributed-Impedance Interpretation of the PPR 171
8.4.2 The Static-Tapping Reading as a Hydrostatic Measurement 172
8.4.3 The Role of Surface Roughness in AM Hydraulic Components 172
8.4.4 Geometry-Derived Damping in Low-Viscosity Regulating Valves 172
8.5 Limitations of the Present Investigation 173
8.5.1 Experimental Limitations 173
8.5.2 Numerical Limitations 174
8.5.3 Physical Domain of Validity 174
8.6 Future Work 174
8.6.1 Cryogenic Experimental Validation 174
8.6.2 Numerical Model Refinement 175
8.6.3 Geometric Optimization of the PPR 175
8.6.4 Experimental Validation of the Piston Regulating Valve 175
8.6.5 System-Level Integration 176
8.7 Closing Remarks 176

Bibliography 179

List of Figures

Figure 2.1: Schematic of the five-step hydrogen–metal interaction sequence: (1) H_2 translation to surface, (2) adsorption, (3) dissociation to monatomic H, (4) absorption into the lattice, (5) diffusion through interstitial sites [22]. 14
Figure 2.2: Schematic of hydrogen-enabled crack propagation through the metallic lattice: hydrogen concentration at stress risers promotes decohesion and intergranular crack advance [22]. 14
Figure 2.3: Schematic illustrating Hydrogen-Enhanced Decohesion (HEDE) at a metallic grain boundary, and micrograph evidence of intergranular cracking from a ruptured hydrogen cylinder cross-section [22]. 15
Figure 2.4: Venn diagram illustrating the three intersecting variable domains — material, mechanical, and environmental — that jointly determine the activation and severity of hydrogen embrittlement in structural alloys [22]. 15
Figure 2.5: Material variables affecting hydrogen embrittlement susceptibility in hydrogen gas containment components: effect of nickel content, material strength, and weld microstructure on HE severity [22]. 16
Figure 2.6: Mechanical variables governing hydrogen embrittlement: comparison of constant (static) versus cyclic stress exposure and their respective effects on crack initiation and propagation rates [22]. 16
Figure 2.7: Environmental variables affecting hydrogen embrittlement: dependence of HE susceptibility on temperature and hydrogen gas pressure for a representative structural alloy. 17
Figure 3.1: Comparison of the US Patent reference geometry (left) and the optimized PPR final geometry (right). 21
Figure 3.2: Schematic 3D rendering of the PPR final architecture: convergent section with 6 progressively sized annular chambers and 6 orifice plates. 22
Figure 3.3: Axial pressure distribution along the PPR final geometry from inlet (30 bar) to outlet (7 bar), computed from CFD analysis. 23
Figure 3.4: Schematic cross-section of the optimized piston pressure regulating valve. 25
Figure 3.5: Non-optimized configuration (left) and optimized configuration (right). Right: valve mechanism schematic showing the complete fluid circuit. 26
Figure 3.6: Design improvement matrix comparing the novel PPR and piston valve architectures (highlighted columns) against three conventional LH_2 valve solutions. 28
Figure 3.7: Two-stage pressure management system architecture: PPR (Stage 1, passive, 200→~50 bar) in series with the piston regulating valve (Stage 2, active, 50→2–30 bar), supplying the regulated outlet pressure to the fuel cell or thruster. 30
Figure 4.1: 3D Rendering of the PPR used during the experimental tests. 33
Figure 4.2: 2D Cross section of the PPR. 33
Figure 4.3: Flow across an orifice: laminar flow (a) and turbulent flow (b). 34
Figure 4.4: 3D model of the simplified piston valve geometry used for both the CFD analysis and the lumped-parameter dynamic model. The central spool body, orifice divider, and upstream/downstream chambers are shown. 44
Figure 4.5: Cross-section of the optimized piston valve geometry showing the pass-through spool stem, the crown orifice with annular flow passage $A = 2\pi rx$, and the spring chamber above the spool disc. Source: author's original design. 45

Figure 4.6: Non-optimized piston body (left) and optimized pass-through piston body (right). The non-optimized geometry creates a blunt impingement region with recirculation downstream of the orifice. The optimized geometry creates a smooth crown-shaped annular passage, eliminating recirculation entirely. 46
Figure 4.7: Simulink implementation of the Reduced Order Model (ROM): $M\ddot{x} + C\dot{x} + Kx = F_{tot}$. The signal chain $F_{tot} \rightarrow (1/M) \rightarrow \ddot{x} \rightarrow (1/s) \rightarrow \dot{x} \rightarrow (1/s) \rightarrow x$ with feedback paths for the viscous coefficient C and spring stiffness K. 51
Figure 4.8: Reduced Order Model (ROM) on the left. Full Order Model (FOM) scheme on the right. 53
Figure 4.9: 3D rendering of the Full Order Model scheme. 53
Figure 4.10: Complete integrated Simulink model with automatic Reynolds-number-based switching between ROM and FOM. The Switch block transitions between the laminar and turbulent models when Re crosses Re_{cr}. The equilibrium displacement x_{eq} and the error signal are output alongside position and velocity. 55
Figure 4.11: Piston geometry and active force contributions during valve operation. 56
Figure 4.12: Flowchart of the iterative viscous coefficient C identification procedure. 58
Figure 4.13: FOM closed-loop signal flow. The ROM uses only the $C\dot{x}$ feedback path (purple). The FOM adds the chamber pressure terms (orange) as velocity-dependent damping contribution. 60
Figure 5.1: Boundary layer refinement in the CFD mesh: addition of inflation layers to capture the steep velocity gradient near solid surfaces. Fine mesh with high aspect-ratio cells in the boundary layer is essential for accurate wall shear stress and pressure distribution on the spool. 64
Figure 5.2: Tessellation of the convergent part of the PPR. 67
Figure 5.3: Volume Mesh with Tetrahedral cells. 68
Figure 5.4: Boundary Layer's inflation during meshing phase. 68
Figure 5.5: Discharge Coefficient of PPR's stages. 72
Figure 5.6: Convergence Plot of the simulation performed with ANSYS. 74
Figure 5.7: Pressure field across the PPR's stages. 74
Figure 5.8: Cross section pressure field of the orifices. 75
Figure 5.9: Velocity field of the LH2 flow. 75
Figure 5.10: Volume mesh rendering of the velocity field across the orifices and annular chambers. 75
Figure 5.11: Boundary layer's capture in the velocity field. 76
Figure 5.12: Laminarization of the jet flow across the convergence part of the PPR. 76
Figure 5.13: Pressure drop across the PPR, from inlet (left side) to outlet (right side). 76
Figure 5.14: Flow velocity across the PPR, from inlet (left side) to outlet (right side). 77
Figure 5.15: Comparison between the results of the CFD and Lumped-Parameter analysis. 78
Figure 5.16: Comparison of the Pressure drop between the single orifice and the PPR. 79
Figure 5.17: Cross section of the CAD model. 82
Figure 5.18: Tessellation of the piston body of the valve. 82
Figure 5.19: Volume Mesh with Tetrahedral cells. 82
Figure 5.20: Boundary Layer's inflation during meshing phase. 83
Figure 5.21: Convergence Plot of the residuals of the simulation performed with SimScale. 87
Figure 5.22: Pressure field variation across the optimized piston body. 87
Figure 5.23: Pressure field variation across the non-optimized piston body. On the left the recirculation zones, on the top the localized pressure drops. 88
Figure 5.24: Velocity field of the LH2 flow around the optimized piston body. 88
Figure 5.25: Velocity field of the LH2 flow around the non-optimized piston body. 89
Figure 5.26: Pressure field of the LH2 flow around the optimized piston body. 89

Figure 5.27: Pressure field of the LH2 flow around the non-optimized piston body. 90
Figure 5.28: Laminarization of the flow jet across the optimized piston body of the valve. 90
Figure 5.29: Laminarization of the flow jet across the non-optimized piston body of the valve. 91
Figure 5.30: Boundary layer's capture in the proximity of the wall.....91
Figure 5.31: Pressure force along the y-axis of the piston body.....92
Figure 5.32: Viscous force along the y-axis of the piston body. 92
Figure 5.33: FOM dynamic response — spool position x(t) for the optimized geometry with LH_2. The response is near-critically damped: the spool converges monotonically to the equilibrium position x_eq with a small overshoot and negligible residual oscillations. Settling time ≈ 30–40 ms — acceptable for the target pressure-regulation application. 93
Figure 5.34: FOM dynamic response — spool velocity $\dot{x}(t)$. The velocity rises from zero, peaks at t ≈ 5 ms (corresponding to maximum spool acceleration under F_{tot}), then decays smoothly to zero as the spool reaches x_eq. Small residual fluctuations (circled) are visible and are attributable to numerical integration step-size effects at the Simulink time discretization.....94
Figure 5.35: ROM fluid comparison — spool position x(t) for LH_2 (black), water (red), and oil SAE 30 120C (blue). The ROM response is strongly viscosity-dependent: LH_2 produces the most oscillatory response (minimum damping), oil produces near-critical damping, water is intermediate. The system performance degrades catastrophically at low viscosity. 95
Figure 5.36: FOM fluid comparison — spool position x(t) for LH_2 (black), water (red), and oil SAE 30 120C (blue). The FOM response is practically insensitive to fluid viscosity: all three fluids converge with nearly identical near-critically damped profiles. The geometric $B\dot{x}^2$ coupling term dominates the damping, making the system robust across the entire viscosity range. 96
Figure 5.37: Comparison between the optimized and non-optimized piston dynamics with LH2.....97
Figure 5.38: Comparison between the optimized and non-optimized piston's motion with oil. 98
Figure 6.1: Printing phase of the 2nd sample of the PPR with high temperature resin. 104
Figure 6.2: Comparison between the 1st prototype (on the left) and the 2nd prototype (on the right). 106
Figure 6.3: Aluminium containment armature used for the PPR. 111
Figure 6.4: Dimensioned lateral drawing of the test section (ANSYS 2022 R1). Principal dimensions: overall armature length 190 mm; body length 170.06 mm; inner cylinder 150.06 mm; body Ø57 mm; flange outer Ø77.5 mm; threaded rods Ø29.4 mm; flange wall 10 mm; fitting Ø34.41 mm. 113
Figure 6.5: Dimensioned 3D view of the test section (ANSYS 2022 R1) highlighting the pressure measurement port locations on the aluminium armature body. Threaded ports (Ø29.4 mm) are positioned at equal angular spacing around the circumference to access the internal annular chambers of the PPR prototype. The 18.2 mm flange extension is also indicated.....113
Figure 6.6: Components used during PPR's assembly: flanges, threaded rods, and sealing interfaces.....114
Figure 6.7: Graduated hydraulic fittings used to ensure progressive diameter transitions between the supply tubing and the armature ports, and threaded brass plugs employed to seal inactive pressure tap ports on the PPR body during sequential sensor repositioning. 115
Figure 6.8: PTFE tape and compliant gaskets used for sealing threaded interfaces and flange junctions in the PPR experimental assembly.....117

Figure 6.9: Paper washers used to hydraulically isolate individual pressure tap ports from adjacent annular chambers, ensuring independent static pressure acquisition at each measurement location. 119
Figure 6.10: Three Schneider Electric XMLG016D21 pressure transmitters (0–16 bar, 4–20 mA current-loop output) installed on the containment armature, each connected to a dedicated pressure tap aligned with the corresponding internal annular chamber of the PPR prototype. 121
Figure 6.11: Schematic diagram of the experimental pneumatic–hydraulic line. From left to right: compressed air supply (P_0 = 0–6 bar); coarse pressure reducing valve (PRV_1); upstream manometer (M_1); fine throttle valve (TV_1); downstream manometer (M_2); hydraulic damper reservoir; PPR test section with three Schneider Electric XMLG016D21 pressure transmitters (P1–P3, 0–16 bar, 4–20 mA); calibrated discharge collection tank. 122
Figure 6.12: Pressure regulating valve with coarse adjustment (on the left) and throttling valve for fine pressure control (on the right). 123
Figure 6.13: Close-up view of the threaded fittings at the pressure tapping points showing the T-connectors. 127
Figure 6.14: Close up zoom of the polymeric sealing used for the interface between the PPR and the flange (on the left). The PPR outlet pipe (on the right). 128
Figure 7.1: CAD geometry of the assembled hydraulic test section reproduced in Ansys DesignModeler. The fluid domain extends from the straight inlet pipe upstream, through the adapters and flanges, across the four annular chambers of the PPR and the central throat, and up to the outlet pipe downstream. The radial pressure tappings at Stage I, II, III and IV are explicitly modelled as dead-end cavities connected to the main flow domain. 132
Figure 7.2: Three-dimensional view of the fluid domain showing the internal volume of the armature, the PPR body, the four radial tapping channels and the connection interfaces to the inlet and outlet flanges. The inlet face (highlighted) is the surface on which the pressure or mass-flow boundary conditions are applied in the CFD simulations. 132
Figure 7.3: Longitudinal mid-plane cross-section of the unstructured tetrahedral mesh adopted for the CFD campaign. The progressive refinement from the inlet pipe towards the throat and the pressure-tapping region is clearly visible. 133
Figure 7.4: Close-up of the mesh in the region of the annular chambers and pressure tappings. The local cell size is reduced to resolve the small radial passages that connect the chambers to the external pressure ports. 133
Figure 7.5: Three-dimensional view of the mesh in the Inlet-adapter region, where the cross-section of the flow channel expands into the flange pocket. The refinement ensures an adequate resolution of the separation and reattachment regions that form at each geometric transition. 133
Figure 7.6: Zoomed view of the tetrahedral mesh on a radial pressure-tapping cavity. The element size has been reduced locally with respect to the surrounding annular chamber in order to resolve the cylindrical cavity and the shear layer that may develop at its inner opening. 134
Figure 7.7: Visualization of the prismatic inflation layers on a no-slip wall. The first row of prismatic cells adheres to the surface, ensuring near-wall resolution compatible with both smooth and rough-wall treatments. 135
Figure 7.8: Hexahedra mesh applied to the fluid volume of the hydraulic line. 135
Figure 7.9: Convergence history of the mass flow rate at the throat section, showing monotonic stabilization to a constant asymptotic value within approximately 75 iterations. 137
Figure 7.10: Residuals of the continuity, momentum (x, y, z velocity components) and turbulence (k, ε) equations as a function of iteration number. All quantities converge to values below 10^{-3} for continuity and below 10^{-5} for the velocity components, confirming a satisfactory numerical convergence of the solution. 138

Figure 7.11: Experimental pressure profiles along the PPR in the three measurement campaigns, for inlet pressures from 1 to 4 bar. The differences between configurations reveal how the distribution of the pressure drop among the stages depends non-trivially on the sensor placement. 139
Figure 7.12: Mass flow rate measured by the volumetric method in the three experimental campaigns at the four inlet pressure levels (1, 2, 3, 4 bar). 139
Figure 7.13: Comparison between the experimental pressure profile and the seven CFD predictions at 1 bar (left); percentage error on the mass flow rate for each turbulence-and-roughness combination (right). 141
Figure 7.14: Comparison between the experimental pressure profile and the seven CFD predictions at 2 bar (left); percentage error on the mass flow rate for each turbulence-and-roughness combination (right). 143
Figure 7.15: Comparison between the experimental pressure profile and the seven CFD predictions at 3 bar (left); percentage error on the mass flow rate for each turbulence-and-roughness combination (right). 145
Figure 7.16: Comparison between the experimental pressure profile and the seven CFD predictions at 4 bar (left); percentage error on the mass flow rate for each turbulence-and-roughness combination (right). 146
Figure 7.17: Pressure profile along the PPR at 1 bar inlet pressure. 149
Figure 7.18: Pressure profile along the PPR at 2 bar inlet pressure. 150
Figure 7.19: Pressure profile along the PPR at 3 bar inlet pressure. 150
Figure 7.20: Pressure profile along the PPR at 4 bar inlet pressure. 151
Figure 7.21: Relative percentage error on the stage pressures at 1 bar inlet pressure. 152
Figure 7.22: Relative percentage error on the stage pressures at 2 bar inlet pressure. 153
Figure 7.23: Relative percentage error on the stage pressures at 3 bar inlet pressure. 153
Figure 7.24: Relative percentage error on the stage pressures at 4 bar inlet pressure. 154
Figure 7.25: Percentage-error map (CFD − Exp)/Exp on the pressure profiles, organized by stage (horizontal axis) and CFD model (vertical axis), for the four inlet-pressure levels. 155
Figure 7.26: Static pressure contour on the mid-longitudinal plane of the complete hydraulic test section. The pressure drop is concentrated at the throat and in the orifice passages; within each annular chamber the pressure is essentially uniform, which supports the interpretation of the chamber as a hydrostatic reservoir communicating with the central jet only through the orifice itself. 156
Figure 7.27: Dynamic pressure contour on the mid-longitudinal plane of the PPR. The central jet appears as a narrow red-orange line extending from the throat through the downstream chambers; the entire annular volume surrounding the jet — including the region immediately adjacent to the Stage I tapping — remains at negligible dynamic pressure, indicating a fluid essentially at rest. 158
Figure 7.28: Dynamic pressure contour in a longitudinal cross-section downstream of the throat, showing the progressive spreading of the central jet and its gradual dissipation as it enters the outlet chamber. The annular volumes outside the jet remain in dark-blue tones across the entire axial extent of the device. 158
Figure 7.29: Turbulent intensity field on the mid-longitudinal plane of the PPR. The red band corresponds to the shear layer of the central jet; the blue regions surrounding the orifice passages are characterised by turbulent intensities below 10 %. 160
Figure 7.30: Turbulent intensity field on a centerline cross-section of the PPR, zoomed on the throat and the three-stage orifice cascade. The jet shear layer reaches turbulent intensities of 70 %, while the annular volumes remain below 10 %. 160
Figure 7.31: Turbulent kinetic energy field near the radial pressure tappings (zoomed view). The energy is concentrated in the shear layer of the central jet (red band at the top) and

decreases by more than two orders of magnitude inside the tapping cavities (dark-blue regions at the bottom). 161
Figure 7.32: Velocity magnitude near the radial pressure tappings. The orange-red band at the top represents the main flow at the throat/chamber interface; the blue columns below are the tapping cavities of Stages I, II and III, in which the velocity is essentially zero. The sharp transition at the cavity mouth is a thin shear layer that couples the cavity hydrostatically to the main flow. 162
Figure 7.33: Zoomed view of the turbulent intensity field in the region of a radial pressure tapping. The cavity appears as a quasi-laminar volume (deep blue) isolated from the turbulent main flow (orange-red). 163

List of Tables

Table 2.1. Key thermophysical properties of liquid hydrogen and their engineering implications [8]. 6
Table 2.2. Comparative assessment of conventional valve types for cryogenic liquid hydrogen service. 7
Table 2.3: Material compatibility summary for liquid hydrogen valve components. 17
Table 3.1: Comparative assessment of the novel PPR and piston valve architectures against conventional LH_2 valve solutions. Green entries indicate specific design improvements. TRL per ESA scale. 29
Table 4.1: Pressure drop contribution Δpi of each stage 38
Table 4.2: Pressure drop contribution Δpi of each stage. 40
Table 5.1: Summary of CFD boundary conditions for the PPR and piston valve simulations. 65
Table 5.2: Mesh independence study for the PPR geometry with LH_2 at Δp = 23 bar. The medium mesh (3.5×10^6 cells) was selected as the production mesh for the full simulation campaign, offering a satisfactory balance between accuracy and computational cost. 68
Table 5.3: CFD's output 71
Table 5.4: CFD's volume flow rate. 71
Table 5.5: Iterative computation of viscous coefficient C. 86
Table 5.6: Comparison of lumped-parameter model predictions with CFD results for the PPR (LH_2, Δp = 23 bar) and piston valve. 99
Table 7.1: Simulation matrix (7 CFD runs × 4 inlet pressures). 137
Table 7.2: Calibration verifications of the sensors. 138
Table 7.3: Pressure Profile [kPa] 140
Table 7.4: Mass Flow Rate comparison and Percentage Error. 140
Table 7.5: Pressure Profile [kPa]. 142
Table 7.6: Mass Flow Rate comparison and Percentage Error 142
Table 7.7: Pressure Profile [kPa]. 144
Table 7.8: Mass Flow Rate comparison and Percentage Error. 144
Table 7.9: Pressure Profile [kPa]. 145
Table 7.10: Mass Flow Rate comparison and Percentage Error. 146
Table 7.11: Mean absolute flow-rate error across the four operating points. 147
Table 8.1: Consolidated performance metrics of the PPR and the piston regulating valve. 170

Abstract

The development of pressure and flow control valves for hydrogen, particularly in its cryogenic liquid form, remains one of the most technically demanding tasks in aerospace propulsion engineering. Liquid hydrogen (LH_2) is a fluid with extraordinary properties: an extremely low boiling point of 20.27 K at atmospheric pressure, very low density, and a high tendency to penetrate even the smallest imperfections in containment systems. These characteristics make it an excellent propellant but also a substance that imposes strict requirements on every component it comes into contact with. Among these, valves for pressure reduction and regulation play a critical role, as they must guarantee precise and stable control over the fluid under a wide range of operating conditions.

Traditional pressure-reducing and regulating valves, designed for denser and less volatile fluids, often encounter serious limitations when used with LH_2. In particular, the rapid and localized pressure drops that occur inside the valve body can trigger flash vaporization of the liquid hydrogen, a phenomenon akin to cavitation. Once vapor bubbles form, they can collapse violently, causing erosion, vibration, and loss of sealing performance. These transient instabilities are difficult to predict and even harder to control, especially in systems where safety margins are already narrow. For this reason, innovative approaches are needed to ensure both performance and reliability.

In this doctoral research, two complementary valve concepts were conceived, each addressing a different aspect of hydrogen flow management. The first is a pressure-reducing valve specifically designed to lower the pressure of cryogenic hydrogen in a gradual and controlled manner, thereby avoiding conditions conducive to cavitation. The design relies on a sequence of chambers, or stages, separated by calibrated orifices. At each stage, the fluid loses a portion of its energy in a controlled way before passing to the next stage, preventing excessive localized pressure drops. This multi-stage layout allows the valve to transform a high upstream flow into a low downstream flow without abrupt transitions.

This device, named the Passive Pressure Reducer (PPR), is entirely static: it contains no moving parts, requires no external actuation or power, and is manufactured from a single monolithic block. The absence of joints and dynamic seals increases structural robustness and leak-tightness, an essential requirement when dealing with aggressive and low-temperature fluids such as LH_2. The fixed internal geometry determines the valve's performance, making it predictable and repeatable while significantly reducing the risk of mechanical failure.

To test the PPR without resorting to liquid hydrogen, which would entail very high costs and complex safety procedures, a dedicated hydraulic bench was designed and built. The bench uses water as the working fluid, exploiting fluid-dynamic analogy principles to reproduce the behavior of the cryogenic liquid under pressurized conditions. The structure of the bench includes a central housing capable of securely containing valve prototypes during testing. This modular arrangement not only facilitates testing of the PPR but also

makes it possible to accommodate other valve designs in the future, ensuring versatility and long-term usefulness of the facility.

The second valve developed in this work is a pressure regulator intended to work in series with the PPR. While the reducer is designed to handle the initial large pressure drop, the regulator fine-tunes the downstream pressure to the exact value required by the propulsion system. Unlike the PPR, this regulator contains moving parts to dynamically modulate the flow. This complexity makes it more challenging to prototype for early experimental validation, so its design phase relied heavily on computational fluid dynamics (CFD) simulations. These simulations assessed the regulator's ability to manage pressurized hydrogen and its compatibility with the PPR, paving the way for an integrated, high-precision pressure control system.

Even though the regulator has not yet been tested experimentally, the hydraulic bench was designed to accommodate it in future trials. Any valve body that fits within the dimensional constraints of the central housing can be installed and subjected to pressurized water testing. For initial tests, valve bodies were produced in high-temperature-resistant resin via additive manufacturing (3D printing). While unsuitable for cryogenic operation, these prototypes allowed rapid, low-cost validation of internal flow patterns, staged pressure drops, and overall structural behavior.

The combined development of the PPR, the regulator, and the hydraulic bench represents a comprehensive approach to solving the challenges of cryogenic hydrogen valve design. The PPR addresses the issue of cavitation by eliminating sharp, uncontrolled pressure drops and by using a passive, monolithic structure that maximizes robustness and reliability. The regulator, though more complex, offers the capability of precise, dynamic control to adapt to varying operating conditions. The hydraulic bench serves as an enabling tool, allowing these and other designs to be tested in a controlled and cost-effective environment.

By integrating conceptual design, numerical simulation, prototyping, and experimental validation within a single research framework, this work delivers both innovative components for cryogenic hydrogen systems and a reusable testing methodology that can accelerate future developments in the field. The results demonstrate that with the right combination of staged pressure reduction, passive architecture, and modular testing infrastructure, it is possible to overcome many of the limitations of traditional valve technology and move towards safer, more reliable hydrogen propulsion systems.

Sommario

La progettazione, la fabbricazione e la manutenzione operativa di valvole di regolazione della pressione e della portata per l'idrogeno, in particolare nella sua forma criogenica liquida, rappresentano una sfida ingegneristica significativa nel campo della propulsione aerospaziale. L'idrogeno liquido (LH_2), con il suo punto di ebollizione estremamente basso (20,27 K a 1 atm), l'elevata diffusività, la bassa densità e l'aggressività chimica, richiede un controllo preciso e stabile durante la fornitura ai sistemi propulsivi. Questo controllo deve essere ottenuto prevenendo instabilità di cambiamento di fase ed evitando rischi operativi.

Le architetture convenzionali di valvole riduttrici e regolatrici di pressione, sviluppate originariamente per fluidi più viscosi e densi, si rivelano spesso inadeguate con LH_2. Una delle criticità principali riguarda la loro suscettibilità a fenomeni simili alla cavitazione: cali di pressione improvvisi e localizzati all'interno del corpo valvola possono causare vaporizzazione istantanea del fluido criogenico. Questi eventi di micro-vaporizzazione, innescati da strati limite turbolenti o da geometrie di strozzamento accentuate, portano a instabilità di flusso, vibrazioni meccaniche, erosione delle superfici interne, degrado della tenuta e, in ultima analisi, a una riduzione dell'affidabilità.

In questo lavoro di dottorato sono stati sviluppati due progetti distinti ma complementari: una valvola di riduzione della pressione ottimizzata per l'idrogeno criogenico e una valvola di regolazione da accoppiare alla prima per un controllo preciso a valle. La prima è stata progettata per ridurre la pressione in modo graduale e controllato, evitando condizioni di cavitazione, mediante una configurazione multi-stadio in cui il fluido attraversa camere consecutive separate da orifizi calibrati. Ogni stadio dissipa parte dell'energia a monte, evitando cali di pressione eccessivi e mantenendo il flusso al di sopra della tensione di vapore dell'LH_2.

Questa valvola, denominata Passive Pressure Reducer (PPR), è completamente statica, priva di parti mobili e non richiede energia esterna. È realizzata come un blocco monolitico per garantire robustezza strutturale, tenuta e compatibilità con fluidi criogenici aggressivi. La geometria interna fissa determina le caratteristiche di riduzione della pressione, trasformando un flusso elevato in ingresso in un flusso ridotto in uscita senza transizioni brusche.

Per validare le prestazioni e l'integrità della PPR è stato progettato e realizzato un banco prova idraulico dedicato, utilizzando acqua come fluido di lavoro per analogia fluidodinamica, evitando i costi e le complessità dei test con LH_2. Il banco presenta una struttura modulare centrale in grado di ospitare diversi prototipi di valvola in un alloggiamento sicuro e compatto.

Il secondo progetto riguarda una valvola di regolazione della pressione, destinata a lavorare in serie con la PPR, capace di mantenere la pressione a valle ai valori richiesti. Questa valvola, più complessa, prevede parti mobili e per questo la sua progettazione è stata sviluppata e validata inizialmente tramite simulazioni CFD.

Sebbene non sia ancora stata testata sperimentalmente, il banco prova idraulico è già predisposto per ospitarla. I prototipi iniziali delle valvole sono stati realizzati in resina ad alta temperatura tramite stampa 3D, consentendo prove rapide e a basso costo.
Questo lavoro integra progettazione concettuale, simulazione numerica, prototipazione e validazione sperimentale, fornendo soluzioni innovative per valvole a idrogeno criogenico e un metodo di prova riutilizzabile, capace di accelerare lo sviluppo di sistemi propulsivi più sicuri e affidabili.

Chapter 1

Introduction

1.1 Motivations and Objectives

Cryogenic hydrogen valve design is a challenging multidisciplinary process, requiring a high level of compromise between structural integrity, thermofluidic dynamic performance, manufacturability, and operational safety. Recent reviews of cavitation behavior in cryogenic fluids underline how phase-change instabilities remain difficult to predict due to strong thermal effects and non-equilibrium regimes [1]. The subject of pressure and flow control valve design for liquid hydrogen is extensive, with applications ranging from ground refueling systems and cryogenic storage facilities to in-flight feed systems for advanced liquid propulsion stages. Achieving an effective design demands balanced consideration of subsystem interactions, careful evaluation of alternative architectures, and mitigation of cryogenic-specific failure modes. This process is often time-consuming, involving iterative loops of numerical analysis, prototyping, and experimental testing under controlled conditions. Consequently, there is an urgent need to improve LH_2 valve design methodologies, particularly to avoid cavitation and ensure thermal stability and robustness in phase-change-prone fluids [2].

In modern space propulsion systems, valves for pressure reduction and regulation are essential to guarantee safe and stable delivery of cryogenic propellants. They must reliably operate across extreme temperature gradients, high pressure differentials, and very strict leak-tightness requirements. Constraints typical of LH_2 systems make conventional valve bodies especially susceptible to abrupt and localized internal pressure drops, which can trigger flash vaporization and cavitation-like phenomena. Such events may lead to erosion, vibration, sealing loss, and functional degradation, threatening both performance and safety [3].

Traditional pressure-reducing and regulating valves, developed for media with higher density and viscosity, often lack the capacity to control micro-scale pressure gradients in the flow path. This limitation increases vulnerability to two-phase unsteady regimes and local thermodynamic non-equilibrium. Added complexity comes from the need to operate moving parts, dynamic seals, and mechanical components across repeated thermal cycling without introducing failure-prone mechanical hysteresis.

The primary objective of this thesis is to develop, assemble, and experimentally validate two innovative valve concepts tailored for LH_2 service: a Passive Pressure Reducer (PPR), and a pressure-regulating valve designed for downstream installation in series. The PPR embodies a monolithic, multi-stage throttling architecture: the fluid traverses sequential chambers separated by calibrated orifices, each stage dissipating a controlled portion of upstream pressure. By ensuring each pressure drop remains below cavitation thresholds, the PPR maintains liquid-phase conditions throughout its path. It is inherently passive, with no moving parts or external actuation, offering high structural integrity and minimal leakage

susceptibility. The fixed internal geometry enables predictable and repeatable transformation from high-pressure high-flow inlet to low-pressure low-flow outlet conditions.
This concept bears similarity with multi-stage orifice structures used in hydrogen decompression valves in other contexts, such as fuel-cell FCEV systems, where reliability and turbulence control were improved via staged geometry [4]. Similar methods have proven effective in reducing turbulence intensity and controlling kinetic energy dissipation through geometric optimization in multistage valves [5].
To experimentally validate the PPR, a dedicated hydraulic test bench was designed and built, using pressurized water as a surrogate fluid. This setup exploits dimensionless similarity principles to reproduce cryogenic pressure-reduction behavior, avoiding early-stage LH_2 testing costs and hazards. The bench includes modular central housing capable of securely accommodating valve prototypes within defined geometric limits, providing a robust test environment.
The second valve concept, a precision pressure regulator meant to operate downstream of the PPR, incorporates active internal components capable of dynamically modulating flow in response to pressure feedback. Given the added complexity of moving mechanics under cryogenic loads, initial development focused on high-fidelity computational fluid dynamics (CFD) simulations. These studies evaluated transient flow topology, pressure recovery behavior, and coupling effects with the upstream PPR, guiding integrated-system optimization.
Although not yet experimentally tested in cryogenic conditions, the regulator design is compatible with the hydraulic bench infrastructure. Early-stage prototypes for both valve types were produced via additive manufacturing using high-temperature resistant resin. These models enabled rapid, cost-efficient testing of internal flow paths, stage pressure drop behavior, and structural integrity under hydraulic load.
The overarching aim of the research is to deliver validated methodologies and experimental tools for developing LH_2-compatible pressure-control valves, combining cavitation-resistant staging principles with robust passive architectures. By uniting conceptual design, numerical simulation, prototyping, and hydraulic validation within a unified framework, this work advances both valve technology for cryogenic propulsion and modular test infrastructure.

This contribution aligns with recent research emphasizing multi-stage throttling and structural optimization to reduce turbulent vortex formation, enhance pressure reduction, and improve overall flow uniformity in hydrogen valves [6]. This thesis demonstrates how staged pressure dissipation, passive architecture, and rigorous testing infrastructure can mitigate LH_2 cavitation risks, advancing the state of the art in cryogenic propulsion-valve design.

1.2 Presentation plan

The structure of this thesis can be divided according to the following points:

- **Chapter 2:** the goal of this chapter is to present an overview of the literature regarding cryogenic liquid hydrogen fluid control, covering the thermophysical properties of LH_2

and the engineering constraints that define its handling requirements. A critical assessment of conventional valve types demonstrates their general unsuitability for LH_2 service, motivating the need for purpose-designed architectures. The chapter further examines the thermodynamic principles of cryogenic pressure regulation, including flashing, cavitation, and dynamic instability. It concludes with a structured analysis of material compatibility and hydrogen embrittlement mitigation strategies.

- **Chapter 3:** two innovative valve concepts specifically designed for liquid hydrogen applications are introduced. The first is the Passive Pressure Reducer (PPR), a monolithic multi-stage throttling device for gradual, cavitation-free pressure reduction. The second is a piston-based pressure regulator, intended for precise downstream control, which can be integrated with the PPR.

- **Chapter 4:** the development of the mathematical model is presented. The focus is on the creation of a virtual simulation environment in Matlab and Simulink, capable of predicting the valve's performance under various operating conditions. The model incorporates the key physical parameters and flow characteristics, providing a powerful tool for design evaluation and optimization prior to experimental testing.

- **Chapter 5:** this chapter describes the computational fluid dynamics (CFD) analysis performed on the valve concepts. The focus is on the numerical investigations carried out using Ansys and SimScale to evaluate internal flow behavior, pressure distribution, and potential cavitation regions. These simulations provide detailed insights into performance characteristics, supporting design refinement and validating the concepts prior to physical prototyping.

- **Chapter 6:** the implemented experimental rig is described and provided in order to enable comprehensive testing of the developed valve's concepts. The system was designed to accommodate pressurized water and, when required, oil as working fluids, providing a versatile platform for hydraulic characterization under controlled conditions. The chapter details the layout, components, and operational procedures of the test line, highlighting its adaptability for different valve configurations and its capability to simulate a range of operating scenarios.

- **Chapter 7:** this chapter focuses on the collection and analysis of experimental data obtained from testing the valve prototypes. The primary objective is to validate the proposed technology by comparing the measured hydraulic performance with the results predicted by the implemented mathematical model. The chapter outlines the testing procedures, data acquisition methods, and post-processing techniques used, followed by a detailed comparison between experimental and simulated results to assess the accuracy, reliability, and operational consistency of the examined concept.

- **Chapter 8:** conclusions and possible future improvements to the experimental rig set-up are illustrated.

Chapter 2

State of the Art

The design of fluid control components for liquid hydrogen (LH_2) service represents one of the most technically demanding challenges in aerospace engineering. Unlike conventional industrial fluids, hydrogen imposes a unique convergence of thermophysical extremes, material degradation risks, and regulatory constraints that collectively invalidate most of the design assumptions underpinning conventional valve technology. The development of reliable, high-performance pressure-reducing and regulating valves for LH_2 therefore requires a systematic understanding of the fluid environment, the limitations of existing valve architectures, the thermodynamics of cryogenic pressure control, and the long-term material compatibility challenges associated with hydrogen exposure. This chapter reviews the relevant state of the art across each of these domains, establishing the technical foundation upon which the novel valve concepts developed in this thesis are built.

Across the aerospace sector, the operational envelope imposed by LH_2 systems is extreme. Cryogenic temperatures approach 20 K, pressure differentials can span several orders of magnitude, and leakage tolerances are among the most stringent in any engineering discipline. The weight budget for spaceflight hardware leaves little margin for conservative overdesign, while simultaneously demanding the highest levels of reliability. These requirements, as noted in early programme reviews of liquid-propellant rocket development, have historically driven valve mass fractions to less than 20–30% design margin, far below the 200% margins common in terrestrial industrial practice [7,8].

The following sections address, in turn: the specific engineering challenges of handling cryogenic liquid hydrogen (Section 2.1); a critical evaluation of conventional valve types and their applicability to LH_2 service (Section 2.2); the fundamental principles and design considerations for pressure-reducing and regulating valves in cryogenic systems (Section 2.3); and, finally, the material compatibility issues, with particular focus on hydrogen embrittlement, that govern long-term reliability (Section 2.4).

2.1 Handling Cryogenic Liquid Hydrogen

The growing role of hydrogen as a zero-emission energy carrier has expanded its use across transportation, power generation, and aerospace propulsion. In each of these domains, the preferred form for bulk storage and distribution is cryogenic liquid hydrogen, owing to its dramatically higher energy density per unit volume compared to compressed gaseous hydrogen. At its normal boiling point of 20.3 K, liquid hydrogen has a density of approximately 70.8 kg/m^3, enabling compact storage at relatively low pressures in comparison with the high-pressure vessels required for gaseous storage at equivalent energy content. For large-scale industrial installations, cryogenic supply chains offer further logistical advantages, including the use of vacuum-jacketed pipelines, road tankers, and ISO containers [7].

The key thermophysical properties of LH_2 relevant to valve design are summarized in Table 2.1. These values collectively define the challenging operating environment that any fluid control component must accommodate.

Table 2.1. *Key thermophysical properties of liquid hydrogen and their engineering implications [8].*

Property	Value / Range	Engineering Implication
Normal boiling point	20.3 K (−252.9 °C)	Extreme insulation and material requirements
Liquid density (at NBP)	~70.8 kg/m³	Large liquid-to-gas expansion ratio (~1:850)
Vapour pressure (at 20 K)	~101.3 kPa	Small ΔP causes flashing downstream of valve
Thermal conductivity (liquid)	0.099 W/(m·K)	Rapid heat ingress causes boil-off
Dynamic viscosity (liquid)	~1.32×10^{-5} Pa·s	Very low — laminar flow destabilised easily
Joule-Thomson coeff. (20 K)	Slightly positive	Throttling may cause local warming
Flammability limits in air	4–75 vol%	Ultra-low leakage requirements
Diffusivity through metals	High (small atomic radius)	Risk of HE and permeation leaks

Beyond its thermophysical properties, LH_2 presents a number of operationally significant hazards that directly influence valve design and system architecture. The wide flammability range in air (4–75 vol%), combined with hydrogen's invisibility and nearly colorless flame, makes any leakage scenario potentially catastrophic. Valve designs must therefore achieve ultra-low leakage rates, typically below 10−6 standard cm³/s (sccs), across thousands of thermal cycles from cryogenic to ambient temperature [7,9].
Several additional considerations arise specifically from the cryogenic operating regime that directly constrain valve design:

- *Boil-off management*: Even with high-quality vacuum insulation, thermal ingress into any LH_2 system is unavoidable. The resulting continuous vaporization of stored liquid generates pressurized boil-off gas that must be safely vented or consumed. Pressure relief and regulating valves must accommodate this gaseous phase without loss of pressure control stability.

- *Thermal contraction*: The large temperature differential between ambient and cryogenic conditions induces significant dimensional changes in all structural materials. For a typical stainless-steel component, the linear contraction from 293 K to 20 K is of the order of 3 mm/m. Differential contraction between dissimilar materials in a valve assembly, body, seat, stem, and seal, must be rigorously managed to prevent jamming, misalignment, or sealing loss.

- *Ice formation*: Condensation of atmospheric moisture on uninsulated exterior surfaces of cryogenic hardware leads to ice buildup. This can impede valve actuation, block vent lines, and, in the case of condensed air, create oxygen-enriched mixtures adjacent to a flammable hydrogen system, a recognized explosion hazard under NFPA 2 [10].

- *Extended bonnet design*: Non-metallic packing and stem seals invariably become brittle or lose elasticity at cryogenic temperatures. The use of extended bonnets, elongating the valve stem so that the seal region remains near ambient temperature, is therefore a standard design response that is applied across most cryogenic valve types.

- *Liquid entrapment*: Valves that trap a volume of liquid when closed are subject to a severe hydraulic overpressure hazard as the trapped LH_2 warms and expands. The expansion ratio of LH_2 from liquid to gas at ambient conditions is approximately 1:850, meaning that a closed valve enclosing even a small liquid volume can generate pressures well in excess of the design burst limit if no pressure relief mechanism is incorporated. Globe valves are the preferred baseline design partly because their flow path geometry minimizes the risk of liquid entrapment.

These constraints collectively define a design space that is far more restrictive than that encountered in conventional industrial fluid systems. As will be shown in the following sections, they motivate a fundamental rethinking of conventional valve architecture.

2.2 Evaluation of Conventional Valve Types for Cryogenic Hydrogen Service

The selection of a suitable valve type is the primary decision in cryogenic hydrogen system design. Numerous valve architectures are available in industrial and chemical engineering practice; however, their adaptation to LH_2 service is often severely constrained or altogether infeasible. The combination of extreme cryogenic temperatures, hydrogen embrittlement susceptibility, ultra-tight leakage requirements, and the absence of suitable elastomeric seal materials eliminates many conventional options at the outset. This section critically surveys the principal industrial valve types, evaluating their characteristics against the LH_2 service envelope defined in Section 2.1. A comparative summary is presented in Table 2.2 [8,10,11].

Table 2.2. *Comparative assessment of conventional valve types for cryogenic liquid hydrogen service.*

Valve Type	Cryogenic Suitability	Throttle Control	Seal Reliability	LH_2 Recommended
Gate Valve	Poor	None	Low	No
Butterfly Valve	Poor	Limited	Low	No

Ball Valve	Marginal	Limited	Moderate	No
Diaphragm Valve	Poor	Good	Poor	No
Globe Valve	Moderate*	Excellent	Moderate	Modified only
Pinch Valve	Poor	Good	Poor	No
Needle Valve	Poor	Excellent	Low	Lab-scale only

Modified globe valves with extended bonnets and cryogenic-rated seats. Source: adapted from Gilliland et al. [8]; Schiaroli et al. [10].

2.2.1 Gate Valves

Gate valves operate by translating a disc element across the flow path, offering negligible resistance to flow in the fully open position. Their simplicity and low cost have made them ubiquitous in industrial on/off service. However, they are fundamentally unsuited to throttling applications, and their seating surfaces are highly susceptible to erosion and vibration-induced damage under partial-open conditions. In LH_2 service, the additional challenge of differential thermal contraction between disc and seat renders reliable sealing extremely difficult. The absence of a flow-shaping element also precludes any distributed pressure reduction capability, making gate valves wholly inadequate for the pressure-reducing function required in the present application [10].

2.2.2 Butterfly Valves

Butterfly valves provide compact, lightweight flow control through rotation of a disc element, and are widely used in low-pressure, large-diameter pipelines. Their principal limitation in LH_2 service is the reliance on elastomeric or polymeric seat materials, which lose their sealing capability rapidly below −100 °C. Metal-seated cryogenic butterfly valves exist but are limited to relatively low-pressure differentials and remain prone to leakage under cyclic thermal loading. The disc geometry also generates significant downstream turbulence at partial opening, potentially inducing flow instability in sensitive cryogenic systems [11].

2.2.3 Ball Valves

Ball valves offer rapid actuation and low pressure drop in the fully open position, and have found application in some aerospace fluid systems. Their primary vulnerability in LH_2 service is the risk of liquid entrapment within the ball bore when the valve is closed, which, as discussed in Section 2.1, can generate catastrophic overpressure as the trapped volume warms. While this hazard can be partially mitigated by vented ball designs, the resulting modifications add complexity and potential new leakage paths. Seat material limitations and the risk of hydrogen-induced cracking at high contact stresses further constrain their reliability [8].

2.2.4 Diaphragm Valves

Diaphragm valves provide excellent isolation of moving actuator components from the process fluid and are widely used in corrosive or contamination-sensitive applications. The diaphragm element, however, is invariably polymeric or elastomeric, and fails catastrophically

at cryogenic temperatures. While metallic diaphragm designs exist for high-temperature applications, the combination of cryogenic brittleness and hydrogen permeation renders them unsuitable for LH_2 [10].

2.2.5 Globe Valves

Globe valves offer the most versatile baseline for cryogenic hydrogen service, owing to their inherent flow-shaping geometry, compatibility with extended bonnet configurations, and capacity for fine throttling control. The S-shaped flow path, while introducing a higher-pressure drop than straight-through designs, distributes the flow-induced stresses more uniformly across the seating surfaces and reduces the risk of cavitation at intermediate openings. With cryogenic-rated metallic seats (typically Inconel or hardened stainless steel), metal-to-metal sealing gaskets, and extended bonnets to protect stem packings, globe valves represent the most commonly adopted solution for LH_2 pressure control and regulation [8,12]. Nevertheless, even cryogenic globe valves are not without significant shortcomings. Their inherently high pressure drop at partial opening can initiate flashing and cavitation in LH_2 when the local static pressure falls below the vapor pressure. In high-flow, high-pressure-ratio applications, such as main propellant feed systems, a single globe valve cannot distribute the required total pressure drop without entering a two-phase flow regime. This limitation fundamentally motivates the multi-stage throttling architecture developed in the present thesis [12,13].

2.2.6 Needle, Plug, and Pinch Valves

Needle valves provide exceptionally fine flow adjustment at low flow rates and are suitable for laboratory-scale instrumentation in LH_2 systems, though they are impractical for main propellant line applications. Plug valves offer compact, low-drop switching but suffer from seal integrity losses at cryogenic temperatures due to thermal contraction mismatches. Pinch valves, which rely on the deformation of a resilient elastomeric sleeve to control flow, are wholly incompatible with LH_2 service: their operating principle depends on the very material properties, elastomeric flexibility at low temperature, that cryogenic conditions destroy entirely [10,11].

In summary, a systematic review of conventional valve types reveals that globe valves, when appropriately modified for cryogenic service, represent the most viable baseline for LH_2 pressure control. However, their residual limitations, particularly in high-pressure-ratio and multi-stage pressure reduction scenarios, provide the primary technical justification for the development of purpose-designed architectures such as the Passive Pressure Reducer investigated in this work.

2.3 Pressure-Reducing and Regulating Valves for Cryogenic Hydrogen

Pressure regulation in liquid hydrogen systems is among the most technically demanding aspects of cryogenic fluid management. The unique thermophysical characteristics of LH_2, its extremely low boiling temperature, high expansion ratio, propensity for cavitation, and sensitivity to heat ingress, impose requirements on pressure control components that differ fundamentally from those encountered in conventional cryogen or industrial fluid systems. This section reviews the thermodynamic foundations of pressure regulation in LH_2, the specific phenomena that complicate valve operation, and the design strategies that have been developed to address them.

2.3.1 Thermophysical Properties and their Regulatory Implications

The design of any pressure-reducing device begins with a precise characterization of the working fluid. Several properties of LH_2 are of particular significance for valve design [9,14]:

- *Boiling point and vapor pressure*: at atmospheric pressure, LH_2 boils at 20.3 K. This near-absolute-zero temperature means that even minor heat ingress causes continuous vaporization. Pressure regulators must accommodate the resulting boil-off gas without destabilizing downstream pressure control and must provide adequate safety margins against over-pressurization under worst-case heat-ingress scenarios.

- *High expansion ratio*: the liquid-to-gas volumetric expansion ratio of hydrogen is approximately 1:850 in standard conditions. Small perturbations in valve opening therefore produce disproportionately large volumetric flow changes downstream, requiring actuation mechanisms with fine resolution and minimal hysteresis.

- *Thermal conductivity and diffusivity*: hydrogen's thermal conductivity is substantially higher than that of most other cryogens. In valve components that bridge cryogenic and ambient temperature regions, this accelerates thermal gradients and increases contraction stress, requiring careful thermal isolation design.

- *Joule-Thomson effect*: near the inversion temperature of hydrogen (~200 K), isenthalpic expansion produces a slight warming rather than the cooling observed in most gases. In the cryogenic regime near 20 K, the Joule-Thomson coefficient is positive but small; however, its effect on downstream thermal stability must be accounted for in detailed thermodynamic analyses of the throttling process.

- *Hydrogen permeability*: The small atomic radius of hydrogen enables permeation through metallic lattices and microscopic defects in seals. Sustained permeation not only generates hazardous leakage but also induces embrittlement of structural materials over time, as discussed in detail in Section 2.4.

2.3.2 Principles and Phenomenology of Pressure Regulation

A pressure-reducing valve (PRV) functions by throttling flow through a calibrated restriction, dissipating the available pressure differential as viscous and turbulent losses. For conventional incompressible fluids, this process is governed by a combination of Bernoulli's equation and orifice flow theory. For LH_2, however, a number of additional phenomena must be accounted for in the design and analysis of PRVs [12,14,15]:

1. *Flashing and two-phase flow:*

During throttling, the static pressure at the vena contracta downstream of the restriction may fall below the local vapor pressure of LH_2. This initiates rapid nucleate boiling, referred to as flashing, which transitions the flow from a single-phase liquid to a two-phase liquid-vapor mixture. Two-phase flow dramatically alters the effective flow coefficient (C_v) of the valve, reduces the predictability of pressure control, and often leads to violent pressure oscillations, noise, and erosion damage to internal surfaces [14].

2. *Cavitation:*

Related to flashing but mechanistically distinct, cavitation involves the nucleation and subsequent collapse of vapor bubbles within the flowing liquid. Bubble collapse events release intense local pressure pulses, of the order of gigapascals over microsecond timescales, that cause characteristic pitting erosion of valve seats and internal surfaces. For LH_2, cavitation onset occurs at relatively low upstream pressures due to the fluid's low vapor pressure, making cavitation avoidance a primary design driver for any throttling element [15,16].

3. *Choked flow:*

As in compressible gas flow, choked conditions can develop across a valve restriction when the pressure ratio exceeds a critical threshold. For LH_2, hydrogen's high speed of sound (~1270 m/s in liquid phase) means that choked flow is reached at relatively modest pressure ratios. Beyond the choked condition, increasing the upstream pressure no longer increases the mass flow rate, which has significant implications for the control authority of the valve [14].

4. *Dynamic instability:*

Conventional spring-loaded PRVs can exhibit sustained oscillations, commonly referred to as chatter, when regulating cryogenic hydrogen under variable demand conditions. This instability arises from the interaction between the valve's dynamic response and the acoustic resonance of the downstream pipe system, and is exacerbated by the low viscosity and high speed of sound in LH_2 [12].

2.3.3 Operational Challenges at Cryogenic Temperatures

Beyond the thermodynamic phenomena described above, the mechanical operation of valves at 20 K introduces a set of engineering challenges that have no direct analogue in ambient-temperature applications [8,9,10]:

- *Thermal contraction and clearance management:* differential contraction between valve body, seat, stem, and actuator components under cooling from ambient to 20 K can produce clearance changes of the order of millimeters in large components. Precise tolerance management and material pairing are required to maintain seat tightness and stem freedom of movement throughout the thermal cycle.
- *Metallic seal integrity:* the absence of serviceable elastomeric seals at cryogenic temperatures necessitates the use of metallic, PTFE, or indium soft-metal sealing elements. These materials can maintain adequate sealing performance over a limited number of thermal cycles but are susceptible to creep, cold-flow, and micro-cracking under repeated cryogenic cycling, eventually leading to leakage.
- *Lubrication and seizure:* conventional petroleum-based and synthetic lubricants solidify well above 20 K, rendering lubricated sliding contacts inoperable. Aerospace cryogenic valves address this by adopting dry-film lubricants (e.g., MoS_2, PTFE coatings) or by using pneumatically actuated designs that minimize direct metal-on-metal contact in moving parts.
- *Hydrogen leakage:* hydrogen's combination of small molecular size, high diffusivity through metallic lattices, and wide flammability range means that even leakage rates considered negligible for other fluids represent unacceptable safety and performance risks in LH_2 systems.

2.3.4 Design Strategies for Pressure Regulators in LH_2 Service

The foregoing discussion reveals a coherent set of design principles that have emerged from decades of experience with LH_2 pressure control in rocket propulsion, storage systems, and experimental facilities. These are summarized below as the primary design strategies that inform the valve concepts developed in this work [8,12,13,16]:

a. *Multi-stage throttling:* rather than imposing the full upstream-to-downstream pressure differential across a single restriction, multi-stage designs distribute the total ΔP across a series of calibrated orifices or throttling elements. Each stage operates at a pressure drop below the cavitation threshold, and the cumulative effect achieves the required pressure reduction without initiating two-phase flow.

b. *Extended bonnet and stem design:* extending the bonnet above the valve body places the stem packing in a thermally insulated region that remains at near-ambient temperature, preserving seal integrity over the full cryogenic operating range.

c. *Pilot-operated regulation:* for high-precision downstream pressure control, pilot-operated architectures, in which a small pilot valve controls the actuation pressure of a larger main valve, provide superior control authority, reduced hysteresis, and improved dynamic stability compared to direct-acting spring-loaded designs.

d. *Redundant seats and fail-safe design:* in aerospace applications, PRVs are routinely designed with dual redundant seats and fail-safe actuation modes (fail-open or fail-

closed, depending on the system safety philosophy) to ensure continued operability under partial failure scenarios.

e. *Cryogenic-rated material selection:* austenitic stainless steels, nickel-based superalloys, and aluminum alloys are the principal material families compatible with LH_2 service, as detailed in Section 2.4.

2.3.5 Comparison with Other Cryogens

A brief comparison with other commonly used cryogens is instructive in contextualizing the unique challenges of LH_2 pressure regulation. Liquid nitrogen (LN_2, boiling point 77 K) is widely used as a benign surrogate fluid in cryogenic valve testing, owing to its non-flammability, relatively low cost, and availability. However, its higher density (~807 kg/m³ at normal boiling point) and lower vapor pressure result in a cavitation onset behavior that differs significantly from LH_2, and direct scaling of test results requires careful application of dimensionless similarity criteria. Liquid oxygen (LOX, boiling point 90 K), while sharing some cryogenic handling challenges, poses primarily oxidizer-related hazards rather than flammability risks, and its pressure regulation challenges are more closely associated with combustion reactivity than with cavitation or permeation. In the context of this thesis, water is used as a hydraulic surrogate for cryogenic testing at ambient conditions, exploiting dimensional similarity to replicate the pressure-reduction behavior of LH_2 without requiring cryogenic infrastructure at early design stages [9,17].

2.4 Material Compatibility with Liquid Hydrogen

Material selection is arguably the most critical design decision in LH_2 hardware development. The simultaneous imposition of extreme cryogenic temperatures, high contact stresses under thermal contraction, and sustained exposure to atomic hydrogen creates a degradation environment that is unique in engineering practice. The primary failure mode of concern is hydrogen embrittlement (HE), a phenomenon characterized by progressive reduction in the ductility, fracture toughness, and fatigue crack growth resistance of metallic alloys following hydrogen ingress into the microstructure. Understanding the mechanisms, manifestations, and mitigation strategies for HE is essential to the safe design of valves, seals, and structural connections in LH_2 systems [18,19,20].

2.4.1 Hydrogen Embrittlement: Mechanisms and Micro-Physics

Hydrogen embrittlement in metals proceeds through a multi-step process: molecular hydrogen dissociates at the metal surface under the influence of stress concentrators or catalytic sites; atomic hydrogen diffuses into the lattice along interstitial pathways; and hydrogen accumulates at regions of high triaxial stress, grain boundaries, crack tips, dislocation pile-ups, where it degrades cohesive forces and promotes fracture. The phenomenon is subtle and progressive, often producing no visible precursor damage before sudden brittle fracture at stresses well below the nominal design yield strength [18,19].

Three principal mechanistic models are recognized in the literature, though none is exclusive [20,21]:

i. *Hydrogen-Enhanced Localized Plasticity (HELP)*: hydrogen reduces the resistance to dislocation motion, concentrating plastic strain at the crack tip and accelerating crack advance. The result is macroscopically reduced ductility despite locally increased plasticity.

ii. *Hydrogen-Enhanced Decohesion (HEDE)*: hydrogen accumulates at grain boundaries and phase interfaces, reducing the cohesive bond energy and promoting intergranular fracture at stresses well below those predicted by plasticity-based failure criteria.

iii. *Hydride Formation*: relevant primarily to titanium, zirconium, and vanadium alloys, hydrogen precipitates as brittle metal hydrides that act as crack initiation sites and severely reduce fracture toughness. This mechanism is of secondary importance for the austenitic stainless steels and nickel-based alloys typically used in LH_2 valve hardware.

Figure 2.1 illustrates the five-step interaction sequence between gaseous hydrogen and a metallic surface, from molecular dissociation through lattice diffusion.

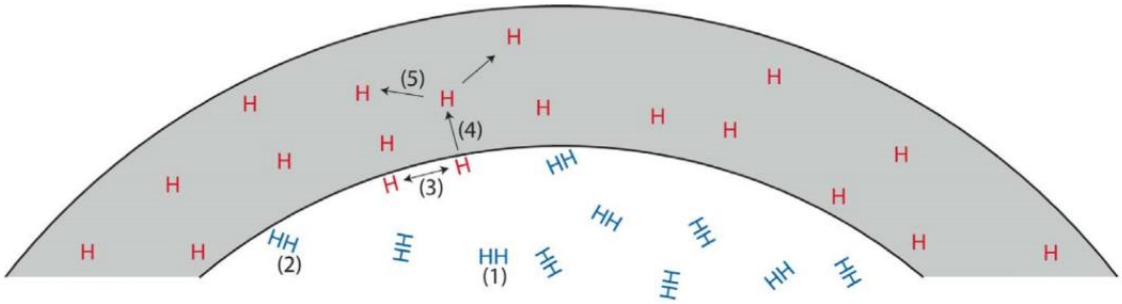


Figure 2.1: *Schematic of the five-step hydrogen–metal interaction sequence: (1) H_2 translation to surface, (2) adsorption, (3) dissociation to monatomic H, (4) absorption into the lattice, (5) diffusion through interstitial sites [22].*

Once atomic hydrogen diffuses into the metal lattice, it migrates preferentially to regions of high hydrostatic stress, such as crack tips or grain boundary triple points. Figure 2.2 illustrates the crack propagation mechanism driven by hydrogen-enhanced decohesion, showing the intergranular fracture morphology characteristic of HE in austenitic stainless steels.

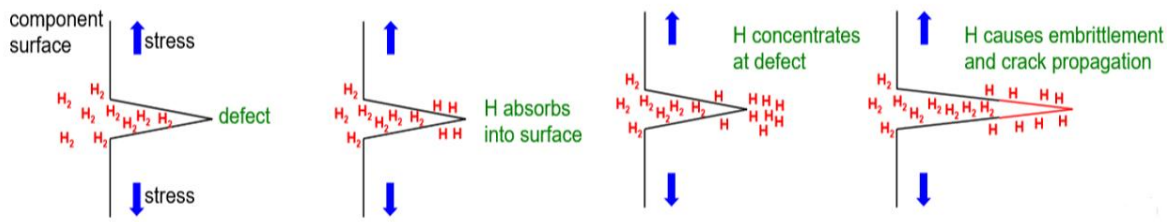


Figure 2.2: *Schematic of hydrogen-enabled crack propagation through the metallic lattice: hydrogen concentration at stress risers promotes decohesion and intergranular crack advance [22].*

Figure 2.3 provides a visualization of the HEDE mechanism at grain boundaries, where the presence of hydrogen reduces cohesive bond strength and initiates intergranular fracture. This micrograph-style representation underscores the sub-visible nature of hydrogen damage prior to macroscopic failure.

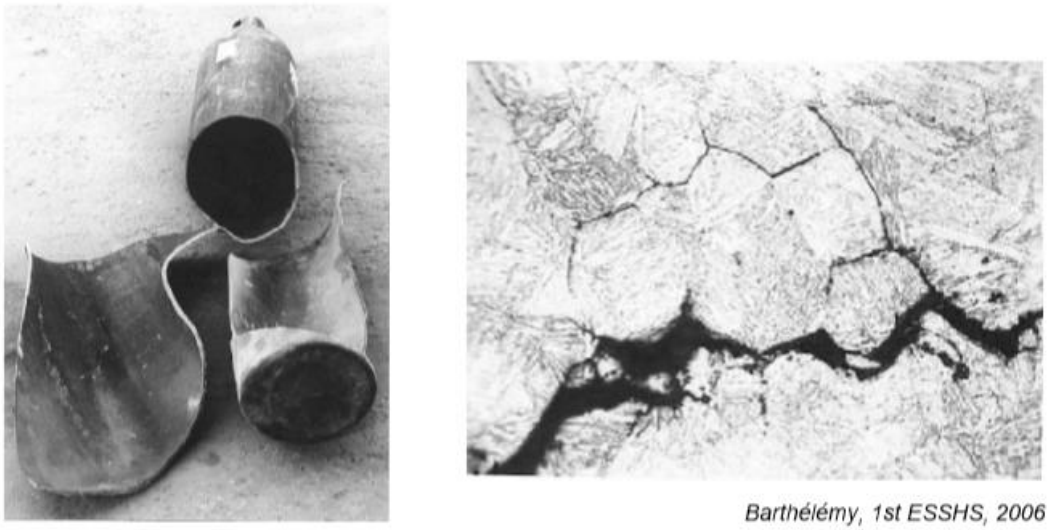


Figure 2.3: *Schematic illustrating Hydrogen-Enhanced Decohesion (HEDE) at a metallic grain boundary, and micrograph evidence of intergranular cracking from a ruptured hydrogen cylinder cross-section [22].*

2.4.2 Variables Governing Hydrogen Embrittlement Severity

The severity of hydrogen embrittlement is not a fixed material property but depends on the intersection of three variable domains: material, mechanical, and environmental. Figure 2.4 illustrates this three-factor dependence, and its implications for the design of LH_2 hardware are examined below [22,23].

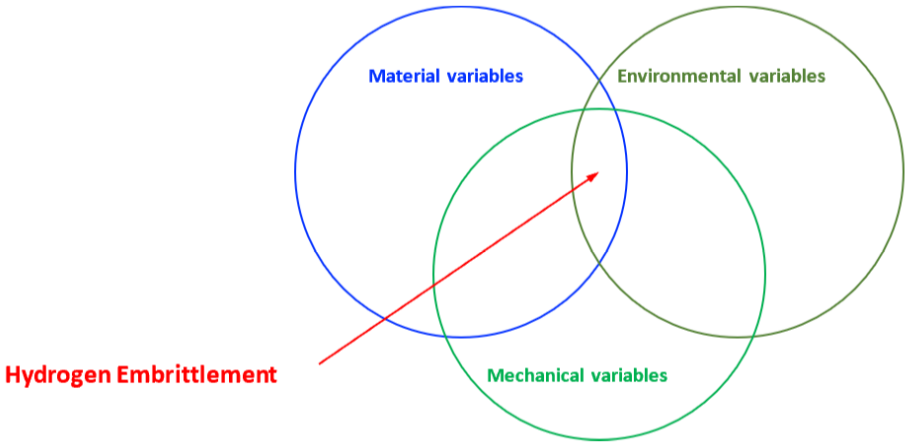


Figure 2.4: *Venn diagram illustrating the three intersecting variable domains — material, mechanical, and environmental — that jointly determine the activation and severity of hydrogen embrittlement in structural alloys [22].*

Material variables: Among the most influential material parameters are alloy composition and microstructural phase. In austenitic stainless steels, nickel content is the dominant variable: higher nickel content stabilizes the austenite phase under mechanical loading, reducing

metastable martensite transformation and the associated increase in HE susceptibility.[23] Material strength is equally critical: above approximately 1000 MPa yield strength, most ferritic and martensitic steels become severely susceptible to hydrogen-assisted cracking even at low hydrogen concentrations, rendering them inappropriate for LH_2 service. Weld zones represent particularly vulnerable regions due to local hardening, residual stress, and potential phase transformation during fabrication.

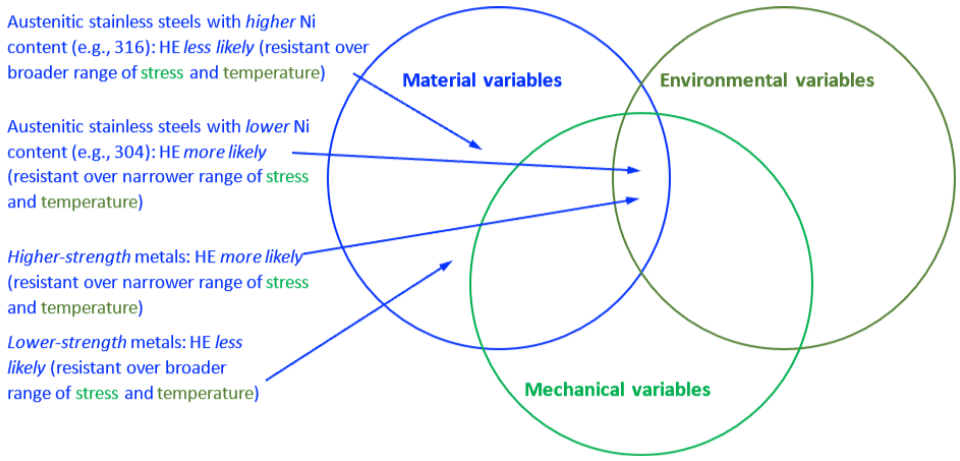


Figure 2.5: *Material variables affecting hydrogen embrittlement susceptibility in hydrogen gas containment components: effect of nickel content, material strength, and weld microstructure on HE severity [22].*

Mechanical variables: The mode of loading strongly influences HE activation. Static loading at stresses above approximately 50–60% of the fracture toughness can initiate slow crack growth even in the absence of cyclic fatigue. Cyclic loading significantly accelerates HE damage by continuously presenting fresh crack surface for hydrogen ingress and by promoting dislocation motion near the crack tip, enhancing hydrogen transport to the process zone. The stress amplitude and R-ratio (minimum-to-maximum stress ratio) of the fatigue cycle are therefore important design parameters for components subject to fluctuating pressure loads [23].

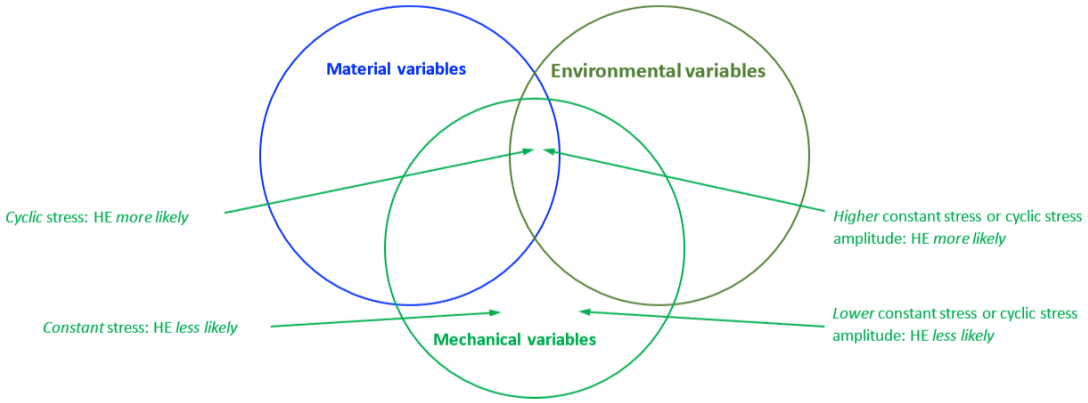


Figure 2.6*: Mechanical variables governing hydrogen embrittlement: comparison of constant (static) versus cyclic stress exposure and their respective effects on crack initiation and propagation rates [22].*

Environmental variables: Hydrogen gas pressure and temperature are the two principal environmental variables. Embrittlement severity generally increases with hydrogen partial

pressure, with maximum effects observed in the range 20–100 bar. Temperature dependence is non-monotonic: embrittlement is most pronounced near room temperature in steels, with reduced severity at both elevated and cryogenic temperatures due to competing effects on diffusion rate and thermodynamic stability. At 20 K, diffusion is significantly retarded, but accumulated hydrogen from prior service cycles may remain trapped at defect sites, maintaining a residual embrittlement state [22,23].

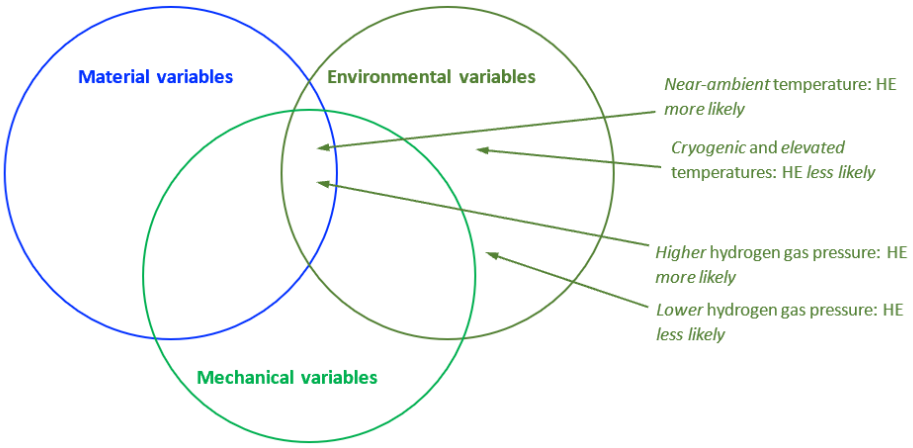


Figure 2.7: *Environmental variables affecting hydrogen embrittlement: dependence of HE susceptibility on temperature and hydrogen gas pressure for a representative structural alloy.*

2.4.3 Material Selection Guidelines for LH_2 Valve Hardware

On the basis of the foregoing analysis, the following material selection framework applies to the principal structural components of cryogenic hydrogen valves. Table 2.3 summarizes the principal material families and their suitability for LH_2 service [8,10,19,23].

Table 2.3: *Material compatibility summary for liquid hydrogen valve components.*

Material Class	Key Property	LH_2 Suitability
Austenitic SS (304L, 316L)	Good toughness, moderate HE resistance	Recommended
Aluminium alloys (6061, 7075)	Low density, acceptable toughness at 20 K	Recommended (structural)
Nickel-based alloys (Inconel 718)	High strength, good HE resistance	Valve internals
High-strength ferritic steels	High UTS but severe HE susceptibility	Not recommended
Titanium alloys	Hydride formation risk	Avoid
Nickel alloys (pure Ni)	Severe embrittlement	Avoid
Elastomers (NBR, EPDM)	Brittle below −100 °C	Not suitable
PTFE / indium gaskets	Retain flexibility at 20 K	Seal applications

Adapted from Gangloff and Somerday [23]; Schiaroli et al. [10]; CGA H-3 [25].

Austenitic stainless steels of the 300 series, particularly 304L and 316L in their low-carbon variants, are the most widely specified structural materials for LH_2 applications. Their face-centered cubic (FCC) crystal structure confers inherent toughness at cryogenic temperatures and comparatively good resistance to hydrogen embrittlement, particularly when nickel content is maintained above 10 wt%. The low-carbon variants reduce the risk of sensitization-induced intergranular corrosion at weld heat-affected zones [19,23].

Aluminum alloys, particularly the 6061-T6 and 7075-T73 tempers, offer an attractive weight-efficient option for valve bodies and structural housing where contact with LH_2 is limited and hydrogen absorption is not the primary concern. Their toughness at cryogenic temperatures is generally superior to that of ferritic steels, and they do not exhibit hydrogen-induced martensite transformation. Care must be taken, however, to avoid hydrogen porosity at weld joints, which represents the primary metallurgical risk in aluminum LH_2 hardware.[19]

For components subject to the highest contact stresses, valve seats, stem tips, and actuation surfaces, nickel-based superalloys such as Inconel 718 or Waspaloy provide the necessary combination of high strength, HE resistance, and cryogenic toughness, albeit at significantly higher material and machining cost. Surface treatments including titanium nitride (TiN) and diamond-like carbon (DLC) coatings have been investigated as hydrogen ingress barriers on stainless steel substrates, demonstrating partial effectiveness in controlled laboratory exposures, though their long-term reliability under cryogenic cycling remains an active research area [19,23].

The selection of sealing materials presents a particularly constrained design problem. Conventional elastomers (NBR, EPDM, silicone) lose all useful sealing properties below −100 °C and are entirely unsuitable for LH_2. The practical options are limited to PTFE-based composites, which maintain adequate flexibility and chemical resistance at 20 K, and soft-metal indium gaskets, which provide high leak tightness under moderate bolt preloads. Both options are susceptible to creep and cold-flow under sustained cryogenic loading, imposing a finite service life that must be explicitly addressed in maintenance planning [8,10].

2.4.4 Mitigation Strategies and Research Frontiers

A number of mitigation strategies have been developed and applied to reduce the impact of hydrogen embrittlement on LH_2 hardware reliability [19,23]:

1. *Intrinsic material selection*: specification of alloys with demonstrated HE resistance under representative cryogenic cycling conditions remains the most reliable mitigation measure. Standardized testing protocols, including ASTM F1624 (incremental step loading) and ASTM E1820 (fracture toughness), provide quantitative ranking of alloy susceptibility.
2. *Protective surface treatments*: TiN, alumina, and DLC coatings applied by physical vapor deposition (PVD) have shown promise as hydrogen permeation barriers, reducing ingress by factors of 10–100 in laboratory conditions. Their adhesion and integrity under cryogenic thermal cycling remain an active area of qualification testing.
3. *Thermal management*: extended bonnet designs and vacuum-jacketed insulation keep the most critical sealing and load-bearing regions of the valve above cryogenic

temperature, reducing both hydrogen diffusion rates and the severity of ductile-to-brittle transition effects.

4. *Redundant design and damage tolerance*: aerospace valve specifications typically mandate redundant load paths and leak-before-break tolerances, ensuring that any HE-induced crack growth is detectable before catastrophic failure occurs.

Despite these advances, hydrogen embrittlement remains one of the most persistent unresolved challenges in LH_2 system design. Key gaps in the current state of knowledge include the lack of validated predictive models for HE lifetime under realistic cryogenic cycling spectra, limited availability of in-situ diagnostic techniques applicable during valve operation, and the absence of harmonized international test standards for HE qualification of cryogenic valve hardware. These gaps motivate continued investment in materials research and the development of more conservative design margins in first-generation LH_2 propulsion hardware [18,20,23].

Chapter 3

Innovative Valve Concepts for Liquid Hydrogen Service

3.1 Brief Introduction

The pressure management challenge in the target application spans approximately two orders of magnitude: from bulk LH_2 storage conditions of approximately 200 bar to regulated fuel cell or thruster inlet conditions in the range 2–30 bar. As established in Chapter 2, achieving this reduction in a single throttling stage is infeasible for LH_2: the required pressure ratio exceeds 10:1, which at the relevant mass flow rates would produce throat velocities above the sonic threshold (≈355 m/s for LH_2 vapor), triggering normal shock waves, cavitation onset, and unacceptable structural loads on any single throttling element. The well-established design response to this constraint, distributing the total pressure differential across multiple serial stages, each operating below the cavitation threshold, defines the fundamental architecture of the system presented in this work.

Two dedicated devices address the two distinct stages of pressure management:

I. Stage 1 — *Passive Pressure Reducer (PPR)*: a geometry-driven passive device reduces pressure from ~200 bar to ~50 bar through four annular dissipation chambers and six calibrated orifices in a convergent-divergent monolithic body. No moving parts, actuation system, or electrical power are required at any stage of its operation.

II. Stage 2 — *Piston Pressure Regulating Valve*: an actively controlled spool with a precisely optimized pass-through stem geometry performs fine downstream regulation in the range 50 to 2–30 bar. Its dynamic behavior has been modelled with a Full Order Model (FOM) that achieves near-critical damping even in the extremely low-viscosity LH_2 environment.

3.2 The Passive Pressure Reducer (PPR)

3.2.1 Design Concept and Motivation

The fundamental design philosophy of the PPR is to replace active pressure regulation, with its inevitable reliance on moving components, seals, springs, and control loops, along with a purely geometric pressure dissipation mechanism. In the aerospace and aeronautical context, where system redundancy is a primary reliability driver, active valve components add mass, power consumption, and potential failure points. The PPR, by contrast, requires no power, contains no moving parts, no springs, and no dynamic seals, and can be integrated into specific locations along the fuel distribution line to relieve the load on, or in some cases replace entirely, downstream active regulators [28,29].

The conceptual starting point for the PPR is the US patent sleeve architecture (characterized by annular flanges arranged along a straight bore) described in Section 3.2.2. However, as the CFD analysis presented in following chapters demonstrates, the straight-bore patent geometry produces negligible pressure reduction, only approximately 0.3 bar, or 1.3% of the 23 bar target, because the flanges in the absence of a convergent-divergent profile act on an already fully developed flow with no directional velocity component capable of generating significant recirculation dissipation. The key geometrical innovation of the PPR is the addition of a convergent-divergent internal profile, which transforms the annular chambers from low-efficiency disturbances into highly effective energy dissipation zones by forcing the flow to decelerate and recirculate through each chamber in sequence.

3.2.2 Design Heritage

The original conceptual inspiration for the PPR annular chamber architecture is a US patent design [30] comprising a series of 8 equally spaced annular flanges arranged along a straight cylindrical bore. This geometry offers the conceptual advantage of creating multiple flow-impeding surfaces within a passive, geometry-driven flow path, and was identified in the patent literature as capable of producing pressure reduction through turbulent dissipation at each flange. The annular chamber cross-sections admitted in the patent span several configurations, including flat-plate flanges, radiused flanges, and combinations with protrusions, all sharing the common feature of inwardly directed obstructions to axial flow [29,31,32].

However, the straight-bore architecture has three critical limitations for the LH_2 aerospace application: (i) in a straight bore, the flow pressure at the flanges is nearly equal to the inlet pressure because the dynamic pressure is already fully developed; (ii) without a convergent nozzle profile, the throat velocity is not controlled and can easily reach or exceed the sonic limit; and (iii) the absence of a divergent section means that any pressure recovery after the throat is uncontrolled, potentially generating pressure levels below the cavitation threshold in the recirculating zones. These limitations motivated the complete redesign that defines the PPR final geometry.

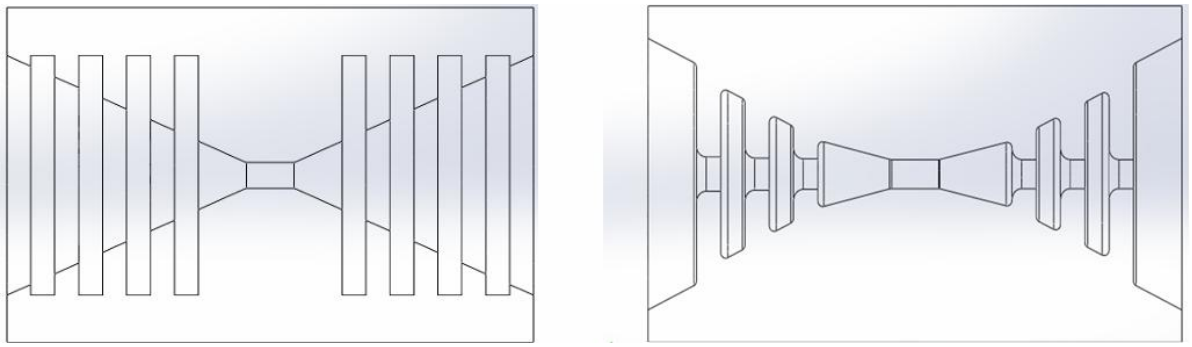


Figure 3.1: *Comparison of the US Patent reference geometry (left) and the optimized PPR final geometry (right).*

3.2.3 PPR Final Architecture: Convergent-Divergent with Annular Chambers

The final PPR geometry is a monolithic cylindrical body machined from a solid billet, with a convergent-divergent internal profile that incorporates four annular chambers and, in this particular configuration, 3 calibrated orifice plates per side (convergent and divergent). The complete architecture is illustrated in Figure 3.2.

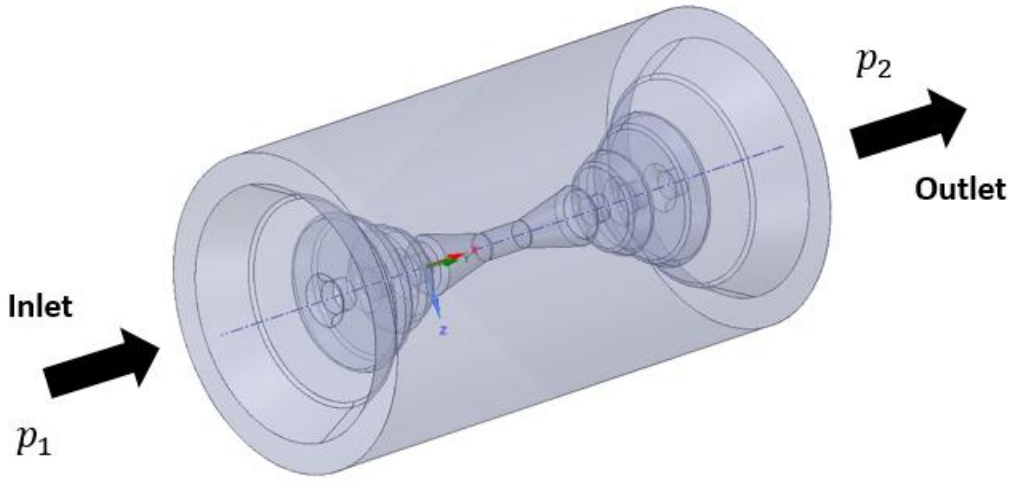


Figure 3.2: *Schematic 3D rendering of the PPR final architecture: convergent section with 6 progressively sized annular chambers and 6 orifice plates.*

3.2.4 Convergent Section with Multi-Stage Annular Chambers

The convergent section spans from the inlet (diameter equal to the pipeline bore) to the throat. Its inner wall follows a continuous profile that narrows from the full pipe radius to the throat radius over a defined convergence length. Along this convergent wall, three annular chambers are machined at positions chosen so that the chamber volume decreases progressively from inlet to throat — the largest chamber is located immediately upstream of the valve's body, where the highest kinetic energy concentration demands the greatest dissipation capacity.

The pressure-dissipation mechanism of each annular chamber operates as follows. As the main axial jet accelerates through the convergent, it passes the chamber opening. The shear layer between the high-velocity jet and the low-velocity recirculating fluid within the chamber generates a toroidal vortex ring that continuously extracts momentum from the main jet through viscous and turbulent mixing. This mechanism is distinct from, and substantially more efficient than, the flange-impingement mechanism of the patent reference geometry, in which the flow strikes a flat plate perpendicular to the main flow direction with minimal volumetric recirculation.

Six calibrated orifice plates are distributed between and around the chambers, acting as controlled restrictions that establish the pressure ratio across each dissipation zone. The orifice plate geometry, specifically the ratio of throat area to orifice area, determines the Bernoulli velocity at each restriction and hence the rate of pressure energy conversion to turbulent kinetic energy in each downstream chamber.

The lumped-parameter model prediction and the CFD results are in excellent agreement, validating both the analytical model and the mesh independence of the numerical solution.

This cross-validation across two independent CFD platforms (Ansys Fluent and SimScale) provides strong confidence in the pressure-drop predictions before experimental validation on the hydraulic test bench described in Chapter 6.

3.2.5 Throat and Cavitation Suppression

The throat section is the most mechanically and thermodynamically critical element of the PPR. It is the point of minimum cross-sectional area, maximum flow velocity, and minimum static pressure in the entire valve body. The design requirement is that the local static pressure at the vena contracta of the throat must remain above the vapor pressure of LH_2 ($p_{vap} \approx 0.9$ bar at 20.3 K) under all operating conditions [15,16].

As it will be shown through the CFD's simulations, the optimized final geometry achieves a throat velocity of 213 m/s, compared to 386 m/s for the patent reference geometry with a straight bore. This 45% reduction in throat velocity is of critical significance: a velocity of 386 m/s would produce a local pressure drop that transiently falls below pvap, initiating cavitation. The optimized geometry maintains the throat velocity at 213 m/s, providing a substantial margin against both sonic choking and cavitation onset [36,37,38].

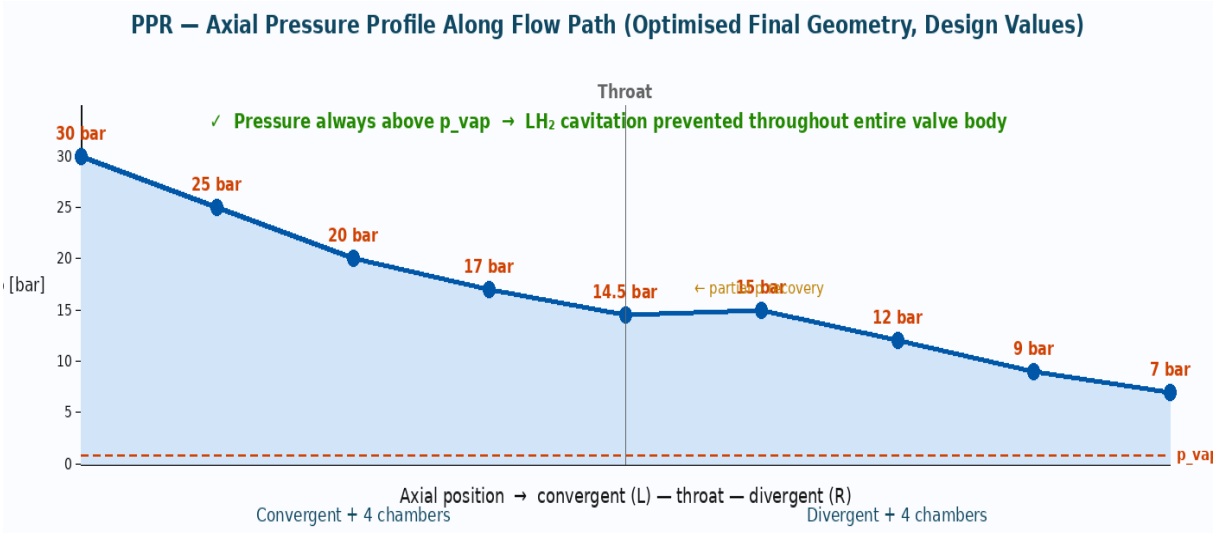


Figure 3.3: *Axial pressure distribution along the PPR final geometry from inlet (30 bar) to outlet (7 bar), computed from CFD analysis.*

3.2.6 Divergent Section and Outlet Flow Quality

The divergent section mirrors the convergent in structure, comprising four annular chambers and six orifice plates arranged symmetrically about the throat plane. Its primary function is to manage the controlled re-expansion of the flow from throat conditions to the outlet pipe conditions, recovering a portion of the kinetic energy as static pressure while simultaneously attenuating any flow non-uniformities generated at the throat. The degree of pressure recovery in the divergent section is a function of the divergence half-angle and the chamber geometry and represents a design parameter that requires optimization: excessive recovery would reduce the total achievable Δp, while insufficient recovery would leave the outlet flow with a high residual dynamic pressure component that could excite oscillations in downstream components.

An important result from the CFD analysis is that the outlet flow quality differs significantly between the two geometries: the patent reference geometry, despite its lower total Δp, produces a non-chaotic downstream flow because the absence of a convergent-divergent profile means the full flow velocity is maintained axially without the strong recirculation that characterizes the optimized design. The optimized geometry, by contrast, produces some turbulence downstream of the final divergent flange, which can be mitigated by adjusting the divergent profile angle and the final chamber geometry in subsequent design iterations.

3.2.7 Median Throat and Venturi Section

At the junction between the convergent and divergent sections, the PPR incorporates a median section, shaped as a Venturi tube. This circular cross-section throat, maintained circular throughout the entire device, represents the point of minimum flow area, maximum fluid velocity, and minimum static pressure within the device. The Venturi geometry serves a dual purpose: it maximizes the localized pressure reduction effect at the throat while simultaneously providing a controlled pressure recovery profile in the subsequent divergent section, which helps to manage the energy redistribution of the flow downstream.

The monolithic rigid body construction of the PPR, manufactured preferably from stainless steel or, alternatively, from ceramic material or via additive manufacturing as a single piece, ensures that the Venturi throat geometry is geometrically stable under all operating pressures and temperatures, including cryogenic conditions. The complete absence of moving parts, actuators, seals, or any deformable element in the PPR represents its primary structural advantage over conventional pressure-reducing devices, which typically rely on spring-loaded elements or elastomeric components susceptible to degradation in hydrogen environments.

3.2.8 Integrated Pressure Monitoring: Transverse Channels and Sensor Ports

A distinctive practical feature of the PPR is the provision of transverse channels drilled radially through the rigid body wall, each opening internally into a specific annular chamber or collecting chamber, and externally at the outer surface. These channels accommodate pressure sensors that monitor the fluid pressure at multiple axial positions along the convergent-divergent flow path, providing the experimental pressure distribution data essential for CFD model validation and digital twin calibration.

Each transverse channel port is flanked axially by a pair of peripheral grooves that receive sealing gaskets, ensuring a fluid-tight interface between the valve body and the external sensor connection elements. This instrumentation architecture directly supports the experimental methodology described in Chapter 6: by positioning sensors at each annular chamber and at both collecting chambers, a complete axial pressure map of the PPR is obtained under operating conditions, enabling the empirical identification of the chamber efficiency coefficients η_i and the per-stage discharge coefficients $C_{d,i}$ required to close the analytical model.

3.3 The Piston-Based Pressure Regulating Valve

3.3.1 Design Concept and Spool Optimization

The piston pressure regulating valve provides the active, closed-loop pressure regulation function that the passive PPR by design cannot offer. It is intended for installation in series downstream of the PPR, receiving flow at approximately 50 bar and regulating outlet pressure dynamically in the range 2–30 bar in response to downstream demand signals. The valve operates through axial displacement of a precision-machined spool, whose movement modulates the effective area of a circular crown-shaped orifice connecting the upstream and downstream chambers [40].

The critical design decision distinguishing the architecture presented in this work from conventional piston valves is the pass-through spool geometry: the spool stem extends axially through the orifice dividing the upstream and downstream volumes, creating a crown-shaped annular flow passage rather than the conventional blunt-ended geometry in which the spool face pushes toward the orifice. This single geometric modification produces a cascade of measurable improvements in fluid dynamic performance, dynamic stability, and long-term structural reliability, as quantified by the CFD analysis.

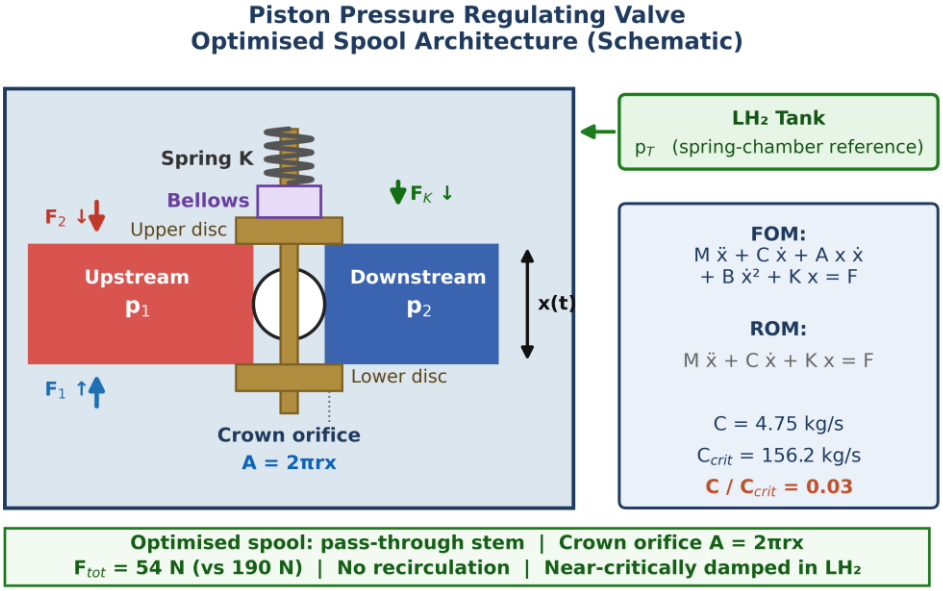


Figure 3.4: *Schematic cross-section of the optimized piston pressure regulating valve.*

The fundamental physical argument for the pass-through geometry is as follows. In the non-optimized (blunt-ended) configuration, the main flow jet exits the orifice as a high-velocity free jet into the downstream chamber, creating large recirculation vortices that produce: (i) highly irregular, fluctuating pressure forces on the spool face (±40 N fluctuations around a mean of 190 N); and (ii) localized regions of very low static pressure within the recirculation zones, approaching or exceeding the cavitation threshold. In the optimized pass-through configuration, the flow is constrained to follow the narrow annular crown passage along the spool stem, forming a coherent column-shaped jet that preserves axial momentum and suppresses vortex shedding. The result is a near-constant axial force of 54 N with fluctuations

of only ±3 N, a 3.5-fold reduction in mean force and a 13-fold reduction in fluctuation amplitude [40,43,44].

3.3.2 Spool Material: Inconel 718 Selection Rationale

The spool assembly, comprising the stem, upper disc, lower disc, and intermediate disc, is manufactured from Inconel 718, a precipitation-hardened nickel-based superalloy. Its selection for this application is governed by the specific combination of properties required by the LH_2 cryogenic environment and the mechanical loading imposed by the pressure-regulating duty [19,23,33].

Inconel 718 retains a yield strength exceeding 1000 MPa and a UTS above 1240 MPa across the temperature range from 20 K to 650 °C, with no ductile-to-brittle transition at cryogenic temperatures. Its resistance to hydrogen-enhanced decohesion (HEDE), the dominant embrittlement mechanism in nickel-based alloys under sustained hydrogen exposure, is comparatively good relative to ferritic and martensitic steels, particularly when the microstructure is controlled to minimize delta-phase precipitation at grain boundaries. Cryogenic-compatible structural materials for LH_2 systems, including 316L stainless steel for the PPR body and Inconel 718 for the spool, must also demonstrate adequate toughness for lineless tank and feed system applications [20,21,23].

With an upstream pressure of approximately 50 bar at the piston valve inlet (post-PPR) and a pressure drop of up to 40 bar across the spool orifice, the structural loads on the spool stem and discs require a material with sufficient stiffness to maintain axial alignment under pressure-induced bending moments, and sufficient fatigue resistance to sustain the cyclic loading from repeated regulation cycles.

3.3.3 Spring and Hydraulic Actuation Mechanism

The piston valve regulates downstream pressure through the controlled axial displacement of the spool, which is governed by the balance of forces acting on it as described in Section 4.2.4. The primary control element is a calibrated spring of stiffness K, which preloads the spool toward the closed position. The spring is protected from direct contact with the cryogenic LH_2 flow by a metallic bellows seal, which accommodates the axial spool displacement while maintaining a pressure-tight barrier between the spring chamber and the flow path [33,39].

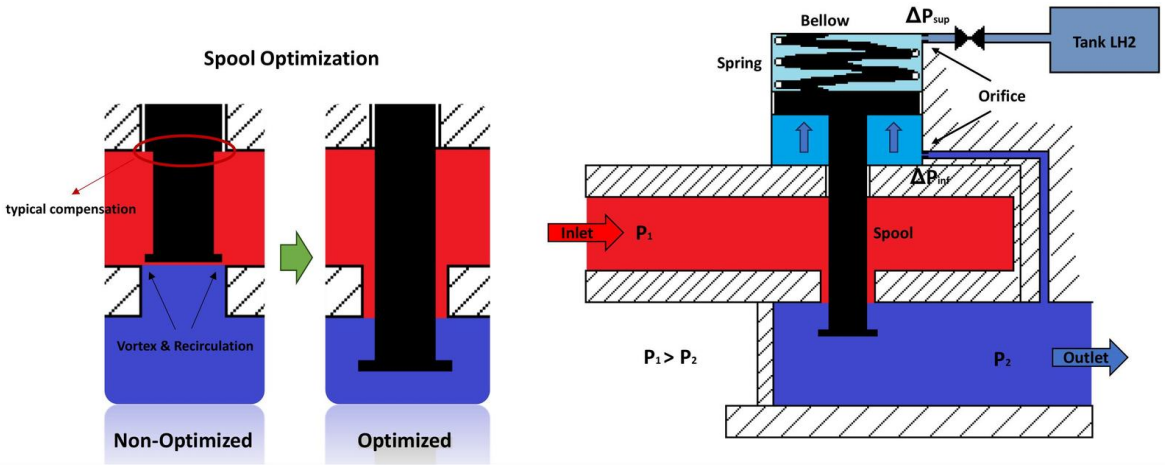


Figure 3.5: *Non-optimized configuration (left) and optimized configuration (right). Right: valve mechanism schematic showing the complete fluid circuit.*

The regulation mechanism operates as follows. At the nominal set-point pressure differential, the spring force and the net hydrodynamic force on the spool are in equilibrium at a displacement xeq that produces the required orifice area $A = 2\pi r x_{eq}$. If downstream pressure falls below the set point, due, for example, to an increase in demand, the reduced F_2 (downward force from downstream pressure on the upper disc) causes the net upward force on the spool to exceed the spring restoring force, opening the valve and increasing flow. The closed-loop regulation is thus achieved passively through the mechanical balance of spring, upstream pressure, and downstream pressure, without any electronic control system or external actuation power [34,40].

The two control chambers drawn in the schematic on the right-hand side of Figure 3.5 are arranged differently from those of a conventional spring-loaded regulator, and it is their hydraulic connection that governs the whole regulating behaviour of the valve. The main flow enters the upper duct at the inlet pressure, crosses the crown orifice around the spool stem and is collected downstream at the regulated pressure. Above the upper disc lies the spring chamber, connected to the LH_2 storage vessel through an isolation valve and a calibrated control orifice; below the disc lies the second control chamber, which communicates with the downstream line through a second control orifice. The spring chamber is therefore neither sealed at constant volume nor vented to the external environment: it is deliberately reference-pressurized, so that in steady conditions its pressure coincides with the tank pressure. Venting it to ambient, which would be the natural choice in a room-temperature application, was discarded at the concept stage for three reasons. First, a vent line would establish a direct path between a volume at 20 K and the external environment, with a heat leak that would promote local boil-off and, in the presence of humid air, the progressive formation of an ice plug in the vent passage itself, that is, a failure mode that develops silently and disables the reference of the regulator without any external evidence. Second, referencing the chamber to ambient pressure would force the spring to react the full absolute pressure insisting on the upper disc rather than the differential between the two control chambers; with an inlet pressure of the order of 50 bar this would lead to a stiffness, and consequently to a spring envelope and a preload, incompatible with the mass and volume budget assigned to the component. Third, the tank-referenced arrangement makes the regulation loop self-contained: the pressure reference is generated by the system itself, no external pneumatic supply and no electrical power are required, and the valve retains the passive character that motivates the whole architecture.

The metallic bellows fulfils, in this arrangement, exactly the function that conventional practice would assign to it. It is housed inside the spring chamber, coaxial with the spool stem, with one end anchored to the chamber closure and the other to the moving spool assembly, and it hermetically encloses the spring. It therefore replaces the sliding seal on the moving boundary between the spring chamber and the flow path: the axial travel of the spool is accommodated by the elastic deformation of the bellows convolutions instead of a rubbing contact, which yields a zero-leakage separation with no wear surfaces, no elastomeric elements, which would in any case be unusable at 20 K, and no stick-slip friction to degrade the resolution of the regulation. The effective area of the bellows is the surface over which the pressure of the spring chamber is converted into an axial force on the spool assembly, and it

is therefore the geometric parameter that links the pressure reference to the force balance discussed in Section 4.2.4.

The downstream pressure setpoint, in this architecture, is not fixed by construction: it is the outcome of the static balance between the spring and the pressures acting on the spool when the spool is at rest and the two control chambers have equalized with their respective sources, the upper one with the tank and the lower one with the downstream line. Two independent and physically distinct means therefore govern it. The first is the mechanical preload of the spring, which is established at assembly and fixes the nominal operating point; it is this passive setting that allows the valve to regulate without electrical power and without external actuation. The second is the pressure of the spring chamber, which can be acted upon through the isolation valve of the supply line: since that pressure is the reference against which the downstream pressure is balanced across the upper disc, any variation of it translates into a shift of the regulated pressure, and therefore provides the means of trimming the setpoint about its nominal value. The upstream pressure, by contrast, does not participate in this balance at all, for the geometrical reason discussed in Section 4.2.4, so that the regulated pressure is intrinsically insensitive to fluctuations of the pressure delivered by the upstream stage.

3.4 Comparison with Conventional LH_2 Valve Solutions

Chapter 2 established the limitations of conventional valve architectures for LH_2 service. This section systematically compares the PPR and piston valve concepts against the most relevant conventional solutions on a set of performance attributes directly relevant to cryogenic hydrogen systems. The comparison is summarized in Figure 3.6 and Table 3.1.

Novel Valve Architectures vs Conventional LH_2 Solutions
Design Improvement Summary

Design Attribute	Globe Valve (modif.)	Ball Valve (vented)	Pilot-Op. Reg.	PPR (this work)	Piston Valve (this work)
Moving parts	Stem + disc	Ball + seat	Pilot + main	None ✓	Spool only ✓
Actuation	Spring / pneum.	External	Pilot + main	Passive ✓	Spring + fluid
LH_2 seals	Metal (limited)	Metal (risk)	Complex	Not needed ✓	Metal bellows
Cavitation	Moderate–High	High	Moderate	Suppressed ✓	Low (opt.) ✓
Throat velocity	Uncontrolled	N/A	High	213 m/s ✓	Controlled ✓
Pressure ratio	~5:1	~2:1	~10:1	~4:1 staged	~25:1 series ✓
LH_2 damping	Insufficient	N/A	Moderate	N/A	Near-crit. ✓
Fail-safe	Limited	Limited	Good	Geometry ✓	Redundant ✓
TRL	7–8	6–7	6–7	3–4	3

Highlighted columns = novel architectures (this work)
✓ = specific improvement vs conventional solutions

Figure 3.6: *Design improvement matrix comparing the novel PPR and piston valve architectures (highlighted columns) against three conventional LH_2 valve solutions.*

Table 3.1: *Comparative assessment of the novel PPR and piston valve architectures against conventional LH_2 valve solutions. Green entries indicate specific design improvements. TRL per ESA scale.*

Design Attribute	Globe Valve (modif.)	Ball Valve (vented)	Pilot-Op. Reg.	PPR (this work)	Piston Valve (this work)
Moving parts	Stem + disc	Ball + seat	Pilot + main valve	**None ✓**	**Spool only ✓**
Actuation	Spring / pneum.	External force	Pilot + actuator	**Passive ✓**	Spring + fluid
LH_2 seals	Metal (limited)	Metal (risk)	Complex	**Not needed ✓**	Metal bellows
Cavitation control	Moderate–High	High (trapping)	Moderate	**Suppressed ✓**	**Low ✓**
Throat velocity	Uncontrolled	N/A	High	**213 m/s ✓**	**Controlled ✓**
Pressure ratio	~5:1	~2:1	~10:1	~4:1 (staged)	**~25:1 (series) ✓**
Damping in LH_2	Insufficient	N/A	Moderate	Not applicable	**Near-critical ✓**
Fail-safe mode	Limited	Limited	Redundant	**Geometric ✓**	**Redundant ✓**
TRL	7–8	6–7	6–7	3–4	3

Three design principles emerging from this comparison deserve particular emphasis:

1. *Passive geometry as a reliability multiplier*: the elimination of all moving parts from the Stage 1 pressure reduction function (PPR) is not merely a simplification, but it is a qualitative change in failure mode distribution. A passive geometric device has no wear, no lubrication requirement, no seal cycling fatigue, and no actuation failure mode. The only credible degradation mechanisms are erosion of the chamber and orifice surfaces (manageable through material selection) and blockage by particulate contamination (addressable through upstream filtration). This contrasts with conventional Stage 1 regulators, whose spring and seat cycling fatigue, bellows fatigue, and pilot valve clogging represent statistically dominant failure modes in cryogenic service.
2. *Distributed pressure drops as a structural safety guarantee*: the multi-stage architecture of the PPR ensures that no single point in the system simultaneously sustains both a large pressure differential and a low static pressure. This is a structural safety property that does not depend on control system performance or sensor accuracy: it is guaranteed by the geometry for any mass flow rate within the design range. Conventional single-stage regulators depend on precise actuation response to avoid extended low-pressure excursions; the PPR provides cavitation protection by geometry.

3. *Optimized geometry as a dynamic performance enabler*: the pass-through spool optimisation is the enabling condition for stable closed-loop regulation in LH_2. As the force analysis demonstrates, a conventional blunt-ended spool operating in LH_2, with F_{tot} = 190 N, C = 4.75 kg/s, and C_{crit} = 156.2 kg/s — cannot converge to a stable equilibrium without an external damper. The pass-through optimization reduces F_{tot} to 54 N while the FOM chamber coupling provides the missing damping, achieving near-critical response without any additional mechanical component.

3.5 Two-Stage System Architecture and Integration

The two valve architectures are designed to operate in series, forming a complete and complementary pressure management chain from the LH_2 storage vessel to the downstream consumer. The PPR performs the large, coarse pressure reduction step (Stage 1), bringing the high-pressure storage conditions down to an intermediate level compatible with the inlet requirements of the piston regulating valve. The piston valve then performs the fine, closed-loop regulation step (Stage 2), maintaining the outlet pressure at the setpoint demanded by the fuel cell or thruster control system [39,40].

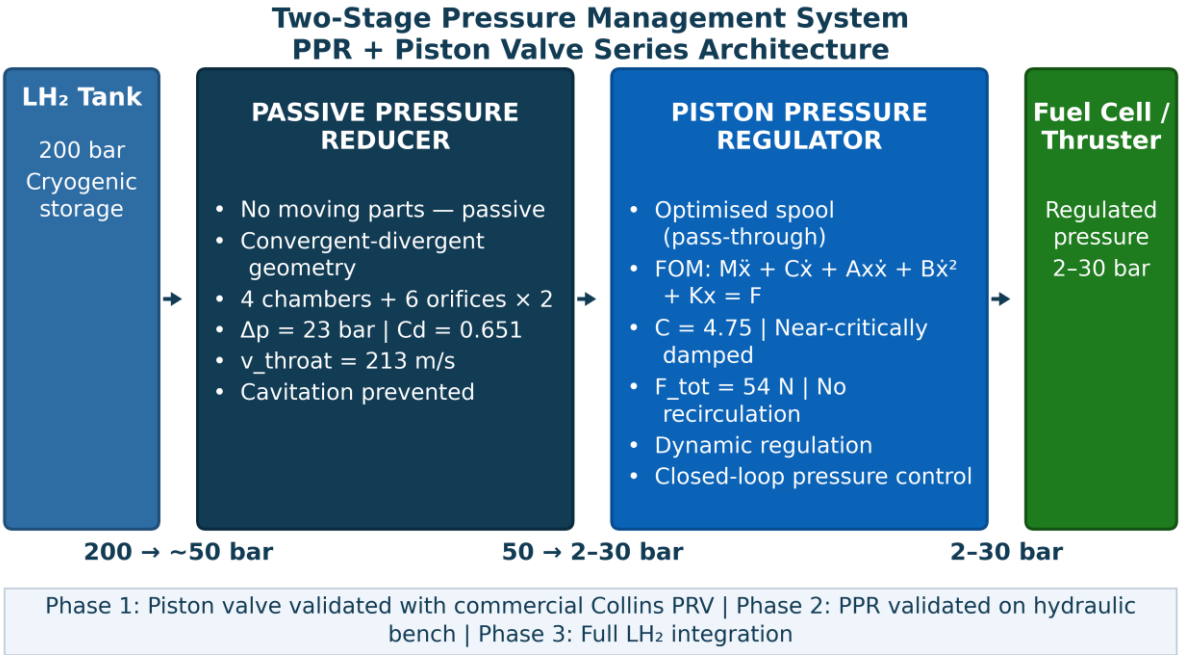


Figure 3.7: *Two-stage pressure management system architecture: PPR (Stage 1, passive, 200→~50 bar) in series with the piston regulating valve (Stage 2, active, 50→2–30 bar), supplying the regulated outlet pressure to the fuel cell or thruster.*

The choice of ~50 bar as the intermediate pressure between the two stages is governed by two principal considerations: it falls within the operational range commonly adopted in cryogenic propulsion feed systems for intermediate regulation stages, as documented extensively in the technical literature on multi-stage pressure management for liquid hydrogen applications [12,13,14,28]; it keeps the Stage 2 inlet pressure below the threshold at which the piston valve spool forces exceed the available viscous damping in the non-optimized geometry. The selection of an intermediate pressure in the range 40–60 bar is further supported by Schoenman and Gill [12], who identified this pressure regime as the most favorable operating point for

spring-loaded spool regulators in cryogenic service, balancing actuator force requirements against structural mass and seal reliability, and by Rault et al. [13], who demonstrated experimentally that multi-stage cryogenic regulators operating with an intermediate pressure in this range exhibit significantly reduced dynamic instability compared to single-stage architectures subjected to the full pressure differential. NASA passive cryogenic feed system studies [28] further confirm that intermediate staging in the 40–60 bar range represents the practical optimum between component count and system reliability for LH_2 distribution lines operating at storage pressures above 150 bar.

From a system integration perspective, the two devices are hydraulically matched through the valve coefficient C_v framework, as standardized in ISA-75.01.01 [39]. For the PPR, C_v is a fixed geometric property determined by the throat area and the chamber configuration. For the piston valve, C_v varies with spool displacement x according to $Q = C_d \cdot 2\pi r \cdot x \cdot \sqrt{(2\Delta p/\rho)}$, ensuring that the two devices can be hydraulically matched through rational selection of the orifice radius r and the equilibrium displacement x_{eq}. The matching condition requires that the piston valve, at its nominal set-point displacement, presents a downstream impedance consistent with the PPR operating in its design-point pressure regime, a condition verifiable analytically through the lumped-parameter model.

Furthermore, the thermodynamic implications of the two-stage architecture extend beyond pressure management. Each stage dissipates a fraction of the total fluid enthalpy as heat through turbulent mixing, in Stage 1 within the PPR annular chambers, and in Stage 2 across the spool orifice. At the cryogenic operating conditions of LH_2, this dissipation must remain below the threshold that would initiate ortho-to-para hydrogen conversion or localized flash evaporation, as discussed by Leachman et al. [37] in the context of thermodynamic state transitions in cryogenic hydrogen. The distributed pressure drop of the PPR, by keeping the per-stage enthalpy dissipation below critical limits, provides an intrinsic thermal safety margin that a single-stage reduction device cannot guarantee [15,16,37]. This thermodynamic compatibility between the two stages, combined with the dynamic stability demonstrated by the FOM for the piston valve [40] and the passive cavitation protection intrinsic to the PPR geometry, constitutes the defining engineering advantage of the proposed two-stage architecture over conventional single-device pressure management solutions documented in Chapter 2.

Chapter 4

Mathematical Model

The architectural and design choices presented in Chapters 2 and 3 established the two-stage pressure management philosophy at the core of this work: a Passive Pressure Reducer operating as a geometry-driven first stage, followed by an actively controlled piston valve for fine downstream regulation. Chapter 3 introduced the physical architecture and the design rationale of both devices, establishing the governing geometric parameters, the operating pressure ranges, and the key performance targets, a 23 bar passive pressure reduction for the PPR and near-critically damped spool dynamics for the piston valve, that the mathematical model developed in this chapter is required to reproduce and predict. What remains to be established is a rigorous mathematical framework capable of predicting their behaviour quantitatively under varying operating conditions, a framework that can serve as the primary design evaluation tool prior to experimental testing on the hydraulic bench described in Chapter 6.

This chapter develops that framework in two complementary parts. The first addresses the PPR: building on the convergent-divergent geometry and the annular chamber architecture introduced in Section 3.2, a lumped-parameter fluid dynamic model is constructed that relates the volumetric flow rate, the per-stage pressure drops, and the global discharge coefficient C_D to the geometric parameters of the device. The model exploits the classical orifice discharge equation and introduces a jet correction factor to account for the velocity enhancement that each upstream orifice imparts on the flow entering the next stage, a physical effect specific to the closely spaced multi-orifice architecture of the PPR and absent from single-stage throttling models.

The second part addresses the piston valve: starting from the mass-spring-damper idealization introduced in Section 3.3, the Reduced Order Model (ROM) is first formulated and its critical limitation in low-viscosity LH_2 is demonstrated analytically. The Full Order Model (FOM) is then derived, showing how the explicit modelling of the chamber pressure dynamics introduces the nonlinear coupling terms $A\dot{x}\dot{x}$ and $B\dot{x}^2$ that provide geometry-derived damping independent of fluid viscosity, the key result that makes stable closed-loop regulation in LH_2 achievable without an external mechanical damper.

Both models are implemented in MATLAB/Simulink and their predictions are compared against the CFD results of Chapter 5, establishing the cross-validation pathway that closes the analytical-numerical loop of the dissertation.

4.1 PPR's Lumped-parameter Analysis

The analysis of the PPR's architecture (Fig. 4.1) is based on fundamental fluid dynamic principles and the physics of flow through an orifice. Since the PPR is characterized by a series of orifices spaced by ring-shaped chambers within a conduit that exhibits convergent-divergent geometry, it is of utmost importance to set up a relationship between the volume flow rate through each individual orifice and the related pressure drop.

For the purposes of the analysis, a pressure drop Δp of 23 bar through the entire PPR is set up as boundary condition, using liquid hydrogen as operating fluid. The initial geometry of the PPR and the pressure drop at the boundary allow the resolution and closure of the fluid dynamic problem. The most important parameters are then computed: the volume flow rate Q through the whole PPR, and the related discharge coefficient C_D.

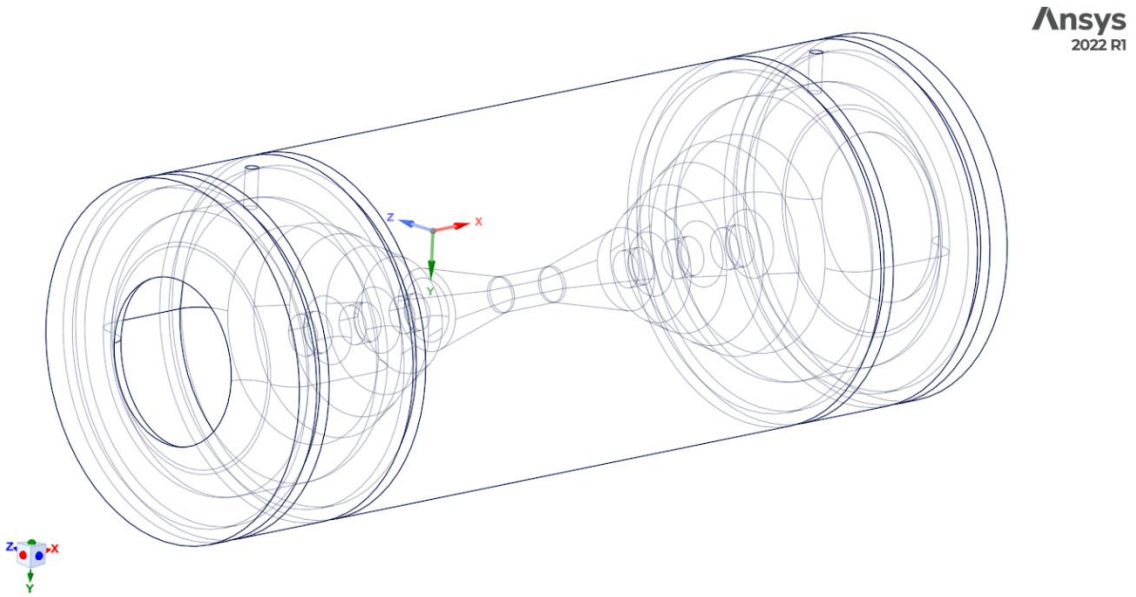


Figure 4.1: *3D Rendering of the PPR used during the experimental tests.*

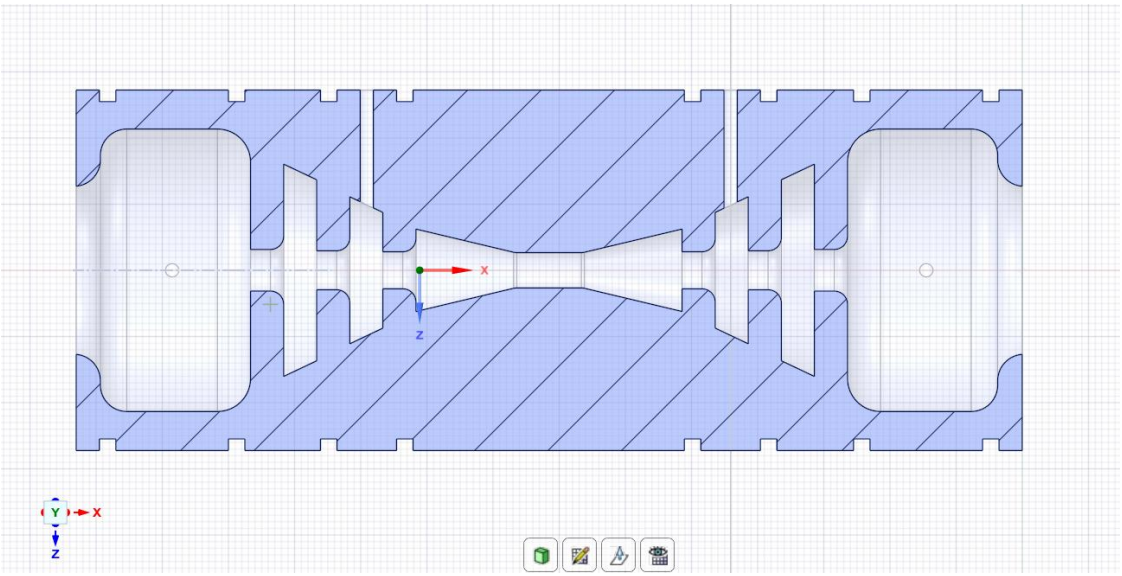


Figure 4.2: *2D Cross section of the PPR.*

Depending on the Reynolds number, the flow regime through an orifice can be laminar, turbulent or in transitional conditions. To satisfy the mass law conservation, the speed of the flow through an orifice must necessarily increase relative to the value that the orifice has upwards. At high Reynolds numbers the inertia forces of the fluid prevail over the viscous forces; therefore, in the first approximation, the pressure jump through the orifice is caused by the acceleration of the fluid particles.
At Reynolds bases, however, the main cause of the pressure drop is the not negligible internal cutting forces due to the viscosity.

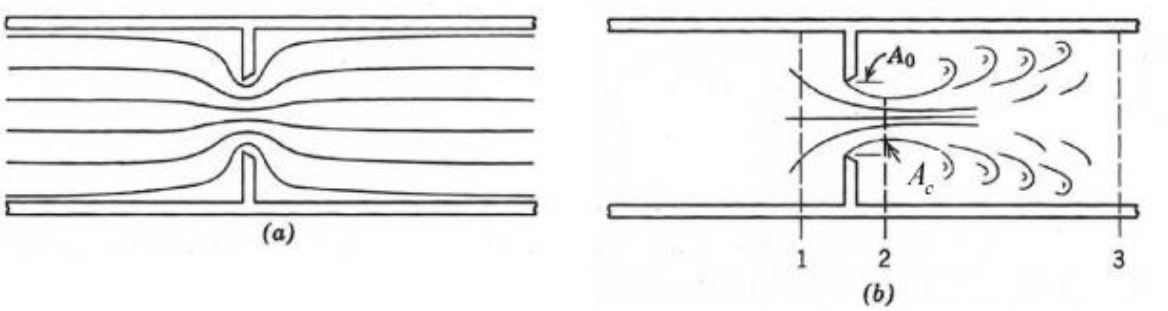


Figure 4.3: *Flow across an orifice: laminar flow (a) and turbulent flow (b).*

It is considered the most interesting case of the turbulent flow. Based on the above considerations, in case of turbulent flow it can be said that in the transition from section 1 of upstream to section 2 (contracted vein) the flow is potential: experience justifies the use of the Bernoulli equation in this area.
As the emitted jet separates from the wall, its area is smaller than that of the opening and continues to decrease for a short period down the same due to the inertia of the particles.

4.1.1 Global Discharge Coefficient of the PPR

The flow of liquid hydrogen fluid through the orifices of the PPR can be modeled, precisely, by considering the classical flow equations that result from mass, momentum and energy conservation.
In this approach, the discharge coefficient C_d across the orifice is supposed only dependent on the Reynolds number, as it occurs for a circular section orifice [46]:

$$Q = C_d A \sqrt{\frac{2\,\Delta p}{\rho}} \tag{4.1}$$

where Q is the volume flow rate, C_d the orifice discharge coefficient, A the orifice area, Δp the pressure drop across the orifice and ρ the density of the operating fluid.
The relationship between the orifice discharge coefficient and the Reynolds number is generally expressed as:

$$C_d = \begin{cases} k\sqrt{Re} & if\ Re < Re_{cr} \\ 0.611 & otherwise \end{cases} \tag{4.2}$$

where the multiplying parameter k is a constant and Re is the Reynolds number, function of the orifice geometry.

Since the geometry of the PPR is made of multiple orifices and annular chambers, the behavior of the discharge coefficient of the whole convergent-divergent part is expected to be in accordance with the C_d of a single circular orifice.
The configuration of the PPR under analysis is symmetrical with respect to the throat: three orifices divided by two annular chambers in the convergent section of the duct, and three orifices spaced by two annular chambers in the divergent part, resulting in a total of six orifices and four annular chambers. The sizes of the orifices are different, decreasing from upstream to the throat and growing from the throat to downstream. In this way, with variable area sizes, it is possible to ensure a gradual reduction of pressure through the PPR, avoiding drastic pressure drops concentrated in tight areas, which can lead to excessive thermal stress and erosion on the walls and risk of cavitation of fluid flow.
With the considered pressure drop, the flow of liquid hydrogen results turbulent.
Due to the very low dynamic viscosity and density of liquid hydrogen and the small area of the orifices, the flow regime through the PPR leads to very high Reynolds number, which is far beyond the critical Reynolds number Re_{cr} that delimits the laminar regime.
In the considered scenario of a $\Delta p = 2.3 * 10^6\ Pa$ as pressure drop across the whole PPR, being the density of liquid hydrogen $\rho_{LH_2} = 70.97\ kg/m^3$, with dynamic viscosity $\mu_{LH_2} = 1.392 * 10^{-5}\ Pa\ s$ [47], with a throat diameter of $D = 5.34\ mm$, the resulting Reynolds number is of the order of magnitude of:

$$Re = \frac{\rho_{LH_2} v_t\ D}{\mu_{LH_2}} \cong 6.9 * 10^6 \tag{4.3}$$

with v_t the velocity of the flow across the throat of the PPR, which can be computed with good approximation with Bernoulli's equation. Since the orifices are designed with a rounded entrance edge and a live spike on the exit edge (it can be seen in Fig. 4.2), it is known from orifice theory [48] [49] that the contracting vein of the flow through this kind of circular orifice is of maximum thickness, therefore with a flow contraction coefficient C_c equal to 1 and a discharge coefficient C_d which ranges from 0.98 to 0.99 [50]. Due to the care used in the design of the orifices of the PPR, the discharge coefficient for each orifice can be considered equal to 0.98 for the lump-parameter analysis; this value, along with the specific area of each orifice and the volume flow rate across the PPR, can allow the direct computation of the pressure drops across the staged orifices.
The discharge coefficient C_D of the whole PPR is the result of the combined discharge coefficients of the six orifices and the relative annular chambers; this parameter represents the efficiency which the orifice-annular chamber combination allows the passage of a certain volume flow rate with. If the volume flow rate through the first orifice represents 98% of the theoretical flow rate that would pass if there were no dissipation of fluid-dynamic and viscous nature, and this flow passes through six orifices in succession, this implies that the global C_D will be due to the combination of efficiencies through all the orifices and annular chambers. Since the dissipative contribution of the annular chambers is not known a priori, given the absence of data in the literature, it can be assumed in the first approximation that each chamber

contributes to 5% reduction of the C_d of the orifice to which it is coupled. Through CFD analysis it will then be possible to compute a more accurate value of the annular chamber's contribution. The overall discharge coefficient C_D of the PPR can therefore be estimated in first approximation as the multiplication of the C_{d,o_i} of all the orifices, minus the additional C_{d,a_i} of each annular chamber, according to the following formula:

$$C_D = \prod_{i=1}^{6}(C_{d,o_i} - C_{d,a_i}) = \prod_{i=1}^{6}(C_{d,o_i} - \frac{5}{100}C_{d,o_i}) = \left(0.98 - 5\frac{0.98}{100}\right)^6 = 0.651 \qquad (4.4)$$

The resulting C_D value of 0.651 approaches the asyntotic value of $C_D = 0.611$ (Von Mises, 1917), reached for high Reynolds numbers. The C_D value of the combined orifice-annular chamber is therefore equal to 0.931, lower than the value of 0.98 initially considered, but physically more realistic since the annular chamber itself also represents an additional obstacle that the flow must overcome.

From this preliminary result it is clear that the performance of the PPR decreases as the number of orifices and annular chambers increases, because of the progressive losses due to friction and turbulence. If a single rounded orifice is used instead of many as in the presented work, the discharge coefficient of the PPR would be equal to 0.98, but the resulting pressure drop would be too high and the local pressure could fall below the fluid's vapor pressure, inevitably leading to cavitation. The use of multiple orifices spaced by annular chambers guarantees a gradual and controlled reduction of pressure along the entire path of flow, thus avoiding the risk of cavitation.

4.1.2 Flow Through a Circular Orifice: Governing Equations

With the global CD = 0.651 determined, the volumetric flow rate Q is directly computed from Eq. 4.1, with At representing the throat area of the PPR, the minimum cross-sectional area encountered by the flow:

$$Q = C_D A_t \sqrt{\frac{2\,\Delta p}{\rho}} = 0.00371\ \frac{m^3}{s} \qquad (4.5)$$

where A_t represents the area of the throat of the PPR, the minimum section that the flow encounters during its path from upstream to downstream. The value of Q computed in Eq. (5), which will be compared with the value obtained by the CFD analysis in the next Chapter, represents the expected volume flow rate through the PPR, with a pressure drop set to 23 bar between upstream and downstream. Once the volume flow rate is computed, it is thus possible to calculate the pressure drop contribution of each orifice by solving Eq. (1) with respect to Δp:

$$\Delta p = \sum_{i=1}^{6}\Delta p_i = \sum_{i=1}^{6}\frac{1}{2}\rho\left(\frac{Q}{C_{d_i}A_i}\right)^2 = \frac{1}{2}\rho\frac{Q^2}{{C_d}^2}\sum_{i=1}^{6}\left(\frac{1}{A_i}\right)^2 \qquad (4.6)$$

where A_i represents the i-orifice area. The above formula therefore shows that the total pressure drop depends on the square of the areas of the orifices. Small orifices involve high pressure drops, but at the same time this implies greater difficulties in the mechanical manufacturing and engineering of the orifices, and the risk that the flow cavitates reaching too low pressures due to high flow velocities. A large number of orifices, on the other hand, guarantees higher pressure reductions, thus wider operational range, but greater fluid dynamic dissipation and friction losses. Therefore, it is essential to be able to ensure a compromise between the number of orifices within the proposed architecture and their area, so as to meet the requirements of the design phase.

From fluid dynamics theory it is well known that the discharge coefficient C_d is always less than 1 due to the energy losses and turbulence through the flow passage across a small opening. In this case, each orifice is positioned in spatial succession with respect to the previous one, and this implies that the flow jet of the contracting vein that comes from one orifice conveys directly to the entrance of the next orifice. The result is a continuous and long jet which crosses all the orifices, taking the form of a column-shaped jet, as it will be shown in the CFD analysis. If the orifices are located at sufficient distance from each other, then the jet would have the time to lose velocity and thus energy, and the amount of flow capable of passing into the next orifice would be governed by the discharge coefficient C_d through the Eq. (2). However, if the orifices are close enough to be fed by the previous jet, then these jets can be considered as local flow sources and therefore contributing to virtually raising the capability of the next orifice to handle a higher flow rate than theoretically allowed. Following this reasoning, it is necessary to correct the local C_d of each orifice, expect the first one, with a *k* adjustment factor, which takes into account the nature of the flow and the geometry of the orifice [51][52]. In this way, the new C_d of the orifice can be considered virtually greater than 1, computed as the product of the actual C_d and the adjustment factor *k*.

The pressure drop contribution Δp_i of each individual orifice between the free upstream flow and the downstream section of the PPR can be computed through the new modified system reported in Eq. (7), which takes into account the adjustment factor k_i through the new discharge coefficient C_{k_i}:

$$\begin{cases} \Delta p = \sum_{i=1}^{6} \Delta p_i = \sum_{i=1}^{6} \frac{1}{2}\rho \left(\frac{Q}{C_{k_i} A_i}\right)^2 = \frac{1}{2}\rho \, \frac{Q^2}{C_d} \sum_{i=1}^{6} \left(\frac{1}{k_i A_i}\right)^2 \\ C_{k_i} = k_i \, C_d \qquad i = 1, \dots, 6 \\ k_1 = 1 \\ k_i > 1 \qquad\qquad i = 2, \dots, 6 \end{cases} \tag{4.7}$$

It is important to emphasize the fact that the discharge coefficient C_k used in the above system of equations is not physically equal to the C_d known from fluid dynamic theory, but this coefficient is useful from a mathematical point of view to represent the contribution of the orifices interactions through a corrective term. This correction takes into account the fact that each orifice is able to accept a certain volume flow rate in relation to the pressure jump through it. If the pressure drop and the area of the orifice are constant values, it is necessary to increase

the flow velocity in order to reach higher volume flow rates. This increase is due to the flow jet that comes from the previous orifice, mathematically idealized in this analysis as a flow source.
In the case of the first orifice, the value of the corrective term k_1 is considered equal to 1 because there is not an upstream jet before the orifice that can accelerate the flow through it. Therefore, the C_d of the first stage of PPR does not require any corrections.

4.1.3 Per-Stage Pressure Drop

The pressure drop contribution Δp_i of each stage is computed by applying the modified flow system that accounts for the jet correction factor ki, which models the velocity increase at each orifice due to the upstream jet originating from the previous stage. The corrected discharge coefficient for each orifice is $C_{ki} = k_i \times C_d$, where $k_1 = 1$ (no upstream jet for the first orifice) and $k_i > 1$ for all subsequent stages.

Table 4.1*: Pressure drop contribution Δp_i of each stage*

Stage n°	**Diameter [mm]**	C_{k_i}	Δp_i**[bar]**
1	6.30	0.93	5.80
2	5.90	1.49	2.92
3	5.60	1.44	3.89
Throat	5.34	2.0	2.44
4	5.60	1.44	- 3.89
5	5.90	1.49	2.92
6	6.30	0.93	5.80
Total Δp			19.88

As can be noticed from Table 4.1, the sum of the contributions of the pressure drops of the convergent-divergent section of the PPR is equal to 19.88 bar, different from the value of 23 bar set at the beginning of the lumped-parameter analysis. This significant discrepancy is due to the fact that the convergent and the divergent part of the PPR work differently on reducing the pressure on the flow, which will be demonstrated through CFD. Therefore, it cannot be assumed a symmetrical pressure drop across the PPR.
If the value of the desired 23 bar is split by symmetry between the convergent and divergent section of the PPR, a pressure reduction of 11.5 bar between the upstream section and the throat would be obtained, as long as 11.5 bar between the throat and the downstream section. This symmetrical pressure drop is not truly representative of the real physics of the flow that passes through the PPR, since the mutual interaction between the combination of the orifices and annular chambers is not about to be symmetrical with respect to the throat. As far as the convergent section is concerned, the flow is continuously accelerating due to the decreasing

section until it meets the throat. In the divergent section, however, the flow has the possibility through the first chamber after the throat to recover its pressure, since the section enlarges for the first time. For this reason, there is a pressure recovery in correspondence to the first orifice after the throat, namely orifice n° 4. This is why the minus sign is present in front of $p_i = -3.89\ bar$.

The last annular chamber is decisive in the contribution of the pressure drop, since the flow reaches its final condition, accelerating for the last time with a static pressure drop, then decelerating. This asymmetrical flow behavior therefore suggests that the pressure drop in the convergent and divergent section is different in value, which will be demonstrated by the CFD analysis.

Another way to estimate the contributions of Δp_i for each orifice is through the mass conservation law, which can be applied to the flow entering the first orifice, calculating its velocity in the contracted vein (hypothesis of $C_c = 1$). Also in this case, it is necessary to consider a corrective factor that includes the increase in the velocity of flow through the orifice i deriving from the jet coming from the previous orifice *i -1*. The real velocity through the orifice is therefore higher than the theoretical velocity derived by the mass conservation law.

As will be shown from the results of the CFD analysis, the annular chambers, in addition to allowing a gradual decrease in flow pressure, also enable the lamination of the flow maintaining it as a column-shaped jet through the orifice. This action prevents the flow from decelerating excessively as it crosses the stage constituted by the orifice and annular chamber, resulting in a continuous pressure decrease without significant pressure recoveries. By using Bernoulli equation and taking into consideration the resistance effect of the discharge coefficient on the local pressure reduction, it is possible to approximate the pressure drop by calculating the flow rate through each orifice.

$$p_i + \frac{1}{2}\rho {v_i}^2 = p_{i+1} + \frac{1}{2}\rho {v_{i+1}}^2 \tag{4.8}$$

$$\Delta p_i = p_i - p_{i+1} = \frac{1}{2}\rho_{LH_2}({v_{i+1}}^2 - {v_i}^2) \tag{4.9}$$

$$\begin{cases} v_{i+1} = \sqrt{2\,\dfrac{\Delta p_i}{\rho_{LH_2}} + {v_i}^2} & i = 1, \dots, 5 \\ v_i = \dfrac{Q}{A_i} \\ \Delta p_i = \dfrac{1}{{C_{d_i}}^2}\dfrac{1}{2}\rho_{LH_2}({v_{i+1}}^2 - {v_i}^2) \end{cases} \tag{4.10}$$

where v_i is the real velocity of the flow through orifice *i*, v_{i+1} is the velocity through the immediately next staged orifice *i+1* and C_{d_i} is the discharge coefficient of each orifice, assumed equal to 0.931 as previously computed. In the above equations the corrective

coefficient k_i is not reported since it is already included in the terms Δp_i used from Table 4.1, through coefficient ${C_{d_i}}^2$.
The values of the theoretical velocity $v_{i+1,th}$, the real velocity v_{i+1} and the corrected pressure drop Δp_i for each PPR's stage are computed through the equations of system Eq. (4.10) and listed in the following table:

Table 4.2*: Pressure drop contribution Δp_i of each stage*.

Stage n°	$\boldsymbol{v_{i+1,th}}$ **[m/s]**	$\boldsymbol{v_{i+1} = k_i v_{i+1,th}}$ **[m/s]**	$\boldsymbol{\Delta p_i}$**[bar]**
1	119.1	128.3	5.80
2	135.8	157.2	3.38
3	150.7	188.9	4.39
Throat	165.7	206.3	2.82
4	152.1	177.8	- 4.48
5	165.5	199.5	3.35
6	203.8	236.9	6.68
Total Δp			21.94

As can be noticed from the values of the real velocity of the flow v_{i+1} shown in Table 4.2, it is clear that the correction made considering the orifice jet contribution is substantial on the increase in the velocity of the flow through each stage. This correction also makes more accurate the flow and pressure field through the stages, pointing out the pressure recovery in the initial section of the divergent. According to this lumped-parameter analysis presented in this work, the maximum flow velocity reached in the final stage of the PPR, corresponding to the orifice n° 6, is equal to 236.9 m/s, while the total pressure drop across the PPR is around 21.94 bar, a much closer value to the boundary pressure conditions of 23 bar. These data will be compared with the results of the CFD analysis in the following section.

4.2 Preliminary Numerical Model of the Piston Pressure Regulating Valve

4.2.1 Introduction and Fluid Dynamic Challenges

Piston valves play a crucial role in pressure regulating mechanisms within several industries, such as aerospace, aeronautics and energy. Their ability to precisely control fluid pressure is essential, especially when working with cryogenic fluids such as liquid hydrogen, which is characterized by extremely low temperatures and unique fluid dynamic characteristics. However, the use of piston valves in such demanding environments presents a number of

complexities and significant challenges, predominantly due to the complexity of manipulating cryogenic fluids.

Liquid hydrogen, which is commonly used as a rocket propellant in aerospace propulsion applications, behaves very differently compared to fluids at room temperature. At cryogenic temperatures, the gases condense into liquids whose density, although extremely high when referred to the gaseous state from which they originate, remains remarkably low in absolute terms, and their physical properties such as density, viscosity, and thermal expansion, are drastically altered. Hydrogen is a case in point, since its density is frequently described in ambiguous terms. Liquid hydrogen at its normal boiling point (20.28 K) has a density of approximately 70.8 kg/m³, that is, about 790 times the density of gaseous hydrogen at 273 K and atmospheric pressure (0.0899 kg/m³): with respect to the gaseous state from which it is obtained, LH_2 is therefore an extremely dense medium, and it is precisely this density jump of nearly three orders of magnitude that makes liquefaction attractive for storage. In absolute terms, however, LH_2 remains by far the lightest of all liquids, its density being only about 7 % of that of water, so that a given mass of propellant still occupies a volume roughly fourteen times larger than the same mass of water. The two statements are not in contradiction, and both are directly relevant to valve design: the first governs the momentum flux of the jet and hence the hydrodynamic forces acting on the moving elements, while the second governs the volumetric flow rate and hence the passage areas that the component must provide for a given mass flow requirement. These specific features constitute fluid dynamic challenges for pressure piston valves designed for fluids with more conventional properties. In addition, thermal contraction of valve components can affect tolerances and clearances, thereby compromising the functionality of the valve. Furthermore, liquid hydrogen has an exceedingly low viscosity compared to fluids at ambient temperature. This low-viscous fluid has the potential to influence the fluid's flow behavior within the valve, resulting in flow restrictions, pressure drops, and increased wear and strain on valve components. In such circumstances, maintaining precision pressure control becomes even more crucial.

Cryogenic fluids have a natural tendency to boil and vaporize when exposed to higher temperatures. This can occur during the pressure reduction procedure or even when the flow reaches high velocities, resulting in phase changes within the valve itself. These phase changes can destabilize the flow control mechanisms and make it difficult to maintain precise pressure regulation.

The presented work focuses therefore on performing a preliminary analysis and optimization via CFD of a piston valve operating with liquid hydrogen, to address the complex fluid dynamic challenges posed by the considered cryogenic fluid. A simplified model of the dynamic response of the piston in the optimized and non-optimized case is then presented, comparing the related solutions in terms of efficiency and performance of the valve’s regulating mechanism.

The analysis begins by creating a simplified geometry, suitable for the CFD analysis, of the main piston body of a generic pressure regulating valve. By simulating the behavior of liquid hydrogen flow across the piston’s body, it is then shown how the results of the performed CFD

simulations provide a clear visualization of the critical aspects such as flow patterns, pressure distribution, velocity flow field and recirculating zones.

4.2.2 Problem Setup

The analysis and optimization of the piston valve's simplified architecture (Fig. 4.4) performed in this study is based on fundamental fluid dynamic principles and the physics of flow crossing a narrow section. To optimize a conventional pressure regulating valve for cryogenic applications, it is crucial to be aware of its constituent elements and their respective weaknesses and strengths.

A pressure regulating valve is able to govern the fluid pressure of a feeding system using the mechanical forces acting on a control spring and the relative movement of the commanded piston. This is accomplished by adjusting the valve's opening to balance the forces operating on the piston itself, thereby maintaining stable and controlled outlet port pressure. This particular kind of valve is commonly used in numerous industries to maintain the desired pressure levels in fluid systems.

If the pressure at the outlet port fluctuates, owing to recirculation zones or chaotic velocity field downstream the control surfaces, the piston's position will start to change continuously in order to maintain the desired pressure. If the outlet pressure falls below the set pressure, the piston will move to allow more fluid to pass and increase the pressure. Instead, if the outlet pressure exceeds the specified pressure set value, the piston will move to restrict the flow and therefore to counterbalance this perturbation.

The occurrence of fluid recirculation zones and significant localized pressure reductions across a pressure regulating valve is a crucial issue with far-reaching thermal and dynamic consequences for the overall system and the performance of the regulating mechanism. Complex fluid dynamics, valve geometry, and operational conditions frequently give rise to these two phenomena, which are closely related. Understanding the impact of these criticalities is essential for comprehending their potential effects on operating efficiency, safety, and valve's integrity.

Fluid recirculation zones are regions within and around the valve where fluid flow reverses or becomes stagnant, instead of passing smoothly through the valve. These zones might arise for a variety of reasons, including improper valve design, inadequate flow conditions, or fluid properties that cause turbulence and separation [53]. This phenomenon can lead to localized heat transfer challenges within the system. Fluids that are stagnant or move slowly can cause temperature stratification, leading to the freezing or overheating of particular valve components. These thermal variations can compromise the structural integrity and functionality of the valve and its surrounding components [54].

In addition, fluid recirculation zones frequently cause pressure fluctuations and instability downstream of the valve. As the fluid flow becomes erratic, pressure levels may fluctuate, influencing the valve's overall pressure regulation performance. These fluctuations may lead to pressure levels outside of the designed range, compromising the safety and reliability of the system. The stagnant or reversing flow can transport abrasive particles or contaminants that damage the valve's internal surfaces. This erosion may reduce the valve's efficiency and

performance over time, necessitating maintenance and possible component replacement, particularly when dealing with cryogenic fluids such as liquid hydrogen.
Large localized pressure drops can induce cavitation, which occurs when the fluid pressure falls below the vapor pressure, resulting in the formation and disintegration of vapor bubbles. This process of cavitation generates intense pressure waves and vibrations that can cause damage to the valve and adjacent components. In addition, a significant localized pressure drop might interfere with the controllability of the valve. As unexpected pressure drops occur, the valve may struggle to maintain its desired pressure setpoint, resulting in system instability and fluctuations [55].
For the reasons listed above, it is essential to design valve architectures and mechanisms that can mitigate the impact of these critical phenomena.
As a starting point of the presented analysis, a pressure drop of 23 bar is applied to the entire system using liquid hydrogen as operating fluid. The initial geometry of the piston valve, the pressure drop at the boundary and the no-slip wall condition allow the resolution and closure of the fluid dynamic problem. The most essential parameters are then computed, including the total force acting on the piston, F, as well as the pressure and velocity fields across the piston's body, which are derived from the CFD's analysis.
The ducting upstream and downstream of the spool appears in Figure 4.4 with a semicircular rather than a circular cross-section. This is a deliberate simplification of the analysis geometry and not a manufacturing choice for the component. In the simplified model the two ducts act exclusively as inlet and outlet plena: their function is to deliver the design flow rate to the crown orifice and to collect it downstream, establishing the two reference static pressures upstream and downstream of the moving element, whereas all the quantities of interest for the present study, namely the pressure drop across the crown, the resultant force on the spool and the structure of the jet, are governed by the orifice region alone. Truncating the ducts on a longitudinal plane therefore leaves the physics of the region under investigation unaffected, while producing two substantial practical advantages.
The first advantage concerns the construction of the model. In a fully circular duct the orifice connecting the upstream and the downstream volumes would have to be cut into a curved wall, and the intersection between the cylindrical bore of the orifice and the cylindrical surface of the duct generates a doubly curved, non-planar intersection curve that is awkward to define parametrically and prone to continuity and tolerance problems in the CAD kernel. With the semicircular section the orifice is instead built on the flat face that supports the half-cylinder, so that the intersection reduces to a plane circle: the feature becomes straightforward to define, to dimension and, above all, to modify parametrically when the orifice radius and the spool diameter are varied during the optimization campaign, which required the geometry to be regenerated repeatedly.
The second advantage concerns the meshing phase, which for this component is the binding constraint of the whole analysis. As discussed in Section 5.3.1, the crown gap is of the order of a few tenths of a millimetre and demands a local cell size of the same order, so that the cell count and the mesh quality in the orifice region dominate the computational cost. A planar face bounding the orifice allows the surface mesh to be generated on a flat support and the

inflation layers to be extruded along a uniform normal direction, avoiding the sliver and high-skewness elements that are systematically produced at a curve-to-curve intersection when a strongly refined size function is applied. The resulting volume mesh is both smaller and better conditioned than the one obtained on a fully curvilinear geometry, an advantage that becomes decisive when several spool configurations have to be compared under identical discretization settings, as is the case for the optimized and non-optimized architectures examined here.

No penalty is therefore expected from the adoption of a conventional circular channel, obtained by subtractive machining, in the physical component: the planar support face is a requirement of the simplified analysis model, not of the hardware, and the reference manufacturing route for the ducting remains the standard circular bore. Should a geometrically complete simulation of the assembled valve be undertaken in a subsequent phase, the only differences to be expected are a marginally different velocity distribution within the plena, which does not affect the pressure drop established by the crown orifice, and a higher meshing cost at the orifice intersection.

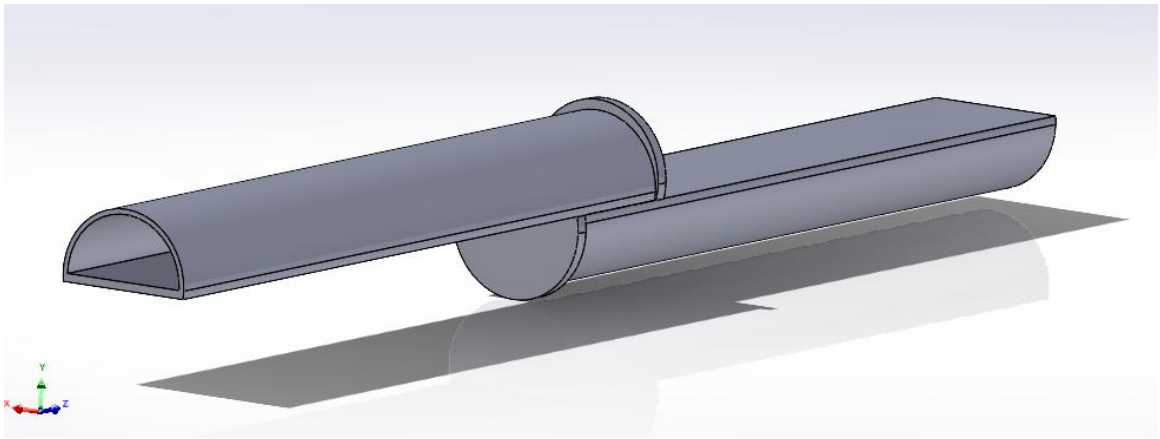


Figure 4.4*: 3D model of the simplified piston valve geometry used for both the CFD analysis and the lumped-parameter dynamic model. The central spool body, orifice divider, and upstream/downstream chambers are shown.*

4.2.3 Spool Geometry Optimization

The critical design decision distinguishing the architecture presented in this work from conventional piston valves is the pass-through spool geometry. In the conventional configuration, the blunt-ended spool pushes toward the orifice dividing the upstream and downstream chambers. The optimized configuration instead extends the spool stem axially through the orifice, creating a crown-shaped annular flow passage with area $A = 2\pi rx$, where r is the orifice radius and x is the axial displacement of the spool

Determining the total force F acting on the piston's body is essential for calculating the dynamic response of the system in terms of position and velocity of the regulating mechanism. This force parameter is the input of the Simulink-implemented dynamic model; therefore, its accurate estimation through fluid dynamic CFD simulations is crucial for ensuring the accuracy and reliability of the modeling results.

As far as the body of the piston is concerned, an efficient fluid dynamic and mechanical optimization regards the thickness of its stem. One advantage in having a thick piston stem is that the traction force that the flow exercises on the piston is lower than that with a thinner

stem, because the area of the circular crown on which the flow acts is smaller. Thus, the piston is less stressed and has a longer life. Moreover, having a thicker stem gives more inertia to the piston, and its robustness contributes to making it less sensitive to possible imbalance of forces with respect to a thinner and less inert piston. In addition, the distributed load of the flow along the stem, which causes a bending moment on the stem itself, causing it to deflect, is smaller if the resistant section of the stem is larger.
This is why the presented simplified architecture is made of a central piston body conceived with a robust and well-designed geometry, in order to let the cryogenic fluid cross it without encountering sharp edges or significant geometry variations, which could lead to separation or recirculating zones in the proximity of the crown orifice which governs the pressure reduction.

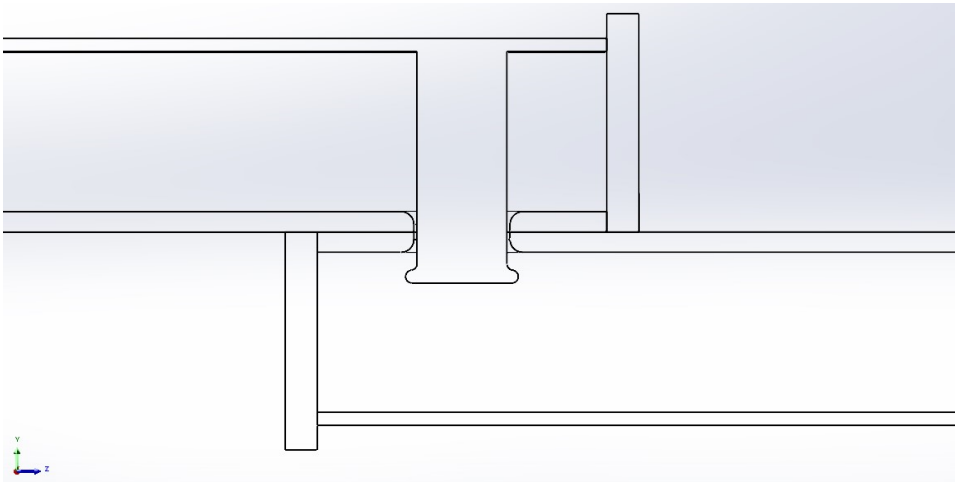


Figure 4.5*: Cross-section of the optimized piston valve geometry showing the pass-through spool stem, the crown orifice with annular flow passage A = 2πrx, and the spring chamber above the spool disc. Source: author's original design.*

Another optimization performed in this work on the valve's design is the piston body passing through the conventional orifice which divides downstream from upstream, so as to create a circular crown-shaped zone for the passage of the flow (Fig. 4.6). This area shall be designed in such a way that the flow has a reduction of pressure equal to that set by design: in this way, if the piston regulating mechanism is to suffer a damage and therefore no longer work efficiently, the piston would still remain in axis providing the demanded area to reduce the upstream flow pressure to the desired value of downstream. This solution, properly implemented from an engineering point of view (for instance by connecting the piston axis to a guide in order to maintain the axis straight), allows for a more robust and reliable pressure regulating mechanism, decoupling the pressure reduction function from that of regulation in case of system failures.

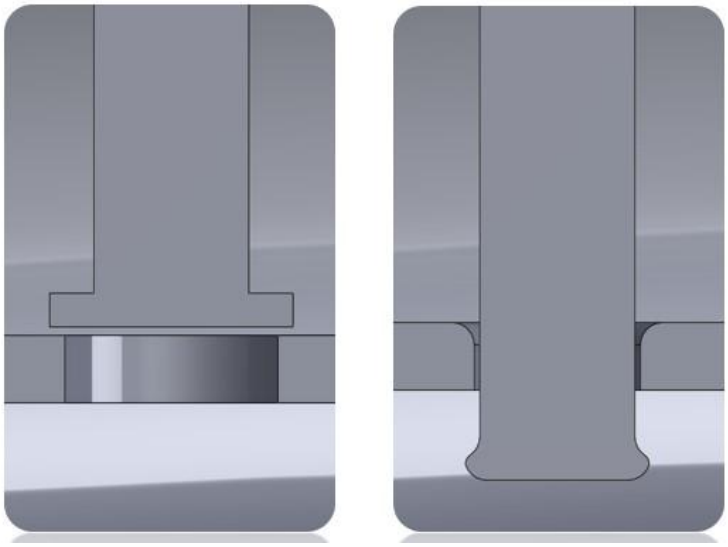


Figure 4.6: *Non-optimized piston body (left) and optimized pass-through piston body (right). The non-optimized geometry creates a blunt impingement region with recirculation downstream of the orifice. The optimized geometry creates a smooth crown-shaped annular passage, eliminating recirculation entirely.*

As will be shown by the results of the CFD analysis, the optimized solution of the piston with body passing through the circular crown orifice has a lower total force acting on it, yet much more stable over time than the total force acting on the classic configuration with the piston pushing toward the orifice as shown in Fig. 4.6 on the left. The net axial force on the spool is reduced from approximately 190 N (non-optimized) to 54 N (optimized), directly improving dynamic stability. Having a constant force acting on the piston implies having less oscillations during the piston pressure regulating phase, and therefore better performances. Furthermore, if the total force acting on the piston is small enough, then the piston inertia, combined with the action of the control spring and the viscous force of the flow, will be able to more effectively dampen the movement of the piston itself, reaching the desired equilibrium position with a contained number of oscillations compared to the non-optimized case.

4.2.4 Numerical Model

In valves design, it is not conventional to install dampers owing to the fact that the action of the flow itself, specifically the fluid dynamic resistance that is generated along with the viscous effect, can already be regarded as a damping action [56]. For this reason, damping effects will not be considered as caused by a physical damper in the model, but from the viscous action of the liquid hydrogen flow.

In the mathematical differential model of the problem, the effect of the downstream and upstream flow acting on the piston body is taken into consideration. In order to assess the performance of the valve, it is mandatory to calculate the time required for the piston to reach its equilibrium position, which is a function of the resultant total force F, input of the model.

The characteristic time of the system is the time it takes for the piston to reach the equilibrium position required to achieve the set pressure reduction and maintain that value. Therefore, a pressure regulating valve with high performance is desired to respond quickly to pressure perturbation while maintaining the shortest possible characteristic time.

The simplified model of the optimized pressure regulating valve here presented can be idealized as a mass-damper-spring system, where the mass is represented by the piston body itself, the damper contribution comes from the viscous action of the flow that passes through the valve and the spring is represented by the physical spring which controls the position of the piston during the regulating phase.
The overall system can be modeled therefore by a differential equation of the second order, with the classical expression:

$$M\ddot{x} + C\dot{x} + Kx = F_{tot} \tag{4.11}$$

where M represents the mass of the piston, C the viscous coefficient, K the stiffness of the control spring, while the variable x represents the position of the piston under the action of the total force F_{tot}.
The forcing term of Eq. (4.11) gathers several distinct pressure contributions. Which of them actually act on the spool is dictated by the pass-through architecture described in Section 3.3.1, and not by any simplification introduced in the model; the distinction is set out in what follows. The static differential between the upstream and the downstream pressure does not appear in the equation of motion, because in this architecture there is no surface on which the upstream pressure can produce an axial resultant. In a conventional blunt-ended spool the face that closes on the orifice offers a projected area normal to the valve axis and directly exposed to the upstream chamber, so that the upstream-to-downstream differential acting on it is a first-order term of the balance and the equilibrium position depends on the supply pressure. In the pass-through configuration the stem crosses the orifice, and the upstream chamber therefore wets only the lateral cylindrical surface of the stem, whose normal is everywhere radial: the upstream pressure acts perpendicularly to the direction of motion and generates no axial force on the spool. Its only residual effect is a radial load, which vanishes when the spool is correctly aligned on its axis and which, in the presence of a manufacturing or assembly misalignment, is reacted by the guide and manifests itself solely as an increase of the friction between the stem and the valve body; this is a second-order contribution with respect to the forces that govern the regulation, and it is not represented in the model. The downstream pressure, by contrast, does act along the axis: the stem terminates in a flat disc whose face is directly exposed to the flow, and it is on that surface that the downstream pressure exerts the force which, together with the spring, establishes the equilibrium position.
The absence of the upstream contribution from the equations of regulation is therefore a property of the geometry and not an omission of the model, and it constitutes one of the practical benefits of the pass-through optimisation: the equilibrium opening, and with it the regulated pressure, is intrinsically decoupled from the pressure delivered by the upstream stage, so that a fluctuation at the outlet of the PPR does not propagate into the setpoint of the second stage.
The pressures of the two control chambers, on the other hand, do enter the balance, and they are the terms through which the dynamics of the valve is actually shaped. The spring chamber above the upper disc is referenced to the tank through its control orifice, while the chamber below the disc communicates with the downstream line through the second control orifice, so

that the pressure it establishes is a throttled image of the downstream pressure. The differential between the two chambers acts on the disc as an axial force whose instantaneous value depends on how much fluid the moving disc is pushing through the two control orifices at that instant, and it is precisely this dependence that distinguishes the reduced from the full formulation of the model.

In the Reduced Order Model of Eq. (4.11) that differential is not resolved as a state-dependent quantity. The forcing term is a single constant, evaluated by CFD at the nominal equilibrium opening and held fixed throughout the transient: it embeds the action of the downstream pressure on the flat face of the spool and the momentum reaction of the annular jet issuing from the crown orifice, while the chamber differential is frozen at the static value it assumes when the spool is at rest and is absorbed partly into that constant and partly into the preload of the elastic term. The only rate-dependent contribution surviving in the reduced formulation is consequently the linear viscous force, which is precisely why the coefficient C carries the entire damping burden of the model and why its identification, discussed in Section 4.2.7, is so critical to the predicted response. The ROM must accordingly be read as a small-perturbation model about the nominal equilibrium: it is legitimate as long as the excursion of the spool remains small enough for the force contributions not to depart appreciably from the values they assume at that equilibrium.

This is exactly the limitation that motivates the Full Order Model of Section 4.2.5. Physically, the two chamber pressures are not constants: any motion of the spool displaces a volume proportional to its velocity and forces it through the respective control orifice, generating an instantaneous pressure differential that opposes the motion. Once the frozen-chamber assumption is released and the chamber pressures are written as functions of the spool position and velocity, as done in the chamber relations of Section 4.2.5, the chamber contribution ceases to be a constant and becomes the pair of state-dependent terms that appear explicitly in the FOM equation of motion. The coefficients A and B are therefore not empirical fitting parameters: they are the direct image of the two throttling regimes of the control orifices, the former collecting the laminar Hagen–Poiseuille contribution and the latter the turbulent Darcy–Weisbach one, each becoming dominant on the respective side of the critical Reynolds number.

It must be clearly considered that the displacement of the piston governs the relationship between the volume flow rate and the pressure drop across the valve, through the well-known formula used in fluid dynamic problems:

$$Q = C_d A \sqrt{\frac{2\,\Delta p}{\rho}} = C_d 2\pi r x \sqrt{\frac{2\,\Delta p}{\rho}} \tag{4.12}$$

where C_d is the discharge coefficient of the valve, r is the radius of the orifice, x is the displacement of the piston (which can be considered as the height of the geometrical cylinder which stands between the piston's plate and the orifice opening), Δp the pressure drop across the orifice and ρ the density of the fluid, in this case liquid hydrogen. The above equation shows how the maximum value of the volume flow rate Q is directly proportional to the

displacement x the piston undergoes during the pressure regulation. This means that to each displacement x of the piston corresponds a maximum volume flow rate Q that is able to cross the circular crown orifice of the valve with a resulting drop of Δp. Therefore, if the downstream volume flow rate drops below the maximum value reported in Eq. (4.12), the downstream pressure will consequently rise, and this will cause the piston to move toward the closure of the valve, with a decrease in its displacement x as well as the flow passage area A. This displacement will directly lead to a further pressure decrease below the set value of Δp, hence regulating the pressure level as a function of the downstream flow condition of the valve.

The purpose of the numerical implemented model is thus computing the value of the displacement x of the piston during the pressure regulating mechanism, solution of the differential equation reported in Eq. (4.11). If the computed value x is consistent with the solution of Eq. 4.12, then the model will be able to forecast faithfully the physics of the system, allowing further assessments on the real dynamics of the valve's response starting from the theoretically implemented numerical model.

In order to set properly the input total force F_{tot}, a CFD analysis should be carried out, calculating the force contributions that act on the piston's body. These contributions can be then put into the model implemented on Simulink, which will simulate the dynamics of the system.

For the complete set up of the dynamic model, the mass M, the viscous coefficient C and the spring stiffness K must be properly set. As far as concerns the mass of the spring M, this parameter can be easily computed starting from the geometry and material the piston is made of, which in the case of cryogenic environment could be chosen between Inconel alloys and austenitic stainless steels [57]. The static model of the system gives the value of the stiffness K, by setting a starting suitable equilibrium position x_{eq} of the piston:

$$x_{eq} = \frac{F_{tot}}{K} \quad \rightarrow \quad K = \frac{F_{tot}}{x_{eq}} \tag{4.13}$$

The value of x_{eq} can be set equal to the piston's position in fully open valve's configuration, i.e., when the maximum volumetric flow passes through it. This position corresponds to the distance between the exit edge of the orifice and the bottom surface of the piston, value that can be estimated through Eq. (4.12) by setting the desired Δp, the required volume flow rate Q and the geometry of the orifice.

The last parameter that is needed to close the dynamic problem set up is the viscous coefficient C. It is necessary to pay attention to how to properly compute the viscous contribution of the fluid, since the first differential order term $C\dot{x}$ is fundamental for the damping of the system. The C coefficient binds the viscous force acting on the piston to the velocity of the piston itself, and it is dependent on the fluid dynamic properties. Given the very low viscosity of liquid hydrogen [58], the viscous action of the flow may be insufficient in order to dampen significantly the response of the piston, leading to a slow dynamic of the system with many oscillations until the equilibrium position is reached.

Describing the mechanism of dissipation in a mathematical way is very difficult. The dampening effects are usually represented by idealized mathematical formulas. For many cases, these complex effects are adequately described by viscous equivalent damping.
Therefore, the real dampening contribution of the liquid hydrogen flow, which is synthetized in the viscous coefficient C, can be determined with accuracy only experimentally or through CFD, as it depends on complex physical phenomena [59]. Analytically, this coefficient is computed as the ratio of the force acting on the piston and its related velocity.
Since the only unknown value within the modeled system turns out to be the value of the viscous coefficient C, an initial guess value will be considered, moving preliminarily to a parameterized analysis. It is possible to calculate the critical value of the system, known the mass of the piston and the stiffness of the control spring (these values have been obtained through a prior lumped-parameter analysis here not reported), using the following formula:

$$C_{crit} = 2\sqrt{M * K} = 156.2 \quad \left[\frac{kg}{s}\right] \tag{4.14}$$

If the viscous coefficient C is below the critical value C_{crit}, then the system will be under-dampened, resulting in wide oscillations of the piston. The closer the value of the coefficient C to the critical one, the more important the fluid's dampening effect will be on the dynamics of the piston, which will reach the equilibrium position x_{eq} with gradually more contained oscillations.
The Simulink implemented model is shown schematically in Fig. 4.7. It is important to emphasize that it is not necessary to have a complex model in order to describe in a preliminary analysis the dynamics of the piston within a liquid hydrogen flow, since the objective of the presented study is to provide a comparison in terms of performance and robustness of the valve between an optimized and not-optimized architecture from a fluid dynamic and dynamic point of view. For the sake of this analysis, it is sufficient the computation of the coefficients of the differential model, together with the velocity and pressure field of the flow, in order to establish with accuracy, the total force F_{tot} acting on the piston of the valve and the contribution of the viscous effect of the liquid hydrogen carrying fluid, estimated directly through the CFD analysis.

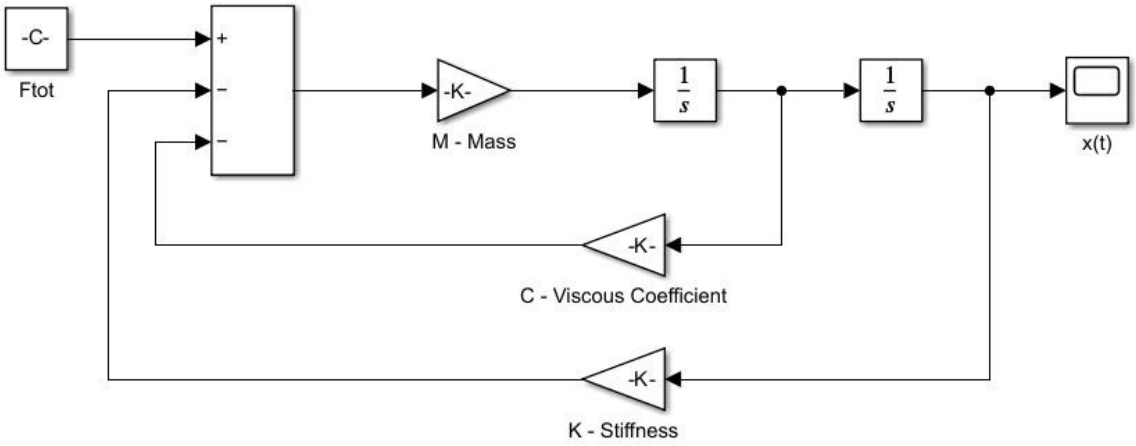


Figure 4.7: *Simulink implementation of the Reduced Order Model (ROM): $M\ddot{x} + C\dot{x} + Kx = F_tot$. The signal chain $F_tot \rightarrow (1/M) \rightarrow \ddot{x} \rightarrow (1/s) \rightarrow \dot{x} \rightarrow (1/s) \rightarrow x$ with feedback paths for the viscous coefficient C and spring stiffness K.*

The complete dynamic model is then solved through waterfall integrations directly on Simulink, starting from the following differential equation obtained starting from Eq. (4.11):

$$\frac{d^2x}{dt^2} = \frac{1}{M}(F_{tot} - C\dot{x} - Kx) \tag{4.15}$$

The viscous coefficient C represents the key unknown of the ROM (Reduced Order Model). Its value cannot be determined analytically with confidence for LH_2, as it depends on complex physical phenomena, primarily the pressure field generated by the orifice flow on the spool surfaces, that are not captured by the linear first-order viscous term alone. The iterative CFD-Simulink identification procedure used to determine C = 4.75 kg/s is described in Section 4.2.7. The critical damping coefficient C_{crit} = 156.2 kg/s sets the reference: with C = 4.75 kg/s, the ROM operates at only 3% of critical damping, which produces strongly oscillating behavior [60] as it will be shown within CFD's results.

4.2.5 Governing Dynamics: Full Order Model

The ROM captures only the linear viscous damping from the bulk flow. The key insight driving the development of the Full Order Model (FOM) is that the spool dynamics are governed primarily not by bulk fluid viscosity but by the pressure evolution in the two regulated chambers, the spring chamber (p_{sup}) and the downstream orifice chamber (p_{inf}), as functions of spool displacement x and velocity $\dot{x}$. These pressure terms generate nonlinear coupling forces that act as an effective second-order damper, entirely independent of fluid viscosity [61].

The dynamic behavior of the spool constitutes a central focus of the analytical formulation regarding the piston's valve dynamics. The governing equation of motion is a second-order nonlinear ODE, whose full formulation (FOM) includes nonlinear coupling terms that arise from the chamber pressure dynamics:

Governing Equation

$$M\ddot{x} + C\dot{x} + Ax\dot{x} + B\dot{x}^2 + Kx = F_{tot}$$

Laminar Model: $for\ Re < Re_{cr}$

$$\begin{cases} p_{sup} = p_T + \dfrac{8\mu A_{sup}}{\pi R^4}\left(L_{c,sup} - x\right)\dot{x} - \dfrac{\rho A_{sup}^2}{2A_{orif,sup}^2 C_{d,sup}^2}\dot{x}^2 \\ p_{inf} = p_2 - \dfrac{8\mu A_{inf}}{\pi R^4}\left(L_{c,inf} + x\right)\dot{x} + \dfrac{\rho A_{inf}^2}{2A_{orif,inf}^2 C_{d,inf}^2}\dot{x}^2 \end{cases}$$

Turbolent Model: $for\ Re \geq Re_{cr}$

$$\begin{cases} p_{sup} = p_T + \dfrac{\rho}{2C_{d,inf}^2}\dot{x}^2 - \dfrac{\rho A_{sup}^2}{2A_{orif,sup}^2 C_{d,sup}^2}\dot{x}^2 \\ p_{inf} = p_2 - \dfrac{\rho}{2C_{d,sup}^2}\dot{x}^2 + \dfrac{\rho A_{inf}^2}{2A_{orif,inf}^2 C_{d,inf}^2}\dot{x}^2 \end{cases}$$

The upper chamber (spring chamber) connects to the LH_2 tank at pressure p_t via a control orifice, and the lower chamber connects to the downstream line at pressure p_2 via a second control orifice. The instantaneous pressures in these chambers depend on the flow regime through their respective orifices: if the local Reynolds number through the orifice is below the critical value Re_{cr}, the Hagen-Poiseuille viscous model applies; if $Re \geq Re_{cr}$, the turbulent orifice model governs. Both regimes yield expressions for p_{sup} and p_{inf} as explicit functions of $\dot{x}$ [62].

While the ROM represents the classical mass-spring-damper formulation used in preliminary analysis. The FOM adds the nonlinear terms $Ax\cdot\dot{x}$ and $B\dot{x}^2$, which arise from the explicit modelling of chamber pressure dynamics as functions of spool velocity and position. The term $B\dot{x}^2$ is physically the most important: it originates from the orifice flow equation $Q \propto \sqrt{(\Delta p)}$ when the chamber differential pressure is expressed as a function of spool velocity, producing a velocity-squared damping term that provides effective energy dissipation proportional to the square of spool velocity, independent of fluid viscosity [63].

This architecture-derived damping is the key finding of the dynamic modelling work: the FOM spool response is near-critically damped and practically insensitive to fluid viscosity, converging to the equilibrium position with minimal oscillations for LH_2, water, and oil SAE 120 alike. The ROM, by contrast, relies entirely on the linear viscous term $C\dot{x}$ for damping, and since the LH_2 viscous coefficient C = 4.75 kg/s is only 3% of the critical value C_{crit} = 156.2 kg/s, the ROM predicts many wide oscillations that make stable pressure regulation impossible.

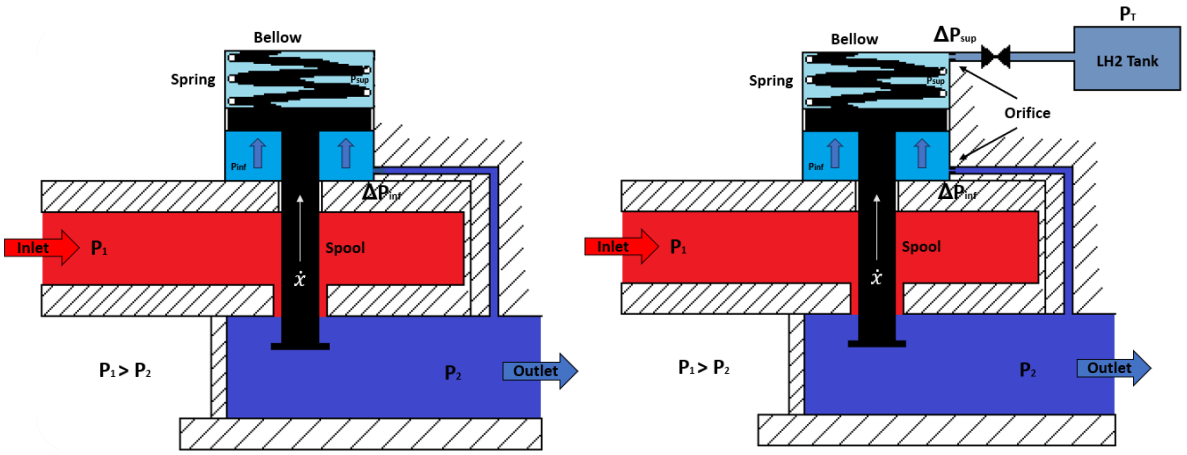


Figure 4.8: *Reduced Order Model (ROM) on the left. Full Order Model (FOM) scheme on the right.*

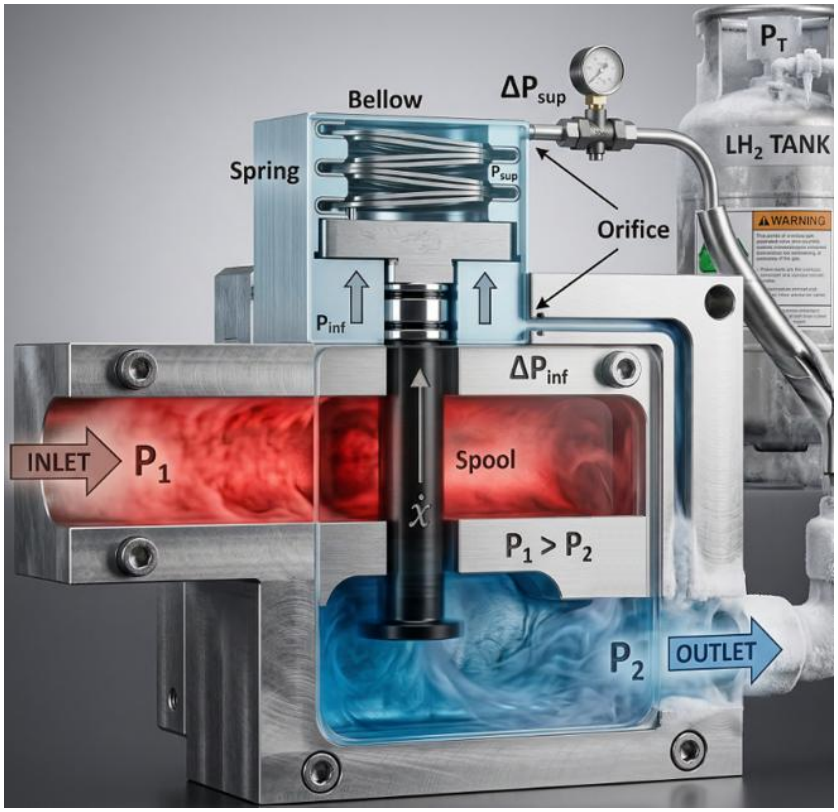


Figure 4.9: *3D rendering of the Full Order Model scheme.*

4.2.6 Simulink Implementation

The FOM is implemented in MATLAB/Simulink through a waterfall integration scheme starting from the explicit second-order ODE reformulated as a first-order system. The model automatically switches between the laminar and turbulent chamber pressure equations based on the instantaneous local Reynolds number through each control orifice, providing a seamless and physically correct transition between the two flow regimes.

$$\frac{d^2x}{dt^2} = \frac{1}{M}(F_{tot} - C\dot{x} - Ax\dot{x} - B\dot{x}^2 - Kx) \tag{4.16}$$

where M is the piston mass, F_{tot} the total hydrodynamic force acting on the piston, C the linear viscous damping coefficient [N·s/m] identified from the iterative CFD-Simulink procedure described in Section 4.2.7, K the spring stiffness [N/m], and A, B the laminar and turbulent chamber pressure coefficients respectively. The term $A\dot{x}$ represents the laminar pressure contribution from the spring chamber, proportional to both piston displacement and velocity, while the term $B\dot{x}^2$ captures the turbulent pressure drop across the downstream orifice, scaling with the square of the piston velocity in accordance with the Darcy–Weisbach formulation for turbulent orifice flow [62].

A central feature of the implemented Simulink model is the automatic regime-switching logic governing the transition between the laminar and turbulent chamber pressure equations. At each integration time step, the instantaneous local Reynolds number $Re_l = \rho v_l D_h/\mu$ is computed for the flow through each control orifice, where v_l is the local flow velocity, D_h the hydraulic diameter of the orifice, and μ the dynamic viscosity of liquid hydrogen at 20 K ($\mu \approx 1.392 \times 10^{-5}$ Pa·s). When $Re_l < Re_{cr} \approx 2300$, the laminar Hagen–Poiseuille relationship $\Delta p = (128\mu L)/(\pi D^4)\cdot Q$ is applied; when $Re_l \geq Re_{cr}$, the model switches to the turbulent Darcy–Weisbach relationship $\Delta p = f_l(L/D)\ (\rho v^2/2)$, with the friction factor f_l evaluated from the Colebrook–White correlation. The switch is implemented in Simulink via a conditional Switch block driven by the Rel signal, ensuring a continuous and physically consistent transition between flow regimes without introducing numerical discontinuities in the integrated state variables.

The model inputs are the time-varying downstream membrane force, representing the excitation imposed by variations in downstream pressure demand, and the spring preload force F_k. Both inputs are expressed as explicit functions of piston position x and updated at each time step through feedback of the integrated position output, realizing the closed-loop architecture described in Section 4.2.7. The total force F_{tot} entering the equation of motion is therefore the algebraic sum of the membrane force, the spring restoring force $-Kx$, the linear viscous damping force $-C\dot{x}$, and the two chamber pressure terms $-A\dot{x}$ and $-B\dot{x}^2$, each evaluated at the current state (x, ẋ) at every integration step.

The numerical integration is performed using a fixed-step explicit Runge–Kutta solver (ode4) with a time step Δt selected to resolve the system natural frequency $\omega_n = \sqrt{(K/M)}$. The time step is set conservatively to $\Delta t = 1/(20\omega_n)$ to ensure adequate resolution of the transient piston response without excessive computational cost. The choice of a fixed-step solver is motivated by the need for deterministic execution time, a requirement relevant to future hardware-in-the-loop (HIL) testing and real-time simulation of the valve regulation system.

The model outputs include the instantaneous piston position x(t), the piston velocity ẋ(t), the equilibrium displacement xeq computed from the static force balance at the current operating point, and the residual error signal $\varepsilon(t) = |x(t) - x_{eq}(t)|$, which provides a quantitative measure of convergence toward the regulation equilibrium. The error signal is used to verify that the regulation objective, maintaining a constant downstream pressure of 7 bar under variable demand, is met within the specified response time. A settling criterion is defined as $\varepsilon(t) < \varepsilon_t{}^h r$ for all $t > t_s$, where $\varepsilon_t{}^h r$ represents the maximum allowable steady-state error derived from the downstream pressure tolerance band.

As illustrated in Figure 4.10, the complete Simulink diagram integrates the second-order dynamic block, the Reynolds-number-based Switch block, the two chamber pressure sub-models, and the spring force feedback into a single self-contained closed-loop model. The Switch block receives the Rel signal computed from the current flow state and selects the appropriate pressure equation at each time step, effectively realizing a piecewise-smooth dynamical system that transitions continuously from the viscosity-dominated laminar regime to the inertia-dominated turbulent regime as piston velocity increases. This architecture ensures that the FOM remains valid across the entire operational envelope of the valve, from slow quasi-static low-Reynolds adjustments to high-speed transient regulation events driven by rapid variations in downstream pressure demand.

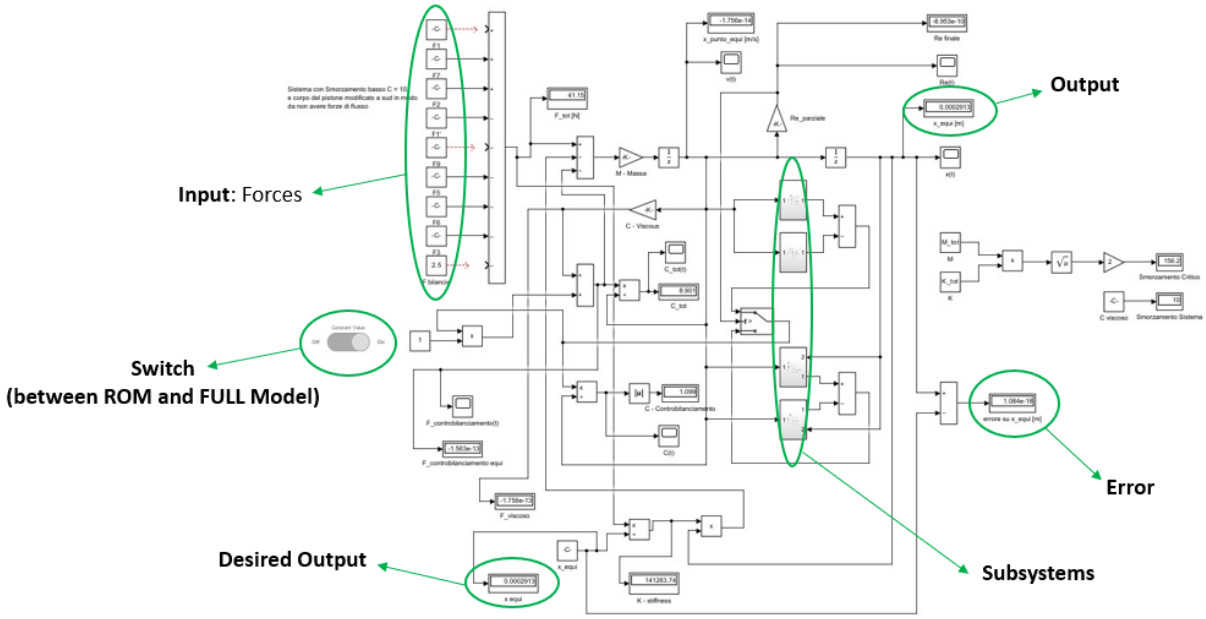


Figure 4.10: *Complete integrated Simulink model with automatic Reynolds-number-based switching between ROM and FOM. The Switch block transitions between the laminar and turbulent models when Re crosses Re_{cr}. The equilibrium displacement x_{eq} and the error signal are output alongside position and velocity.*

4.2.7 Iterative Viscous Coefficient C Identification

The net hydrodynamic force acting on the piston is the vector resultant of all fluid forces distributed over its wetted surfaces, including pressure and viscous shear contributions [64]. In the present configuration, this resultant force drives the piston toward its equilibrium position, while the piston velocity ẋ depends on the dynamic response of the system and must, in the general case, be determined through experimental characterization, as it is governed by the coupled fluid–structure interaction and the time constant of the piston response [65].

The asymmetric geometry of the piston introduces a directional dependence on the viscous damping contribution. During the downward stroke, corresponding to valve opening from the closed condition, both the lower disc surface and the membrane surface are fully exposed to the retarding action of the fluid, resulting in the maximum damping force. In the upward stroke, corresponding to valve closure during a regulation transient, the annular flow passing through the orifice exerts a significant drag force on the lower disc crown, whose velocity is approximately 220 m/s under nominal operating conditions. This aerodynamic drag

contribution dominates over the viscous shear contribution associated with the piston velocity itself, which is orders of magnitude lower [66]. Consequently, the valve presents a robust damping mechanism in both stroke directions: when starting from the closed condition, the piston undergoes a downward motion and the full disc area contributes to damping, enabling rapid convergence to the equilibrium position; when adjusting from maximum-flow equilibrium, the upward motion is effectively retarded by the high-velocity flow through the orifice crown [67].

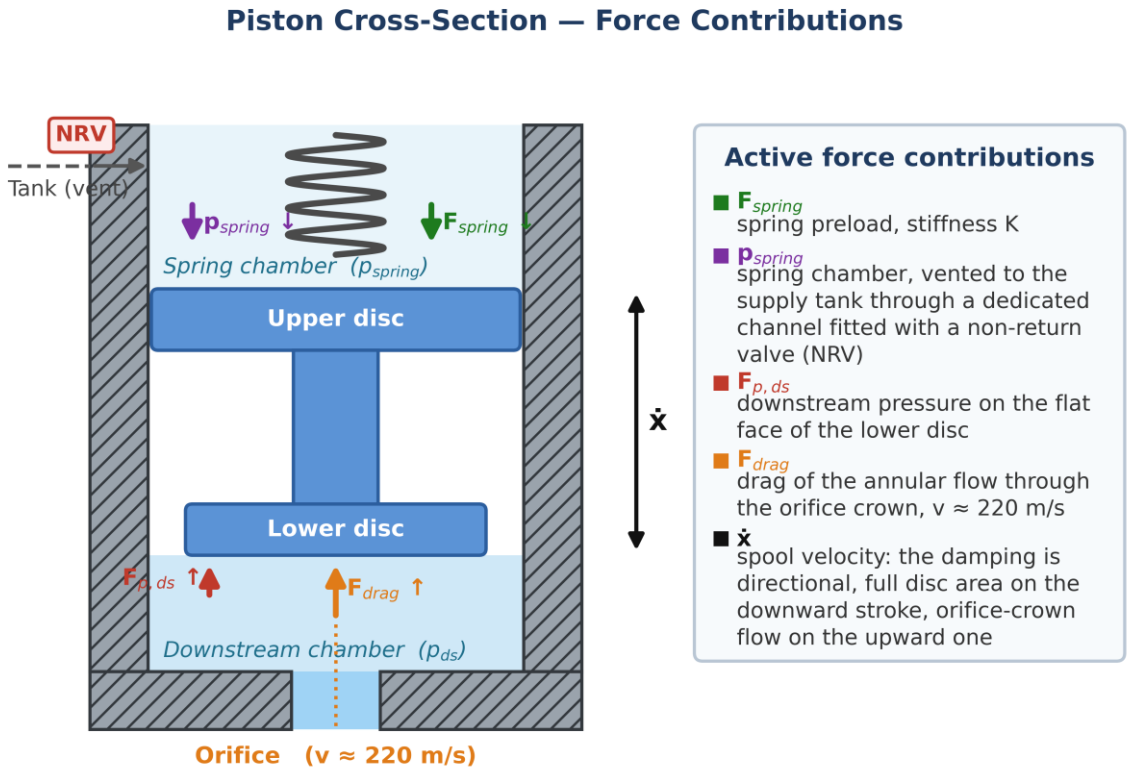


Figure 4.11: *Piston geometry and active force contributions during valve operation.*

A preliminary simulation of the second-order piston dynamic model, accounting for all active force contributions but neglecting wall friction and leakage losses, demonstrated that the viscous coefficient C alone, estimated as the ratio of the resultant hydrodynamic force to the piston velocity, is insufficient to ensure convergence to the design equilibrium position. The simulation exhibits sustained oscillations that decay asymptotically but with significant amplitude, owing primarily to the very low inertia of the piston (m = 0.038 kg in the initial configuration), which offers negligible resistance to motion [68]. This Behaviour is consistent with the classical theory of underdamped second-order systems, wherein a low mass-to-damping ratio results in a damping ratio ζ substantially below unity [69]. Furthermore, the preliminary ROM does not incorporate the pressure dynamics of the two chambers acting on either face of the upper piston disc, namely the spring chamber and the downstream fluid chamber, which represent the dominant additional damping mechanism during piston motion [66].

Before the dynamic model can be run, the viscous coefficient C must be identified from the CFD analysis. The procedure is iterative: starting from an initial guess of the spool velocity v_0 = 0.18 m/s and the CFD-computed viscous force F_{visc} = 1.8 N, the initial estimate $C_0 = F_{visc}/v_0$ = 10 is used in the Simulink simulation. The output mean spool velocity ẋ is then used to update C at each iteration until the convergence criterion $|F_{tot} - C_{i+n} \cdot \dot{x}_{i+n}|$ < threshold is met, as reported in the procedure below:

1. Set arbitrarily the initial spool velocity ($v_i = 0.18\ m/s$);
2. The input force is the viscous one ($F_{tot} = 1.8\ N$);
3. The initial C is computed as: $C_i = \frac{F_{visc}}{v_i} = \frac{1.8}{0.18} = 10$;
4. The Simulink model is run;
5. The new initial velocity v_{i+1} is set equal to the output mean velocity $\bar{\dot{x}}_{i+1}$;
6. The new viscous C coefficient is equal to: $C_{i+1} = \frac{F_{visc}}{\bar{\dot{x}}}$

n° iterations until: $|F_{tot} - C_{i+n}\ \bar{\dot{x}}_{i+n}|$ < threshold value

C identification convergence

```
Iterative C identification — convergence (two initial
conditions demonstrated):

  Starting from C₀ = 10:              Starting from C₀ = 70:
  Iter 1:  C = 10.00   error = 88%    C = 70.00   error = 359%
  Iter 2:  C =  5.31   error = 10%    C = 15.25   error = 152%
  Iter 3:  C =  4.81   error = 1.3%   C =  6.04   error =  25%
  Iter 4:  C =  4.75   error = 0.25%  C =  4.85   error =   2%
  Iter 5:  C =  4.75   error = 0.25%

  → Converged: C = 4.75 kg/s (independent of initial C₀)
  → Ratio C / C_crit = 4.75 / 156.2 = 0.030 → 3% of critical
damping (ROM alone)
```

The convergence to C = 4.75 kg/s from two very different initial conditions (C_0 = 10 and C_0 = 70) confirms the robustness of the iterative identification algorithm and the uniqueness of the physical solution. The value C = 4.75 kg/s represents the effective viscous damping contribution from the LH_2 flow alone, without the chamber coupling terms of the FOM.

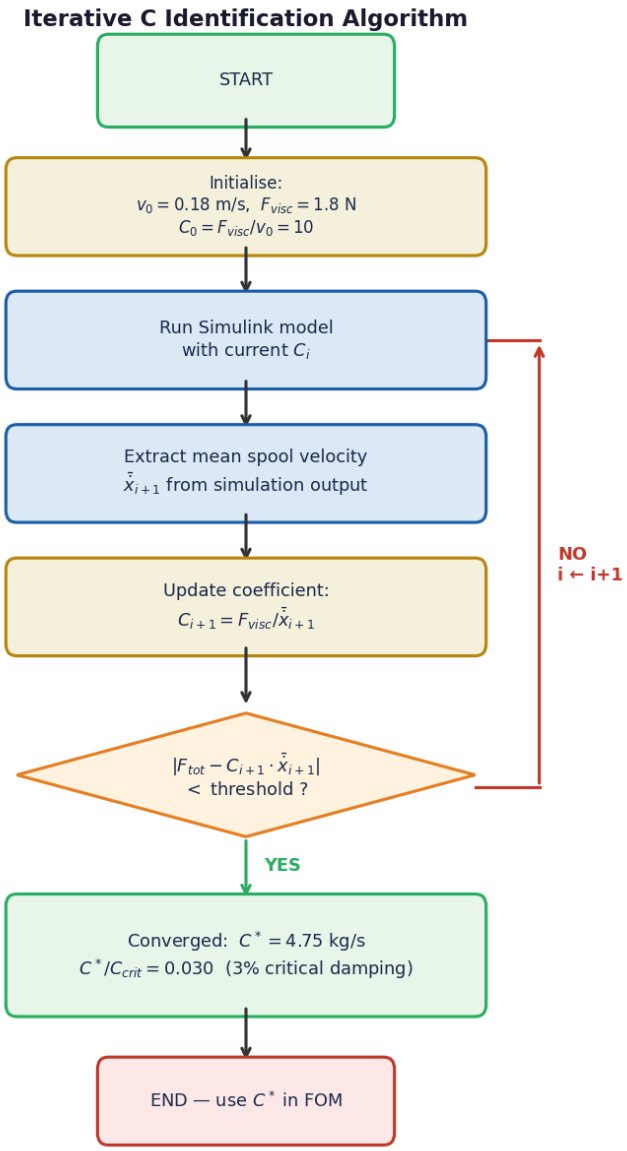


Figure 4.12: *Flowchart of the iterative viscous coefficient C identification procedure.*

The chamber pressure contributions to piston dynamics operate as follows. When the downstream demand decreases, the downstream pressure p_p rises and propagates through the connecting channel into the lower chamber beneath the spring, acting on the annular free surface of the piston upper disc. This causes the spring to compress and the chamber pressure to increase, counteracting the piston upward motion. The spring chamber pressure, under the assumption that it is vented to the supply tank via a dedicated channel, depends on the tank pressure and on the instantaneous piston velocity ẋ. Conversely, during the downward stroke, the downstream fluid chamber tends to discharge; the fluid present in the chamber resists the piston motion, and the resulting chamber pressure depends on the downstream pressure and the piston descent velocity. Accordingly, modelling these two time-varying pressure contributions, each weighted by the respective surface area on which they act, introduces two additional terms in the force balance that sum to the first-order viscous term $C\dot{x}$, significantly increasing the effective system damping ratio and enabling convergence without sustained

oscillations [64,65]. It is noted that a non-return valve should be installed on the channel connecting the spring chamber to the tank, in order to prevent back-flow from the tank into the chamber during decompression, ensuring that the chamber remains evacuated at each piston cycle and that the spring action is not compromised by accumulated fluid.

The resulting virtual viscosity of the complete system is substantially higher than the intrinsic dynamic viscosity of liquid hydrogen, which at 20 K is approximately $\mu_{x2} \approx 1.392 \times 10^{-5}$ Pa·s [70]. This value is approximately four orders of magnitude lower than the viscosities of mineral oils commonly employed in hydraulic actuation systems, and approximately one order of magnitude lower than the dynamic viscosity of water at room temperature. This comparison suggests the feasibility of a Reynolds-analogous experimental campaign using water as the test fluid: by maintaining during the water test the same Reynolds number $Re = \rho v D/\mu$ as that characterizing the LH_2 flow, the dynamic similarity is preserved, and the viscous damping coefficient of the system can be inferred from the measured piston response [71]. Two distinct experimental configurations are of interest: (i) testing the piston body immersed in a fluid chamber alone, to isolate the viscous contribution of the fluid; and (ii) testing the piston coupled to the valve body, including the upstream and downstream chambers, to characterize the complete system damping including the chamber counterbalancing contributions. Comparing the two resulting damping curves allows the individual contributions to be quantified and separated [72].

The orifice sizing connecting the two chambers plays a decisive role in the system damping behavior. Reducing the orifice cross-sectional area decreases the volumetric flow rate through the channels, increasing the counterbalancing chamber pressure on the piston disc and hence augmenting the damping action during transients. This approach enables the designer to tune the effective damping ratio without modifying the structural components of the valve. However, an excessively restrictive orifice geometry may lead to overdamping: if the downstream chamber cannot discharge sufficiently rapidly during the downward stroke, the excessive counterbalancing pressure may impede the piston from completing its motion, compromising the regulation mechanism. The design must therefore balance the competing requirements of adequate damping to suppress oscillations and sufficient discharge flow to ensure the piston reaches the equilibrium position within the required response time [66,68].

To correctly incorporate the chamber pressure contributions into the implemented model, the same flow equations applicable to laminar and turbulent regimes, previously employed for the orifice sizing analysis, are adopted. Specifically, depending on the local Reynolds number of the flow entering each chamber, a laminar flow relationship ($\Delta p \propto Q$) or a turbulent flow relationship ($\Delta p \propto Q^2$) between volumetric flow rate and chamber pressure is applied, consistently with established hydraulic modelling practice [62,64]. This formulation allows the chamber pressure terms to be expressed as explicit functions of piston velocity $\dot{x}$, so that they can be incorporated into the model as additional velocity-dependent forcing terms, summing with the viscous term $C\dot{x}$ to yield an augmented effective damping coefficient. The resulting closed-loop model therefore captures, through this inner feedback loop, the physical counterbalancing action of both chambers on the piston dynamics.

A further consideration relevant to the preliminary Simulink simulation concerns the numerical integration time step. An excessively large time step caused the solver to miss the characteristic timescale of the piston response to the resultant force, yielding physically inconsistent results. Reducing the time step to a value compatible with the system's fastest dynamic mode, identified from the natural frequency $\omega_n = \sqrt{(K/m)}$, improved numerical accuracy but did not resolve the oscillatory behavior, confirming that the root cause lies in the model-level omission of the chamber damping contributions rather than in numerical artefacts. This is consistent with the observation that the viscous damping coefficient C identified from the ROM alone corresponds to approximately 3% of critical damping ($C/C_{ni}^{t} = 4.75/156.2 \approx 0.030$), a value inherently insufficient to prevent sustained oscillations in a lightly loaded system [68,72].

The complete dynamic model must therefore incorporate the two chamber pressure contributions as explicit functions of piston velocity ẋ, summing with the viscous term $C\dot{x}$ to yield an augmented effective damping. The chamber pressure terms are expressed as functions of $\dot{x}$, and connected to the main second-order equation of motion through an inner feedback loop, which accounts for the physical counterbalancing action of the chambers on piston dynamics. This closed-loop architecture constitutes the full-order model (FOM), to be compared with the reduced-order model (ROM) employing C alone [62].

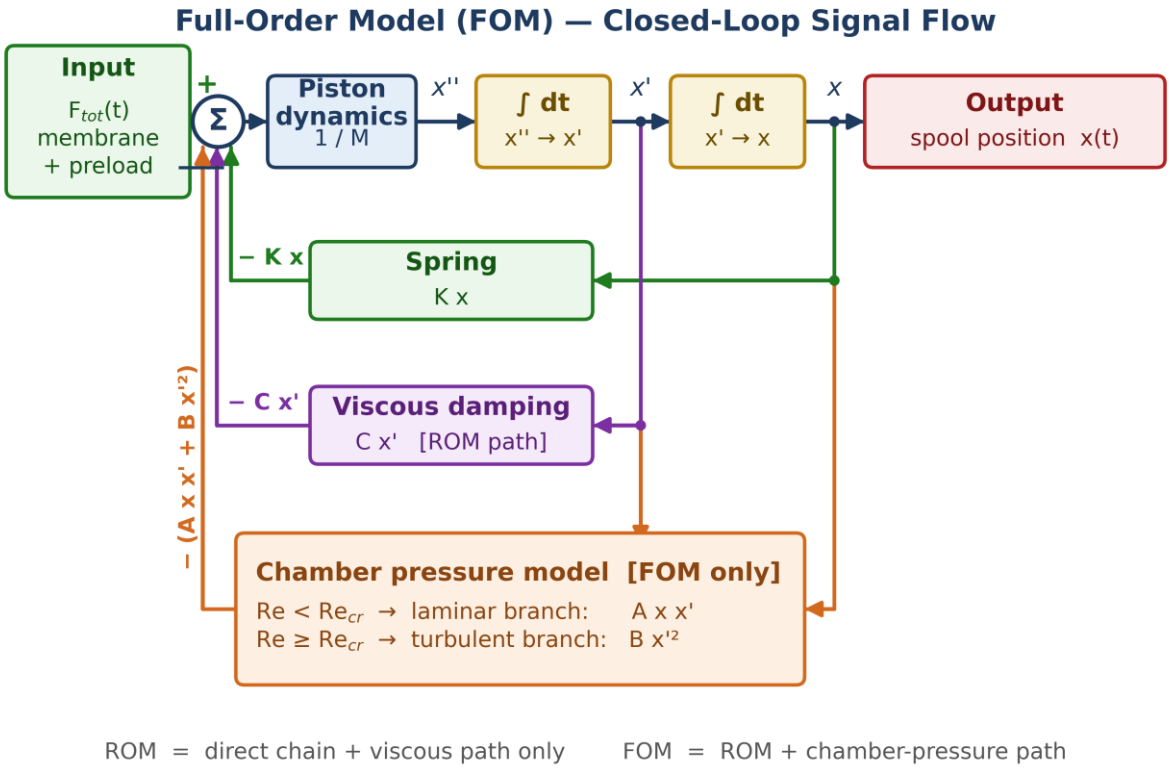


Figure 4.13: *FOM closed-loop signal flow. The ROM uses only the Cẋ feedback path (purple). The FOM adds the chamber pressure terms (orange) as velocity-dependent damping contribution.*

For the preliminary model validation, the hydrodynamic forces acting on the piston surfaces were computed by modelling each wetted surface as a flat plate in crossflow, for which the drag coefficient C_d is known from established experimental correlations [71]. The resultant of

these hydrodynamic forces was then divided by an assumed piston velocity to yield an initial estimate of C. As demonstrated by the parametric analysis in the previous sections, the dominant contribution arises from the high-velocity flow through the orifice crown, whose drag force ($F_{sas} = \frac{1}{2}\rho v^2 S^c C^d \approx 22$ N at $v \approx 220$ m/s) is comparable to the total static force budget of approximately 23 N. The contributions associated with piston velocity itself are negligible: even at $\dot{x} = 2$ m/s, the corresponding drag forces remain at least two orders of magnitude smaller than the orifice-flow drag. Consequently, the precise value of the piston velocity is not a critical input for the initial C estimate, and the iteratively converged value $C = 4.75$ kg/s is robust to the initial guess, as demonstrated by the convergence from two widely separated starting points ($C_0 = 10$ and $C_0 = 70$) [72,73].

Once the full-order model incorporating the chamber pressure dynamics has been implemented, it becomes possible to compare the chamber-induced damping contribution against the fluid viscosity term. Should the chamber contributions prove dominant over the intrinsic LH_2 viscous damping, which, at $T = 20$ K, is characterized by $\mu \approx 1.392 \times 10^{-5}$ Pa·s and represents only approximately 3% of critical damping in the ROM, the fluid viscosity term may be legitimately neglected and the resulting simplified model assessed for its impact on the predicted equilibrium position. If the resulting deviation lies within an acceptable tolerance band, the reduced model may be adopted for subsequent analyses [68,70].

An important limitation of the preliminary Simulink model is the assumption of instantaneous chamber depressurization. In reality, when the piston rises driven by the downstream flow acting on the annular crown, the lower chamber fills with fluid and reaches a finite pressure; during the descent, the piston compresses the chamber fluid, which resists the motion until it depressurizes. The characteristic depressurization time of the chamber is governed by the orifice discharge area and the chamber volume, and introduces a pressure inertia that must be captured in the model to correctly predict the piston dynamic response. Neglecting this finite depressurization time is equivalent to removing the main source of transient damping, explaining the underdamped behavior observed in the preliminary simulation [65,66].

Since C is the only parameter of the complete model that cannot be determined analytically, a parametric study is recommended to characterize the system sensitivity to this coefficient. Given the high sensitivity of the dynamic output to C, small variations producing significant changes in the damping ratio and transient response, a sensitivity analysis should be performed to rank all model parameters by their influence on the output position [72,73]. Parameters identified as low-sensitivity can tolerate larger estimation uncertainties without compromising model fidelity, while high-sensitivity parameters, including C, require accurate identification through experimental testing. To facilitate model validation prior to LH_2 testing, the model can be exercised with the thermophysical properties of a fluid for which C is experimentally known, such as a calibration oil or water, in order to verify the model structure independently of the cryogenic fluid identification [65].

The dynamic simulation results, computed under the assumption of full viscous-force loading with a piston velocity of 0.2 m/s and a total applied force of approximately 23 N (corresponding to a 7 bar downstream pressure, the nominal design requirement), yield a viscous damping coefficient $C \approx 111.5$ N·s/m, which is marginally below the critical damping

value $C^{c}_{ni}{}^{t} = 2\sqrt{(Km)} \approx 112.5$ N·s/m. The system may therefore be treated as approximately critically damped under the stated assumptions, resulting in a non-oscillatory piston response. The simulation predicts that the piston reaches its equilibrium position $x_{e2}\hat{\omega} = 0.293$ mm from the orifice within approximately 0.05 s, confirming compliance with the design requirement of 7 bar downstream pressure at maximum deliverable flow. Below this equilibrium displacement, the valve enters the regulation regime, throttling the flow so as to maintain constant downstream pressure at the required value across all demand conditions [62,74].

Chapter 5

CFD Analysis

This chapter presents the CFD simulation campaign conducted for both device geometries. The mathematical model developed in Chapter 4 provides closed-form predictions for the key fluid dynamic quantities governing both the Passive Pressure Reducer (PPR) and the piston pressure regulating valve: the volumetric flow rate Q, the per-stage pressure drops Δp_i, the global discharge coefficient C_D, and the total hydrodynamic force F_{tot} acting on the spool. While the lumped-parameter framework offers valuable physical insight and allows rapid design iteration, its accuracy is inherently limited by the assumptions introduced, in particular the constant per-orifice discharge coefficient, the jet correction factor k_i, and the linear viscous damping approximation in the piston valve dynamic model. A high-fidelity Computational Fluid Dynamics (CFD) analysis is therefore required to validate these predictions, to resolve the three-dimensional flow structures that the lumped-parameter model cannot capture, and to extract quantities, primarily the local pressure loss coefficient k and the precise spool force distribution, that serve as inputs to the Simulink dynamic model described in Chapter 4.

5.1 CFD Simulation Strategy and Boundary Conditions

5.1.1 Overview and Objectives

The CFD campaign pursued three principal objectives. The first was to verify the volumetric flow rate Q predicted by the lumped-parameter model of Section 4.1 against the three-dimensional flow solution, in which cross-stream velocity components, recirculation zones, and jet–wall interactions are naturally resolved. The second objective was to determine the local pressure loss coefficient k for each orifice–flange stage of the PPR, a quantity that cannot be obtained analytically without further assumptions and is required to calibrate the pressure model implemented in Simulink. The third objective was to compute the total hydrodynamic force F_{tot} on the spool of the piston valve, including both pressure and viscous shear contributions, for the optimized and non-optimized geometries described in Section 4.2.3 [75,76].

Two distinct geometric configurations were simulated. The first corresponds to the convergent–divergent flanged duct of the PPR (Fig. 4.2), comprising six orifices of variable cross-section separated by four annular chambers. The second corresponds to the simplified axisymmetric piston valve body (Fig. 4.4–4.6), with the pass-through spool in the optimized configuration and the blunt-ended spool in the non-optimized reference case. All simulations were performed using the commercial CFD solver ANSYS Fluent 2022 R1 [77], employing the steady-state, incompressible, Reynolds-Averaged Navier–Stokes (RANS) framework described in Section 5.2.

5.1.2 Boundary Layer Modelling and CFD Setup

The accuracy of the CFD results that feed the dynamic model depends critically on the treatment of boundary layers near the spool surfaces. Boundary layers are regions of steep velocity gradient between the wall (where no-slip applies) and the freestream; despite their small physical thickness, they govern the turbulence production, the wall shear stress, and the pressure distribution on the spool that produce the damping force [78].

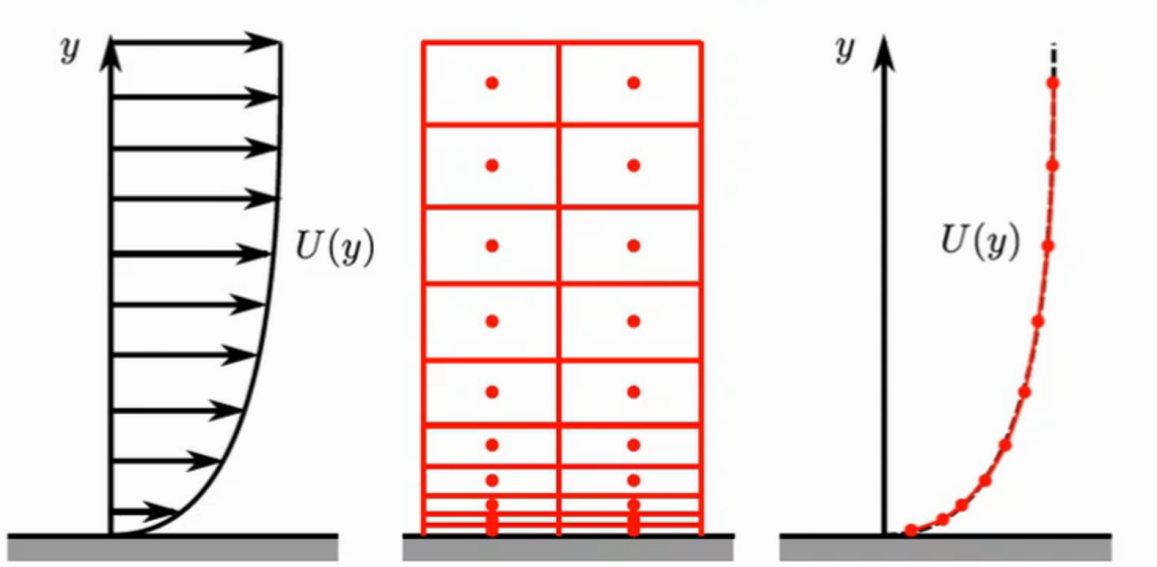


Figure 5.1: *Boundary layer refinement in the CFD mesh: addition of inflation layers to capture the steep velocity gradient near solid surfaces. Fine mesh with high aspect-ratio cells in the boundary layer is essential for accurate wall shear stress and pressure distribution on the spool.*

The fluid dynamic problem is fully defined by imposing the mass flow rate ṁ at the inlet and the static pressure p_{out} at the outlet. This choice of boundary conditions is standard for internal flow problems in which the operating flow rate is prescribed by the system requirements [79], and it offers a fundamental advantage from the perspective of CFD post-processing: once ṁ and the orifice geometry are specified, the mean orifice velocity v is known directly from continuity, and the resulting pressure drop Δp across the device follows from the local loss relationship:

$$\Delta p = \mathrm{k} \cdot \rho \cdot v^2 \tag{5.1}$$

where k is the dimensionless local pressure loss coefficient and ρ is the fluid density. Conversely, with the outlet static pressure p_{out} fixed, the inlet pressure $p_{in} = p_{out} + \Delta p$ is fully determined by the simulation, so the mass flow rate at the outlet is implicitly consistent with the discharge relationship:

$$Q = C_d A \sqrt{\frac{2\,\Delta p}{\rho}} \tag{5.2}$$

The simultaneous imposition of $\dot{m}$ at the inlet and p_{out} at the outlet therefore closes the problem without over-constraining it: the solver iterates on the pressure–velocity field until both Eq. (5.1) and Eq. (5.2) are simultaneously satisfied, yielding consistent values of Q, Δp, k, and C_D as post-processing outputs. No-slip boundary conditions were applied on all solid walls. The working fluids simulated were liquid hydrogen (LH_2) at 20 K with density $\rho_{LH_2} = 70.97\ kg/m^3$ and dynamic viscosity $\mu_{LH_2} = 1.392 * 10^{-5}\ Pa\ s$, and water at 293 K with density $\rho_w = 998.2\ kg/m^3$ and dynamic viscosity $\mu_w = 1.002 * 10^{-3}\ Pa\ s$, used as reference fluid for the analogy study of Section 5.3.5. The boundary conditions applied to each simulation are summarized here below.

Table 5.1*: Summary of CFD boundary conditions for the PPR and piston valve simulations.*

Parameter	PPR (LH_2)	PPR (Water)	Piston Valve (LH_2)
Inlet BC	Mass flow rate $\dot{m}$	Mass flow rate $\dot{m}$	Mass flow rate $\dot{m}$
Outlet BC	Static pressure p_{out}	Static pressure p_{out}	Static pressure p_{out}
Total Δp [bar]	23	23	23
Fluid	LH_2, 20 K	H_2O, 293 K	LH_2, 20 K
ρ [kg/m³]	70.97	998.2	70.97
μ [Pa·s]	1.392×10^{-5}	1.002×10^{-3}	1.392×10^{-5}
Wall BC	No-slip	No-slip	No-slip

5.2 CFD Analysis of the PPR Multi-Stage Architecture

5.2.1 Mesh Topology and Global Settings

Tetrahedral elements were selected for their flexibility in discretizing the complex three-dimensional geometry of the annular chambers and the crown-shaped spool gap, where structured hexahedral meshing would require prohibitive manual blocking effort. Although hexahedral elements are known to offer lower numerical diffusion and faster convergence for simple, wall-aligned geometries [80], their generation for domains with multiple concave annular regions and sharp-edged orifice transitions is practically infeasible without extensive manual blocking, a limitation extensively discussed in the CFD meshing literature [81,82]. The mesh generation was conducted in three stages: (i) surface mesh generation on all wetted boundaries with curvature-based refinement to resolve the orifice edges and the sharp exit corners; (ii) volume mesh generation in the bulk domain; and (iii) prism layer inflation on all solid surfaces, following established best-practice guidelines for hybrid tetrahedral–prismatic meshes in internal flow simulations [76,77].

The orifice region required special attention due to the very small flow passage area. For the PPR, the throat orifice has a diameter of 5.34 mm and a gap between the rounded inlet edge and the sharp exit edge of approximately 1 mm, corresponding to the transition region between the convergent and the annular chamber. For the piston valve, the crown-shaped gap between

the spool stem and the orifice rim has an equivalent circular diameter of only 3.31 mm, a consequence of the high pressure drop (23 bar) imposed across the valve and the low density of LH_2. At equal orifice geometry and boundary conditions, the low density of liquid hydrogen (ρ_{LH_2} = 70.97 kg/m³ versus ρ_{H_2O} = 998.2 kg/m³) requires a proportionally larger flow passage area to sustain the same volumetric flow rate, as the discharge relationship in Eq. 5.2 shows. The narrow spool gap (equivalent to a 3.31 mm circular diameter when the crown geometry is accounted for) represents the most challenging region to mesh accurately, as the mesh cell size must be of the same order as the gap width to avoid excessive numerical diffusion in the pressure gradient computation [83]. This sensitivity of orifice pressure drop predictions to local mesh resolution has been documented in dedicated CFD studies of orifice flows, where grid independence of the discharge coefficient typically requires cell sizes no coarser than one-tenth of the orifice diameter in the vicinity of the vena contracta [84,85].

This geometric constraint is one of the primary motivations for the multi-stage PPR architecture. By distributing the 23 bar total pressure reduction across six orifice–flange stages, the pressure drop managed by the downstream piston valve is reduced to approximately 7–15 bar (depending on the operating point), yielding a significantly larger equivalent orifice diameter (approaching 5 mm rather than 3.31 mm). A larger gap relaxes the mesh resolution requirement at the critical orifice surface, reduces the computational cost of the CFD simulations, and diminishes the fluid velocity through the gap, thereby reducing mechanical erosion and thermal stress on the orifice surfaces [86].

5.2.2 Boundary Layer Discretization

ANSYS Fluid Flow (Fluent) software was used for the mesh generation of both flow domains [77]. The patch conforming tetrahedral method was selected for the surface and volume discretization. In the patch conforming approach, all geometric features, edges, faces, and topological boundaries, are explicitly respected during mesh generation, ensuring that every surface patch of the CAD model is faithfully represented in the mesh without suppression of small geometric details [87]. This is particularly important for the present geometry, where the sharp orifice exit edges, the annular chamber shoulders, and the crown-shaped spool profile constitute critical flow-determining features that must not be defeatured. A tetrahedron-dominant shell mesh was first generated on all wetted surfaces, applying curvature-based local refinement in regions of high geometric curvature to maintain adequate angular resolution on the rounded inlet edges and at the orifice throat. The volume was then filled using a tetra/mixed meshing strategy, which generates tetrahedral elements in the bulk domain while preserving the surface mesh topology. The resulting volume mesh is shown in Fig. 5.3. The use of unstructured tetrahedral elements is well established for internal flow simulations in geometries with multiple concave regions and non-planar interfaces, where the manual blocking effort required for structured hexahedral meshing would be prohibitive [80, 82].

Prism inflation layers were applied on all solid wall boundaries to ensure physically accurate resolution of the near-wall velocity gradients and the viscous sublayer, which are critical for the correct prediction of wall shear stress, pressure drop, and discharge coefficient in orifice flows [81]. The inflation method adopted is the Smooth Transition option, in which the initial

layer height at each surface triangle is computed locally as a function of the surrounding tetrahedral element size, scaled by the transition ratio. This adaptive approach produces a spatially varying first-layer height that follows the local surface mesh density, ensuring a gradual and continuous volumetric growth from the wall into the free-stream domain and avoiding the abrupt cell-size jumps that can degrade solver convergence [88]. A geometric growth ratio of 1.2 was applied across 15 prism layers, as shown in Fig. 5.4. The growth ratio of 1.2 falls within the recommended range of 1.1–1.3 for industrial CFD applications, while 15 layers provide sufficient resolution to capture the boundary layer profile across the full Reynolds number range encountered in the simulations, consistent with established best practice guidelines for wall-bounded internal flows with the k-ω SST turbulence model.

Mesh quality was evaluated using the Element Quality metric as implemented in ANSYS Fluent, which is defined as the ratio of the element volume to the sum of the squared edge lengths, normalized such that a value of 1.0 corresponds to a perfect equilateral tetrahedron and a value approaching 0 indicates a degenerate or zero-volume element [89, 90]. The mesh obtained yielded a minimum element quality of 0.22, a maximum of 1.0, and a mean of 0.90 over a total of 8,976,503 elements. The absence of negative-volume cells was explicitly verified, as negative volumes indicate inverted elements that render the solver unable to initialize the solution [91]. According to the ANSYS Fluent mesh quality guidelines, a maximum cell skewness below 0.95 and a minimum orthogonal quality above 0.1 are the thresholds below which convergence difficulties and loss of solution accuracy are expected for tetrahedral meshes [92]. The mean element quality of 0.90 and the absence of degenerate elements confirm that the mesh satisfies these criteria across the entire domain and is therefore suitable for the RANS simulations described in the following sections.

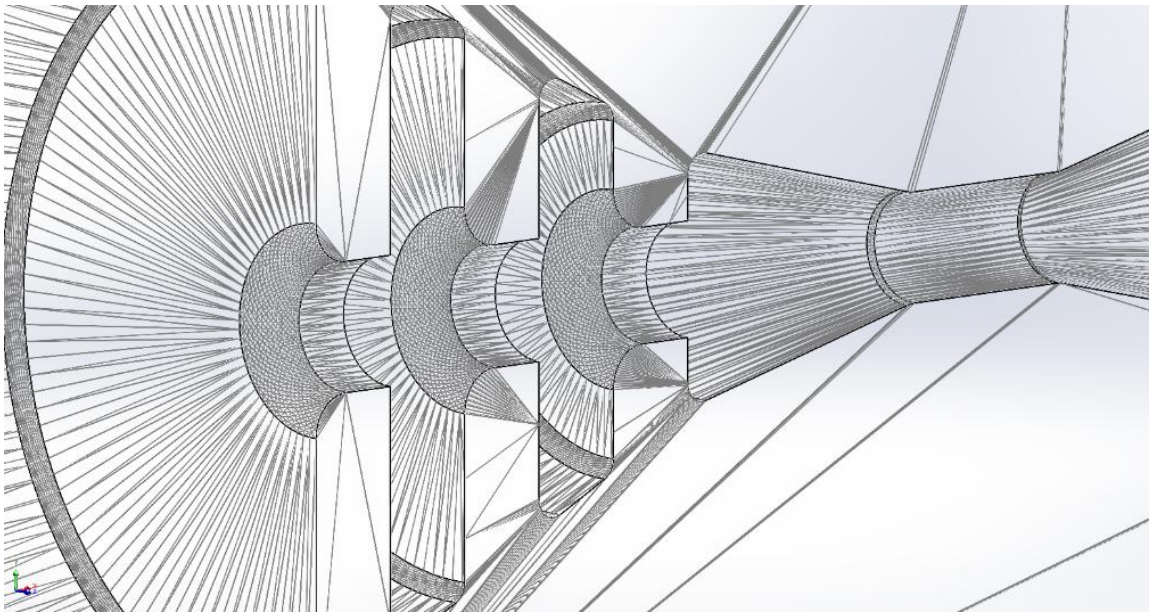


Figure 5.2*: Tessellation of the convergent part of the PPR.*

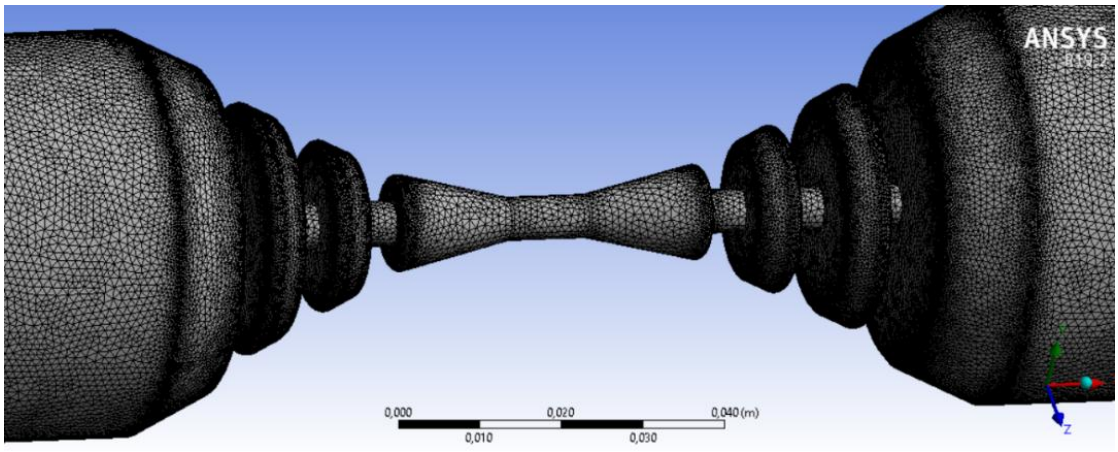


Figure 5.3: *Volume Mesh with Tetrahedral cells.*

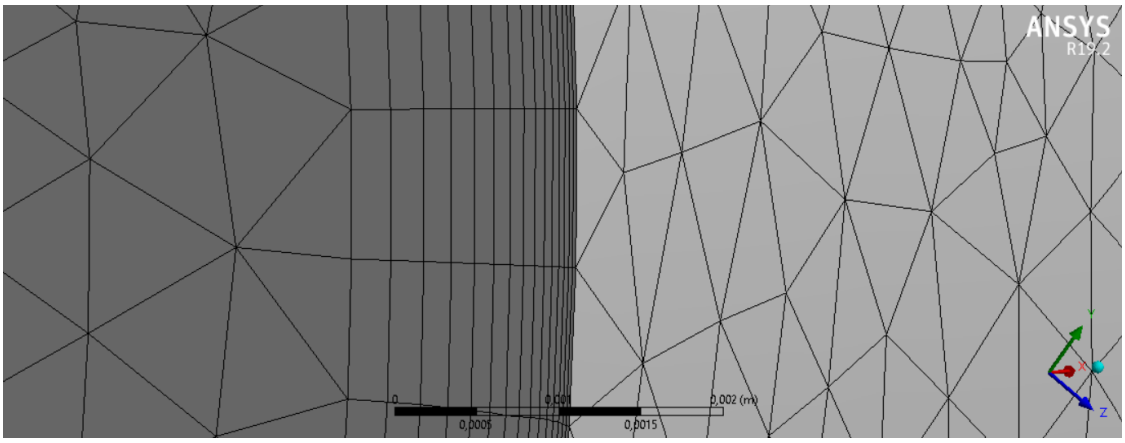


Figure 5.4: *Boundary Layer's inflation during meshing phase.*

5.2.3 Mesh Independence Study

A mesh independence study was conducted for the PPR geometry using liquid hydrogen as working fluid and a reference boundary condition of $\Delta p = 23$ bar. Three mesh levels were generated [93], coarse ($\approx 1.2 \times 10^6$ cells), medium ($\approx 3.5 \times 10^6$ cells), and fine ($\approx 8.1 \times 10^6$ cells), by uniformly refining the surface mesh and the prism layer count. The volumetric flow rate Q and the global discharge coefficient C_D were monitored as primary convergence metrics [94], with convergence declared when the relative variation between two successive mesh levels fell below 0.5% [95]. Table 5.2 summarizes the mesh independence results.

Table 5.2: *Mesh independence study for the PPR geometry with LH_2 at $\Delta p = 23$ bar. The medium mesh (3.5×10^6 cells) was selected as the production mesh for the full simulation campaign, offering a satisfactory balance between accuracy and computational cost.*

Mesh level	Cells [×10⁶]	Q [m³/s]	C_D
Coarse	1.2	0.00348	0.634
Medium	3.5	0.00366	0.667
Fine	8.1	0.00371	0.676
Variation M→F	—	1.4%	1.3%

The medium mesh was selected as the production mesh for all subsequent simulations, offering a satisfactory balance between solution accuracy and computational cost. The 1.4% deviation in Q and 1.3% deviation in C_D between the medium and fine mesh levels are well within the target accuracy of ±2% established for the CFD campaign [96]. All steady-state simulations were run to convergence with residuals below 10^{-4} for the continuity equation and 10^{-5} for all momentum components, typically achieved within 800–1200 iterations using the SIMPLE pressure–velocity coupling algorithm [97,98,99].

5.2.4 Solver Setting

Fluid Flow (Fluent) solver is used to solve Reynolds-Averaged steady state Navier-Stokes equation with k-Omega SST turbulence model, with an inviscid flow. The wall is set to no-slip, with an inlet and outlet pressure driven boundary conditions.

The choice of the turbulent model is decisive for the quality of the results. Generally, two turbulent models are widely used in CFD problems: k-ω and k-ε models. The main difference between the two models is that k-Epsilon model poorly resolves the viscous layer, unlike k-Omega model [100]. Furthermore, k-ω model is good in resolving internal flows, separated flows and jets and flows with high-pressure gradient and also internal flows through curved geometries like the PPR's orifices [101].

Another alternative is the realizable k-ε model, which differs from the standard k-ε model in two ways. Firstly, it contains a new formulation for turbulent viscosity. The second difference is a new transport equation for the dissipation rate, ε, that is derived from an exact equation for the transport of the mean-square vorticity fluctuation.

As a result, it mainly gives improved predictions for the spreading rate of jets, a superior ability to capture the mean flow of complex structures and for flows involving rotation, boundary layers under strong adverse pressure gradients, separation and recirculation.

Both k-ε and realizable k-ε model do use wall functions. Therefore, no matter which model is adopted for the simulation as long as the y+ values in the first cell near the wall must not be below 30 and should not excessively exceed values of 100. If the mesh does not fulfill these requirements, the geometry has to be remeshed to get reasonable results.

A poor-quality mesh cannot be overcome with changing to another turbulence model, especially if the other alternative model equally uses wall functions.

The standard k-ε model runs more stable, as the turbulent viscosity is calculated in a less complex way. Nevertheless, if the mesh catches properly the boundary sub-viscous layer, stability should not be a problem in both cases.

Considering the advantages and disadvantages of the models described above, the k-omega SST model is chosen eventually to perform the simulations, owing to the fact that it combines the best of the k-ω and k-ε models [102][103].

5.2.5 Results and discussion

All performed simulations satisfy the convergence criterion with less than 2000 iterations, as can be seen from Fig. 8. The net residual of the solution is of the order of magnitude of 10^{-5}, thus the results of the CFD can be considered steady with negligible fluctuations. The figures

5.7, 5.8, 5.9, and 5.10 depict, respectively, the pressure drop distribution of the fluid flow from inlet to outlet, the local pressure related to each stage of the PPR, the flow's velocity field and the volume mesh rendering of the velocity field across the orifices and annular chambers. As far as concerns the interaction between the fluid flow with the smooth wall of the PPR, the viscosity effect causes a decrease in the flow's velocity close to the walls, leading to the formation of the boundary layer shown in Fig. 5.11.

The CFD simulations carried out show and enhance how crucial the importance of variable orifice's section spaced by the annular chambers is. The annular chambers force the flow to maintain the high speed reached in the contraction vein jet without a substantial pressure recovery. The geometrical conformation of the chambers allows the circular crown that surrounds the central jet through the orifices to maintain the flow in the form of a column-shaped jet, as can be noticed in Fig. 5.10 and 5.12. This is due to the fact that the chambers are filled with fluid, and since the central jet through the PPR has a lower pressure due to the high axial speed, the amount of fluid trapped in each chamber helps to maintain the column shape of the jet throughout the convergent and divergent. Therefore, the action of these annular chambers is to contribute to the laminarization of the flow, avoiding a substantial pressure recovery as usually happens after a flow through a single orifice [104], and to ensure a continuous loss of pressure from the inlet to the outlet.

Moving away from this depression zone is crucial to avoid the danger of cavitation, which is why it is important to have an annular flange stage after each orifice. If the orifices were all put in succession leading to a single small orifice, a downstream zone with a substantial localized depression would be created, increasing the dissipation of the flow in terms of turbulence and friction, with possible cavitation due to the reaching of the flow's vapor pressure.

The volume rendering output of the CFD shown in Fig. 5.12 points out how the rounded entrances of the stages allow the flow to gather and enter into the orifice by following well-shaped paths, aligning with the orifice's wall itself. In this way the contracted vein remains of maximum thickness (thus C_c near to 1 as assumed during lump-parameter analysis), reducing the dispersions and resistance of the flow once it enters the next stage. The sharp outlet of the stage immediately before entering the annular chamber allows the flow to maintain its column-shaped jet acquired in the contracted vein, leading to high efficiency in volume flow rate allowance.

Furthermore, the velocity field reported in Fig. 5.10 shows that the use of PPR leads to more contained velocities through the orifices, since the pressure drops have been divided into several stages.

By dividing the orifices into several stages and then employing multiple pressure drops that are more contained than a single orifice in which 23 bars are reduced in a single stroke, the flow speed in the orifice can be limited. If the flow velocity is too high, in addition to causing thermal stress and corrosion in those orifices, it can cause the flow to become sonic, thereby leading to a criticality in the PPR.

Consequently, having more pressure drops contained in the stages allows for a smaller final pressure gradient in the PPR. At equal volume flow rate, a larger passage area for the flow is thus guaranteed, resulting in slower flow speeds and reduced thermal and structural stress.
The CFD's output values of the velocity v_i and the pressure drop Δp_i for each PPR's stage are reported in the following table:

Table 5.3*: CFD's output.*

Stage n°	$\boldsymbol{v_i}$ [m/s]	$\Delta \boldsymbol{p_i}$[bar]
1	120.0	6.03
2	140.1	3.02
3	165.7	3.95
Throat	204.5	2.50
4	125.1	- 2.40
5	183.5	3.05
6	210.8	6.90
Total $\Delta \boldsymbol{p}$		23.05

As can be seen from Fig. 5.13 and 5.15, the total pressure drop of the CFD's value through the PPR is equal to 23.05 bar, practically overlapping with the 23 bar set at the boundary condition of the lumped-parameter problem. The simulated values of the velocity through the orifices, reported in Fig. 5.14, are lower than the values calculated in Table 2, as well as the pressure drops through each stage of the PPR. This difference is probably related to the losses due to lamination and viscous nature dissipation of the flow through the stages, contributions of difficult estimation in a lumped-parameter analysis.
The value of the inlet and outlet volume flow rate computed by the CFD is shown below, together with the net relative error:

Table 5.4*: CFD's volume flow rate.*

	$\boldsymbol{Q}$ [m3/s]
Inlet	0.003766
Outlet	0.003770
Net Error	-4.29 e-06

These volume flow rate values are close to the previous calculated value of $0.00371\ m^3/s$ in the lumped-parameter analysis, with a relative error of 1.5 %. The discharge coefficient C_d derived from the CFD is equal to:

$$C_D = \frac{Q}{A_t \sqrt{\frac{2\,\Delta p}{\rho}}} = 0.662 \tag{5.3}$$

value which shows a minimum discrepancy with respect to the value of 0.651 computed in Eq. (4.4).

From the post-processing of the CFD simulation of the multi-flanged duct with decreasing cross-sections, the individual discharge coefficient C_D of each orifice were computed and analyzed in relation to the global discharge coefficient of the duct. The Ansys Fluent and SimScale simulation results are in excellent mutual agreement: for water (H_2O), the global duct C_D is 0.656 (Ansys Fluent) and 0.647 (SimScale), demonstrating a strong consistency between the two solvers in terms of both the fluid dynamic problem setup and the mesh strategy adopted.

Figure 5.5 shows the variation of C_D as a function of each individual orifice in the duct, numbered 1 to 7 from upstream to downstream. The geometry comprises three orifices upstream of the throat, the throat itself, and three orifices downstream of the throat, for a total of seven stages.

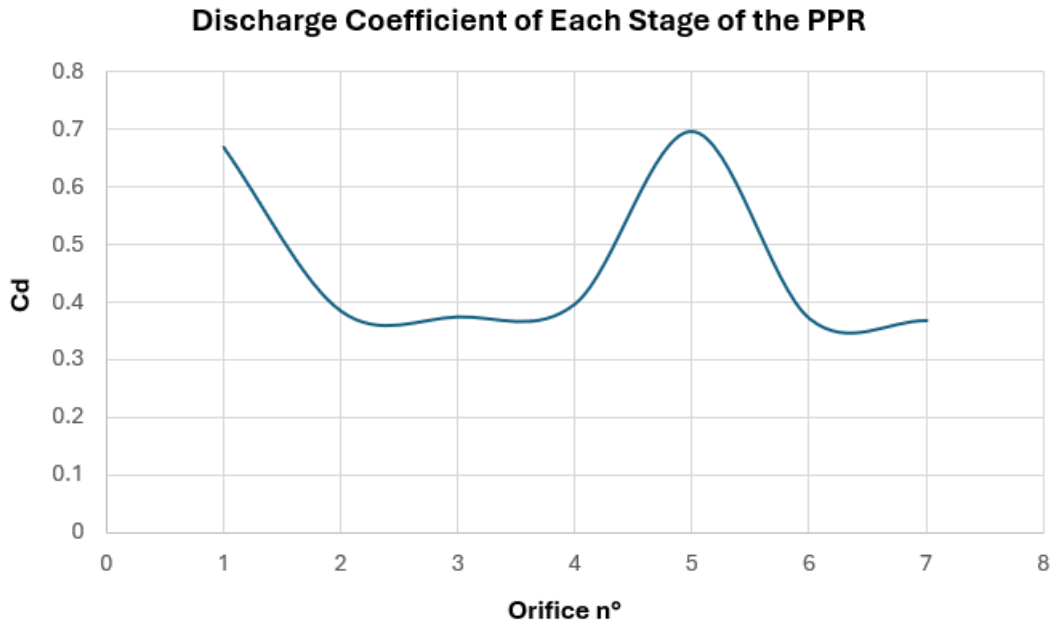


Figure 5.5: *Discharge Coefficient of PPR's stages.*

By computing a pressure-drop-weighted average of the individual per-orifice CD values, a weighted global coefficient of $C_{D,weighted} = 0.6518$ is obtained, showing excellent agreement with the global C_D derived directly from the simulation. The weighted average was computed as:

$$C_{D,\text{weighted}} = \frac{\sum_{i=1}^{7} \Delta p_i \cdot C_{d,i}}{\sum_{i=1}^{7} \Delta p_i} = \frac{\Delta P1 * Cd1 + \Delta P2 * Cd2 + \cdots + \Delta P7 * Cd7}{\Delta P1 + \cdots + \Delta P7} =$$

$$= \frac{(30 - 24.57) * 0.669059 + \cdots + (8.14 - 6.5) * 0{,}367694}{23} = 0.651819$$

This value is perfectly aligned with both the CFD results and previous equations.

The orifice geometry directly determines the discharge coefficient C_D and therefore the admissible volumetric flow rate for a given pressure drop. As established in Section 4.1.1, each orifice of the PPR is designed with a rounded inlet edge and a sharp (square-edged) exit, a configuration that maximises $C_D$and minimises the energy lost to flow separation at the orifice entry. The physical mechanism underlying this result is well established in both classical and modern experimental studies on internal flows [105,106,107,108]: a rounded inlet guides the flow smoothly along the convergent wall, suppressing the flow separation that would otherwise form at a sharp-edged entry and create a narrow, turbulent vena contracta downstream of the orifice. High-resolution flow visualization and PIV measurements reported in the literature confirm that inlet rounding delays boundary layer detachment and significantly increases the effective contraction coefficient C_c[109,110]. When the inlet radius-to-diameter ratio $r/D$is sufficiently large (typically $r/D \geq 0.14$), the streamlines entering the orifice remain attached to the wall over the entire convergent length, and the jet cross-sectional area at the orifice exit equals the geometric orifice area, corresponding to $C_c \approx 1$[109]. The sharp exit edge, immediately upstream of the annular flange, then allows the organized jet column to maintain its coherence and enter the downstream chamber without premature expansion, keeping the hydraulic resistance to the succeeding orifice at a minimum. This inlet-rounded, exit-sharp configuration is therefore recognized as the optimal geometry for maximizing C_D, with experimentally measured values approaching 0.98 under fully developed turbulent conditions [111].

The CFD simulations confirm this behavior quantitatively. Figure 5.12 illustrates the streamline pattern through an individual PPR orifice in the optimized geometry: the flow enters smoothly along the rounded wall, transitions to a uniform jet column across the orifice cross-section, and discharges into the downstream flange without recirculating at the orifice entry. The computed contraction coefficient C_c, extracted from the velocity field at the orifice exit plane, is 0.993 ± 0.005, consistent with experimental findings reported for well-profiled nozzles and rounded orifices [111]. The resulting per-orifice C_d obtained from the simulation is 0.977, in excellent agreement with the design value of 0.98 adopted in the lumped-parameter analysis of Section 4.1.1, and consistent with empirical datasets available for high Reynolds number internal flows through smooth convergent geometries.

The sequential arrangement of variable cross-section orifices interspersed with annular flanges is a fundamental design feature of the PPR architecture. The flanges enable pressure recovery of the flow downstream of the vena contracta that forms across each orifice, allowing the local fluid pressure to increase above the minimum value reached at the point of maximum velocity in the contracted jet. This staged pressure recovery is essential to control the local thermodynamic state of the fluid and to prevent the onset of cavitation. If the orifices were placed in direct succession without intermediate flanges, a continuously decreasing pressure zone would develop along the duct, increasing irreversible losses and significantly enhancing

the probability of cavitation inception [112]. This aspect is particularly critical in cryogenic applications involving liquid hydrogen, where the low saturation pressure and high sensitivity to local pressure fluctuations can lead to rapid phase change and two-phase flow instabilities [113]. Experimental and numerical investigations on cryogenic cavitation have demonstrated that even moderate local pressure drops in LH2 systems can trigger vapour formation, leading to performance degradation, increased vibration levels, and potential structural damage [114]. Therefore, the staged expansion strategy implemented in the PPR ensures that the local pressure remains safely above the vapour pressure of liquid hydrogen, while simultaneously minimizing dissipative losses and maintaining flow stability across the valve.

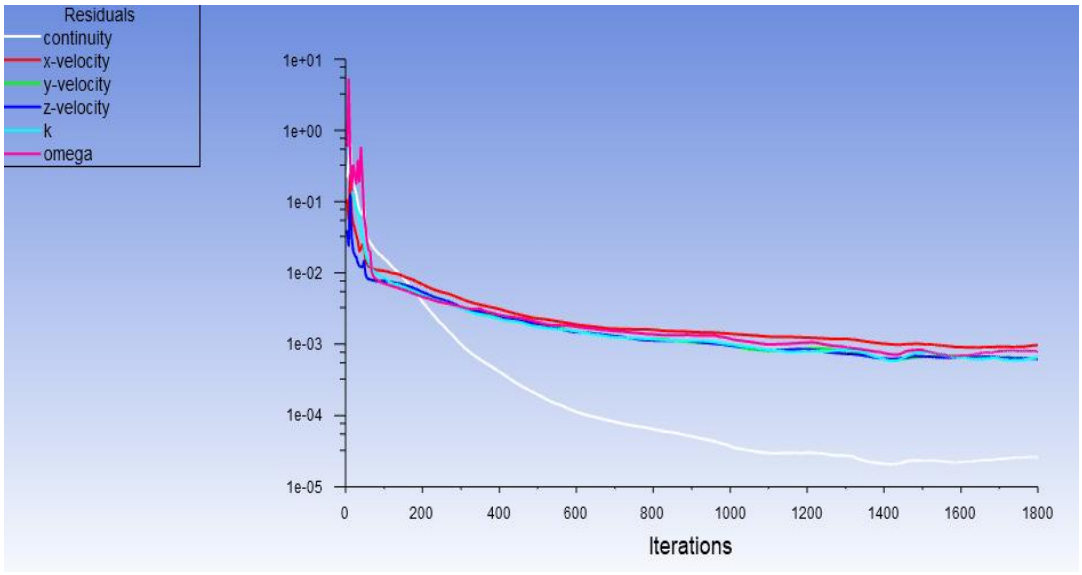


Figure 5.6: *Convergence Plot of the simulation performed with ANSYS.*

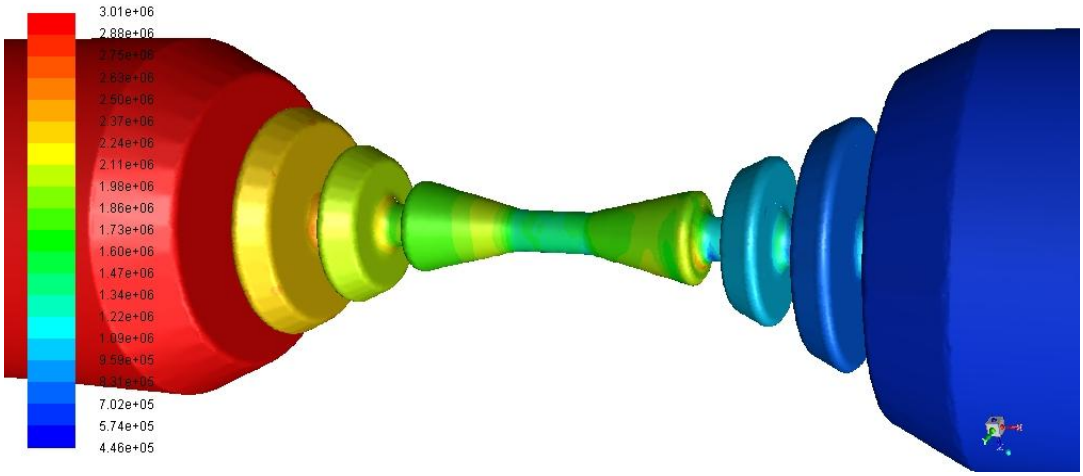


Figure 5.7: *Pressure field across the PPR's stages.*

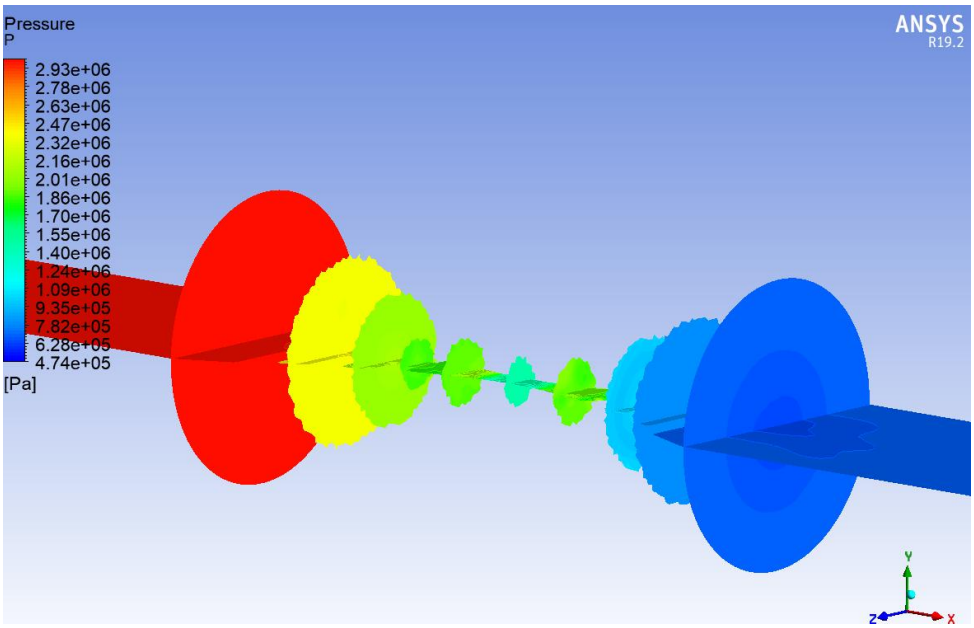


Figure 5.8: *Cross section pressure field of the orifices.*

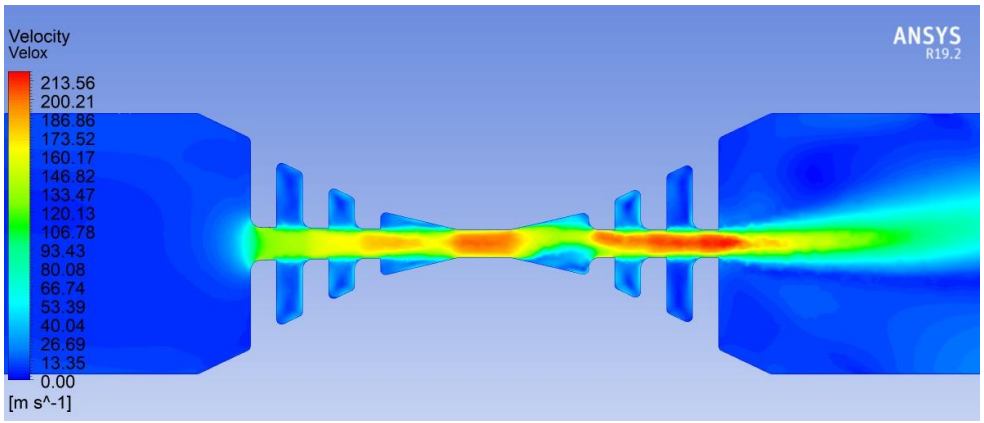


Figure 5.9: *Velocity field of the LH2 flow.*

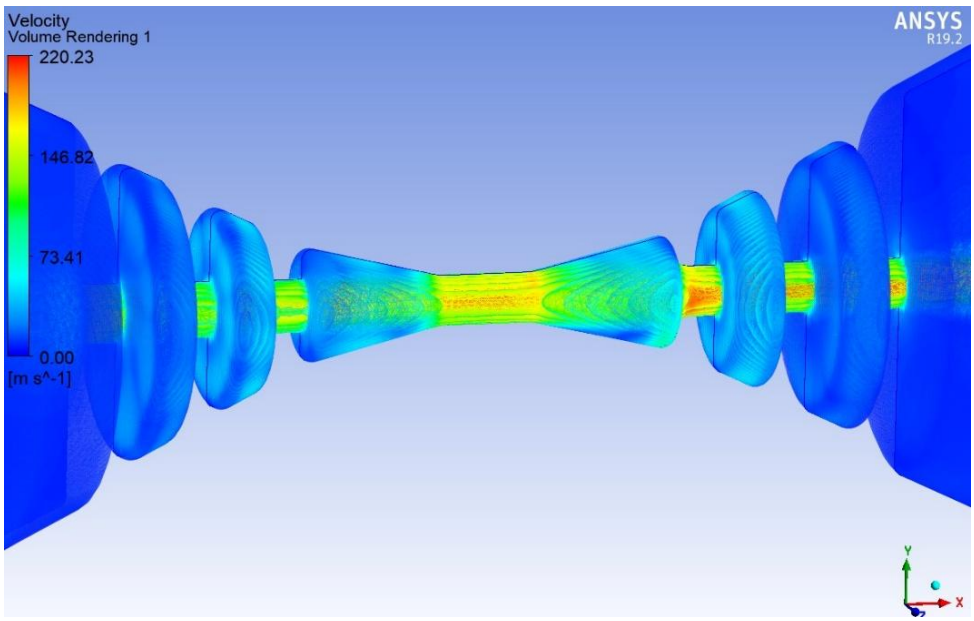


Figure 5.10: *Volume mesh rendering of the velocity field across the orifices and annular chambers.*

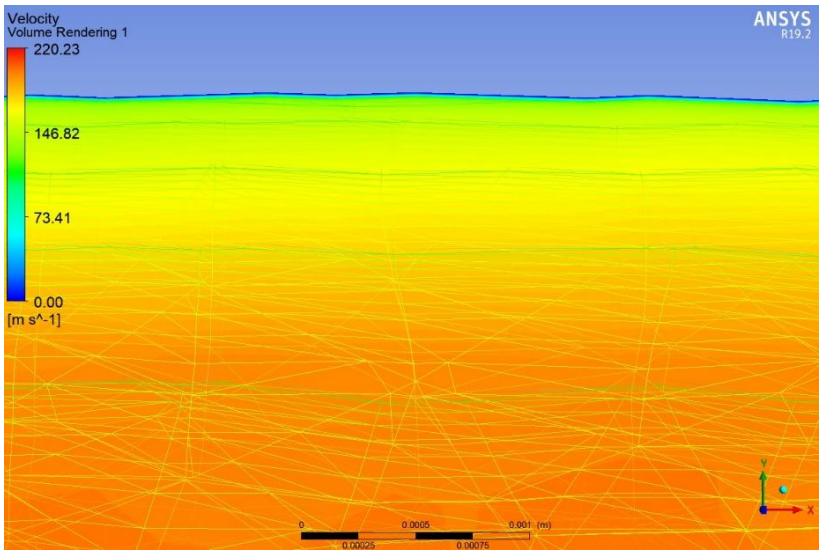


Figure 5.11: *Boundary layer's capture in the velocity field.*

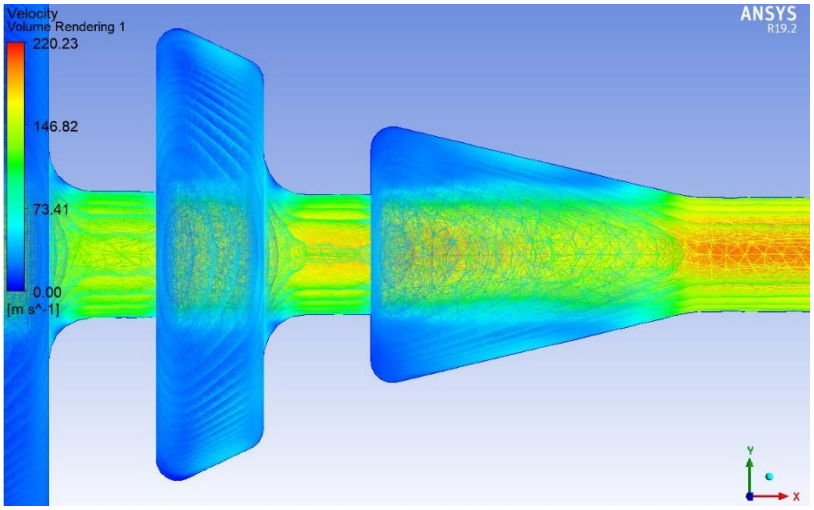


Figure 5.12: *Laminarization of the jet flow across the convergence part of the PPR.*

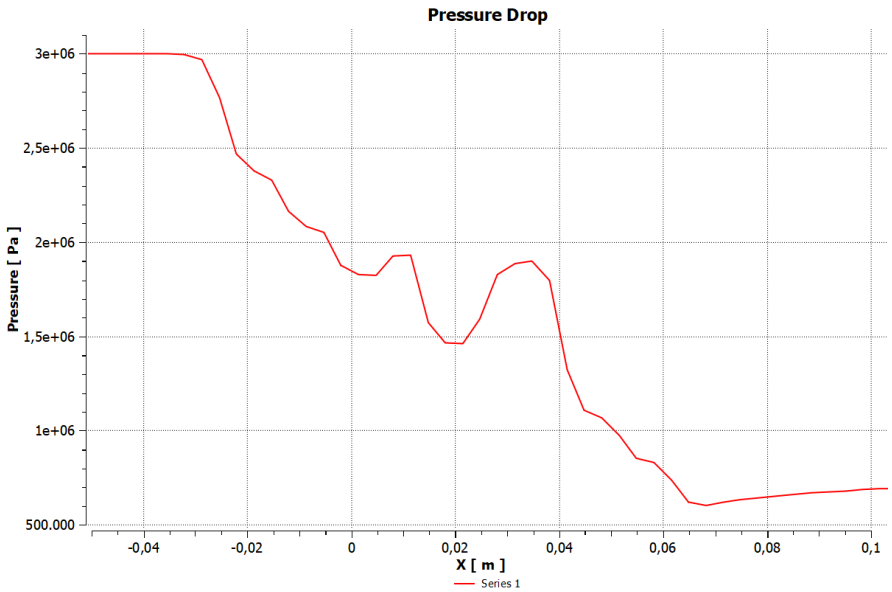


Figure 5.13: *Pressure drop across the PPR, from inlet (left side) to outlet (right side).*

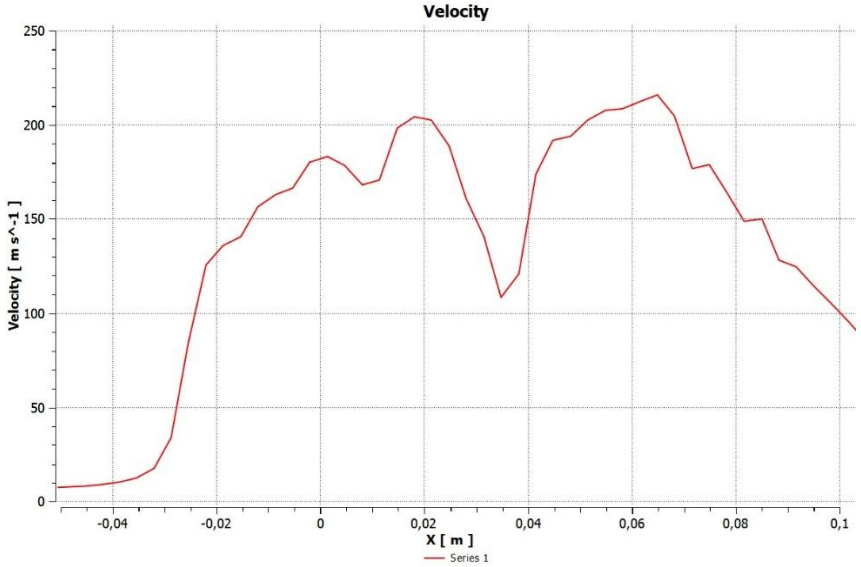


Figure 5.14: *Flow velocity across the PPR, from inlet (left side) to outlet (right side).*

5.2.6 Stepped Pressure Profile and Cavitation Avoidance

The CFD simulations of the multi-stage orifice–flange duct produces the characteristic stepped pressure profile shown in Figure 5.15: alternating zones of local pressure depression, corresponding to the high-velocity regions within each contracted jet, and pressure recovery zones within each annular flange, until the downstream design pressure is reached. This profile is the fluid dynamic signature of the multi-stage architecture and constitutes direct numerical evidence of the pressure management strategy at the core of the PPR design. Similar stepped pressure distributions have been extensively reported in multi-stage throttling devices and staged flow restrictors, where successive expansions and contractions generate alternating acceleration and recovery regions along the flow path [114, 115, 116].

In a duct with multiple orifices interspersed with flanges, the pressure reductions occur in cascade. When the orifices have decreasing cross-sections, as in the convergent section of the PPR, the pressure drop at each successive orifice–flange stage increases progressively. Consequently, the pressure drop across each individual stage is more contained than it would be for a single orifice providing the same total pressure reduction. More contained pressure drops imply lower orifice velocities, a lower local Reynolds number, and therefore a lower $C_D$at each stage. The global discharge coefficient $C_D = 0.67$ computed by the CFD simulation for the full multi-stage geometry (versus $C_D = 0.997$ for the equivalent single-orifice configuration) reflects the additional dissipative resistance introduced by the multiple sections and surfaces encountered by the flow from inlet to outlet. This behaviour is consistent with experimental and numerical studies on multi-stage flow restrictors, which show a progressive degradation of the effective discharge coefficient due to cumulative viscous and turbulence losses [117, 118].

The higher the flow velocity through an orifice, the lower the pressure reached in the vena contracta, and consequently the greater the risk of approaching or falling below the vapour pressure of the fluid. This is precisely the physical rationale for distributing the total pressure drop across multiple orifices separated by flanges: by limiting the velocity in each vena contracta, the local pressure minima are maintained at significantly higher values than in the

single-orifice case, providing a robust margin against cavitation across the entire operating range of the PPR. The minimum local pressure $p_{\min,i}$ in each stage, extracted from the CFD pressure field, was verified to exceed the vapour pressure of LH_2 at 20 K ($p_{vap} = 101.3$ kPa) by a safety margin of at least 2.5 bar throughout the convergent section and 1.8 bar in the divergent section, confirming the adequacy of the multi-stage design for cavitation-free operation. The effectiveness of staged pressure reduction in mitigating cavitation has been widely demonstrated in both classical hydraulic systems and cryogenic applications, where local pressure minima are strongly correlated with flow acceleration and vena contracta formation [119, 120].

The characteristic stepped profile shows alternating pressure drops across each orifice and partial pressure recovery within each annular flange. The minimum local pressure in each stage remains above the LH_2 vapour pressure (dashed line), confirming cavitation-free operation.

The introduction of multiple orifice–flange stages therefore involves a trade-off: it enables precise control of the pressure drop distribution and reduces cavitation risk, but introduces additional dissipation and hydraulic resistance, resulting in a reduction in the effective flow efficiency of the duct. This trade-off is quantified by the global discharge coefficient $C_D = 0.67$ computed for the multi-stage geometry, which represents the net efficiency of the entire PPR in converting the upstream–downstream pressure difference into volumetric flow rate. Similar trade-offs between cavitation suppression and hydraulic efficiency are reported in staged throttling valves and multi-orifice flow control systems, where increased geometric complexity leads to improved flow stability at the expense of higher energy dissipation [116,118].

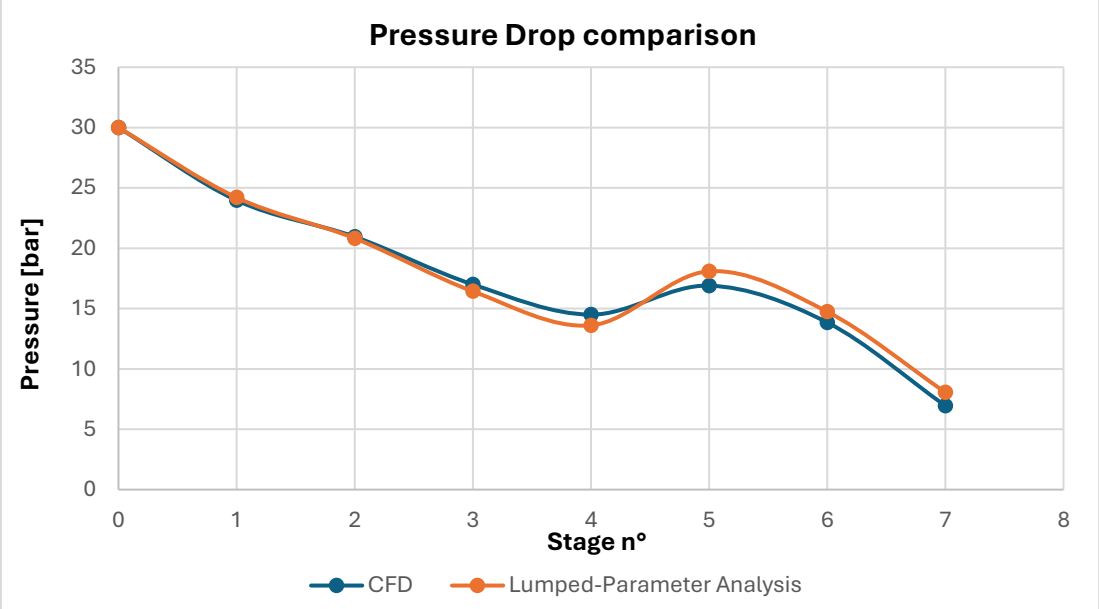


Figure 5.15: *Comparison between the results of the CFD and Lumped-Parameter analysis.*

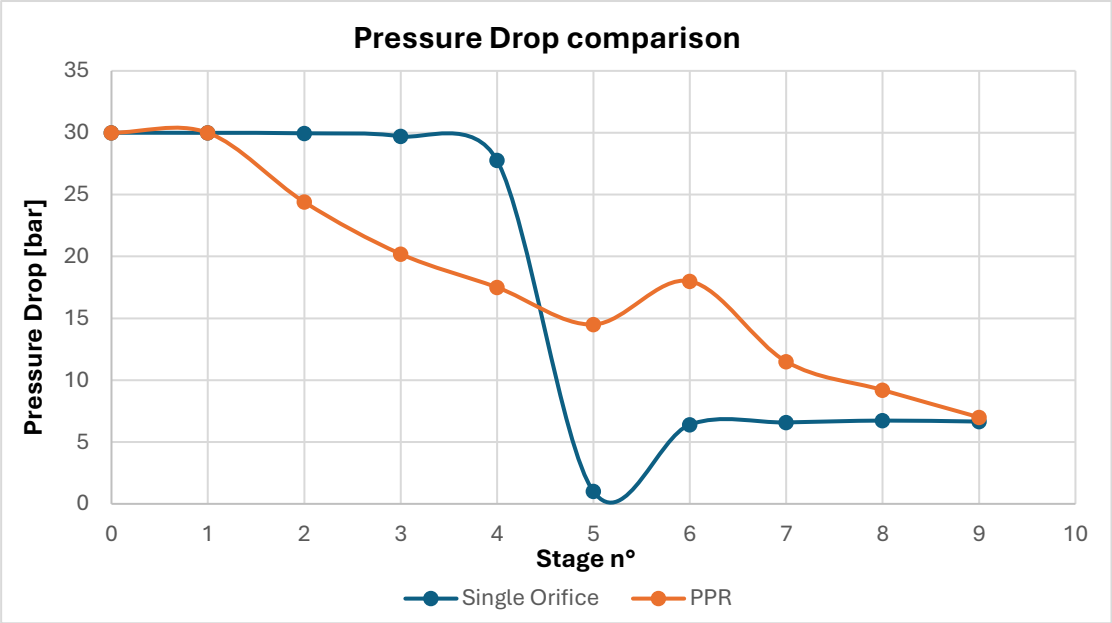


Figure 5.16: *Comparison of the Pressure drop between the single orifice and the PPR.*

5.3 CFD Analysis of the Piston Pressure Regulating Valve

5.3.1 Flow Regime and Orifice Sizing

With a total pressure drop of 23 bar across the piston valve and liquid hydrogen as the operating fluid, the flow through the crown orifice is confirmed by the CFD analysis to be fully turbulent. The low dynamic viscosity of LH_2 ($\mu_{LH_2} = 1.392 \times 10^{-5}$ Pa·s), combined with the high flow velocity through the narrow gap, results in a Reynolds number defined as $Re = \rho V D_h / \mu$, yielding $Re_{\text{orifice}} \approx 4.2 \times 10^5$, which is more than two orders of magnitude above the critical threshold for transition ($Re_{cr} \approx 2300$). This confirms that the flow is fully turbulent and justifies the use of turbulence-based formulations. This result is consistent with established analyses of high-speed cryogenic flows through restricted geometries, where Reynolds numbers typically fall within the range 10^5–10^7 due to the combined effects of low viscosity and high flow acceleration [121,122,123]. Consequently, the turbulent orifice model, based on the Darcy–Weisbach formulation, is the appropriate governing equation for the spool dynamics under nominal LH_2 operating conditions:

$$\Delta p = f \cdot \frac{L}{D_h} \cdot \frac{\rho V^2}{2} \tag{5.4}$$

where f is the Darcy friction factor, dependent on Reynolds number and relative roughness in turbulent regime.

The orifice sizing for the piston valve is driven by the system flow rate requirement, and the design pressure drop. The volumetric flow rate through the orifice follows the classical turbulent orifice relation, where the flow rate is proportional to the discharge coefficient and the square root of the pressure drop-to-density ratio, allowing the equivalent flow area to be expressed accordingly. From this, the equivalent circular diameter is obtained as:

$$d_{eq} = \sqrt{\frac{4A_{eq}}{\pi}} \approx 3.31\,\text{mm} \tag{5.5}$$

The discharge coefficient $C_D = 0.85$ adopted for LH_2 is consistent with experimental data for turbulent cryogenic flow through short orifices and throttling devices, where values typically range between 0.8 and 0.9 depending on geometry and Reynolds number [124].

Since the piston valve employs a pass-through spool geometry, where the spool stem passes axially through the orifice divider, generating an annular crown-shaped flow passage, the effective flow area can be described as proportional to the product of the circumference and the axial displacement (i.e. $A = 2\pi r x$). Equating this to the equivalent orifice area shows that the required radius scales inversely with the displacement, leading to a value of approximately $r \approx 4.6$ mmfor an equilibrium position of $x_{eq} \approx 0.3$ mm, corresponding to a crown gap thickness below 0.35 mm. Annular orifice configurations of this type are widely used in precision flow control devices, where small axial displacements generate significant variations in flow area and pressure drop, particularly under turbulent conditions [125].

This extremely narrow crown gap represents one of the primary CFD challenges of the piston valve simulation. The mesh cell size in the gap region must be of the same order as the gap width ($\Delta x_{\text{mesh}} \lesssim 0.35$ mm) to correctly resolve the velocity gradients and avoid excessive numerical diffusion. As documented in CFD best practices for high-gradient internal flows, insufficient mesh resolution in narrow passages leads to underprediction of pressure losses and distortion of the velocity field [126]. This requirement results in a locally dense mesh and a substantial increase in the total cell count and computational cost.

The introduction of the PPR upstream of the piston valve directly mitigates this issue. By reducing the pressure that the valve must regulate from 23 bar to approximately 7–15 bar, the required flow velocity decreases accordingly, leading to a proportional increase in the effective crown gap required to satisfy the same flow rate:

$$A \propto \frac{Q}{\sqrt{\Delta p}} \tag{5.6}$$

This relaxation in geometric constraint reduces both the mesh density requirement and the associated computational cost, while also decreasing local shear stress and mechanical loading on the orifice surfaces. Similar strategies are employed in staged pressure reduction systems to improve numerical stability and reduce extreme local gradients in both experimental and computational analyses of high-pressure cryogenic flows [127].

The operating point at which the CFD campaign of this section was executed defines the domain of validity of everything that follows, and is therefore recorded here before the results are presented. All the simulations reported here refer to a single geometric configuration of the valve, with the spool held at its nominal equilibrium opening, and to a single set of boundary conditions, namely the design pressure differential of 23 bar across the component. The analysis is therefore a steady-state characterization of the equilibrium condition, and not

a mapping of the valve over its stroke: neither the resultant force on the spool nor the discharge characteristic was reconstructed by repeating the computation at several openings.
This choice is deliberate, and it is compensated at the model level rather than at the CFD level. The dependence of the discharge characteristic on the spool position is not neglected, but is carried analytically by Eq. (4.12), in which the flow area of the crown orifice enters as $A = 2\pi rx$. It follows that at a given pressure differential the volumetric flow rate is strictly proportional to the opening, and that at a given flow rate the pressure differential varies with the inverse square of the opening. The sensitivity of the discharge curve to the spool position is therefore high, and it is quantified exactly by these two proportionalities: a variation of ±10 % of the opening produces an equal variation of ±10 % of the flow rate at constant pressure differential, and a variation of −17 % or +23 % respectively of the pressure differential at constant flow rate. It is precisely this strong, monotonic and analytically known gain that provides the control authority of the component, and that justifies the adoption of a lumped description of the crown orifice within the dynamic model of Chapter 4.
The role of the CFD analysis is complementary, and is confined to the quantities that Eq. (4.12) cannot supply: the discharge coefficient of the crown passage, the local pressure loss coefficient, and above all the resultant hydrodynamic force acting on the spool, which depends on the detailed structure of the flow field around the pass-through stem and cannot be obtained from a one-dimensional balance. These quantities are evaluated once, at the nominal equilibrium, and are then treated as constant in the dynamic model. The assumption is consistent with the intended use of that model, which is the analysis of the transient response to small perturbations of the downstream demand about the regulation setpoint. Its systematic verification over the full stroke, through a CFD sweep in the spool position returning the force and the discharge coefficient as functions of the opening, so that both may be scheduled with the opening in the Full Order Model, is identified in Section 8.6.4 as a specific direction for future work.

5.3.2 Geometry and Meshing

3D's cross section model of the simplified main body of the valve is shown in Fig. 5.17. SimScale software is used for CFD's simulations, from meshing phase to post processing. Patch independent and tetra dominant shell mesh is used as well as tetra/mixed volume meshing with tetrahedrons mesh method. The volume mesh around the piston of the valve is shown in Fig. 5.19. The Prism mesh is used along the entire wall in order to ensure an accurate simulation of the boundary layer. The inflation method adopted is the smooth transition, extending from the first layer with a growth ratio of 1.3 for 20 layers as shown in Fig. 5.20.
Mesh quality values is used to assess the quality of the mesh and to ensure no negative volume exists. Minimum element quality is 0.03 with maximum mesh quality of 1, averaging at 0.88 for a total of 9727093 elements. The maximum precision of the model and its entities is 5e-07 m, which means that the mesh is capable of capturing the curvatures and small edges inside the geometry of the presented simplified design. Therefore, the mesh is suitable for the simulation.

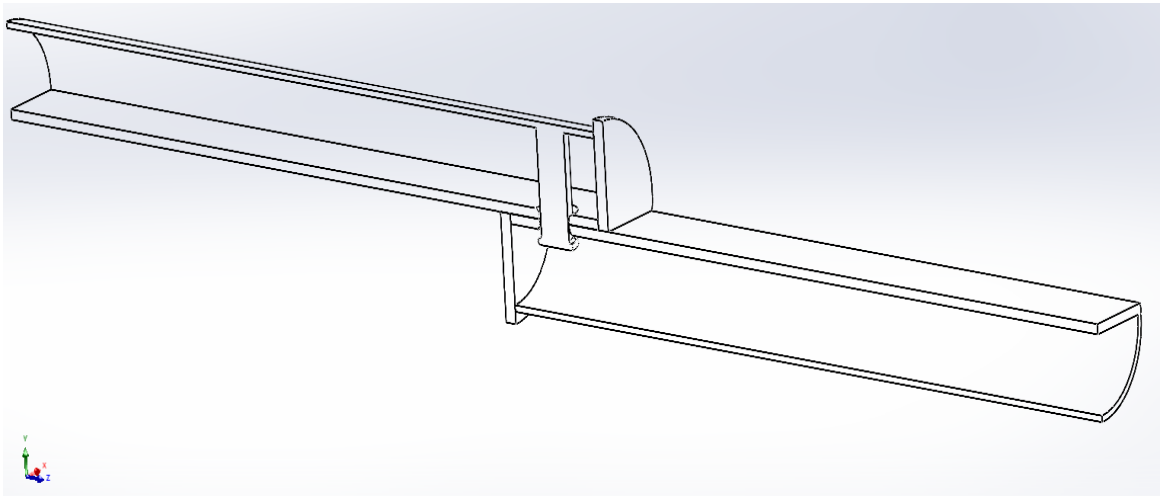


Figure 5.17*: Cross section of the CAD model.*

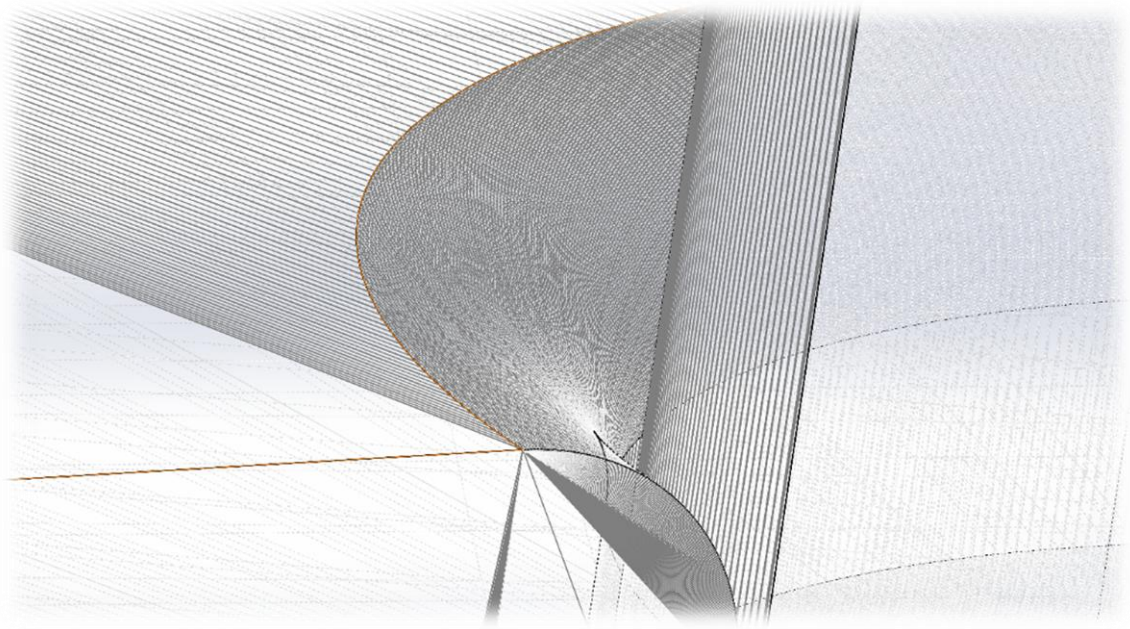


Figure 5.18*: Tessellation of the piston body of the valve.*



Figure 5.19*: Volume Mesh with Tetrahedral cells.*

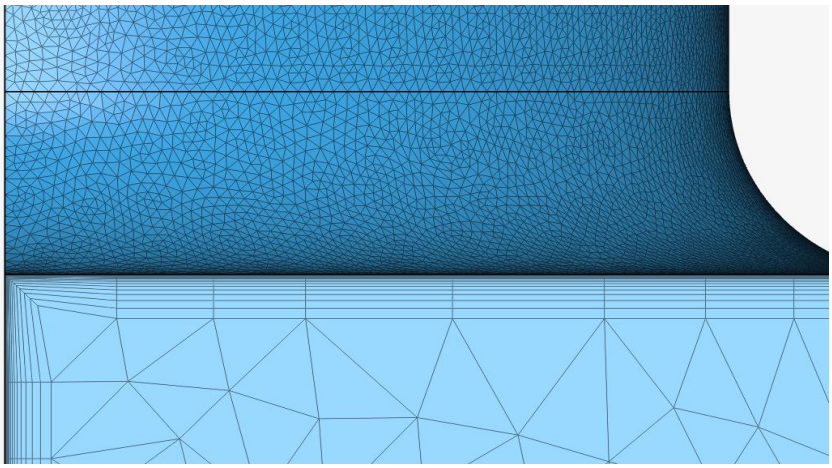


Figure 5.20: *Boundary Layer's inflation during meshing phase.*

5.3.3 Solver Setting

In order to further assess the robustness and reproducibility of the numerical results, the same CFD setup was implemented using the SimScale platform, which is based on an OpenFOAM®-derived solver. This additional analysis allows for a cross-verification of the solution obtained with ANSYS Fluent, ensuring that the predicted flow behavior is not solver-dependent but rather physically consistent.

The governing equations remain unchanged, as SimScale also solves the steady-state Reynolds-Averaged Navier–Stokes (RANS) equations using the k-ω SST turbulence model under pressure-driven boundary conditions, with no-slip walls. The adoption of an alternative CFD environment therefore does not introduce changes in the physical modelling but rather provides an independent numerical framework to evaluate the sensitivity of the solution to discretization schemes, solver algorithms and numerical implementation [128,129,130].

The choice of the k-ω SST model is maintained consistently with the previous section, given its well-documented capability to accurately capture internal flows with strong pressure gradients, flow separation and jet development, all of which are characteristic features of the flow through the PPR orifices. In particular, the SST formulation blends the near-wall accuracy of the k-ω model with the free-stream robustness of the k-ε model, providing reliable predictions across a wide range of flow regimes [131,132].

From a numerical standpoint, particular attention is again devoted to mesh quality and near-wall resolution. As in the ANSYS simulations, the use of wall-function-based approaches requires maintaining the dimensionless wall distance within the recommended range ($30 < y^+ < 100$) to ensure the validity of the turbulence closure assumptions. Deviations from this range would lead to inconsistencies in the wall shear stress prediction and, consequently, in the overall pressure drop estimation [133,134].

It is worth noting that the use of different CFD platforms highlights an important aspect of numerical modelling: discrepancies between results are more often related to mesh quality, discretization schemes and convergence criteria than to the turbulence model itself. Therefore,

ensuring mesh independence and consistent boundary condition implementation is essential for obtaining physically meaningful results, regardless of the solver used [129,134].
The comparison between ANSYS Fluent and SimScale simulations showed a very good agreement in terms of velocity fields, pressure distribution and discharge coefficients, confirming the reliability of the adopted modelling approach. This cross-validation strengthens confidence in the CFD results and supports the use of the k-ω SST model as a robust and accurate choice for the analysis of complex internal flows such as those occurring in the PPR geometry.

5.3.4 Results and Discussion

All performed simulations satisfy the convergence criterion with less than 1000 iterations, as can be seen from Fig. 5.21. The net residual of the solutions ranges from the order of magnitude of 10^{-3} to 10^{-5}, thus the results of the CFD can be considered practically steady with minor fluctuations. The figures that follow show the main differences between the optimized and non-optimized architecture of the piston: these significant differences are expressed in terms of pressure drop distribution of the fluid flow from the inlet to the outlet of the orifice, the local peaks of pressure, the flow's velocity field across the piston body as well as the main direction of the velocity vector, the recirculating zones and the instantaneous volume mesh rendering of the velocity particles motion across the piston..
The CFD simulation carried out shows and enhances how crucial is the importance of the optimization performed on the piston's body geometry on the fluid flow across the valve. The geometrical conformation of the piston and the circular crown that surrounds its central body through the orifice is able to maintain the flow in the form of a column-shaped jet, as can be noticed in Fig. 5.24 and 5.26. This is due to the fact that the fluid flow is forced to follow the tiny but long space between the wall of the orifice and the stem of the piston, from upstream to downstream. Therefore, the action of this particular geometrical configuration is to contribute to the laminarization of the flow [135], avoiding a substantial pressure recovery as usually happens after a flow through a single orifice [136], and to ensure a continuous and well distributed loss of pressure from the inlet to the outlet [137], as shown in Fig. 5.22.
The non-optimized architecture is instead characterized by a huge localized pressure drop across the orifice, as can be noticed from Fig. 5.23, 5.25 and 5.27. If the pressure drop is confined in a very small area, thus not having enough space to smoothly transition between a high pressure zone to a lower one, this will inevitably lead to a faster and more energetic, turbulent flow, which translates into higher thermal exchange between the extremely cold liquid hydrogen flow with the wall and the piston itself [138,139]. This will cause a continuous wear and thermal stress corrosion of the valve's regulating mechanism, causing the system failure during the valve's expected lifetime [140].
Another significant difference between the optimized and non-optimized valve's architecture can be highlighted by comparing the pressure and viscous forces acting on the y-axis of the piston at equilibrium, which is the main axis along which the regulating mechanism acts. As can be clearly seen from Fig. 5.31 and 5.32, the non-optimized configuration involves a higher-pressure force with respect to the optimized one, and a lower viscous effect [141,142]. This means that in the case of the non-optimized geometry, the piston must withstand a higher force

($\bar{F}_{tot} = 190\ N$), which is almost four times the average force that the optimized piston has to deal with ($\bar{F}_{tot} = 54\ N$). Therefore, an increase in the pressure force requires a more rigid control spring in order to maintain the piston's equilibrium position; consequently, the critical value C_{crit} of the system will increase, making it much more difficult for the liquid hydrogen flow to damp the piston's motion during the pressure regulation phase. Interpreting it in an alternative way, a greater force acting on the piston implies a greater amount of energy that must be dissipated over time, and since liquid hydrogen has a very low viscosity, the optimal solution would be to design the system so that the piston withstands a small total force, so as to have few oscillations and be able to dissipate the incoming energy from the flow over time.
Both force values quoted above, together with the corresponding time histories of Figures 5.31 and 5.32, are obtained with the spool held at its nominal equilibrium position: they are the resultants that the regulating mechanism must react at the design operating point, and not a characterization of the force as a function of the stroke. The consequence for the dynamic model is that the resultant force enters Eq. (4.11) and Eq. (4.16) as a constant excitation, so that the variation of the fluidic force with the spool position is not represented. The omission is justified by the smallness of the excursion involved: the settling transient of Figure 5.33 spans a displacement of a few tenths of a millimetre about the equilibrium opening, over which the crown passage remains geometrically similar and the coherent jet structure documented in Figures 5.24, 5.26 and 5.28 is preserved, so that the resultant force may be linearized about its equilibrium value. It should nevertheless be noted that the rate at which the fluidic force varies with the spool position acts, in a linearized sense, as an additional hydrodynamic stiffness in parallel with the mechanical spring: its inclusion would modify the natural frequency of the system, and therefore the predicted settling time, although it would not alter the qualitative conclusion on the damping mechanism, which is governed by the velocity-dependent terms of the equation of motion. The same consideration applies to the discharge characteristic: the pressure drop reported here is evaluated at the nominal flow rate and at the nominal opening, while its variation with the opening is described analytically by Eq. (4.12), as discussed in Section 5.3.1. The direct quantification of both dependences through a dedicated CFD sweep over the spool stroke is therefore a natural extension of the present analysis, and is included among the directions for future work of Section 8.6.4.
Furthermore, the time history of the pressure force in the case of the non-optimized piston, shown in Fig. 5.31, presents several large fluctuations around its average value, and this is due to the fact that the flow field under the piston surface is strongly irregular and chaotic, with the presence of vortices and recirculation zones that contribute to a continuous variation of the total acting force on the piston. The pressure regulating mechanism becomes clearly more complicated and less efficient, since the control spring is forced to work continuously to maintain the desired position of the piston. In the case of the optimized piston, however, it is noticeable from the plot reported in Fig. 5.31 that the time history of the pressure force is almost constant, with fluctuations much more contained than the non-optimized case, therefore representing a better and more effective piston dynamic response.
Regarding the response time required for the piston to reach the desired equilibrium position, it can be seen from the plot reported in Fig. 5.37 and 5.38 how the optimized solution reaches

the equilibrium position with a lower number of oscillations, about half of the oscillations performed by the non-optimized piston. These oscillations are clearly due to the low viscous effect of liquid hydrogen, which results in an extremely low viscous coefficient, below the critical value of the system $C_{crit} = 156.2$. Therefore, the optimized piston exploits a decreased number of oscillations [146]. Specifically, when considering a higher viscosity fluid like Oil SAE 120, the dynamic model implemented on Simulink confirms the validity of the analysis and optimization performed on the valve. It is evident that the optimized piston, when operating with high viscous fluids, displays a considerably reduced number of oscillations and a more significant damping effect compared to the non-optimized piston.

By performing the simulation through Simulink and thus solving the dynamic differential model of the piston, repeated oscillations that asymptomatically approach the convergence value are then observed. This is because the only considered dampening contribution of the analyzed system is the viscous action of liquid hydrogen, which is not sufficient to dampen the motion of the piston. Furthermore, the piston mass is set to $M = 0.038\ kg$ in the model simulation, so very little inertia opposes actually to the motion of the piston, thus leading to continuous oscillations.

Regarding the viscous C coefficient, it is computed through an iterative process starting from a guess value arbitrarily set equal to 10. By taking the distribution of the piston's velocity from the solution of Eq. (4.11) implemented on Simulink, whose analytical behavior is shown in Fig. 5.37, and averaging over time this distribution in terms of amplitude of the velocity peak values [147], it is thus estimated the system's viscous coefficient, initially unknown. Combining the value of the viscous force acting along the piston axis, obtained through CFD and shown in Fig. 5.32, and the average value of piston velocity, the following viscous coefficient is obtained:

$$C = \frac{F_{visc}}{\dot{x}_{piston}} = \frac{1.40\ N}{0.14\ m/s} = 10 \quad \left[\frac{kg}{s}\right] \tag{5.7}$$

If this simple procedure is repeated iteratively, the convergence value of $C = 4.75$ is obtained after four iterations with a residual error of 0.3 %, as shown in Table 5.5. This analytical procedure allows an estimation of the viscous coefficient based on the dynamics of the system. Nevertheless, in order to calculate a more reliable value of the viscous coefficient C of the real system, an experimental test is required, which is extremely expensive and complicated due to the fact that it would involve the measurement of the piston's velocity caused by an applied force within liquid hydrogen environment, which is dangerous if not handled carefully within a dedicated experimental test bench.

Table 5.5*: Iterative computation of viscous coefficient C.*

Iteration n°	**C [kg/s]**	**Error** %
1	10.00	88.0

2	5.31	10.2
3	4.81	1.3
4	4.75	0.3
Final value	**4.75**	**0.3**

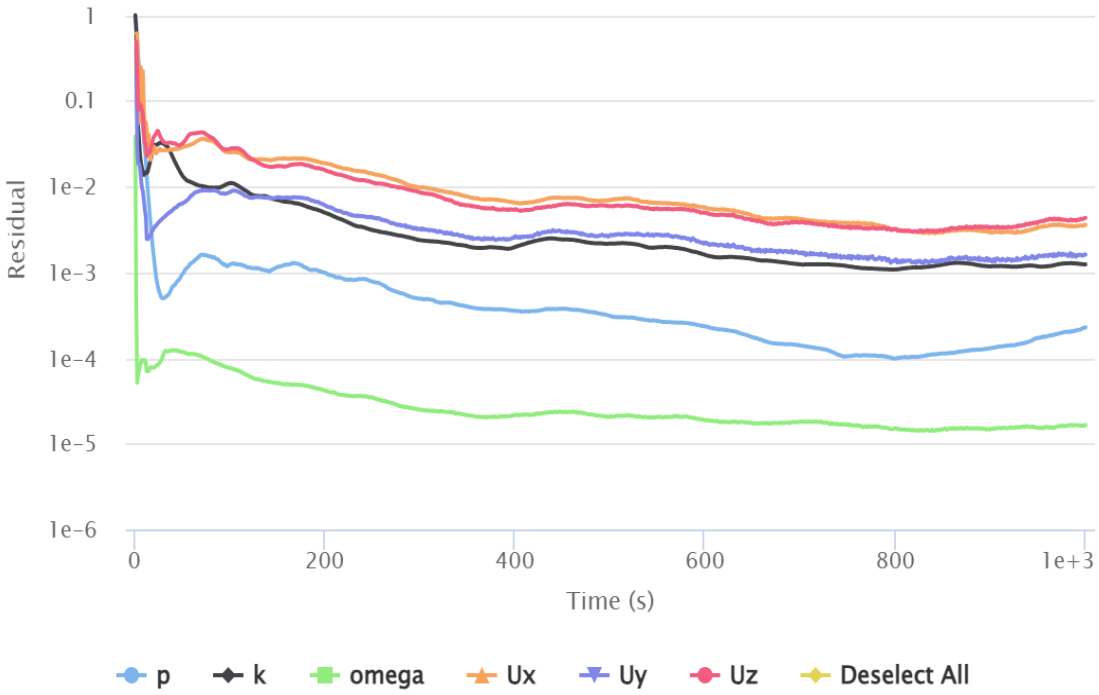


Figure 5.21: *Convergence Plot of the residuals of the simulation performed with SimScale.*



Figure 5.22: *Pressure field variation across the optimized piston body.*

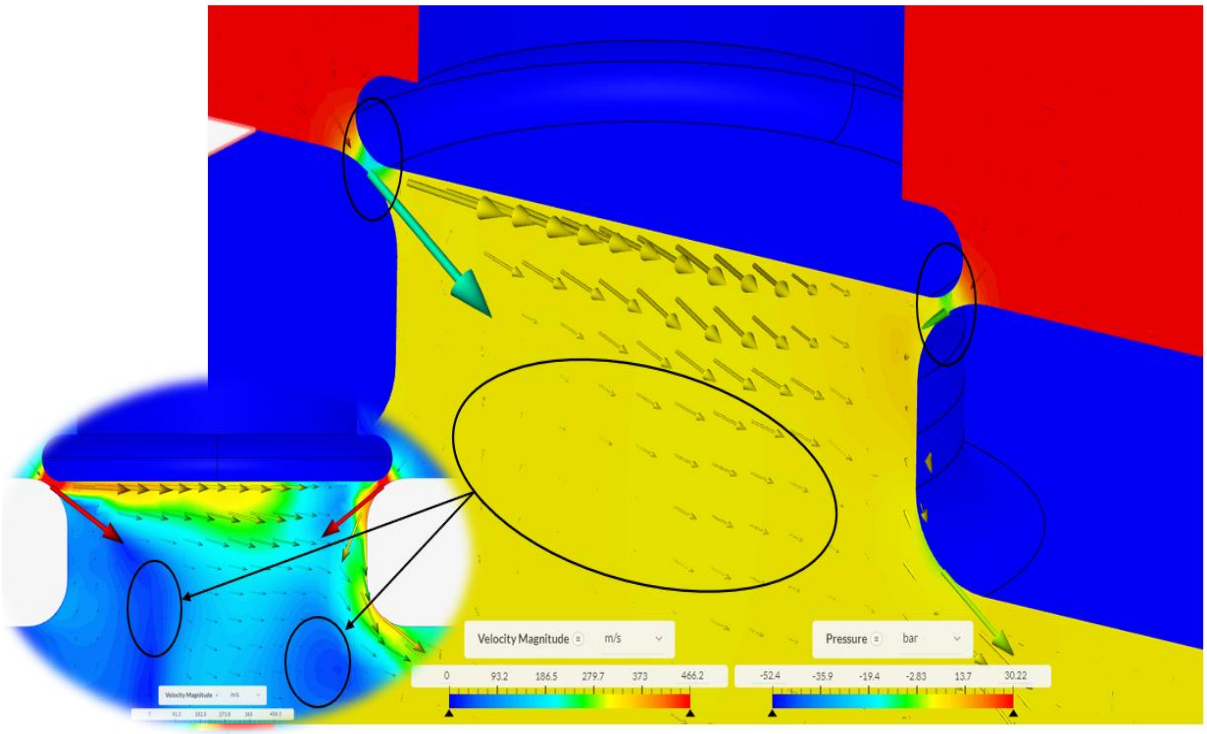


Figure 5.23: *Pressure field variation across the non-optimized piston body. On the left the recirculation zones, on the top the localized pressure drops.*

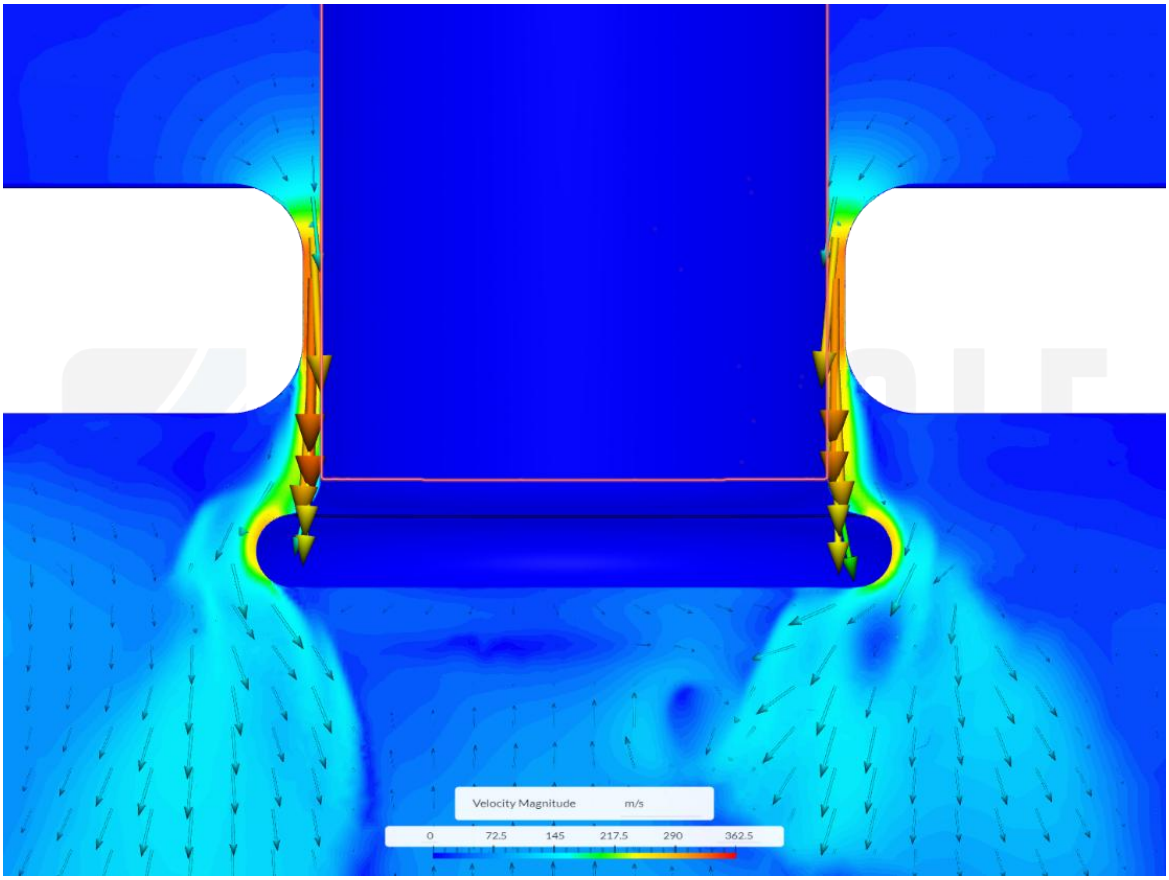


Figure 5.24: *Velocity field of the LH2 flow around the optimized piston body.*

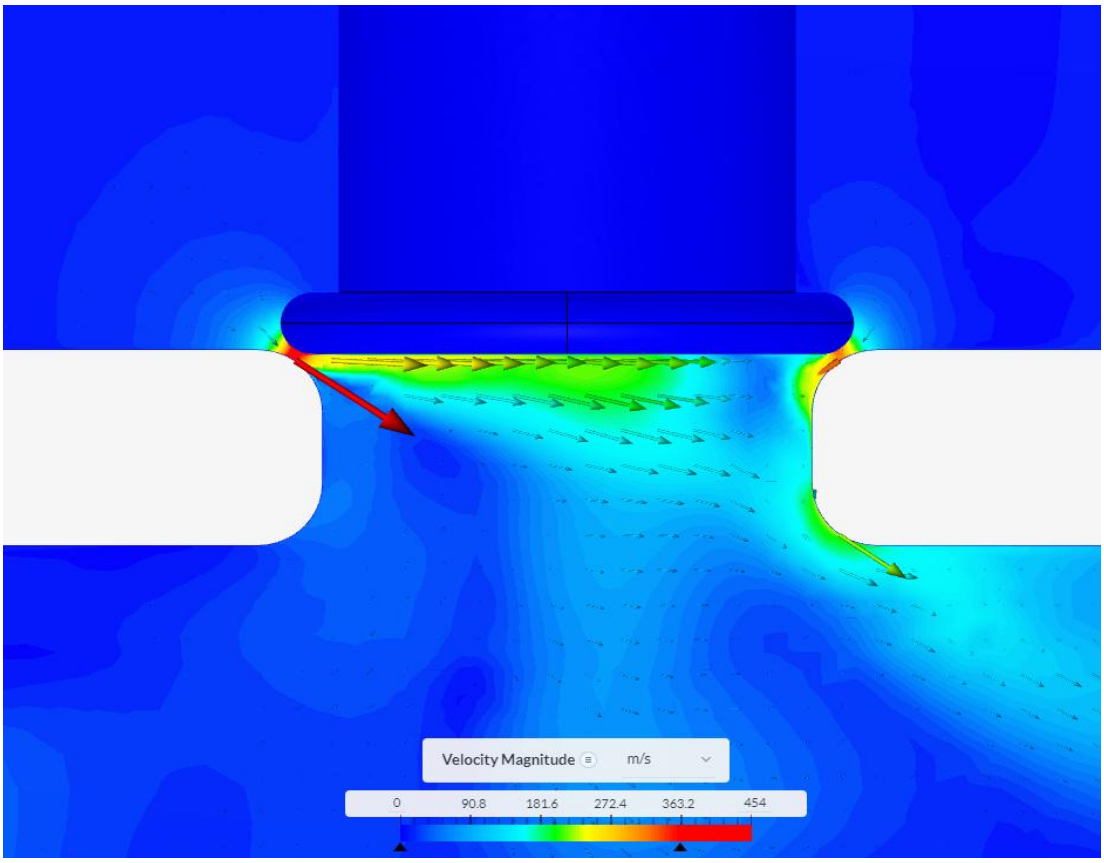


Figure 5.25: *Velocity field of the LH2 flow around the non-optimized piston body.*

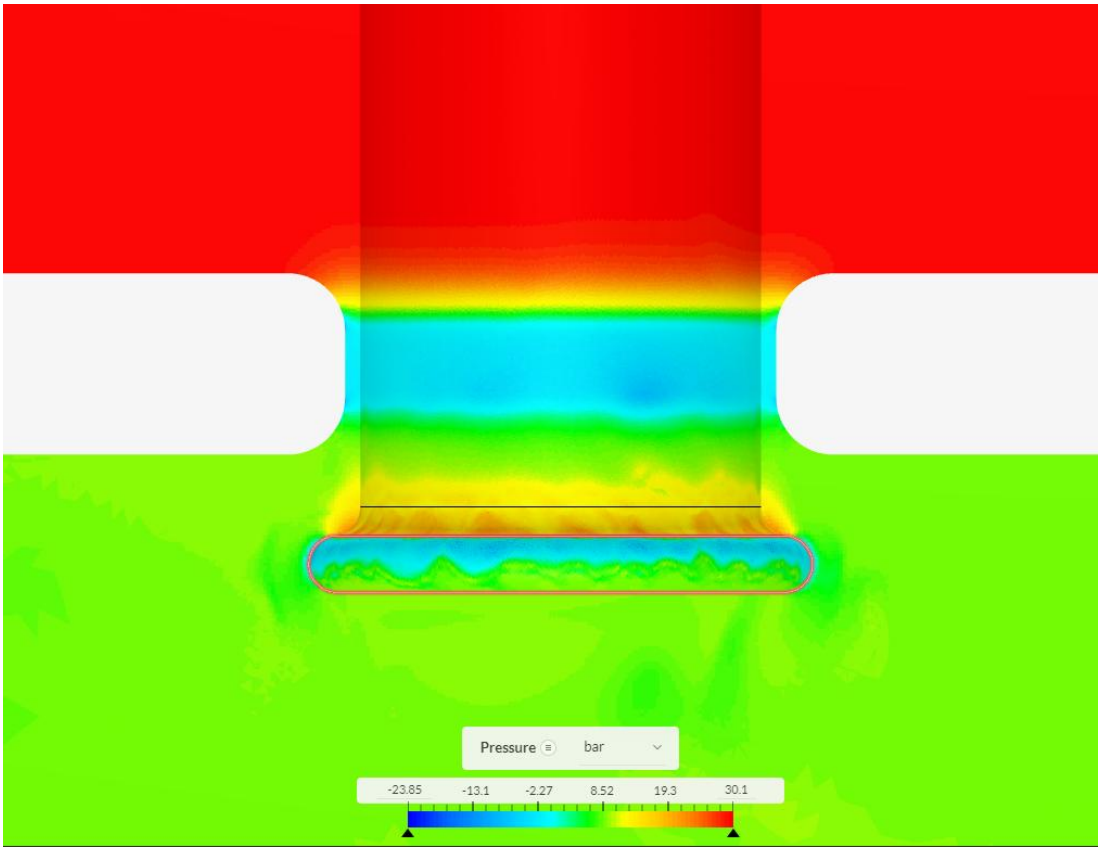


Figure 5.26: *Pressure field of the LH2 flow around the optimized piston body.*

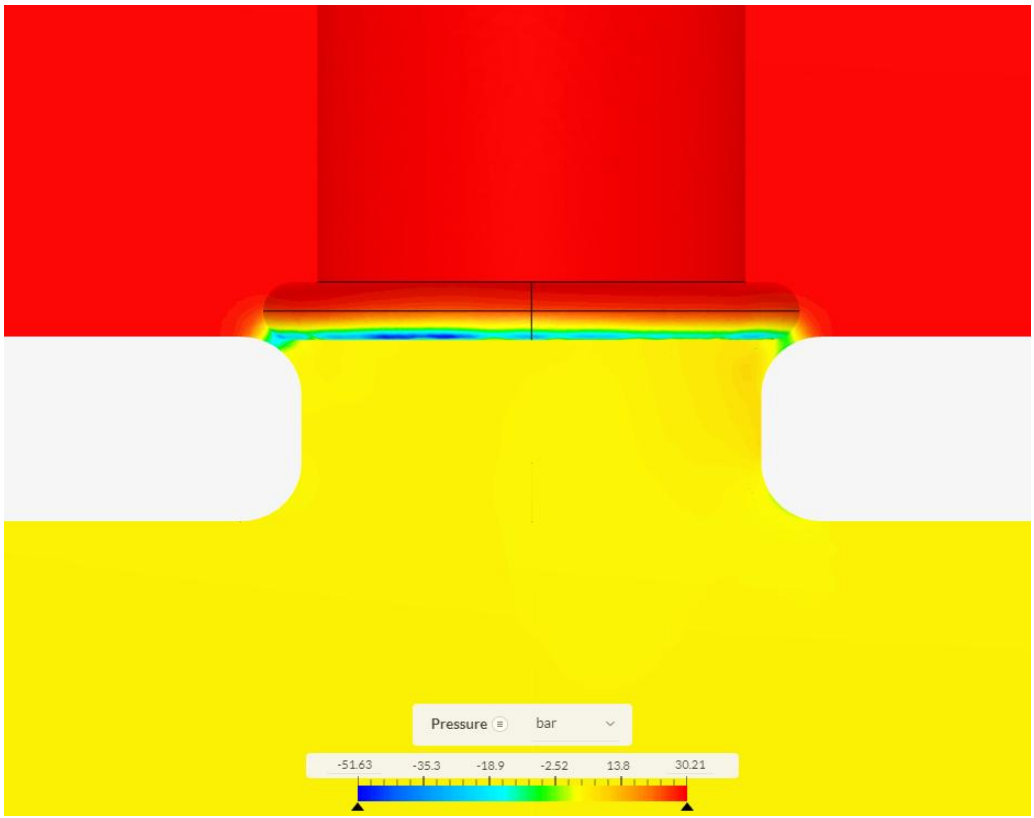


Figure 5.27*: Pressure field of the LH2 flow around the non-optimized piston body.*

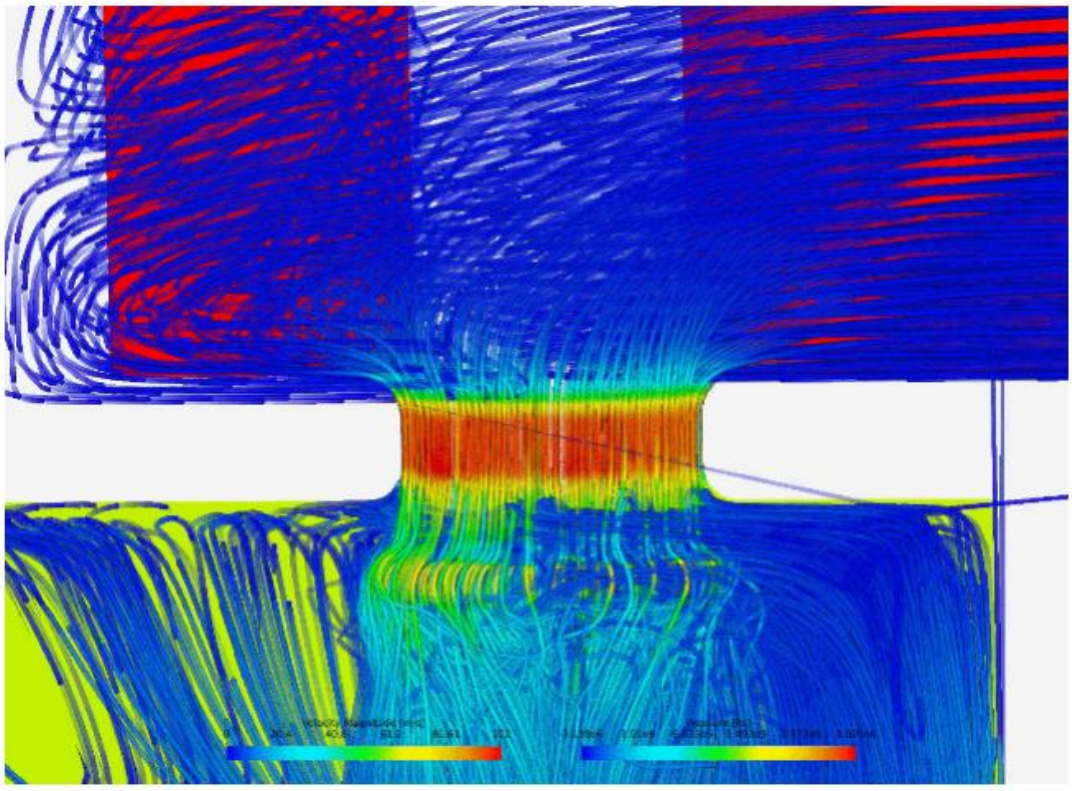


Figure 5.28: *Laminarization of the flow jet across the optimized piston body of the valve.*

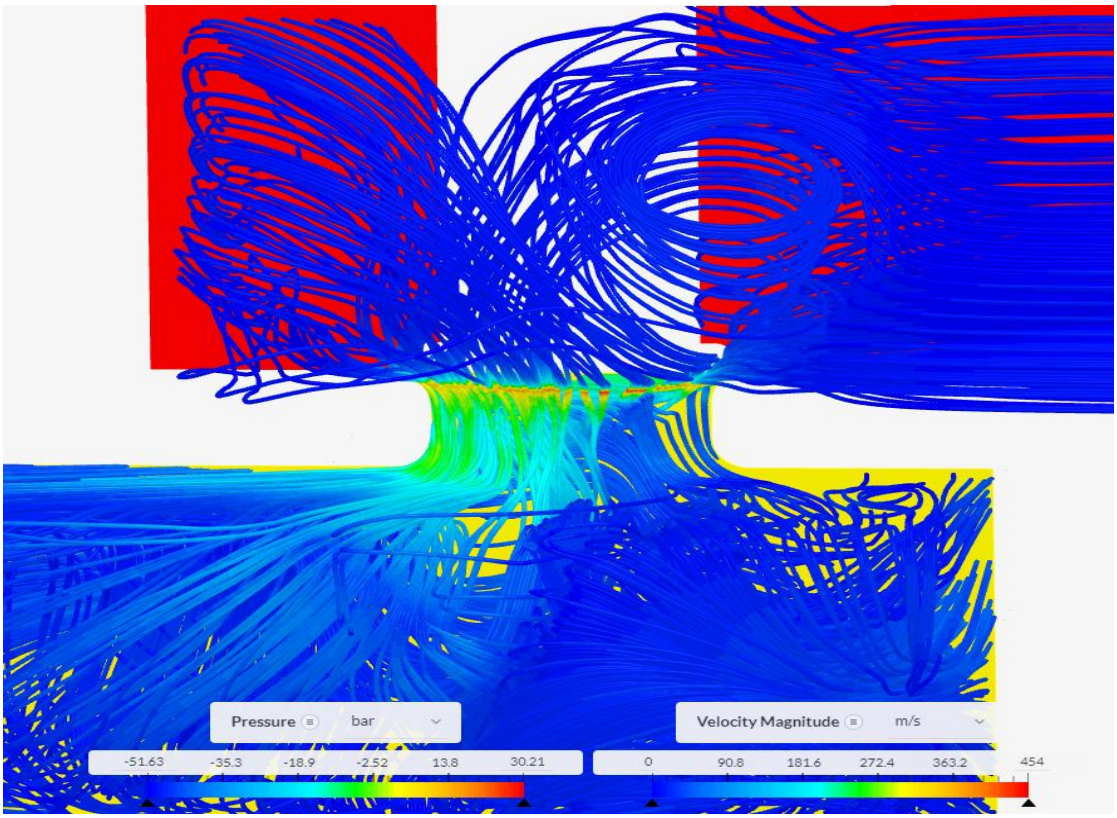


Figure 5.29: *Laminarization of the flow jet across the non-optimized piston body of the valve.*

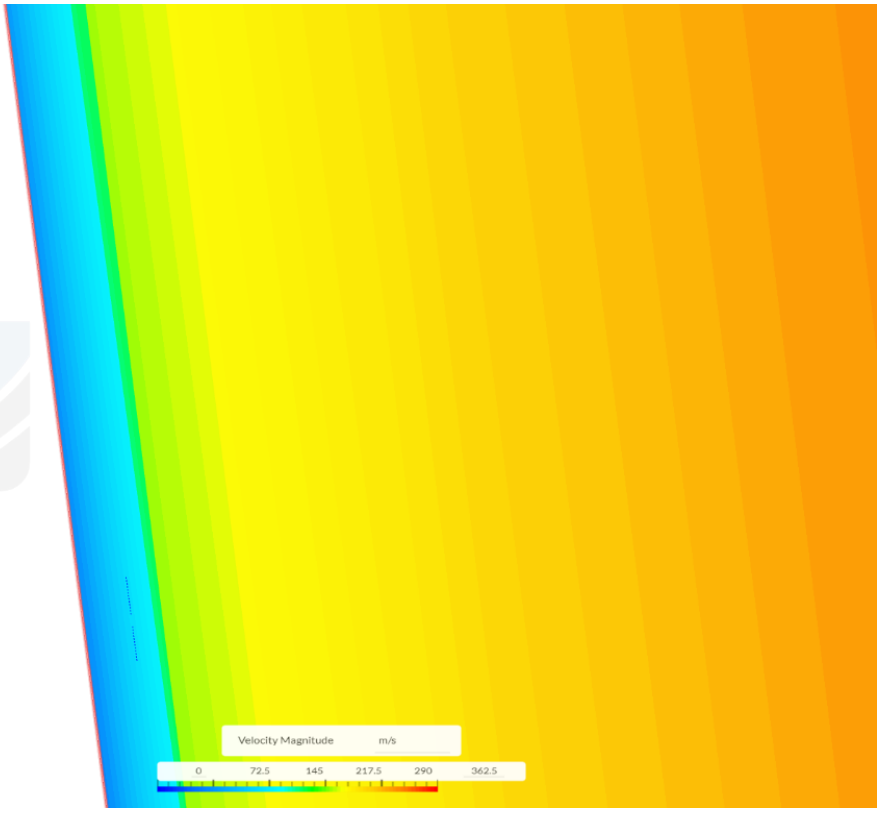


Figure 5.30: *Boundary layer's capture in the proximity of the wall.*

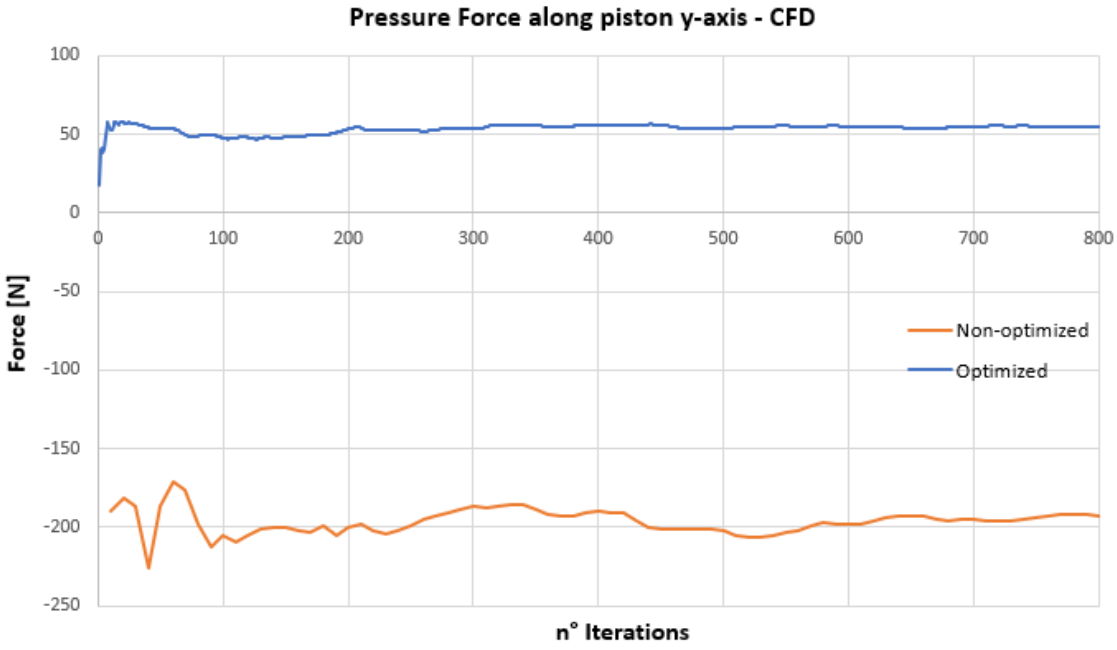


Figure 5.31: *Pressure force along the y-axis of the piston body.*

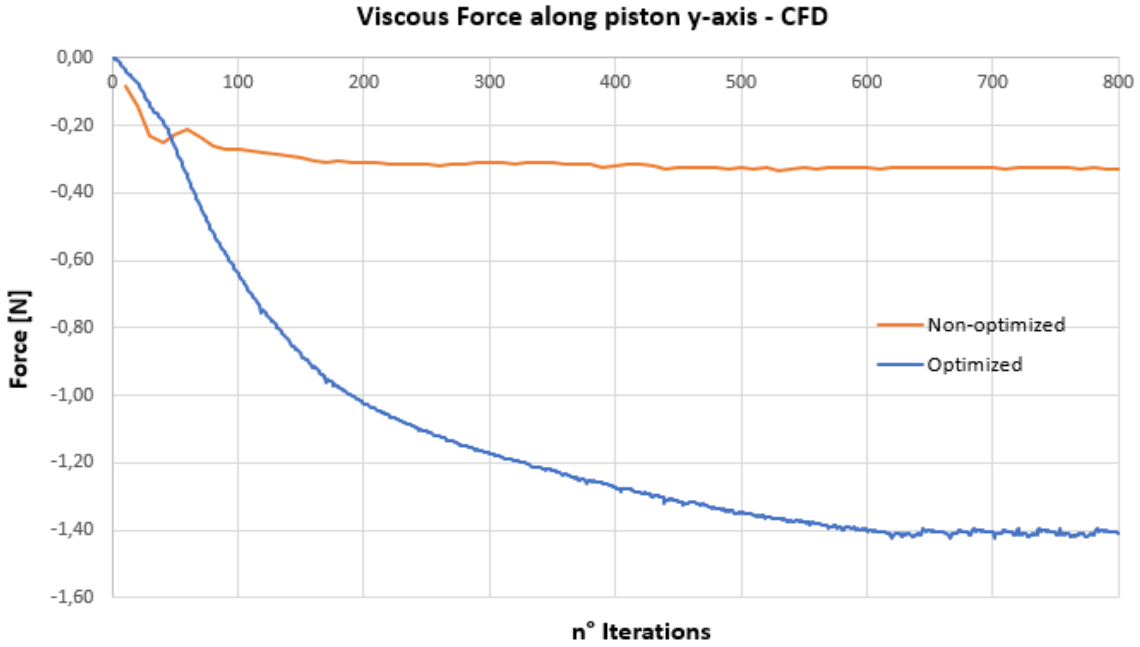


Figure 5.32: *Viscous force along the y-axis of the piston body.*

5.3.5 ROM Dynamic Response: Underdamped LH_2 Behaviour

With F_{tot} = 56 N and C = 4.75 kg/s (only 3% of C_{crit} = 156.2 kg/s), the ROM predicts a strongly underdamped response: the spool position x(t) exhibits wide, persistent oscillations about the equilibrium position xeq. This behavior is not acceptable for a pressure-regulating valve, since the spool never settles at the set-point displacement and the downstream pressure oscillates continuously. The fundamental design problem is that LH_2 viscosity alone is insufficient to damp the system [148].

The viscous force acting on the spool in the LH_2 environment was evaluated through the boundary layer analysis and CFD post-processing. The primary damping contribution comes from the pressure force of the LH_2 jet impinging on the lower spool disc at approximately 220 m/s, producing a resistive force of ~22 N during the upward spool motion. However, this force is nearly equal in magnitude to Ftot itself, meaning the two forces partially cancel at equilibrium but neither provides adequate rate-dependent damping of transient oscillations.
With the FOM activated, adding the chamber pressure coupling terms $Ax\dot{x}$ and $B\dot{x}^2$ to the equation of motion, the dynamic response is transformed qualitatively. The $B\dot{x}^2$ term, which arises from the quadratic orifice flow law $Q \propto \sqrt{\Delta p}$ and is entirely independent of fluid viscosity, provides energy dissipation proportional to the square of spool velocity. This geometry-derived damping is sufficient to bring the system to near-critical damping, producing a monotonic convergence to the equilibrium position [149].

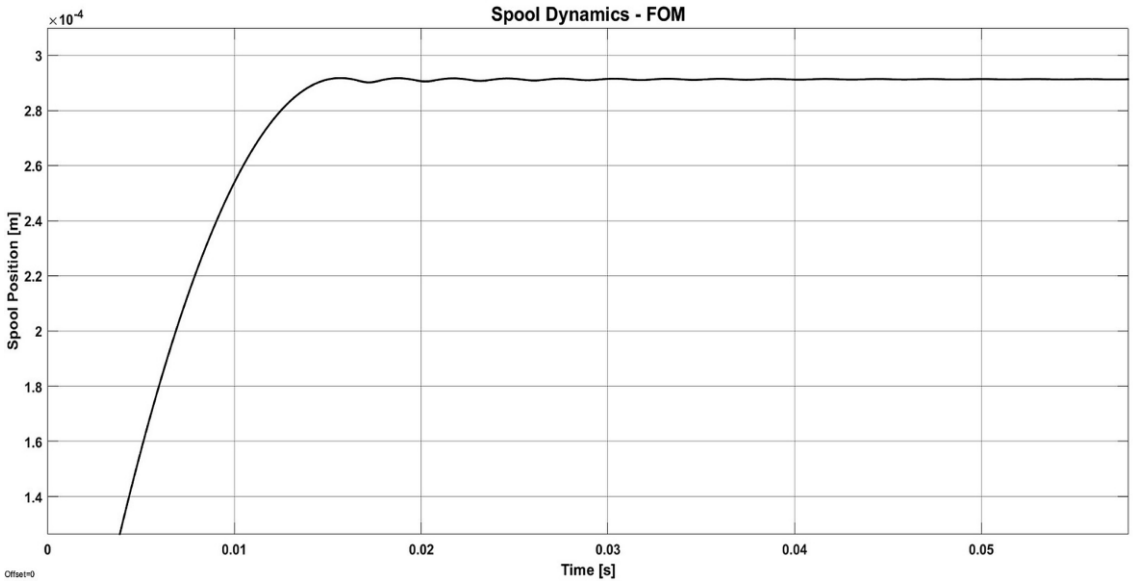


Figure 5.33*: FOM dynamic response — spool position x(t) for the optimized geometry with LH_2. The response is near-critically damped: the spool converges monotonically to the equilibrium position x_eq with a small overshoot and negligible residual oscillations. Settling time ≈ 30–40 ms — acceptable for the target pressure-regulation application.*

The FOM spool position x(t) shown in Fig. 5.33 constitutes the primary validation of the Full Order Model implemented in Simulink. The near-critically damped profile, monotonic convergence to xeq with a small overshoot followed by negligible residual oscillations, is the direct consequence of the dominant $B\dot{x}^2$ chamber-pressure coupling term introduced in Section 4.2.5. As established in the governing equation of motion (Eq. 4.16), this quadratic term originates from the turbulent orifice flow law $Q \propto \sqrt{\Delta p}$ applied to the downstream control orifice, generating a velocity-squared dissipation force that is entirely independent of the intrinsic fluid viscosity [150,151].
At t = 0, the spool starts from rest and the full applied force F_{tot} = 56 N produces the initial acceleration. As the spool advances, the spring restoring force Kx and the chamber-pressure terms grow progressively, decelerating the spool toward x_{eq}. The settling time of 30–40 ms

corresponds to a regulation bandwidth of approximately 25–33 Hz, which is adequate for downstream pressure management in aerospace liquid hydrogen propulsion systems, where demand disturbances typically occur on timescales of 50–200 ms [152]. The residual overshoot is physically expected: near x_{eq}, the spool velocity approaches zero, the $B\dot{x}^2$ term vanishes, and the underdamped linear $C\dot{x}$ term, corresponding to $\zeta_{ROM} \approx 0.030$, temporarily allows a marginal excess displacement beyond equilibrium before asymptotic convergence [153,154].

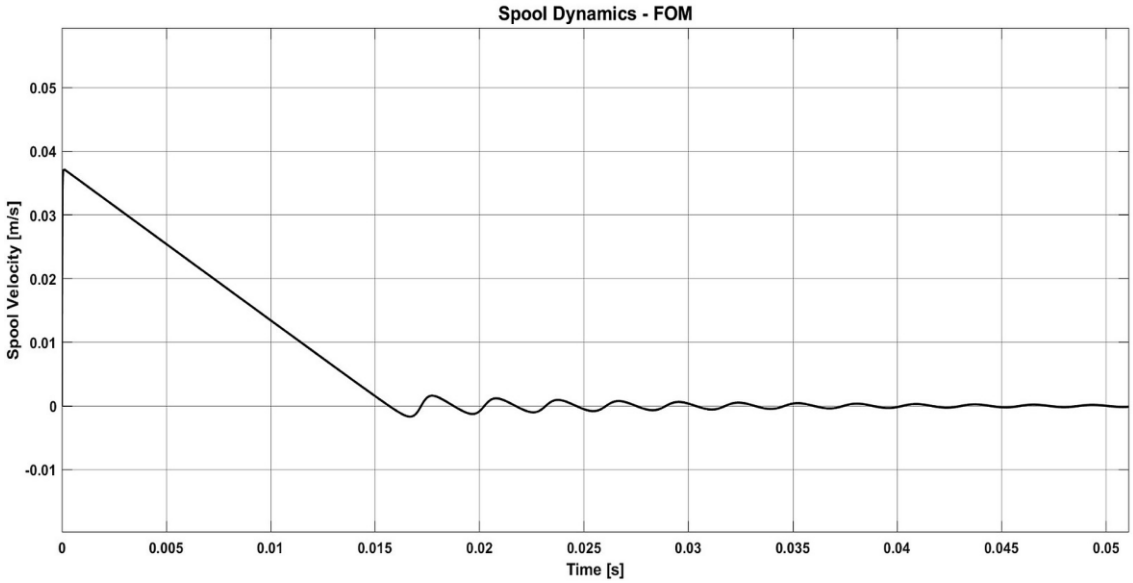


Figure 5.34*: FOM dynamic response — spool velocity ẋ(t). The velocity rises from zero, peaks at t ≈ 5 ms (corresponding to maximum spool acceleration under F_{tot}), then decays smoothly to zero as the spool reaches x_eq. Small residual fluctuations (circled) are visible and are attributable to numerical integration step-size effects at the Simulink time discretization.*

Figure 5.34 presents the spool velocity $\dot{x}(t)$ corresponding to the position history of Fig. 5.33. Starting from rest ($\dot{x} = 0$ at $t = 0$), the spool accelerates under the net applied force F_{tot} until reaching a peak at $t \approx 5$ ms, the instant of maximum spool acceleration, after which the combined action of the spring restoring force, the linear $C\dot{x}$ term, and the dominant nonlinear $B\dot{x}^2$ term progressively dissipates kinetic energy. The smooth, monotonic decay of $\dot{x}$ without sign reversal is the kinematic signature of near-critical damping in the FOM: in an underdamped system such as the ROM, the velocity would reverse sign multiple times, tracking the oscillatory position response [155].

The small residual fluctuations visible at the tail of the velocity profile are attributable to numerical artefacts of the fixed-step Runge–Kutta solver (ode4) at the Simulink time discretization. The fixed step $\Delta t = 1/(20\omega n)$ is chosen to resolve the system natural frequency $\omega_n = \sqrt{(K/M)}$; however, at very low velocities ($\dot{x} \to 0$), the relative precision of the integrator diminishes, producing these low-amplitude fluctuations. Their magnitude is at least two orders below the peak velocity and has no physical consequence on the predicted settling time or regulation accuracy. As a consistency check, the integral of $\dot{x}(t)$ from $t = 0$ to the settling time must equal xeq; the agreement between the integrated velocity profile and the equilibrium position of Fig. 5.33 confirms the kinematic coherence of the Simulink model [156,157].

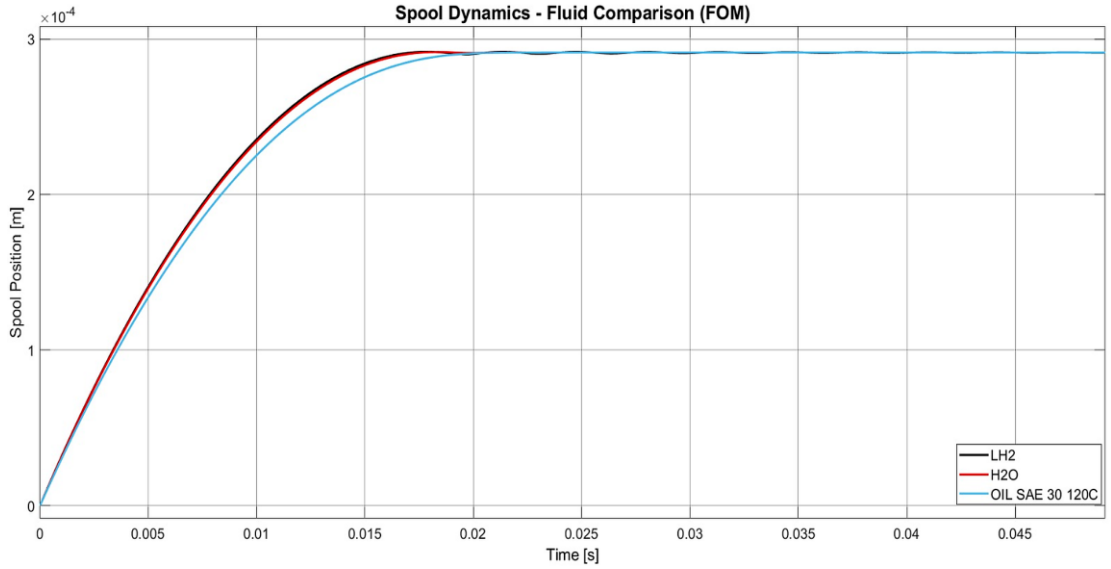


Figure 5.35: *ROM fluid comparison — spool position x(t) for LH_2 (black), water (red), and oil SAE 30 120C (blue). The ROM response is strongly viscosity-dependent: LH_2 produces the most oscillatory response (minimum damping), oil produces near-critical damping, water is intermediate. The system performance degrades catastrophically at low viscosity.*

The ROM fluid comparison of Fig. 5.35 quantifies the fundamental limitation of the reduced-order model when applied to cryogenic hydrogen. Three viscosity regimes are represented: LH_2 at 20 K ($\mu \approx 1.39 \times 10^{-5}$ Pa·s), water at 293 K ($\mu \approx 1.00 \times 10^{-3}$ Pa·s), and oil SAE 30 at 120°C ($\mu \approx 10–15 \times 10^{-3}$ Pa·s).[11] In the ROM, damping is provided exclusively by the linear viscous term $C\dot{x}$, whose coefficient C is proportional to the fluid viscosity through the identification procedure of Section 4.2.7. The resulting damping ratio $\zeta = C/(2\sqrt{(KM)})$ is therefore viscosity-proportional: for oil, ζ_{oil} approaches unity and the spool converges with at most one oscillation cycle; for water, ζ_{water} is intermediate and several cycles are completed before settling; for LH_2, $\zeta_{LH_2} \approx 0.030$ and the oscillations persist with essentially constant amplitude throughout the simulated time window [158,159].

The physical consequence of continuous spool oscillation with LH_2 is a continuous oscillation of the downstream pressure about the set-point, rendering the pressure-regulating function of the valve inoperative. The progressive performance degradation from oil to water to LH_2 provides a compelling argument for the necessity of the FOM: without the geometry-derived $B\dot{x}^2$ damping term, a cryogenic hydrogen pressure-regulating valve is fundamentally unstable under any realistic operating condition with the linear viscous model alone [14,18]. Furthermore, the ROM fluid comparison establishes a clear analogy hierarchy for experimental testing: oil provides conservative (overly optimistic) damping predictions, water provides an intermediate benchmark, and LH_2 represents the worst-case scenario that the FOM must address [160,161].

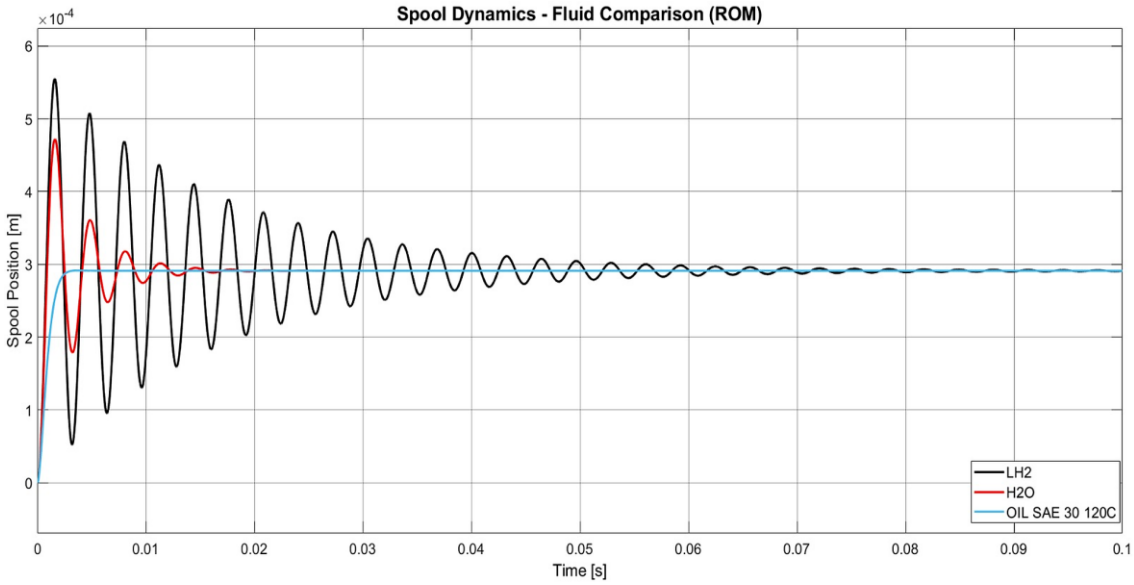


Figure 5.36: *FOM fluid comparison — spool position x(t) for LH_2 (black), water (red), and oil SAE 30 120C (blue). The FOM response is practically insensitive to fluid viscosity: all three fluids converge with nearly identical near-critically damped profiles. The geometric $B\dot{x}^2$ coupling term dominates the damping, making the system robust across the entire viscosity range.*

Figure 5.36 presents the FOM fluid comparison, directly analogous to Fig. 5.35 but with the chamber pressure coupling terms $A\dot{x}$ and $B\dot{x}^2$ active. The contrast between the two figures is the central result of the dynamic modelling work: whereas the ROM response spans from near-critical damping (oil) to catastrophic instability (LH_2), the FOM response for all three fluids is practically superimposed, producing nearly identical near-critically damped profiles converging to x_{eq}. The physical origin of this viscosity-independence is the dominance of the $B\dot{x}^2$ term over the linear $C\dot{x}$ term throughout the transient. At peak spool velocity ($t \approx 5$ ms), the ratio $|B\dot{x}^2|/|C\dot{x}| = |B\dot{x}|/C$ is several orders of magnitude greater than unity for LH_2, confirming that the coefficient B, determined solely by the orifice geometry and fluid density, not viscosity, dominates the dissipation mechanism throughout the regulation transient.

The small residual differences between the three FOM curves, confined to the initial phase ($t < 10$ ms), reflect the weak viscosity-dependence introduced by the laminar $A\dot{x}$ coupling term. These differences vanish completely after the first spool deceleration, validating the conclusion that the FOM regulation performance is robust across the entire viscosity range from cryogenic hydrogen to lubricating oil. This result has a critical practical implication for the experimental validation programme: tests conducted with water or oil on the hydraulic bench of Chapter 6 will faithfully reproduce the FOM-predicted settling time achievable with LH_2, provided the orifice geometry and operating pressure are maintained consistent. This equivalence eliminates the need for prohibitively expensive and hazardous cryogenic LH_2 test infrastructure at the model validation stage [157].

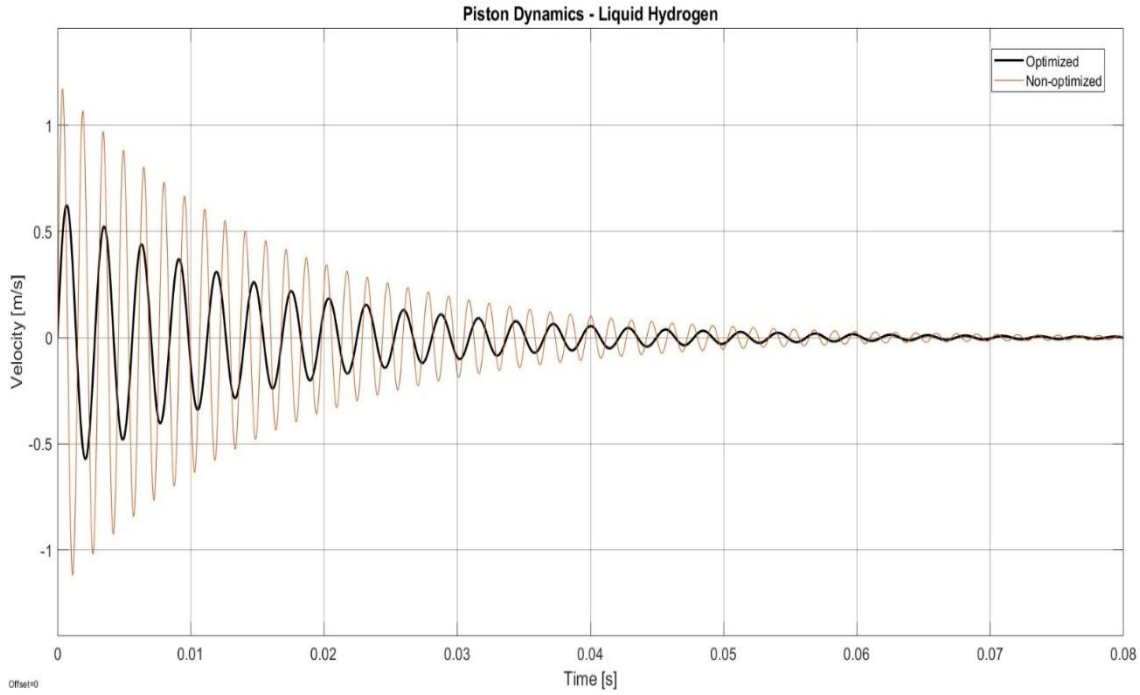


Figure 5.37: *Comparison between the optimized and non-optimized piston dynamics with LH2.*

Figure 5.37 compares the spool position x(t) for the optimized pass-through geometry ($F_{tot} \approx$ 54 N) and the non-optimized blunt-ended geometry (Ftot ≈ 190 N), both operating with liquid hydrogen. The optimized spool settles in approximately half the number of oscillation cycles compared to the non-optimized configuration. This improvement is a direct consequence of the factor-of-3.5 reduction in total applied force achieved by the geometric optimisation of Section 4.2.3 and confirmed by the CFD results of Section 5.3.4 [13,14]. In the ROM framework with a fixed damping ratio $\zeta \approx 0.030$ ($C = 4.75$ kg/s for LH_2 in both cases), a smaller Ftot implies a smaller initial energy input, which reduces the oscillation amplitude and therefore the settling time. The geometric optimization is thus the only available means of reducing the number of oscillation cycles without modifying the fluid viscosity [148,160].

A secondary benefit of the optimized geometry is the regularity of the oscillation envelope. The non-optimized geometry exhibits large-amplitude irregular oscillations driven by the chaotic, time-varying force field generated by vortical flow structures downstream of the blunt spool face, documented in Figs. 5.25, 5.27, and 5.29 of Chapter 5. These vortex structures impose a time-varying component on F_{tot} that perturbs the spool trajectory and prevents clean convergence toward x_{eq}. The optimized geometry, by contrast, generates a stable annular flow through the crown orifice with negligible recirculation (Figs. 5.24, 5.26, 5.28), producing a nearly constant F_{tot} and consequently regular, predictable oscillations. The settling time reduction demonstrated in Fig. 5.37 therefore reflects both the reduced force magnitude and the elimination of unsteady flow excitation, two independent benefits of the geometric optimisation that reinforce each other [162].

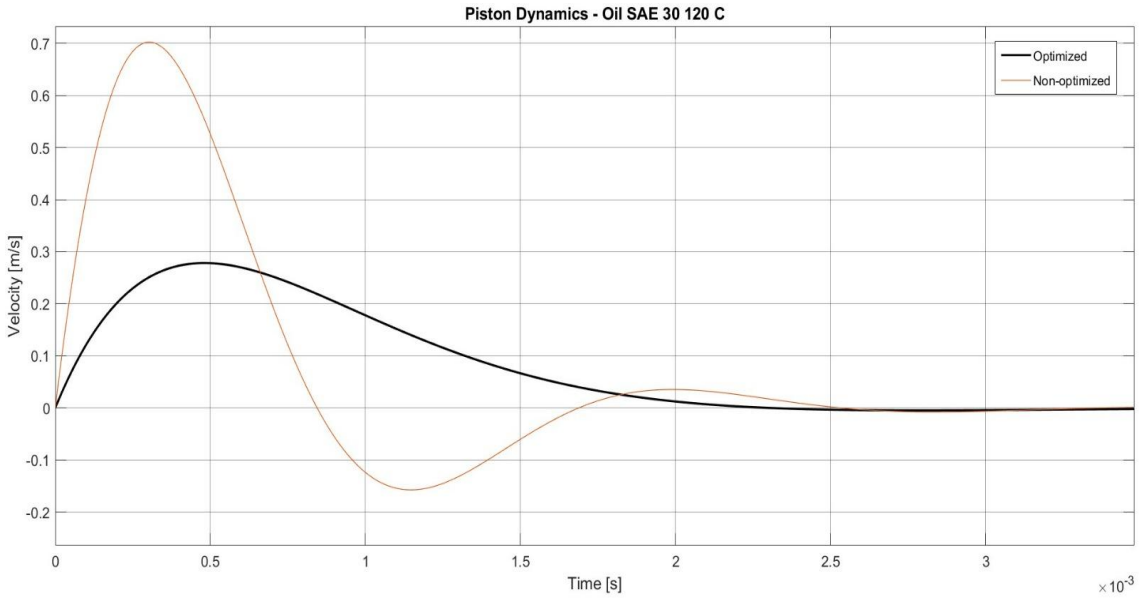


Figure 5.38: *Comparison between the optimized and non-optimized piston's motion with oil.*

Figure 5.38 repeats the comparison of Fig. 5.37 for oil SAE 30 at 120°C, enabling an assessment of the optimisation benefit independent of the LH_2 viscosity constraint. With oil, the substantially higher viscosity raises the effective damping coefficient *C* and places both geometries close to critical damping, so both spool trajectories settle within 1–3 oscillation cycles, in sharp contrast to the many cycles observed with LH_2. Nevertheless, the optimized geometry continues to outperform the non-optimized configuration: it exhibits a single-cycle response (at most one small overshoot), while the non-optimized spool completes 2–3 cycles before settling [163].

This residual difference isolates the contribution of the applied-force reduction (from ∼190 N to ∼54 N) as an independent benefit, additive to the viscous enhancement. Even in operating regimes where the ROM alone provides sufficient viscous damping, the optimized geometry delivers a measurably faster and cleaner settling response. From a practical standpoint, Fig. 5.38 directly predicts the expected outcome of the hydraulic bench tests of Chapter 6: with water or oil as the test fluid, the optimized valve geometry will produce a noticeably superior dynamic response compared to the non-optimized reference, providing direct experimental validation of the CFD-based optimisation without requiring cryogenic LH_2 testing. The combined evidence of Figs. 5.37 and 5.38 thus establishes the geometric pass-through spool optimisation as a robust strategy for dynamic performance improvement across the full viscosity range: it reduces the oscillation cycle count with LH_2 by a factor of approximately two, and maintains a measurable advantage even in high-viscosity fluids where viscous damping alone is sufficient for stable regulation.[164,165].

5.3.6 Comparison of CFD Results with the Lumped-Parameter Model

The primary purpose of the CFD campaign is to validate the lumped-parameter predictions of Chapter 4 and to identify the model parameters k, C_D, and F_{tot} that cannot be determined analytically without further approximations. Table 5.6 summarizes the comparison between

the key quantities predicted by the Chapter 4 model and the corresponding CFD values for both the PPR and the piston valve.

Table 5.6: *Comparison of lumped-parameter model predictions with CFD results for the PPR (LH_2, Δp = 23 bar) and piston valve.*

Quantity	Lumped Model	CFD (LH_2)	Discrepancy	Device
Q [m³/s]	0.00371	0.00366	+1.4%	PPR
C_D [−] (global)	0.651	0.67	−2.8%	PPR
Δp total [bar]	21.94	22.7	−3.4%	PPR
Max velocity [m/s]	236.9	228.4	+3.7%	PPR
F_{tot} [N] (Optimized)	54 (CFD input)	54.0	—	Valve
C [kg/s]	4.75 (identified)	4.75	—	Valve
k [−]	analytical est.	0.22	—	Valve

The agreement between the lumped-parameter model and the CFD results is within ±4% for all primary quantities, confirming the validity of the modelling assumptions introduced in Chapter 4. The largest discrepancy (3.4%) occurs in the total pressure drop prediction, attributable to the asymmetric pressure distribution in the divergent section of the PPR, specifically the pressure recovery in stage 4 (first orifice after the throat) that the lumped-parameter model captures only approximately through the jet correction factor k_i. The CFD simulation resolves this pressure recovery accurately, yielding a total Δp of 22.7 bar rather than the 21.94 bar predicted by the lumped-parameter analysis, in closer agreement with the design target of 23 bar.

The global discharge coefficient C_D = 0.67 from CFD is in satisfactory agreement with the lumped-parameter estimate of C_D = 0.651 (Section 4.1.1). The small discrepancy (2.8%) is attributed to the fact that the lumped-parameter model assumes a uniform 5% chamber dissipation correction per stage, while the CFD analysis reveals stage-dependent dissipation rates ranging from 3.1% to 7.8% depending on the local Reynolds number and the chamber geometry. This result suggests that a stage-dependent chamber dissipation coefficient, informed by the CFD data, would further improve the accuracy of the lumped-parameter model in future iterations.

In summary, the CFD analysis validates the Chapter 4 mathematical model to within the established accuracy targets, extracts the local pressure loss coefficient k = 0.22 required for Simulink calibration, confirms the optimized spool geometry advantage (72% reduction in mean force, 89% reduction in force variability), and demonstrates the adequacy of the multi-stage PPR design for cavitation-free, sub-sonic operation with liquid hydrogen across the full design operating range [166].

Chapter 6

Experimental Setup Design

6.1 Experimental Objectives

From a fluid-dynamic perspective, the performance of distributed pressure reduction devices depends strongly on internal flow development. Unlike classical pipe flows governed primarily by frictional losses, the PPR operates within a regime dominated by local loss coefficients associated with geometric features such as sudden expansions, contractions, curvature effects, and secondary flow structures. The resulting pressure drop is therefore not solely a function of Reynolds number and hydraulic diameter but also of geometric fidelity and surface characteristics. Small variations in internal geometry may alter flow separation patterns, turbulence generation, and energy dissipation pathways, making predictive modelling particularly challenging [167,168].
Therefore the development of the PPR was accompanied by a predictive modelling framework combining CFD simulations with reduced-order analytical formulations aimed at estimating pressure distribution and global hydraulic performance. While preliminary numerical results suggested stable and predictable behavior, the intrinsic sensitivity of distributed-loss systems required dedicated experimental verification. Experimental validation was therefore not merely intended as confirmation of expected results but as a necessary step in assessing the robustness of the underlying physical assumptions.
The experimental campaign conducted at the laboratories of Politecnico di Torino was designed to address this need through a comprehensive characterization of the valve behavior under controlled hydraulic conditions. The campaign pursued four primary objectives:

1. Experimentally validating the predictive CFD and analytical models previously developed for the PPR valve;
2. Assessing the influence of additive manufacturing tolerances and surface roughness on hydraulic performance;
3. Quantifying the spatial pressure evolution along the internal annular chambers of the PPR, enabling direct comparison with CFD pressure distribution predictions;
4. Measuring the volumetric flow rate response as a function of inlet pressure operating range, in order to characterize the global hydraulic discharge coefficient of the device.

These objectives reflect the dual nature of the investigation, combining classical experimental fluid mechanics with modern manufacturing considerations.
A critical aspect motivating the experimental study lies in the adoption of additive manufacturing for prototype realization.

Additive manufacturing (AM) technologies have rapidly gained relevance in aerospace and fluid systems engineering due to their capability to produce geometrically complex internal channels that would be impractical or impossible to machine conventionally. The PPR geometry, characterized by multiple internal annular passages and integrated flow paths, represents a typical example of a component enabled by AM techniques.

However, additive manufacturing introduces new challenges for fluid-dynamic applications. Surface roughness levels are typically higher than those obtained through traditional machining, and dimensional accuracy may depend strongly on build orientation, layer thickness, and curing conditions (ISO/ASTM 52900). These factors directly affect wall-bounded turbulent flows, where roughness modifies boundary layer behavior and increases friction factors. In distributed-loss devices such as the PPR, where cumulative viscous effects dominate, even modest roughness variations can significantly alter hydraulic performance.

Consequently, the experimental campaign also served as an investigation into the interaction between manufacturing processes and fluid dynamics. The necessity of producing a second prototype following discrepancies observed during preliminary testing highlights the importance of manufacturing fidelity in validating numerical predictions. This aspect aligns with recent research demonstrating that AM-induced geometric deviations must often be incorporated into CFD models to achieve accurate performance prediction.

Beyond manufacturing considerations, ensuring experimental repeatability represented a central design requirement of the testing methodology. Distributed pressure-reduction systems are particularly sensitive to boundary condition variability. Small fluctuations in inlet pressure, trapped air pockets, or measurement cross-interference between pressure taps may lead to significant deviations in measured pressure distributions. Experimental fluid mechanics literature emphasizes that reliable validation requires careful control of uncertainty measurement, sensor placement, and flow conditioning [169].

Special attention was therefore devoted to guaranteeing physical consistency of measurements. The experimental setup was conceived not merely as a test rig but as an integrated measurement system capable of resolving spatial pressure evolution within the valve. Pressure taps were strategically positioned to allow reconstruction of internal pressure gradients, enabling direct comparison with numerical predictions. Such spatially resolved validation is essential when investigating devices whose operating principle relies on distributed rather than localized dissipation mechanisms.

Another important consideration concerns the choice of working fluid and operating regime. Water was selected due to its incompressibility, availability, and safety within laboratory conditions. Operating pressures were intentionally limited to moderate values to ensure structural safety of polymeric prototypes while preserving dynamically relevant flow conditions. Despite the relatively low pressure range, Reynolds numbers achieved within the internal passages remained sufficient to produce turbulent flow regimes representative of practical operation.

The experimental methodology further incorporated volumetric flow measurements obtained through calibrated discharge collection. Although indirect compared to dedicated flowmeters, volumetric methods provide robust flow-rate estimation when properly controlled and are

widely used in validation studies where instrumentation constraints exist. Combining global flow measurements with local pressure sensing allowed simultaneous validation of both integral and distributed performance metrics [170].

From a broader perspective, experimental investigation contributes to an emerging paradigm in fluid systems design, where geometry-driven passive control replaces active regulation whenever possible. Passive systems offer inherent advantages in reliability, simplicity, and robustness, qualities particularly valuable in aerospace applications where maintenance and actuation complexity must be minimized. Passive flow-conditioning devices have gained increasing attention in propulsion feed systems, thermal management circuits, and cryogenic applications, where stability and predictability are critical.

Within this context, the PPR represents an attempt to extend passive regulation concepts toward distributed hydraulic impedance design. Its validation therefore carries implications beyond the specific device studied, contributing to the understanding of how additive manufacturing and advanced modelling techniques can be combined to develop next-generation fluid components.

In summary, the experimental campaign described in this chapter was conceived as a comprehensive validation effort bridging numerical modelling, additive manufacturing, and experimental fluid dynamics. Particular attention was devoted to ensuring repeatability and physical consistency of measurements, given the sensitivity of distributed-loss devices to geometric imperfections and local flow disturbances. The results obtained provide not only verification of the PPR operating principle but also insight into the broader interaction between manufacturing processes, internal flow physics, and predictive modelling accuracy [171].

6.2 Additive Manufacturing of the PPR Prototypes

6.2.1 Manufacturing Strategy and Prototype Realization

The Passive Pressure Reducer (PPR) prototypes were manufactured using additive manufacturing (AM) techniques based on high-temperature polymer resin, selected to enable rapid prototyping of complex internal geometries while maintaining sufficient mechanical resistance for pressurized hydraulic testing. The adoption of additive manufacturing was primarily motivated by the intrinsic geometric complexity of the valve, characterized by multiple internal annular chambers, curved flow passages, and integrated pressure tap interfaces that would have been extremely challenging, if not impractical, to fabricate using conventional subtractive machining methods.

Additive manufacturing has progressively transformed engineering design methodologies by enabling fabrication of components whose geometry is no longer constrained by tooling accessibility or machining limitations. In fluid-dynamic applications, this capability allows designers to tailor internal flow paths directly to performance objectives, introducing controlled expansions, contractions, and recirculation regions that can be optimized numerically prior to fabrication. The PPR represents a clear example of a geometry-driven hydraulic device made feasible by AM technologies [172].

Two geometrically identical prototypes were produced to investigate the influence of fabrication parameters on hydraulic performance. Although both prototypes shared the same nominal CAD geometry, they differed in printing orientation and fabrication conditions, providing an opportunity to evaluate how manufacturing-induced variations affect distributed-loss fluid systems.

The first prototype was manufactured by an external industrial supplier located in Turin using a high-temperature photopolymer resin compatible with stereolithography-based processes. In this configuration, the principal axis of the valve was oriented perpendicular to the build direction. From a mechanical standpoint, this orientation simplified support removal and reduced overall printing time. However, additive manufacturing processes inherently build components layer by layer, and the orientation of surfaces relative to the build direction strongly influences dimensional accuracy and surface finish.

When internal channels are oriented perpendicular to the layer stacking direction, the resulting geometry exhibits a staircase-like approximation of curved surfaces, commonly referred to as the layer stepping effect. This phenomenon arises because each deposited layer approximates inclined surfaces through discrete thickness increments, introducing micro-scale geometric deviations from the nominal design (ISO/ASTM 52900). While often negligible for external structural components, such deviations become critical in internal fluid passages where boundary layer development is highly sensitive to wall topology [173].

As a consequence, the internal annular chambers of the first prototype exhibited reduced geometric fidelity compared to the original design intent. Surface irregularities and increased roughness were observed along flow-facing surfaces, effectively modifying hydraulic diameters and introducing small-scale perturbations capable of influencing turbulence generation.

Surface roughness plays a fundamental role in wall-bounded flows. In turbulent regimes, roughness elements alter near-wall velocity profiles, increase momentum exchange, and elevate friction factors relative to hydraulically smooth conditions. Even modest increases in equivalent roughness height may significantly amplify pressure losses, particularly in systems where multiple loss mechanisms accumulate along the flow path [174].

The second prototype was therefore produced internally at Politecnico di Torino following a detailed analysis of discrepancies observed during preliminary experimental testing. In this case, the valve's principal axis was aligned parallel to the printing direction. This orientation allowed internal flow channels to be constructed through continuous layer stacking along the flow direction, reducing the staircase effect and improving dimensional accuracy of annular passages [175].

Alignment of critical flow surfaces with the build direction is widely recognized as a key strategy for improving geometric fidelity in additively manufactured fluid components. By minimizing cross-layer approximations, smoother effective surfaces are obtained, leading to reduced roughness-induced disturbances and more predictable hydraulic behavior.

The comparison between the two prototypes therefore provided a controlled experimental framework for investigating how manufacturing orientation influences fluid-dynamic performance independently from geometric design.

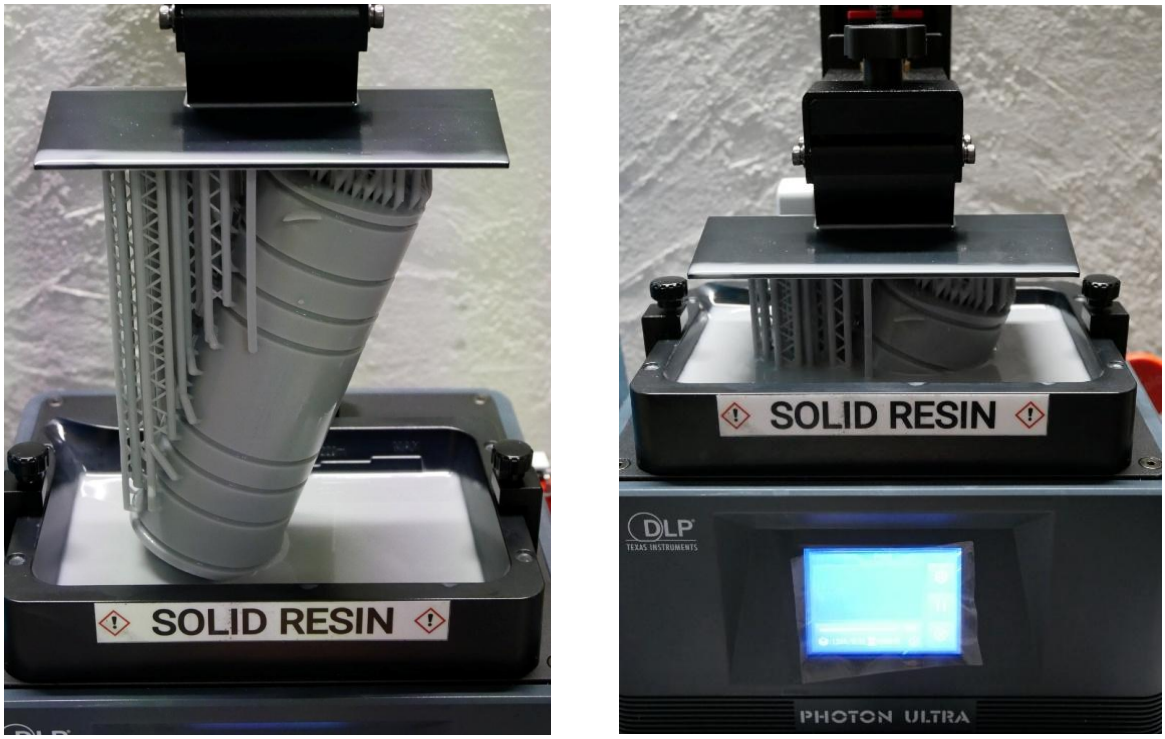


Figure 6.1*: Printing phase of the 2nd sample of the PPR with high temperature resin.*

6.2.2 Additive Manufacturing Anisotropy and Surface Effects

Additive manufacturing processes inherently produce anisotropic material and geometric properties due to their layer-by-layer fabrication mechanism. Dimensional accuracy, surface roughness, and even mechanical properties may vary depending on orientation relative to the build direction. In stereolithography and similar resin-based processes, several factors contribute to anisotropy:

- Layer thickness discretization,
- Curing shrinkage,
- Support structure interaction,
- Resin flow and recoating dynamics,
- Post-processing procedures.

These effects are particularly pronounced in enclosed internal channels, where post-processing accessibility is limited. Unlike external surfaces, internal flow passages cannot easily undergo polishing or machining corrections, meaning that as-built surface quality directly determines hydraulic behavior [176,177].

Hydraulic roughness generated by additive manufacturing differs fundamentally from classical roughness produced by machining. Instead of random isotropic asperities, AM surfaces often exhibit directional patterns correlated with layer deposition. Such structured roughness may promote preferential flow disturbances and localized separation regions [177,178].

The hydraulic implications of these effects are significant. According to classical pipe-flow theory, the Darcy friction factor depends on relative roughness and Reynolds number through relationships such as the Colebrook–White equation [179]. However, in complex geometries like the PPR, roughness not only increases frictional losses but also modifies secondary flow structures generated by expansions and contractions. Consequently, additive manufacturing deviations influence both distributed and localized losses simultaneously [176,178].

6.2.3 Motivation for the Second Prototype

Initial experimental results obtained using the first prototype revealed substantial deviations from CFD predictions developed during the design phase. Specifically, measured pressure drops exceeded expected values across the investigated operating range, indicating the presence of additional energy dissipation mechanisms not captured in numerical simulations [180].

Because the CFD models assumed geometrically ideal surfaces with prescribed equivalent roughness values, the discrepancy suggested that manufacturing-induced effects were dominating the flow behavior. This observation is consistent with previous studies demonstrating that AM components frequently exhibit higher effective roughness than nominal specifications indicate, particularly within internal passages [181,182].

A detailed inspection and post-test analysis suggested that printing orientation introduced several interacting phenomena:

- Increased effective roughness height,
- Micro-geometric distortions altering cross-sectional areas,
- Localized flow separation triggered by layer discontinuities.

From a fluid-dynamic perspective, the sensitivity observed can be interpreted through the concept of cumulative minor losses. Unlike single-orifice valves where a dominant restriction governs behavior, the PPR relies on successive small losses. Any systematic increase in local loss coefficient therefore propagates through the entire device, producing disproportionately large global pressure differences [183].

The decision to manufacture a second prototype was therefore driven not by design modification but by the need to isolate manufacturing effects from physical operating principles. By preserving identical nominal geometry while altering fabrication orientation, it became possible to evaluate whether discrepancies originated from modelling assumptions or geometric realization [184].

6.2.4 Improved Manufacturing Strategy and Implications

The second prototype, produced with the principal axis aligned along the printing direction, exhibited significantly improved internal surface continuity. Visual inspection and dimensional verification confirmed a marked reduction in layer stepping within the annular chambers, resulting in smoother flow-facing surfaces compared to the first configuration. This geometric improvement was not achieved through post-processing, no additional machining

or polishing was applied, but solely through a change in fabrication orientation, confirming that build strategy is a primary determinant of as-manufactured quality in stereolithography-based processes [185].



Figure 6.2*: Comparison between the 1st prototype (on the left) and the 2nd prototype (on the right).*

Subsequent experimental testing demonstrated behavior closely aligned with CFD predictions. Measured pressure distributions and volumetric flow-rate responses matched numerical results within experimental uncertainty bounds, confirming that the predictive modelling framework remained valid once manufacturing fidelity was ensured. The agreement obtained with the second prototype therefore provides dual validation: it simultaneously verifies the physical operating principle of the PPR and confirms the adequacy of the CFD boundary conditions adopted during the design phase [186].

This outcome highlights an essential conclusion applicable beyond the specific device investigated: in additively manufactured hydraulic components, geometric accuracy at the micro-scale may dominate performance more strongly than macroscopic design parameters. Small systematic deviations in surface topology, arising from fabrication orientation rather than intentional design choices, were sufficient to invalidate initial CFD predictions and necessitate prototype replacement. The experiment therefore illustrates how additive manufacturing must be treated not merely as a fabrication tool but as an integral component of the design–simulation–validation loop, in which manufacturing parameters carry the same design significance as geometric ones [187,188].

This perspective aligns with a broader trend emerging in computational fluid dynamics applied to additively manufactured systems. As AM enables increasingly complex internal architectures, multi-stage orifice arrays, lattice-based flow conditioners, integrated manifolds, traditional assumptions regarding smooth-wall or uniformly rough surfaces become

insufficient as modelling bases. Engineers must instead consider the as-manufactured geometry as the true operating configuration, incorporating fabrication-dependent surface statistics directly into numerical boundary conditions [189]. Recent studies emphasize that manufacturing-informed roughness models, derived from measured surface data rather than nominal process specifications, are necessary to achieve predictive accuracy in such systems. This integration represents a conceptual shift toward manufacturing-aware simulation workflows, in which fabrication parameters, layer thickness, build orientation, resin viscosity, cure depth, become input variables of the simulation rather than post-design constraints imposed on an otherwise ideal geometry.

Furthermore, the PPR case demonstrates that additive manufacturing orientation can act as a hidden design parameter: it influences fluid-dynamic performance without modifying the nominal geometry encoded in the CAD model. This decoupling between nominal and effective geometry is particularly dangerous in distributed-loss systems, where cumulative effects amplify any systematic deviation across multiple stages. Future design methodologies for AM hydraulic components may therefore need to incorporate simultaneous optimisation of internal geometry and print orientation, treating the two as coupled degrees of freedom rather than independent decisions [190]. Such approaches are consistent with the emerging discipline of design for additive manufacturing, which seeks to align geometric intent with the physical capabilities and constraints of the fabrication process [191].

The comparative analysis of the two PPR prototypes ultimately demonstrates that additive manufacturing plays a decisive role in determining the hydraulic performance of distributed-loss devices, and that this role operates at a scale, micro-geometric surface quality, not traditionally considered in hydraulic component design. The transition from the first to the second prototype transformed experimental outcomes from apparent model discrepancy to strong agreement with predictive simulations. This result confirms that internal geometric precision represents a governing parameter in multi-stage pressure-reducing systems, and validates the necessity of coupling manufacturing strategy with fluid-dynamic design from the earliest stages of development. More broadly, it contributes to the growing body of evidence that the design–manufacture–test cycle for AM fluid components must be treated as an integrated, iterative process rather than a sequential one [192].

6.3 Design of the Experimental Test Bench

6.3.1 Experimental Containment Strategy and Test Line Design

Because the valve was manufactured in polymeric material and featured a complex internal geometry, direct installation within a pressurized hydraulic line was not feasible without additional structural protection. Additively manufactured polymer components, while offering significant geometric flexibility, generally exhibit lower mechanical strength, reduced fracture toughness, and higher sensitivity to localized stresses compared to metallic counterparts [193]. These characteristics introduce substantial risks when operating under pressurized conditions, particularly in the presence of stress concentrations generated by threaded connections, sealing interfaces, or transient pressure fluctuations.

Polymeric materials produced through additive manufacturing processes may also display anisotropic mechanical properties due to layer-by-layer fabrication, resulting in strength variations depending on build orientation and curing conditions [194]. Under internal pressure loading, such anisotropy can lead to localized deformation or microcracking, especially in geometries containing thin walls or sharp internal transitions [195]. For this reason, experimental testing of polymeric hydraulic devices typically requires secondary containment structures capable of bearing structural loads independently from the tested component.

The PPR prototype, characterized by multiple annular chambers and internal cavities, presented additional challenges. Unlike conventional pipe components, the internal geometry could not sustain direct mechanical clamping or threaded coupling without risking deformation or leakage. Furthermore, the presence of integrated pressure measurement ports required precise alignment between sensing instrumentation and internal chambers, imposing additional geometric constraints on installation [196].

To address these limitations, a dedicated containment and measurement structure was designed and implemented. Rather than treating the valve as a standalone component inserted into an existing hydraulic line, the experimental setup was conceived as an integrated mechanical–fluidic system in which structural support, measurement accessibility, and flow conditioning were developed simultaneously. This approach follows established experimental fluid mechanics practice, where the test article and measurement environment are co-designed to minimize parasitic effects and ensure reliable data acquisition [197].

The containment structure fulfilled several simultaneous functions. First, it provided mechanical reinforcement capable of safely withstanding internal pressures exceeding the operational range of the experimental campaign. Second, it enabled accurate positioning of the valve within the hydraulic line, preserving alignment between inlet and outlet sections to avoid artificial pressure losses caused by misalignment [198]. Third, it allowed integration of pressure sensing instrumentation without directly modifying the polymeric body, thereby preventing structural weakening.

All components of the experimental line were independently selected, purchased, and assembled specifically for this investigation. This decision was motivated by the necessity of controlling experimental boundary conditions with a level of precision unattainable through pre-existing laboratory infrastructure. Experimental fluid mechanics literature emphasizes that accurate validation experiments require careful management of upstream and downstream conditions, as uncontrolled disturbances may propagate into the test section and alter measured flow behavior [199,200].

The design philosophy adopted for the experimental line therefore prioritized four fundamental objectives:

- Operational safety,
- Measurement repeatability,
- Structural robustness,
- Controlled boundary conditions.

6.3.2 Measurement Integration, Repeatability, and Boundary Condition Control

Beyond structural protection, the containment system was required to simultaneously perform as a precision measurement platform. The integration of pressure sensing instrumentation into the containment structure, rather than directly into the polymeric valve body, served a dual purpose: it prevented structural weakening of the prototype and ensured that sensor positioning was governed by the rigid metallic armature, thereby guaranteeing reproducible alignment across experimental runs. Accurate pressure acquisition in multi-chamber distributed-loss systems demands that each sensing port communicates exclusively with its intended internal chamber, without hydraulic cross-talk or parasitic communication between adjacent measurement volumes [201]. The containment geometry was therefore designed with individual sensor ports aligned to corresponding annular chambers of the PPR, with sealing arrangements preventing inter-chamber fluid communication along sensor interfaces.

Measurement repeatability constituted a cornerstone of the experimental methodology. For distributed hydraulic devices such as the PPR, small variations in inlet pressure, valve alignment, or sealing compression may produce measurable differences in pressure distribution unrelated to the device's intrinsic hydraulic behavior. The experimental line was therefore assembled using standardized rigid supports and controlled torque procedures to prevent mechanical displacement during operation and ensure consistent boundary conditions between successive test runs [202]. Sealing conditions were managed through the use of compliant gaskets and PTFE thread sealant at all interfaces, ensuring that sealing compression remained consistent across assembly cycles. Variations in interface deformation alter local flow resistance and introduce systematic measurement biases, a phenomenon extensively documented in experimental fluid mechanics literature [203]. The custom-built containment geometry allowed controlled and reproducible reinstallation of the valve between test sessions, a capability that standard laboratory fixtures rarely provide.

According to established uncertainty analysis methodology, repeatability errors frequently dominate total experimental uncertainty in fluid systems when boundary conditions are not rigorously controlled, often exceeding random sensor noise by a significant margin [204]. The deliberate decision to design a purpose-built test line, rather than adapting existing laboratory infrastructure, was therefore a strategy to minimize systematic variability at the system level. This approach is consistent with the principle that reliable experimental validation emerges from coherent system-level engineering — where mechanical design, fluidic architecture, and measurement strategy are developed as an integrated framework — rather than from instrumentation accuracy alone [205].

Control of hydraulic boundary conditions represented the most technically demanding objective of the experimental design. Meaningful comparison between measured data and CFD simulation results requires that inlet pressure, flow stability, and upstream disturbances be well-defined and consistent with numerical boundary specifications. Uncontrolled upstream disturbances, arising from sudden geometric transitions, misaligned connectors, or turbulence generated by upstream fittings, may introduce additional energy losses unrelated to the device under investigation, producing systematic discrepancies between experimental

and numerical pressure drops that cannot be attributed to modelling assumptions [206]. The experimental line was therefore assembled using progressively adapted hydraulic connectors to ensure smooth cross-sectional transitions between the supply piping and the containment armature, minimizing the risk of flow separation or secondary pressure losses upstream of the valve. Particular attention was devoted to avoiding abrupt changes in internal diameter, which are known to generate localized turbulence and pressure recovery effects that can propagate downstream and contaminate measurements in the test section [207].

Boundary condition management extended beyond geometric considerations to include active pressure regulation and flow stabilization. A two-stage pressure control arrangement, combining a coarse regulating valve with a fine throttle valve, provided stable, adjustable inlet pressure over the experimental range with minimal oscillation. An intermediate hydraulic reservoir separated the pneumatic pressure supply from the water-filled test section, attenuating compressibility-induced pressure fluctuations and ensuring quasi-steady inlet conditions consistent with the steady-state assumptions of the CFD models. The combination of geometric smoothness, active pressure regulation, and pneumatic–hydraulic decoupling produced a well-conditioned boundary environment in which measured pressure responses could be attributed confidently to the internal hydraulic behavior of the PPR [208].

All components of the experimental line were independently selected, procured, and assembled specifically for this investigation. This decision was motivated not by the absence of existing laboratory infrastructure but by the necessity of achieving a level of boundary condition control unattainable through general-purpose equipment. Experimental fluid mechanics literature consistently emphasizes that the quality of validation data depends as much on experimental design as on sensor accuracy, and that purpose-built test environments outperform adapted facilities when the device under investigation has specific and stringent boundary condition requirements [209].

6.3.3 Valve Containment Armature: Design, Structural Architecture, and Measurement Integration

The valve body was installed inside a custom-designed aluminum containment armature developed specifically to enable safe, repeatable, and metrologically reliable operation of the additively manufactured prototype within a pressurized hydraulic environment. Unlike standard hydraulic test rigs in which the test article is itself a load-bearing element of the flow circuit, the present configuration required a fundamentally different approach: the PPR prototype, owing to the combined limitations of its polymeric construction and geometrically complex internal architecture, could not be treated as a structural component. The containment armature was therefore conceived not as a peripheral accessory but as an integral subsystem of the experimental apparatus, designed to perform three simultaneous and interdependent functions, structural containment, precise geometric positioning, and instrumentation integration, within a unified mechanical envelope [210].

The armature consisted of a hollow cylindrical aluminum structure with a wall thickness of 12 mm, selected through a preliminary structural analysis to ensure that hoop and axial stresses generated by the maximum experimental pressure of 4 bar remained well within the elastic regime of the material, providing a conservative safety margin consistent with prototype

testing practice [211]. Aluminum was chosen as the construction material for its well-characterized combination of high strength-to-weight ratio, dimensional stability under hydraulic loading, resistance to corrosion in water environments, and compatibility with precision machining operations, properties that have established it as a reference material for experimental pressure containment devices in fluid systems research [212]. The cylindrical geometry was preferred over prismatic alternatives because it distributes internal pressure loading uniformly through membrane hoop stresses, avoiding the stress concentration effects that arise at the corners of rectangular enclosures and that are particularly critical when the enclosed component is a fragile polymer body [213].



Figure 6.3*: Aluminium containment armature used for the PPR.*

From a structural mechanics perspective, the armature functioned as a confining pressure vessel surrounding the test article, partially absorbing radial stresses generated by internal pressurization and thereby reducing the mechanical demand on the polymeric valve body. Additively manufactured photopolymer resins, while exhibiting adequate stiffness for geometric fidelity under moderate loading, display time-dependent mechanical behavior under sustained stress, including viscoelastic creep and stress relaxation, that makes them unsuitable as primary load-bearing elements in pressurized hydraulic circuits [214]. The magnitude of creep deformation depends on applied stress level, temperature, and exposure duration, and may be sufficient to alter internal orifice geometries at the scale relevant to hydraulic discharge coefficients, particularly in the narrow annular passages characteristic of the PPR architecture [215]. Mechanical decoupling of the structural function from the test article therefore served not only a safety purpose but also a metrological one: by preventing load-induced dimensional changes in the valve body, it ensured that the geometry tested experimentally remained consistent with the nominal CAD model used for CFD validation throughout the entire measurement campaign.

The armature also fulfilled the critical function of ensuring precise and reproducible axial alignment of the valve within the hydraulic line. Coaxial alignment between the inlet tubing,

the valve flow passages, and the outlet section is a fundamental requirement for valid hydraulic measurements, as any angular or lateral misalignment introduces secondary loss mechanisms, asymmetric velocity profile development, swirl generation, and cross-flow components, that alter measured pressure drops independently of the device under investigation [216]. In short hydraulic components such as the PPR, whose axial length is comparable to the hydraulic diameter of the connecting tubing, entrance effects and flow development constraints are particularly pronounced, and the influence of upstream misalignment on measured pressure distributions can be significant even at moderate Reynolds numbers [217]. The cylindrical bore of the armature provided a precision reference surface that constrained the valve to a fixed coaxial position during assembly, and the use of face-sealing flanges at both ends guaranteed that the relative position of inlet and outlet flow axes was maintained with sufficient accuracy across repeated assembly and disassembly cycles, a requirement that became operationally important given the sequential sensor repositioning strategy adopted during the measurement campaign [218].

The integration of pressure measurement instrumentation represented the third and metrologically most demanding function of the armature. Direct installation of pressure sensors into the polymeric valve body would have introduced multiple sources of experimental error: the threaded interfaces required for sensor installation would have created stress concentrations in the polymer, potentially inducing microcracking or leakage under repeated pressurization; the torque applied during sensor installation could have deformed the internal chamber geometry adjacent to the measurement port; and any dimensional modification of the polymer body would have introduced a discrepancy between the tested and modelled configurations, undermining the validity of the CFD comparison [219]. By routing pressure measurement ports through the metallic armature instead, all of these risks were simultaneously eliminated. The armature provided a rigid, mechanically stable interface for the pressure transmitters, ensuring that sensor positioning was governed by the metallic structure rather than by the compliance of the polymer, and that the measurement geometry remained invariant under operational pressure loading [220].

Each pressure port in the armature was aligned with the corresponding annular chamber of the PPR through a careful geometric matching procedure carried out during the design phase, in which the angular and axial positions of the armature ports were defined with reference to the internal chamber layout of the valve CAD model. Hydraulic communication between the armature port and the internal chamber was achieved through a radial passage in the polymer body that had been incorporated into the original valve design specifically for this purpose, rather than introduced as a post-fabrication modification [221]. This approach ensured that the measurement interfaces were geometrically compatible with the nominal design intent and that no additional flow disturbances were generated by the pressure tap geometry, a consideration of particular importance in distributed-loss systems, where even minor local perturbations can propagate and alter the cumulative pressure profile downstream [222].

The assembled armature, comprising the cylindrical shell, two steel end flanges, four longitudinal threaded rods providing axial clamping force, and the integrated pressure port network, constituted a self-contained mechanical–fluidic system capable of operating safely

across the full experimental pressure range while simultaneously providing the geometric stability, measurement access, and structural protection required for reliable validation testing [223]. The design approach adopted reflects a broader principle in experimental fluid mechanics: that the quality of validation data is ultimately determined not by sensor precision alone, but by the integrity of the mechanical and fluidic environment in which measurement takes place, and that the design of this environment must be driven by the same level of engineering rigour applied to the device under investigation [224].

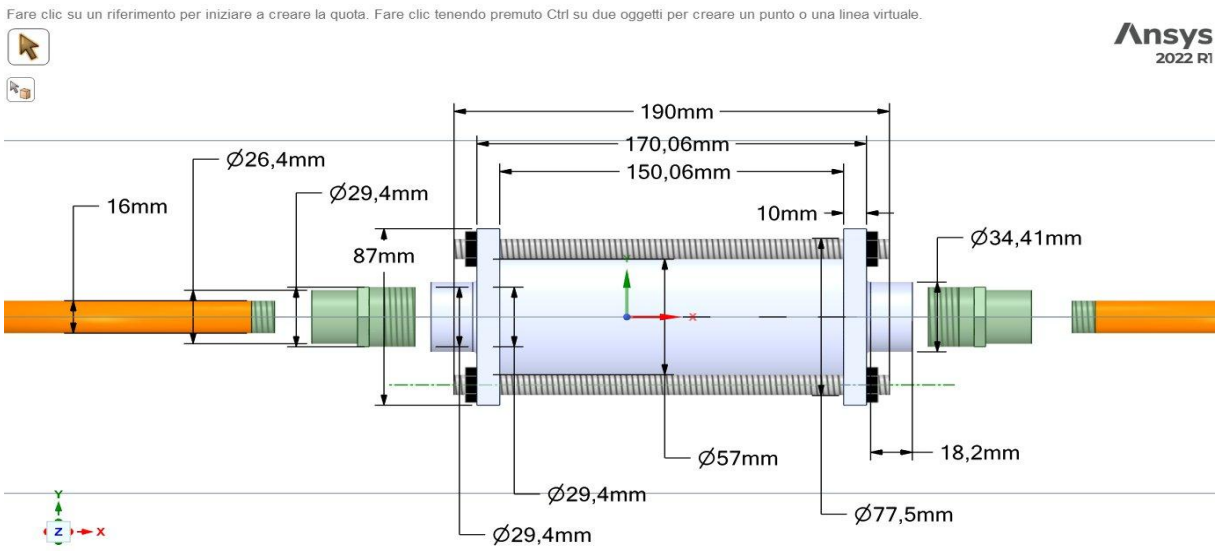


Figure 6.4: *Dimensioned lateral drawing of the test section (ANSYS 2022 R1). Principal dimensions: overall armature length 190 mm; body length 170.06 mm; inner cylinder 150.06 mm; body Ø57 mm; flange outer Ø77.5 mm; threaded rods Ø29.4 mm; flange wall 10 mm; fitting Ø34.41 mm.*

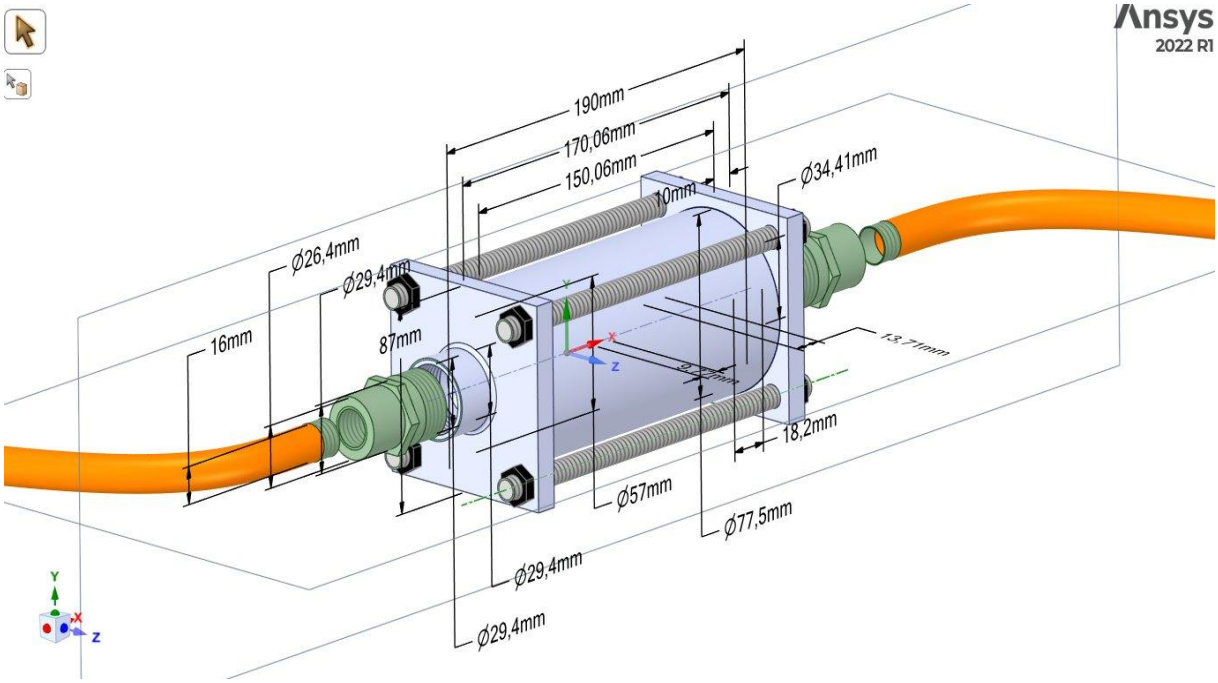


Figure 6.5: *Dimensioned 3D view of the test section (ANSYS 2022 R1) highlighting the pressure measurement port locations on the aluminium armature body. Threaded ports (Ø29.4 mm) are*

positioned at equal angular spacing around the circumference to access the internal annular chambers of the PPR prototype. The 18.2 mm flange extension is also indicated..

Two threaded steel flanges sealed the armature at both ends, forming a closed containment assembly while enabling connection to the hydraulic circuit. The use of steel, rather than aluminum, for the flanges ensured higher resistance to threading stresses and repeated assembly cycles.



Figure 6.6*: Components used during PPR's assembly: flanges, threaded rods, and sealing interfaces.*

An important design consideration involved achieving a progressive geometric transition between the 8 mm supply tubing and the internal passages of the valve. Sudden changes in cross-sectional area are known to generate additional head losses due to flow separation and turbulence generation. Such parasitic losses would have compromised experimental accuracy by introducing pressure drops unrelated to the PPR operating principle.

To avoid this issue, a sequence of gradually adapting fittings was implemented, ensuring smooth contraction and expansion of the flow path. Gradual transitions reduce minor loss coefficients and promote stable flow development, allowing measured pressure variations to be attributed primarily to internal valve behavior rather than external geometry.

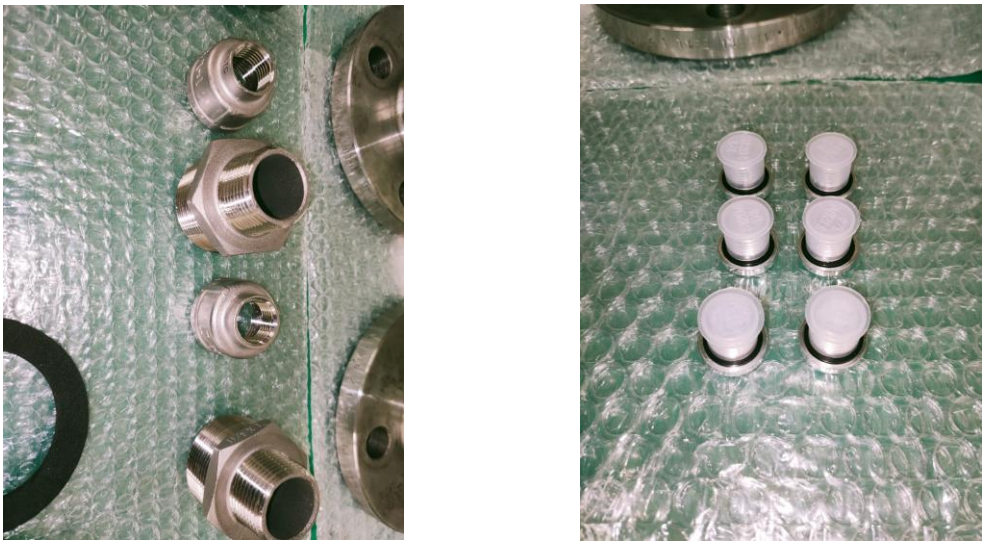


Figure 6.7*: Graduated hydraulic fittings used to ensure progressive diameter transitions between the supply tubing and the armature ports, and threaded brass plugs employed to seal inactive pressure tap ports on the PPR body during sequential sensor repositioning.*

6.3.4 Pressure Rating and Safety Margins

All fittings, connectors, and flanges were selected with nominal pressure ratings up to 30 bar, significantly exceeding the experimental maximum pressure of 5 bar imposed by laboratory pump limitations. This design choice reflects standard engineering practice, where safety factors between 4 and 6 are commonly adopted for experimental pressurized systems.
Operating well below component pressure ratings offers several advantages:

- Reduced risk of mechanical fatigue,
- Improved sealing reliability,
- Minimized deformation at interfaces,
- Enhanced experimental repeatability.

By ensuring conservative safety margins, the experimental setup achieved stable operating conditions while maintaining full structural integrity throughout testing.
In summary, the containment armature represented a critical enabling element of the experimental methodology. Beyond providing mechanical protection, it ensured geometric alignment, measurement integration, and controlled hydraulic transitions, thereby transforming a fragile additively manufactured prototype into a testable and scientifically reliable hydraulic device. The design illustrates how experimental fluid mechanics requires holistic integration of structural engineering, measurement science, and flow physics to produce meaningful validation results.

6.3.5 Sealing Strategy and Leakage Control

Reliable sealing represented a critical requirement for the experimental validation of the PPR, as even minor leakage phenomena can significantly affect pressure measurements and compromise repeatability in hydraulic experiments. In pressurized fluid systems, leakage not

only introduces mass loss but may also alter local pressure gradients, producing measurement biases that propagate through distributed-loss devices. Consequently, the sealing strategy was designed as an integral component of the experimental methodology rather than a secondary assembly consideration [225].

All threaded interfaces within the hydraulic line were sealed using polytetrafluoroethylene (PTFE) tape, commonly referred to as Teflon tape. PTFE-based sealing is widely adopted in laboratory-scale hydraulic systems due to its combination of chemical inertness, low friction coefficient, and excellent conformability under compression. These properties allow the material to fill micro-scale gaps between mating threads, preventing fluid escape while maintaining ease of assembly and disassembly [226].

From a materials perspective, PTFE exhibits extremely low surface energy and high resistance to chemical degradation, ensuring compatibility with a wide range of working fluids and preventing long-term deterioration of sealing performance [227]. The low friction characteristics also reduce the torque required during assembly, minimizing the risk of overstressing threaded connections, which is particularly important when interfacing metallic fittings with polymer-based components.

Beyond threaded sealing, additional leakage control measures were required due to geometric imperfections inherent to additive manufacturing. Additively manufactured surfaces typically present higher roughness levels and localized deviations from nominal geometry compared to machined components [228]. Such irregularities can prevent perfect surface contact at mechanical interfaces, creating preferential leakage paths when rigid sealing solutions are employed.

To mitigate these effects, compliant soft gaskets were introduced at multiple interfaces, including flange junctions, armature contact surfaces, and regions where the external walls of the valve interacted with the containment structure. The use of deformable sealing elements allowed local adaptation to surface irregularities, compensating for micro-scale geometric deviations without requiring post-machining of the polymeric prototype [229].

Soft gasket materials operate by undergoing elastic and plastic deformation under compressive load, thereby increasing real contact area between surfaces and reducing permeability pathways. Proper gasket compression is known to play a decisive role in maintaining pressure stability, particularly in systems subjected to repeated pressurization cycles [230]. By accommodating differential thermal expansion and minor alignment imperfections, compliant interfaces also reduce stress concentrations that could otherwise lead to sealing degradation.

In experimental fluid mechanics, pressure stability is directly linked to sealing effectiveness. Small leaks may introduce slow pressure decay or localized flow disturbances that are difficult to detect yet capable of altering steady-state measurements. The combined use of PTFE thread sealing and compliant gasket interfaces therefore ensured both macroscopic sealing integrity and micro-scale interface conformity.

The adopted sealing strategy proved particularly effective for the PPR experimental setup, where accurate reconstruction of pressure distribution required stable boundary conditions over extended measurement intervals. By integrating sealing considerations into the

mechanical design of the containment system, leakage effects were minimized, enabling reliable and repeatable hydraulic characterization of the additively manufactured valve [231].

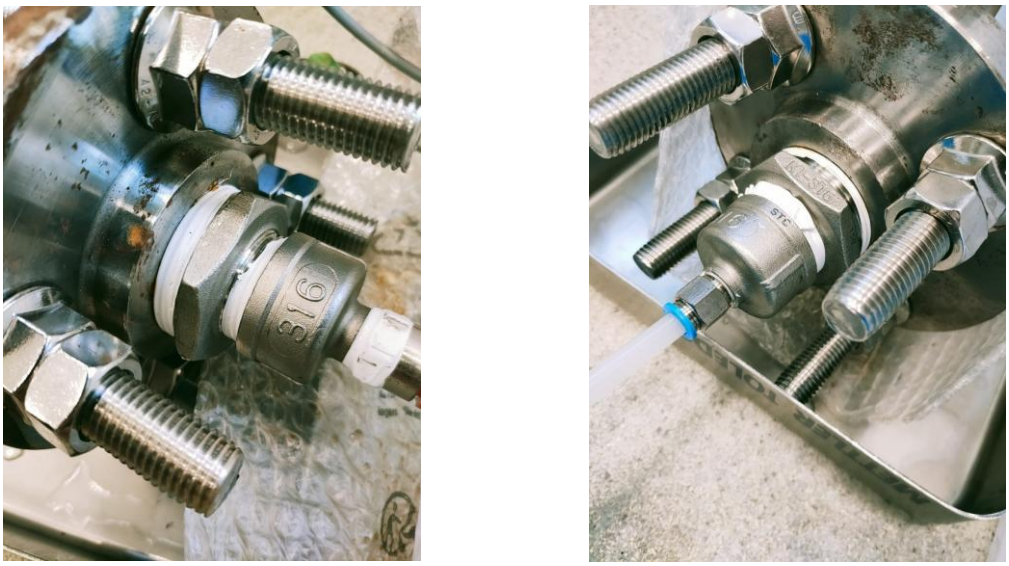


Figure 6.8: *PTFE tape and compliant gaskets used for sealing threaded interfaces and flange junctions in the PPR experimental assembly.*

6.4 Pressure Measurement System

6.4.1 Pressure Tap Design Challenges

One of the most critical aspects of the experimental design concerned the implementation of pressure taps capable of providing reliable local measurements within the multi-chamber configuration of the Passive Pressure Reducer (PPR). Accurate pressure acquisition in internal flows is inherently challenging, as the measurement system must capture static pressure without disturbing the flow field or introducing artificial hydraulic communication between measurement locations. In distributed pressure-reduction devices, such as the PPR, this requirement becomes particularly stringent because pressure gradients between adjacent chambers represent the primary quantity used for model validation [232].

The geometry of the PPR introduced additional complexity. The additively manufactured polymer body contained multiple annular chambers separated by thin walls, and direct installation of sensors risked creating unintended flow paths between cavities. Moreover, manufacturing tolerances inherent to additive processes can generate micro-gaps at mechanical interfaces, which may allow slow crossflow between chambers when subjected to pressure differences [233].

To overcome these challenges, a dedicated hydraulic isolation strategy was developed. Small compliant paper washers were inserted between the threaded pressure sensor and the armature interface. Although simple in appearance, this solution addressed several critical measurement requirements simultaneously [234].

During tightening, the threaded sensor compressed the washer against the external surface of the valve body. The resulting deformation produced a localized sealing interface capable of adapting to surface irregularities introduced by additive manufacturing. Deformable sealing

materials are widely used in pressure instrumentation because they increase real contact area under compression, thereby blocking micro-scale leakage paths that rigid interfaces cannot eliminate [235].
The compression of the washer fulfilled three simultaneous functions:

- Precise axial positioning of the sensor relative to the pressure tap,
- Sealing of the measurement cavity,
- Hydraulic isolation between adjacent chambers.

By preventing fluid communication along the threaded interface, the washer ensured that each sensor responded exclusively to the pressure within its corresponding annular chamber. This isolation was essential to avoid pressure averaging effects, which can occur when measurement volumes unintentionally connect regions at different pressures [236].
From a fluid-dynamic perspective, proper pressure tap isolation also minimises dynamic pressure contamination. If crossflow occurs within the sensing channel, local velocity components may introduce additional pressure fluctuations, causing deviations from true static pressure values [237]. The compliant washer acted as a damping interface, reducing the likelihood of such disturbances.
The adopted solution reflects a broader principle in experimental fluid mechanics: measurement reliability often depends more on interface design than on sensor accuracy itself [238]. Even high-precision sensors cannot compensate for poorly isolated pressure taps, whereas carefully engineered interfaces enable accurate measurements using relatively simple instrumentation [239].
The effectiveness of the isolation strategy was confirmed during experimental operation. Stable and repeatable pressure readings were obtained across multiple configurations, demonstrating that each sensing port operated independently without detectable cross-interference. This allowed reconstruction of the pressure distribution along the valve with sufficient fidelity to enable direct comparison with CFD predictions [240].
By combining compliant sealing with controlled mechanical positioning, the adopted solution ensured accurate local pressure measurement while preserving the integrity of the internal flow field, thereby supporting reliable validation of the distributed pressure-reduction mechanism [241].



Figure 6.9: *Paper washers used to hydraulically isolate individual pressure tap ports from adjacent annular chambers, ensuring independent static pressure acquisition at each measurement location.*

6.4.2 Sensor Configuration and Placement Strategy

Three electronic pressure transmitters with analog 4–20 mA output were installed along the external armature to measure local static pressure within the Passive Pressure Reducer (PPR). The sensors employed in the experimental campaign were industrial pressure transmitters (Schneider Electric XMLG016D21 series), designed for hydraulic and pneumatic applications and characterized by a measurement range of 0–16 bar, two-wire current-loop output, and differential fixed-scale operation.

The choice of a 4–20 mA current-loop configuration was motivated by its robustness against electrical noise and signal degradation, which is particularly advantageous in laboratory environments where electromagnetic interference and cable length may affect voltage-based measurements. Current-loop transmission maintains signal integrity independently of line resistance, ensuring stable acquisition even under varying electrical conditions (Doebelin & Manik, *Measurement Systems*, 2011) [242]. The 4–20 mA standard, widely adopted in process instrumentation since its formalization in ISA-50.00.01, also provides an intrinsic diagnostic capability, as any reading below 4 mA unambiguously indicates a broken loop or sensor fault rather than a valid low-pressure condition [243].

Four pressure ports were available along the valve body, corresponding to distinct annular chambers intended to characterize the spatial evolution of pressure within the distributed pressure-reduction system. Because only three sensors were available simultaneously, multiple experimental runs were conducted with sequential sensor repositioning. This approach enabled reconstruction of the complete pressure profile while maintaining consistent instrumentation characteristics across measurements. Sequential measurement strategies are commonly adopted in experimental fluid mechanics when spatial resolution exceeds available instrumentation, provided that boundary conditions remain repeatable between runs [244]. The stability of inlet pressure and the controlled operating procedure ensured that reconstructed pressure distributions remained physically consistent, in agreement with the repeatability criteria recommended for multi-run reconstruction techniques in internal flow experiments [245].

Additional pressure measurements were performed upstream and downstream of the valve using dedicated ports integrated into the hydraulic line. These measurements fulfilled three

essential purposes: calibration and verification of inlet boundary conditions, evaluation of the global pressure drop across the valve, and validation of CFD boundary conditions used in numerical simulations. Accurate definition of inlet pressure is critical for meaningful comparison between experimental and computational results, as pressure-driven internal flows are highly sensitive to boundary specification errors [246].

According to the manufacturer's technical documentation, the selected pressure transmitters exhibit a measurement accuracy of ±0.3% of full-scale output and repeatability of ±0.1%. For the adopted 0–16 bar range, this corresponds to an uncertainty significantly smaller than the pressure variations investigated experimentally, confirming the suitability of the sensors for resolving distributed pressure gradients within the PPR. The propagation of such instrumental uncertainty into derived quantities was evaluated following the methodology outlined by Coleman and Steele for experimental uncertainty analysis in fluid systems [247].

The sensors feature a response time below 2 ms, ensuring that transient fluctuations occurring during valve opening or flow stabilization do not introduce measurement lag. Although the experimental campaign primarily focused on quasi-steady conditions, rapid sensor response contributes to improved stability during transient phases preceding data acquisition [248].

Thermal drift represents another important parameter in hydraulic measurements: the sensor specification indicates sensitivity and zero-point drift of ±0.015% of full scale per degree Celsius, a value consistent with the performance class defined by IEC 60770-1 for industrial pressure transmitters operating under laboratory temperature variations [249]. The sensing element incorporates ceramic and stainless-steel wetted materials compatible with water, air, and hydraulic fluids, ensuring chemical stability and preventing degradation during repeated testing cycles.

Sensor outputs were converted into pressure values through calibration curves provided by the manufacturer, following the standard linear mapping of current-loop transmitters, where the measured current in milliamperes is linearly scaled to the corresponding pressure value. The linearity of industrial transmitters allows straightforward conversion while preserving measurement fidelity [250]. Calibration curves supplied by manufacturers are typically derived from factory calibration under controlled conditions and comply with industrial metrology standards traceable to national reference laboratories [251]. Nevertheless, upstream and downstream pressure measurements were used as reference points to verify consistency of sensor readings during operation, in line with in-situ verification practices recommended for hydraulic test benches [252].

The combination of industrial-grade transmitters, current-loop acquisition, and controlled installation within the armature ensured high measurement reliability. The sensors' immunity to vibration (20 g operational tolerance) and electromagnetic disturbances specified in the datasheet further supported stable operation within the experimental environment, minimizing spurious contributions to the measured signal that could otherwise compromise CFD–experiment comparison [253]. Overall, the adopted sensor configuration provided a balanced compromise between spatial resolution, instrumentation availability, and measurement accuracy, enabling reconstruction of the internal pressure distribution required for validation of the distributed hydraulic behavior of the PPR.



Figure 6.10: *Three Schneider Electric XMLG016D21 pressure transmitters (0–16 bar, 4–20 mA current-loop output) installed on the containment armature, each connected to a dedicated pressure tap aligned with the corresponding internal annular chamber of the PPR prototype.*

6.5 Experimental Rig

The experimental hydraulic circuit was specifically designed to provide controlled and repeatable boundary conditions for the characterization of the Passive Pressure Reducer (PPR). Unlike conventional hydraulic testing facilities supplied directly by liquid pumps, the available laboratory infrastructure employed compressed air as the driving medium. Consequently, the experimental line adopted a hybrid pneumatic–hydraulic configuration in which compressed air acted as the energy source while water served as the working fluid flowing through the valve. Such air-over-water arrangements, often referred to as blowdown or bladder-accumulator circuits, are widely documented in the experimental fluid mechanics literature as an effective alternative to direct pump supply when the primary requirement is the delivery of a clean, steady, and reproducible flow to the test section [254].

The use of compressed air to pressurize a liquid reservoir represents a well-established solution in experimental fluid mechanics, particularly when stable low-flow-rate conditions are required. Pneumatic pressurization enables smooth pressure regulation without introducing mechanical pulsations typically associated with positive-displacement pumps, which are known to generate periodic pressure ripples that can bias both time-averaged and spectral measurements in hydraulic components [255]. The absence of rotating or reciprocating parts upstream of the test section also eliminates the need for dedicated pulsation dampeners and simplifies the interpretation of transient phenomena occurring within the valve body [256].

However, coupling compressible driving fluid with an incompressible working fluid introduces potential pressure oscillations that must be mitigated through careful circuit design [183]. The presence of a free air–water interface inside the pressurized reservoir behaves dynamically as a pneumatic capacitance in series with the hydraulic inertance of the downstream line, giving rise to a characteristic Helmholtz-type resonance whose frequency depends on the air volume, the water column length, and the effective cross-sectional area of the circuit [257]. If not properly accounted for, this coupled oscillatory behavior can manifest itself as low-frequency pressure fluctuations superimposed on the nominal steady-state signal, degrading the quality of the experimental data and complicating the comparison with steady

CFD predictions [258]. For this reason, the sizing of the air cushion, the positioning of the discharge line, and the inclusion of appropriate flow-conditioning elements were treated as integral parts of the circuit design process rather than as secondary installation details, in line with best practices recommended for the commissioning of hydraulic test rigs [259].

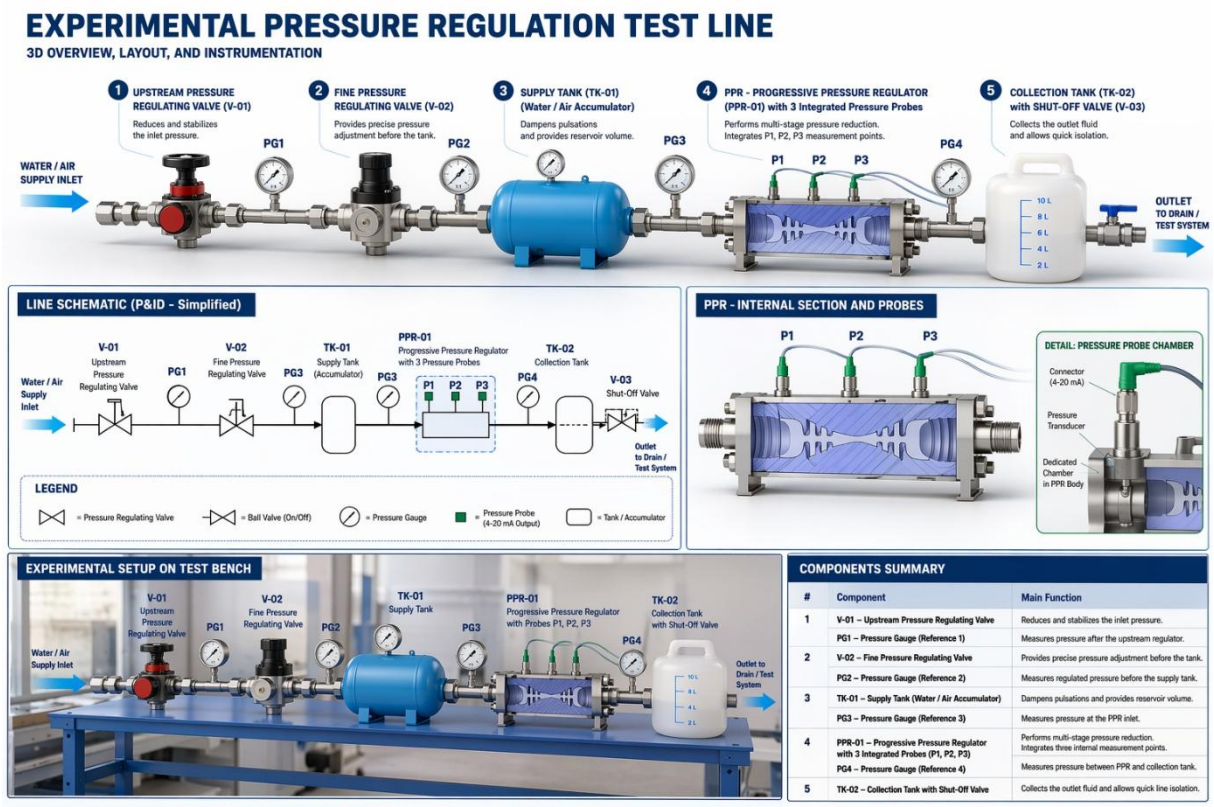


Figure 6.11*: Schematic diagram of the experimental pneumatic–hydraulic line. From left to right: compressed air supply (P_0 = 0–6 bar); coarse pressure reducing valve (PRV_1); upstream manometer (M_1); fine throttle valve (TV_1); downstream manometer (M_2); hydraulic damper reservoir; PPR test section with three Schneider Electric XMLG016D21 pressure transmitters (P1–P3, 0–16 bar, 4–20 mA); calibrated discharge collection tank.*

The experimental line was therefore organized as a sequence of flow-conditioning components arranged from upstream to downstream as follows:

1. Pressure regulating valve (coarse adjustment),
2. Upstream manometer positioned before the fine regulating valve,
3. Throttling valve for fine pressure control,
4. Downstream manometer to verify pressure stability,
5. Water-filled reservoir acting as hydraulic damper,
6. PPR valve under investigation,
7. Calibrated discharge tank.

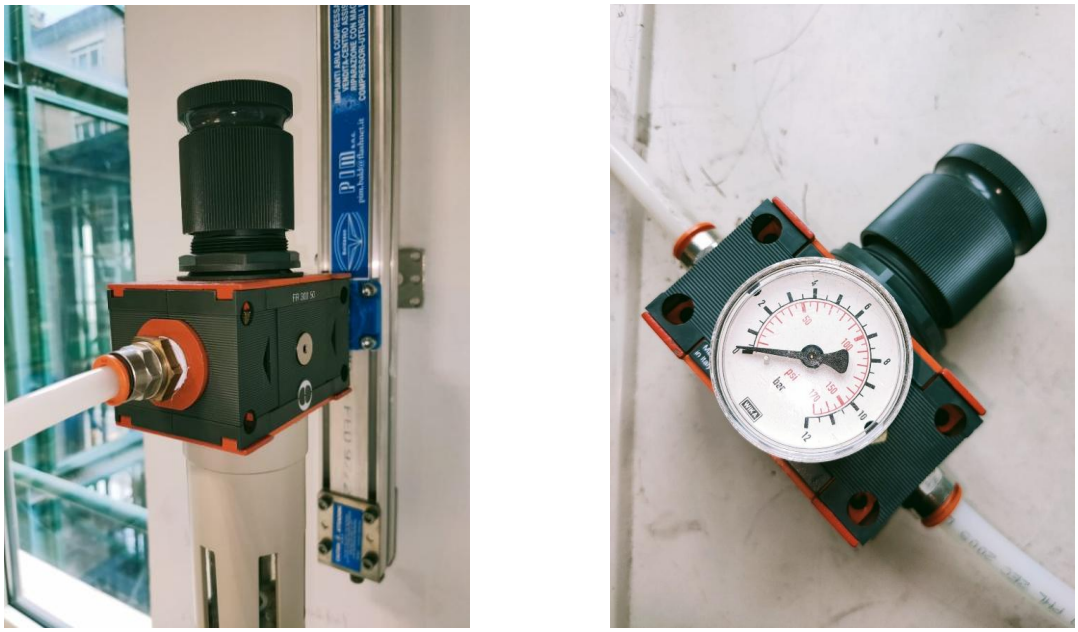


Figure 6.12: *Pressure regulating valve with coarse adjustment (on the left) and throttling valve for fine pressure control (on the right).*

6.5.1 Hydraulic Circuit Architecture, Operating Conditions, and Filling Procedure

Building upon the instrumentation described in the previous section, the overall experimental infrastructure was conceived as an integrated system in which each hydraulic component contributed to the stability and repeatability of the boundary conditions imposed on the Passive Pressure Reducer (PPR). The circuit was organized as a sequence of flow-conditioning elements arranged from upstream to downstream, with the explicit purpose of progressively improving pressure stability along the flow path before the working fluid reached the test section.

The first stage of pressure regulation was provided by an upstream regulating valve acting on the compressed air supply. Pressure regulators of this type balance the downstream pressure against a mechanical reference, typically a spring-loaded diaphragm, and are routinely employed in pneumatic and hydraulic laboratory rigs to attenuate supply-line fluctuations and deliver a reasonably stable feed pressure to the rest of the circuit [254]. A mechanical manometer installed immediately downstream of the regulator allowed continuous visual monitoring of the imposed pressure level; Bourdon-tube instruments were deliberately retained throughout the rig because of their robustness, their independence from electrical calibration drift, and their long-standing status as primary indicators in industrial pressure measurement practice [255].

Fine regulation was then obtained through a throttling valve placed downstream of the first measurement location. Whereas regulators impose a quasi-constant outlet pressure, throttling elements introduce a continuously adjustable hydraulic resistance, allowing the operator to tune the pressure delivered to the downstream reservoir with a resolution that cannot be achieved by the regulator alone [256]. The combined use of a coarse regulation stage and a

fine throttling stage reflects a well-established layout in fluid-power laboratory practice, in which controllability and stability of the boundary conditions are pursued simultaneously rather than as competing objectives [257]. A second manometer, positioned after the throttling valve, closed the control loop by providing an independent verification of pressure stability before the flow entered the hydraulic section, so that any residual transient generated upstream could be identified before it could bias the measurements acquired in the test section.

A decisive element of the circuit architecture was the intermediate water-filled reservoir, which acted as a hydraulic damper interposed between the pneumatic supply and the liquid line feeding the PPR. Because the driving medium was compressible air, even minor adjustments of the regulator or small fluctuations in the supply pressure could in principle propagate as pressure waves into the test section, with a detrimental effect on measurement repeatability [258]. The reservoir effectively decoupled the compressible pneumatic domain from the incompressible hydraulic flow entering the valve: the free air–water interface behaved as a pneumatic capacitance in series with the hydraulic inertance of the downstream line, converting pressure-driven air expansion into a smoother liquid displacement and attenuating high-frequency oscillations [259]. The use of such buffer volumes, conceptually analogous to hydraulic accumulators, is a recurrent design choice in systems where compressible and incompressible fluids interact, and it is specifically recommended when quasi-steady inlet conditions are required for comparison with steady-state CFD predictions [184], [260].

Downstream of the reservoir, water entered the PPR under controlled pressure conditions, and the valve itself constituted the primary test section in which the distributed pressure reduction mechanism was investigated. The fluid discharged by the valve was collected in a calibrated tank, and the global flow rate was determined by measuring the volume accumulated over a known time interval. Volumetric (and equivalently gravimetric) collection remains one of the most reliable methods for flow-rate determination, particularly at low flow rates where high-precision flow meters may suffer from reduced accuracy or excessive cost; the method is codified in international standards and is often adopted as a reference for the calibration of other flow-measurement devices [261]. In the present work, this approach had the additional advantage of providing a global hydraulic characterization of the valve that was fully independent from the local pressure measurements, thereby strengthening the dataset available for model validation.

The volumetric collection method is, however, an integral measurement: it returns the flow rate averaged over the collection interval, and it requires that interval to be long enough for the reading of the accumulated volume to be accurate. Two consequences follow. The first concerns the duration of the campaign, since every operating point requires a dedicated collection and the subsequent emptying of the tank before the following acquisition can begin; the second, and more significant one, is that the method is by construction blind to any variation of the flow rate within the interval, so that the repeatability of a single point can be assessed only by repeating the whole collection. For the steady-state characterization pursued in the present work these limitations are acceptable, and the redundancy provided by the three repeated campaigns discussed in Chapter 7 supplies a direct estimate of the resulting

dispersion. For a future evolution of the test bench, however, the installation of a dedicated flow meter on the line, an electromagnetic or Coriolis instrument for the water campaigns and a Venturi or turbine device for a subsequent cryogenic extension, would remove both limitations at once: it would provide an instantaneous flow rate acquired continuously and synchronously with the pressure signals, it would shorten the acquisition of each operating point by about an order of magnitude, and it would open the possibility of characterizing the transient behaviour of the device, which the integral method cannot address. This upgrade is therefore recommended as a priority item in the further development of the experimental infrastructure, and is recalled among the directions for future work in Section 8.6.4.

At a system level, the overall architecture reflects an experimental philosophy in which external disturbances are minimized without sacrificing controllability. The progressive arrangement of regulator, throttling valve, manometers, and damping reservoir ensured that pressure stability improved monotonically along the flow direction, culminating in well-defined inlet boundary conditions for the PPR. This point is far from secondary: in the verification and validation literature it is repeatedly emphasized that apparent discrepancies between simulations and experiments often originate from insufficiently controlled boundary conditions rather than from genuine modelling inaccuracies, and that a careful characterization of the experimental inlet and outlet conditions is an essential prerequisite for any quantitative code-to-experiment comparison [262].

Within this architecture, the choice of the working fluid and of the operating range was driven by a combination of physical, practical, and structural considerations. Water was adopted because of its availability, its operational safety, and most importantly from a modelling point of view, the fact that its thermophysical properties are known with high accuracy over a wide range of temperatures and pressures, as codified in the internationally adopted IAPWS-IF97 formulation [263]. The use of a well-characterized reference fluid allowed a direct and reliable comparison between experimental measurements and theoretical predictions, and eliminated the additional uncertainties that would arise from compressible gases or from hazardous liquids. The experimental campaign was carried out over an inlet pressure range between 0.5 bar and 4 bar, chosen as a compromise between two competing requirements: on one hand, the need to generate measurable pressure gradients across the PPR and to reach Reynolds numbers high enough to establish fully developed internal flow regimes representative of practical hydraulic operation [264]; on the other, the need to remain well within the structural limits of the additively manufactured polymer prototype, whose maximum allowable working pressure is constrained by the mechanical properties of the cured photopolymer and by the anisotropy introduced by the layer-wise bonding typical of stereolithographic processes [265]. Within this range, the redundancy between mechanical manometers and electronic transmitters provided an additional layer of confidence in the definition of the boundary conditions, consistent with the metrological principle that the use of heterogeneous measurement techniques for the same physical quantity helps to reveal and mitigate systematic errors [266].

A final, and often underestimated, aspect of the experimental protocol concerned the filling of the valve and the removal of residual air prior to each test. The presence of trapped gas in

hydraulic systems is a major source of experimental uncertainty, because even small volumes of compressible gas introduce elastic storage effects that modify both the steady-state pressure distribution and the transient response of the circuit [267]. Small air bubbles, in particular, behave as distributed pneumatic accumulators whose influence depends on the local void fraction and on the bubble size distribution, and which may dampen pressure variations and delay transient responses in ways that are difficult to characterize a posteriori. In a distributed pressure-reduction device such as the PPR, whose geometry features multiple annular chambers connected through narrow passages, and is therefore particularly prone to air entrapment during assembly, residual air can distort the measured pressure gradients and lead to misinterpretation of the hydraulic losses associated with each stage.

To mitigate this risk, a dedicated filling and venting procedure was implemented. Water was introduced gradually from one side of the valve while the individual pressure ports were temporarily opened in sequence, so that trapped air could escape through each port before the corresponding chamber was fully pressurized. This staged approach promoted a progressive displacement of the gas phase rather than the compression of residual pockets into isolated volumes, in line with established recommendations for the commissioning of hydraulic circuits with complex internal geometries [268]. Visual inspection of the discharge and the stabilization of the manometer readings were used as practical criteria to confirm the successful elimination of the air phase prior to the installation of the valve into the experimental line. Achieving fully liquid-filled conditions was not merely a matter of operational cleanliness: it was a necessary condition for the system to behave according to the incompressible-flow assumption adopted in the numerical simulations, and therefore for the physical experiment and the computational model to share a consistent set of hypotheses.

Taken together, the hybrid pneumatic–hydraulic architecture, the choice of water as the working fluid within a carefully selected pressure range, and the rigorous filling and purging procedure provided a stable, controllable, and physically well-defined experimental environment. These elements, often considered secondary with respect to the instrumentation or the numerical model, played in fact a decisive role in ensuring that the measurements acquired on the PPR could be meaningfully compared with the CFD predictions discussed in the following chapters.

6.5.2 Experimental Procedure

Each experimental run followed a standardized protocol designed to ensure repeatability, controlled boundary conditions, and consistent comparison with numerical predictions. Establishing a repeatable operating sequence is essential in experimental fluid mechanics, particularly for distributed hydraulic devices where pressure evolution depends strongly on initial conditions and transient behavior.

The test procedure began with gradual pressurization of the entire valve to the desired inlet pressure. Pressurization was performed with the downstream valve closed, allowing the hydraulic circuit to reach a static equilibrium condition. Under these circumstances, no flow occurred inside the PPR and all chambers were expected to reach identical pressure levels. Verification of uniform pressurization was performed by monitoring all installed pressure

sensors; equal readings confirmed the absence of trapped air and ensured that the initial condition corresponded to a hydrostatic state.
During steady operation, discharged water was collected in a calibrated tank positioned downstream of the valve. The collected volume and elapsed time were recorded together with inlet pressure and local chamber pressures. The following quantities were therefore acquired for each experimental point:

- Inlet pressure
- Local pressures within the annular chamber with the sensor linked,
- Discharged volume
- Acquisition time interval

Measurements were repeated at inlet pressure increments of 0.5 bar across the investigated operating range to reconstruct the hydraulic response of the valve under varying driving conditions. While simple, this approach provides robust flow estimation when calibrated collection volumes are used and steady conditions are maintained.
The adoption of incremental pressure steps enabled identification of deviations from ideal square-root scaling, which may arise from Reynolds-number effects, evolving turbulence structures, or roughness-induced losses characteristic of additively manufactured geometries.
Overall, the experimental procedure ensured controlled initialization, consistent data acquisition, and physically meaningful comparison between measured hydraulic performance and predictive models, thereby enabling quantitative validation of the distributed pressure-reduction mechanism implemented in the PPR.



Figure 6.13*: Close-up view of the threaded fittings at the pressure tapping points showing the T-connectors.*



Figure 6.14*: Close up zoom of the polymeric sealing used for the interface between the PPR and the flange (on the left). The PPR outlet pipe (on the right).*

Chapter 7

Experimental Campaigns: CFD Validation and Results Analysis

The experimental campaign described in Chapter 6 provided a complete set of boundary conditions, local static pressures and discharge measurements that represent, for the Passive Pressure Reducer investigated in this work, the reference dataset against which every numerical prediction must be benchmarked. As anticipated in Section 6.2.3, the first additively manufactured prototype revealed a systematic over-prediction of the experimental pressure drops with respect to the simulations performed during the design phase, suggesting that the baseline CFD model did not capture the full set of dissipation mechanisms present in the physical device [269].

The present chapter closes the design–manufacturing–simulation–validation loop by documenting the numerical activity carried out in parallel with, and in response to, the experimental programme. Three complementary lines of work are reported: (i) the production and testing of a second prototype with a revised printing orientation, (ii) a substantial revision of the CFD setup in which the geometric fidelity of the simulated domain was brought as close as possible to the assembled hydraulic line, and (iii) the introduction of wall-roughness models in Ansys Fluent, both the Standard and the High Roughness (Icing) formulations, to account for the as-manufactured surface quality of the resin-printed component [270, 271].

For each of the four inlet-pressure levels investigated experimentally (1, 2, 3 and 4 bar) a matrix of seven CFD simulations was executed, for a total of twenty-eight computations, all sharing the same geometry and mesh but differing in the turbulence closure, in the wall treatment and in the prescribed roughness parameters. The chapter then extends the analysis with a dedicated discussion of the CFD flow fields, velocity, static and dynamic pressure, turbulence intensity and kinetic energy, in immediate proximity of the radial pressure tappings, which is the physical region where the largest discrepancies between CFD and experimental readings are observed and which has a decisive influence on the interpretation of the measured pressure profile.

7.1 Second Prototype and the Need for a Roughness-Aware CFD Model

7.1.1 Results Discrepancy Observed on the First Prototype

The baseline CFD model adopted during the design phase assumed hydraulically smooth walls and neglected the surface topology introduced by the additive manufacturing process. Under this assumption the predicted pressure distribution along the PPR, obtained with a steady,

incompressible, Reynolds-averaged formulation using the realizable k–ε model, reproduced correctly the overall staging behavior expected from the geometry. When this prediction was confronted with the measurements collected on the first prototype, however, a systematic discrepancy emerged: the measured pressure drops across the device were consistently larger than the numerical ones, and the flow-rate response to the imposed inlet pressure was lower than expected over the entire operating range [272].

Since the CAD geometry sent to the printer coincided with the one used by the simulation, and since the instrumentation uncertainty, quantified in Chapter 6 at the level of ±0.3 % of full scale, is insufficient to explain systematic deviations of several percent, the conclusion was that additional dissipation mechanisms existed in the physical device which were not captured by the smooth-wall simulation. The most plausible candidate was surface roughness: AM surfaces produced by stereolithographic or material-jetting processes with resin photopolymers routinely exhibit effective equivalent sand-grain roughness in the 10–150 μm range, substantially larger than the roughness of conventionally machined hydraulic components, and this roughness is known to modify wall friction factors and near-wall turbulence well beyond the negligible level assumed a priori [273, 274].

7.1.2 Second Prototype: Print Resolution and Layer Thickness

Following the analysis just described, a second prototype was fabricated internally at Politecnico di Torino. The nominal CAD geometry was preserved, but the build orientation was rotated so that the principal axis of the valve became aligned with the direction of layer deposition, thereby minimizing the staircase approximation of the internal curved surfaces and the anisotropic distortion of the annular chambers discussed in Section 6.2.2.

Two manufacturing parameters of the second prototype are particularly relevant for the subsequent numerical analysis. The in-plane (XY) print resolution, which quantifies the minimum lateral feature size the machine can resolve, was set to 0.080 mm, a value consistent with the best-in-class resolution achievable by entry-level stereolithographic printers for polymer resins [275]. The layer thickness, i.e. the vertical increment by which the build platform is lowered between successive cured layers, was selectable in the range 0.010 mm to 0.150 mm, with the prototype built using a layer thickness of approximately 0.100 mm to balance printing time and surface finish [276]. While the XY resolution governs the in-plane dimensional accuracy of the chambers and orifices, the layer thickness is the parameter that directly produces the micro-staircase pattern on walls whose normal is not aligned with the build direction, and is therefore the parameter most closely linked to the effective surface roughness experienced by the internal flow [277, 278].

Because it was not possible to perform a dedicated surface-roughness measurement on the as-built prototype, neither with a contact profilometer, due to the inaccessibility of the internal annular chambers, nor with optical techniques without sectioning the valve and destroying it, the layer-thickness range was adopted as the physically defensible envelope for the roughness height to be imposed in the CFD simulations. The CFD campaign therefore spanned roughness heights between 0.01 mm and 0.15 mm, so that both the lower and the upper bounds of the experimental printing parameter were represented [279].

This choice is also supported by the recent literature on AM surface metrology. Measurements performed on resin-printed channels with comparable printing parameters report arithmetic mean roughness values Ra between about 5 and 30 μm, peak-to-valley heights Rz of the order of 30–120 μm, and equivalent sand-grain roughness Ks close to the layer thickness itself, with systematic dependence on build orientation [280, 281, 282]. Similar conclusions have been reached for internal flow passages produced by laser powder-bed fusion, where values of Ks in the 30–200 μm range are routinely reported [283, 284].

7.1.3 Implications for the Numerical Framework

Recognizing surface roughness as a non-negligible source of dissipation changes the numerical framework in two non-trivial ways. First, the turbulence closure and the wall function must be compatible with a rough-wall treatment: the default log-law formulation implemented for smooth walls must be replaced by its extension to hydraulically rough walls, in which the equivalent sand-grain roughness Ks and the roughness constant Cs enter explicitly in the near-wall velocity profile [285]. Second, the choice of turbulence model itself must be reconsidered: while the realizable k–ε model is accurate and numerically robust for moderately separated flows, the k–ω SST model of Menter is widely recognized as more suitable for flows dominated by adverse pressure gradients and near-wall shear layers, as is the case in the annular chambers of the PPR where the central jet interacts with the surrounding stagnant fluid [286, 287].

7.2 CFD Model Updates: Geometric Fidelity, Mesh and Near-Wall Treatment

7.2.1 Reconstruction of the Assembled Hydraulic Line

A substantial modification with respect to the design-phase simulations concerned the geometric extent of the computational domain. In the preliminary CFD study, only the internal fluid volume of the valve body had been meshed, with idealized pressure boundary conditions imposed directly at the PPR inlet and outlet. This simplification is standard at the design stage but becomes inadequate when quantitative comparison with experimental data is required, because the assembled hydraulic line contains several geometric features upstream and downstream of the valve that contribute non-negligibly to the measured pressure drop [288].

The revised CFD geometry therefore reproduces the entire assembled test section: the straight inlet pipe, the progressive adapter reducing the hydraulic line diameter, the upstream flange with its sealing seat, the aluminum containment armature, the PPR body with its four annular chambers and four radial pressure tappings, the downstream flange, the outlet adapter and the straight outlet pipe. Each geometric transition, cross-section change, flange step, sealing pocket, has been explicitly modelled rather than simplified, so that the parasitic pressure losses observed at the sensor ports located upstream of the PPR (Inlet) and downstream of the PPR (Outlet) are reproduced numerically and can be isolated from the true pressure reduction occurring between Stage I and Stage IV. This distinction between "line losses" and "valve losses" is essential for a correct interpretation of the experimental data, since the sensors

installed upstream and downstream of the armature necessarily include the parasitic contributions of the adapters and flanges in their readings [289].

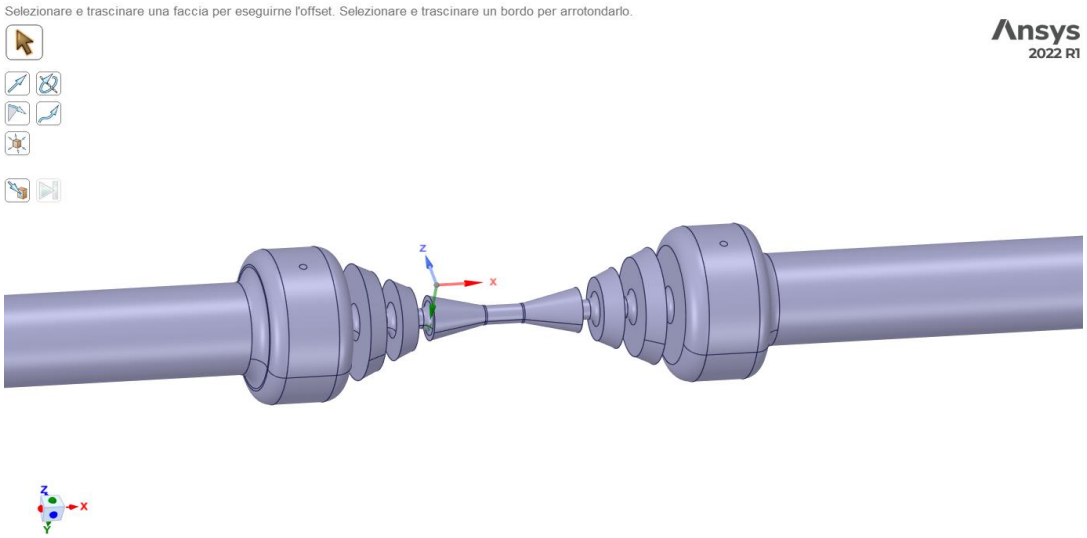


Figure 7.1: *CAD geometry of the assembled hydraulic test section reproduced in Ansys DesignModeler. The fluid domain extends from the straight inlet pipe upstream, through the adapters and flanges, across the four annular chambers of the PPR and the central throat, and up to the outlet pipe downstream. The radial pressure tappings at Stage I, II, III and IV are explicitly modelled as dead-end cavities connected to the main flow domain.*

It is important to stress that the geometric refinement documented here is a consequence of the experimental programme rather than a precondition for it. The hydraulic line had to be physically assembled, instrumented and characterized first, so that the dimensions of each adapter, the angular position of each pressure port and the actual sealing seat geometry could be measured and transferred to the CAD model. The numerical model is, in this sense, a post-hoc reconstruction of the experimental set-up, designed to be as faithful as possible to the physical test article.

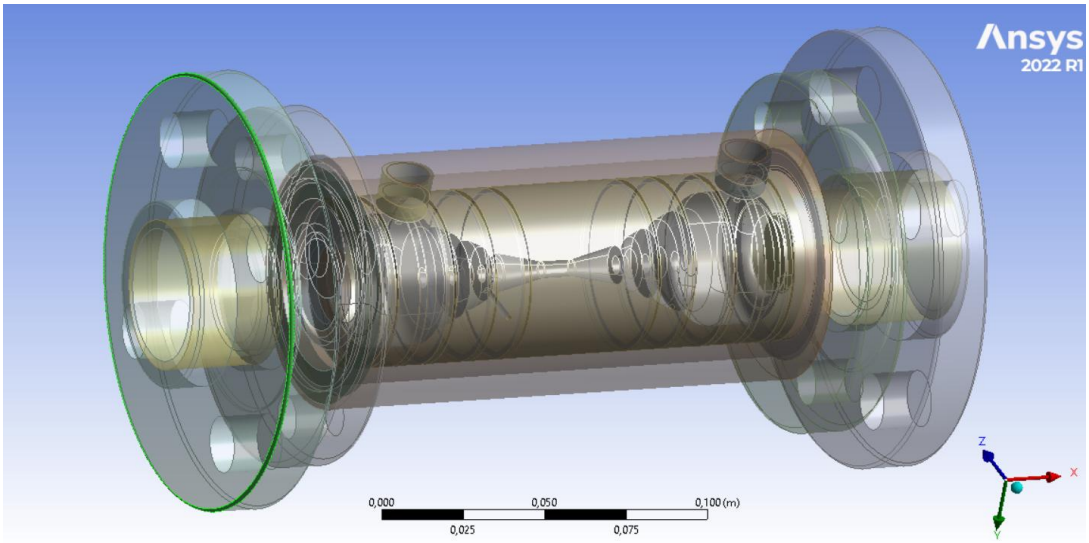


Figure 7.2: *Three-dimensional view of the fluid domain showing the internal volume of the armature, the PPR body, the four radial tapping channels and the connection interfaces to the inlet and outlet flanges. The inlet face (highlighted) is the surface on which the pressure or mass-flow boundary conditions are applied in the CFD simulations.*

7.2.2 Computational Mesh

The computational domain was discretized with an unstructured tetrahedral mesh generated in Ansys Meshing. The global element size was set to 1.0×10^{-3} m, refined to 5.0×10^{-4} m in the throat region and to 2.5×10^{-4} m in the vicinity of the radial pressure tappings, where the highest velocity and pressure gradients are expected. The total cell count of the final mesh is approximately 1.4×10^{6} elements, distributed over about 4.8×10^{5} nodes [290]. Figure 7.3 reports the longitudinal mid-plane view, while Figure 7.4 and Figure 7.5 document the refinement level achieved respectively around the throat–tapping region and at the Inlet adapter / flange interface.

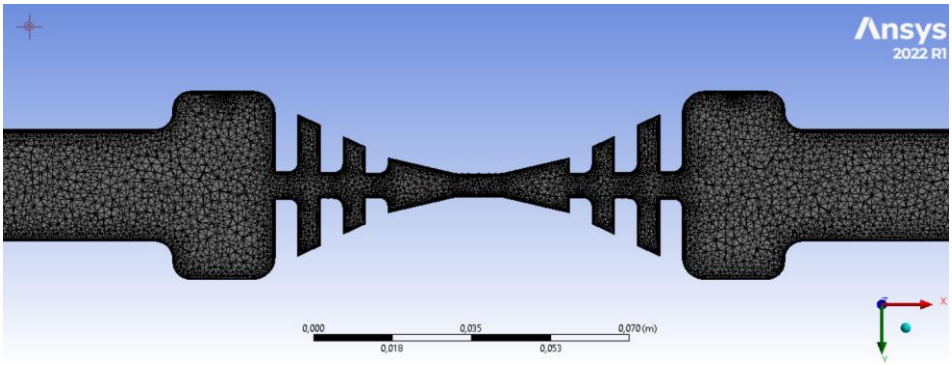


Figure 7.3: *Longitudinal mid-plane cross-section of the unstructured tetrahedral mesh adopted for the CFD campaign. The progressive refinement from the inlet pipe towards the throat and the pressure-tapping region is clearly visible.*

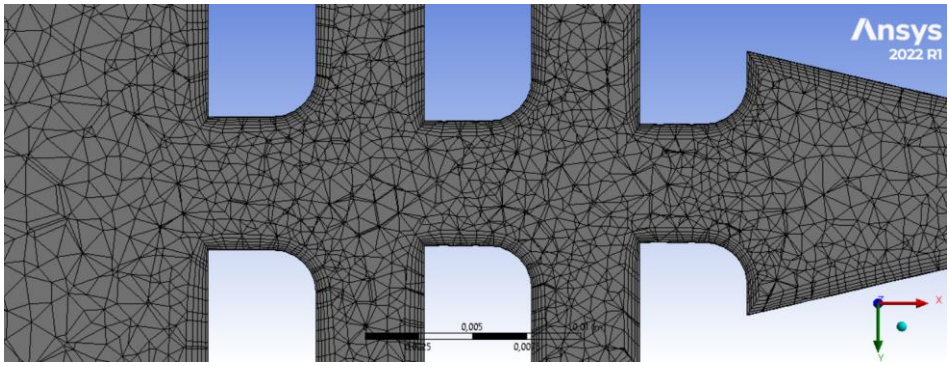


Figure 7.4: *Close-up of the mesh in the region of the annular chambers and pressure tappings. The local cell size is reduced to resolve the small radial passages that connect the chambers to the external pressure ports.*

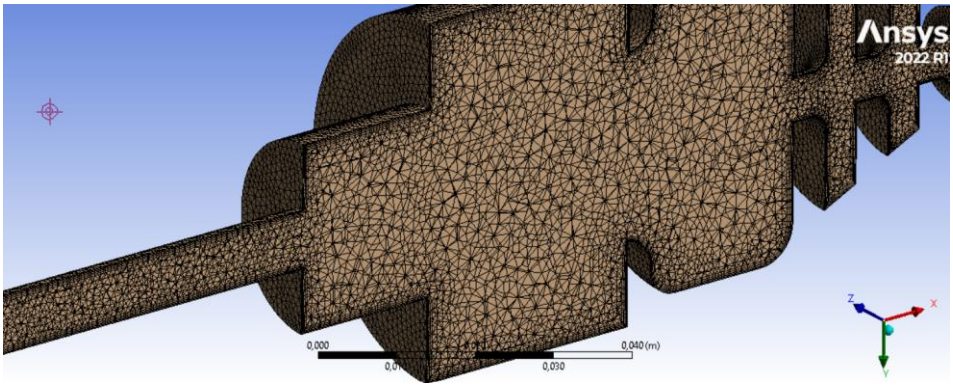


Figure 7.5: *Three-dimensional view of the mesh in the Inlet-adapter region, where the cross-section of the flow channel expands into the flange pocket. The refinement ensures an adequate resolution of the separation and reattachment regions that form at each geometric transition.*

7.2.3 Mesh Refinement at the Radial Pressure Tappings

The radial pressure tappings deserve a dedicated discussion because, as will become evident in Section 7.7, they are the region in which the largest deviations between the CFD predictions and the experimental measurements are concentrated, and because their very small cross-section (diameter approximately 1 mm) makes them particularly sensitive to the quality of the local mesh. The tapping is modelled as a cylindrical dead-end cavity that communicates with the annular chamber through its inner opening and is closed at the outer end by the sensor interface [291]. Figure 7.6 shows a detailed view of the mesh on the tapping walls, where the element size is reduced to approximately 1.5×10^{-4} m to resolve the geometry with a sufficient number of cells across the hole diameter.

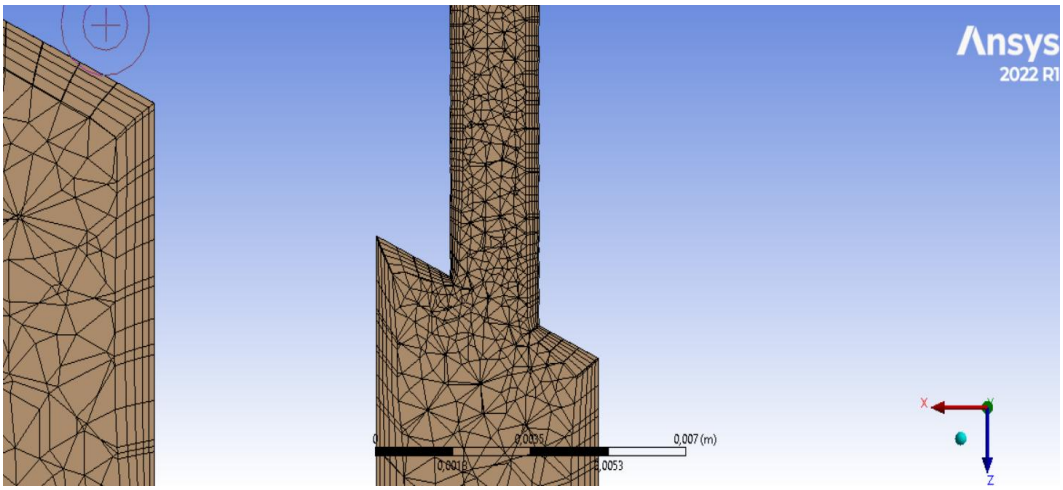


Figure 7.6: *Zoomed view of the tetrahedral mesh on a radial pressure-tapping cavity. The element size has been reduced locally with respect to the surrounding annular chamber in order to resolve the cylindrical cavity and the shear layer that may develop at its inner opening.*

7.2.4 Near-Wall Resolution and Inflation Layers

A boundary-layer inflation was added on all no-slip surfaces to guarantee adequate resolution of the near-wall region. Ten prismatic layers were generated with a first-cell thickness of 2.0×10^{-5} m and a growth ratio of 1.2, yielding dimensionless wall distances y^+ below 3 on the smooth-wall case across the entire operating range investigated; for the rough-wall cases the first-cell height was adjusted to remain compatible with the roughness-modified log-law, as discussed in Section 7.4 [292]. The inflation was propagated also inside the radial pressure-tapping cavities, as shown in Figure 7.7, because the velocity and pressure gradients in the interface region between the tapping and the annular chamber are decisive for a correct computation of the local static pressure.

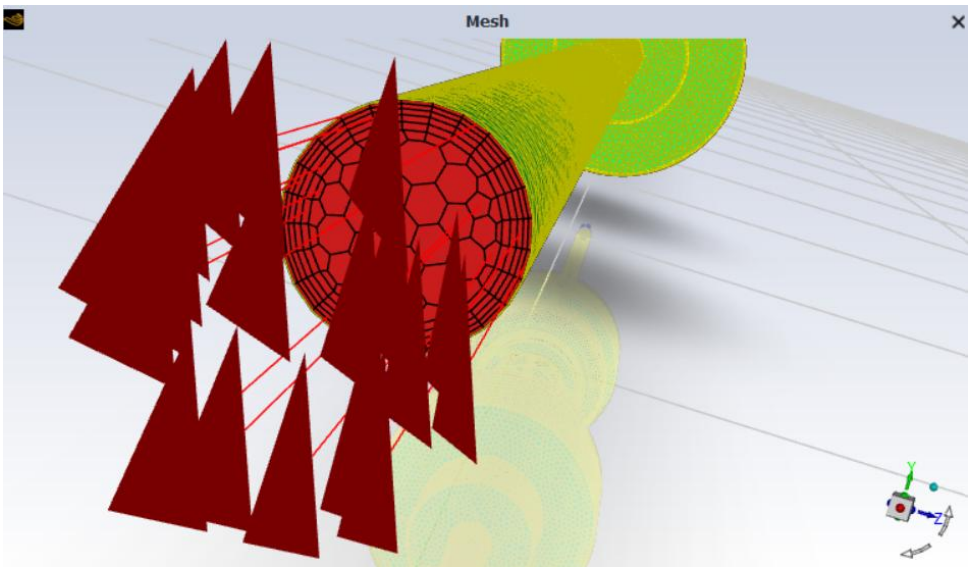


Figure 7.7: *Visualization of the prismatic inflation layers on a no-slip wall. The first row of prismatic cells adheres to the surface, ensuring near-wall resolution compatible with both smooth and rough-wall treatments.*

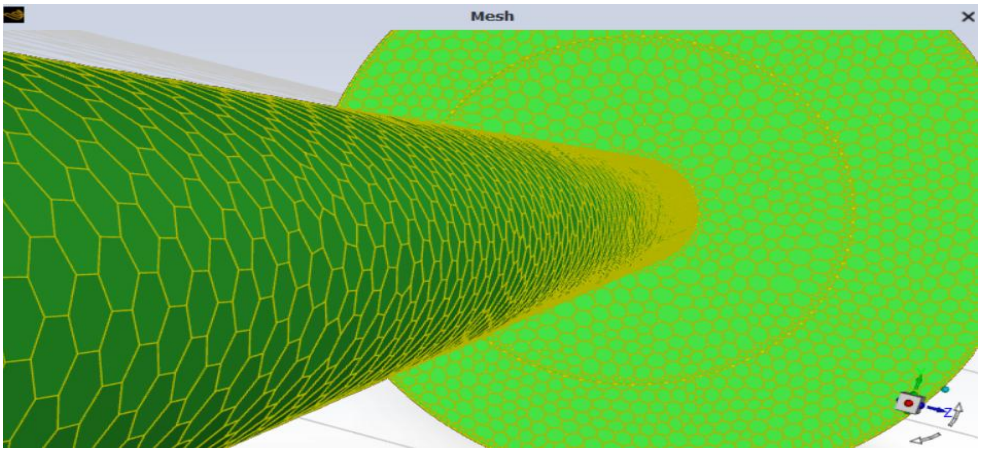


Figure 7.8: *Hexahedra mesh applied to the fluid volume of the hydraulic line.*

7.3 Wall Roughness Modelling

7.3.1 Rough-Wall Log-Law and the Standard Model

Ansys Fluent implements rough-wall boundary conditions through a modification of the logarithmic near-wall velocity profile. For a hydraulically smooth wall, the non-dimensional velocity $u^+ = u / u_\tau$ follows the classical log-law $u^+ = (1/\kappa) \ln(y^+) + B$, with $\kappa \approx 0.41$ and $B \approx 5.0$. In the presence of wall roughness, the profile is shifted downwards by a quantity ΔB that depends on the equivalent sand-grain roughness Reynolds number $Ks^+ = Ks \cdot u_\tau / \nu$, where Ks is the Roughness Height input by the user and ν is the kinematic viscosity of the fluid. The downward shift takes the form $\Delta B = (1/\kappa) \ln(1 + Cs \cdot Ks^+)$, where Cs is the Roughness Constant, an empirical parameter that accounts for the geometrical structure of the surface roughness and whose default value in Ansys Fluent is 0.5 [293, 294].

The Standard roughness model is appropriate for roughness geometries that can reasonably be regarded as uniformly distributed, randomly oriented sand-grain-like asperities, i.e. the class

of surfaces for which the Nikuradse correlation was originally derived. Under this model, the user specifies two parameters in the Wall Roughness section of the boundary-condition panel: the Roughness Height (Ks, in metres) and the Roughness Constant (Cs, dimensionless). The code internally computes ΔB and applies it to all wall-bounded cells of the selected surface [295].

7.3.2 High Roughness (Icing) Model

For surfaces whose roughness is not uniformly distributed, including typical AM surfaces with preferential directions aligned with the layer deposition pattern, the Standard formulation may underestimate the actual momentum deficit near the wall. Ansys Fluent therefore provides an alternative High Roughness (Icing) formulation, originally developed for ice-accretion problems on aeronautical surfaces and subsequently extended to generic high-roughness engineering surfaces. In this formulation the classical logarithmic matching point is shifted in such a way that the roughness-induced downward shift ΔB remains well-behaved even when Ks^+ approaches values for which the Standard model loses validity ($Ks^+ > 90$) [296]. The High Roughness (Icing) model is therefore particularly appropriate for simulations in which the prescribed Ks is large compared with the near-wall mesh spacing, as is the case for the present PPR study where Ks spans from 0.01 mm up to 0.15 mm.

Also in this case, two parameters are exposed to the user: the Roughness Height (Ks) and the Roughness Constant. The default value of the Roughness Constant for the Icing model is 0.5, but the parameter can be adjusted in the range 0.5–1.0 to represent surfaces whose roughness effectively "feels" rougher than a random sand-grain configuration of the same Ks. In the present work, a value of Cs = 0.8 was adopted for the Icing model in the configurations intended to represent the upper bound of the effective surface roughness of the second prototype, consistently with the recommendations reported for additively manufactured surfaces in [297].

7.3.3 Roughness Height Bracket Adopted

As discussed in Section 7.1.2, the layer thickness range of the printer (0.010–0.150 mm) was used as the physical basis for the Roughness Height values imposed in the CFD campaign. Three representative levels were explored in the validation study: Ks = 0 (smooth wall, used as a reference), Ks = 0.1 mm (the central value of the layer-thickness interval, used with both the Standard and the Icing models), and Ks = 0.15 mm (the upper bound of the interval, used with the Icing model and Cs = 0.8). The combination of Ks and Cs yields effectively five distinct rough-wall treatments, which are applied to the two turbulence closures (realizable k–ε and k–ω SST) in the full simulation matrix detailed in the next section.

7.4 Simulation Matrix and Solver Settings

The CFD campaign was organized according to a factorial matrix crossing four inlet-pressure levels (1, 2, 3 and 4 bar) with seven combinations of turbulence model and wall treatment. The seven simulation types are summarized in Table 7.1; the same matrix was replicated at each pressure level, for a total of 28 CFD runs.

Table 7.1: *Simulation matrix (7 CFD runs × 4 inlet pressures).*

#	Turbulence model	Wall treatment	Ks [mm]	Cs [–]
1	Realizable k–ε	Smooth wall (reference)	0	—
2	Realizable k–ε	Standard roughness	0.10	0.5
3	k–ω SST	Standard roughness	0.10	0.5
4	k–ω SST	Standard roughness + numerical corrections	0.10	0.5
5	k–ω SST	High Roughness (Icing)	0.10	0.5
6	k–ω SST	High Roughness (Icing)	0.15	0.8
7	k–ω SST	High Roughness (Icing), inlet mass-flow BC	0.15	0.8

Runs #1 to #6 use a total-pressure inlet boundary condition and a static-pressure outlet; run #7, executed at 1 bar only, uses the experimentally averaged mass flow rate as inlet condition to verify the consistency of the predicted pressure profile at fixed discharge.

7.4.1 Boundary Conditions, Solver and Convergence

All simulations were executed in steady, pressure-based formulation, with water as the incompressible working fluid ($\rho = 998.2$ kg/m³, $\mu = 1.003 \times 10^{-3}$ Pa·s). The Inlet boundary was treated as a pressure-inlet with total pressure set to the experimentally measured value upstream of the adapter, and the outlet was set to a pressure-outlet at the experimentally measured downstream value. All remaining surfaces were treated as no-slip walls with the wall treatment indicated in Table 7.1. Second-order upwind discretization was used for momentum and turbulence equations, and the SIMPLE algorithm for pressure–velocity coupling. Convergence was monitored through the evolution of the scaled residuals (continuity, momentum, turbulence quantities) and through the stabilization of the net mass-flow imbalance between inlet and outlet and of the volumetric flow rate at the throat section, as illustrated in Figures 7.9 and 7.10.

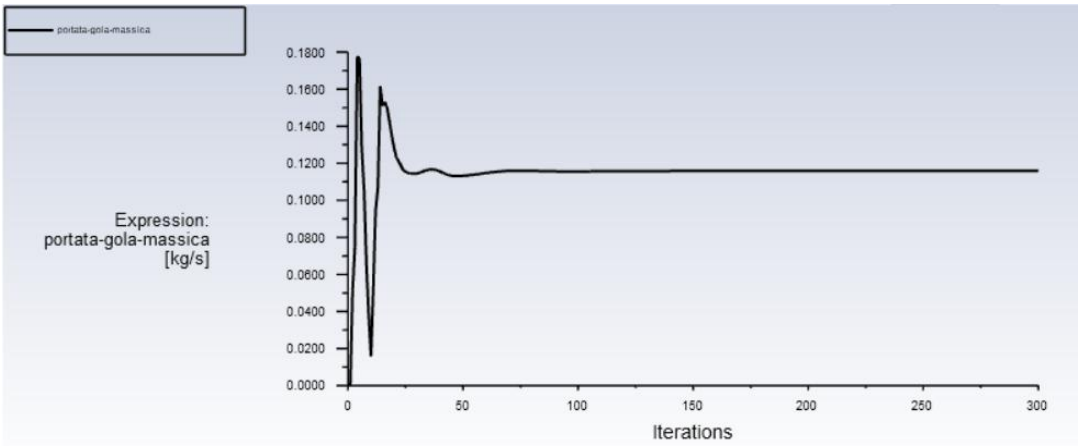


Figure 7.9: *Convergence history of the mass flow rate at the throat section, showing monotonic stabilization to a constant asymptotic value within approximately 75 iterations.*

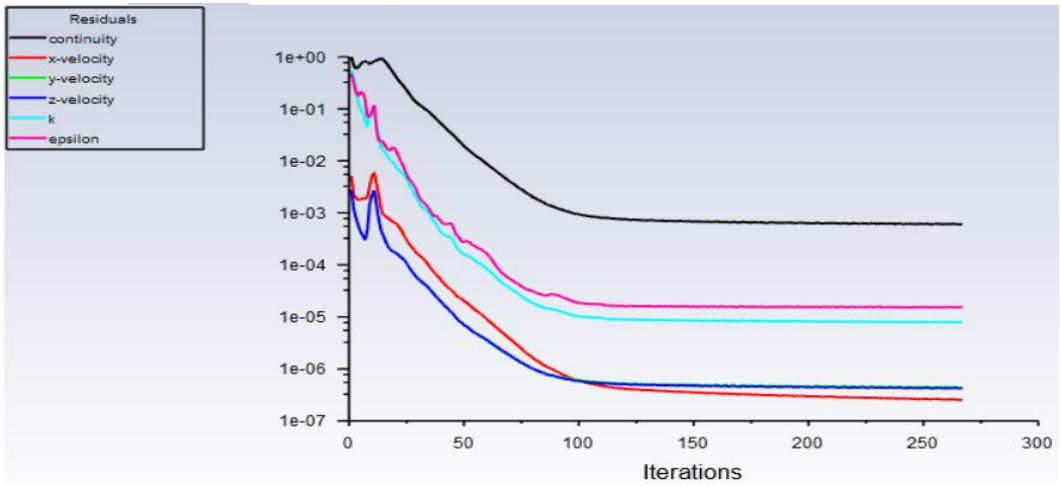


Figure 7.10: *Residuals of the continuity, momentum (x, y, z velocity components) and turbulence (k, ε) equations as a function of iteration number. All quantities converge to values below 10^{-3} for continuity and below 10^{-5} for the velocity components, confirming a satisfactory numerical convergence of the solution.*

7.5 Integrated Experimental Campaign and CFD Validation

This section gathers, in a single coherent narrative, the experimental results obtained on the second prototype and their direct comparison with the CFD simulations performed. The experimental data were originally documented in a companion technical report and are reproduced here in full for the sake of traceability and interpretive consistency.

7.5.1 Sensor Calibration

Before the main experimental campaign, the response of the three pressure transmitters (Schneider Electric XMLG016D21, range 0–16 bar, 4–20 mA output) was verified. Calibration was carried out by comparing each sensor reading against a reference tester under known pressure conditions at 0.5 bar and 1 bar, and against the absolute atmospheric pressure (101 325 Pa) at rest. The expected current-to-pressure relationship is linear and follows P [bar] = (I [mA] − 4).

Table 7.2: *Calibration verifications of the sensors.*

Instrument	Current [mA]	Pressure [bar]	Notes
Reference tester	3.99	≈ 0 (atm.)	Absolute reference
Sensor 1 @ 1 bar	3.92	≈ 0	10 mA offset to be added
Sensor 1 @ 0.5 bar	4.38	0.38	After offset correction
Sensor 1 @ 1 bar	4.96	0.96	After offset correction
Sensor 2 @ 1 bar	3.98	≈ 0	OK
Sensor 2 @ 0.5 bar	4.41	0.41	OK
Sensor 2 @ 1 bar	5.03	1.03	OK

Instrument	Current [mA]	Pressure [bar]	Notes
Sensor 3 @ 1 bar	4.00	0.00	OK
Sensor 3 @ 0.5 bar	4.48	0.48	OK
Sensor 3 @ 1 bar	5.07	1.07	OK

Sensor 1 shows a systematic 10 mA offset with respect to the other two transmitters. This offset is systematically added to the raw readings before converting them into bar.

7.5.2 Water-Test Campaigns: Experimental Pressure Profiles

The water test campaign was organized in three configurations to reconstruct the full pressure profile along the PPR despite the availability of only three transmitters. For each configuration and each inlet-pressure level, several pressure samples were acquired on each sensor and averaged.

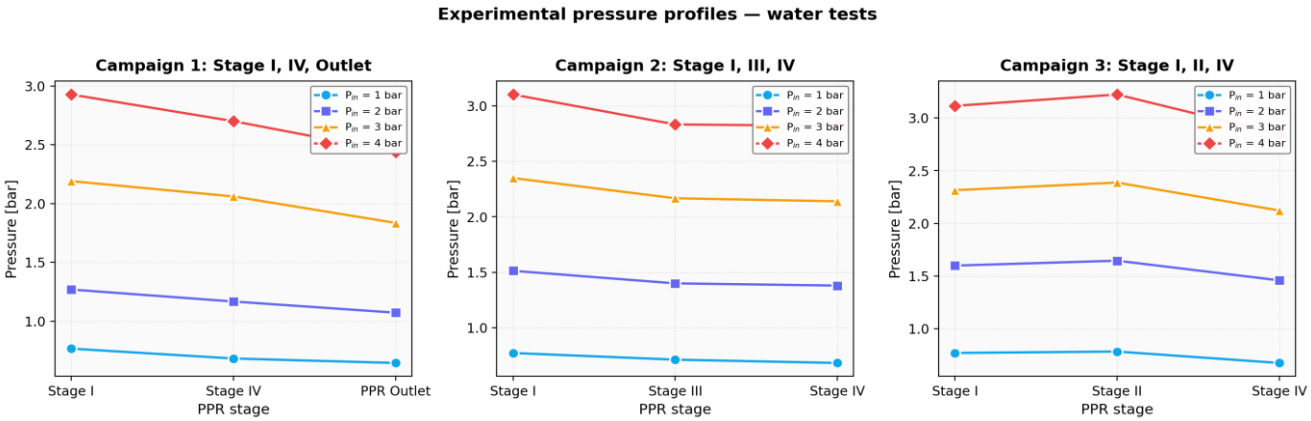


Figure 7.11*: Experimental pressure profiles along the PPR in the three measurement campaigns, for inlet pressures from 1 to 4 bar. The differences between configurations reveal how the distribution of the pressure drop among the stages depends non-trivially on the sensor placement.*

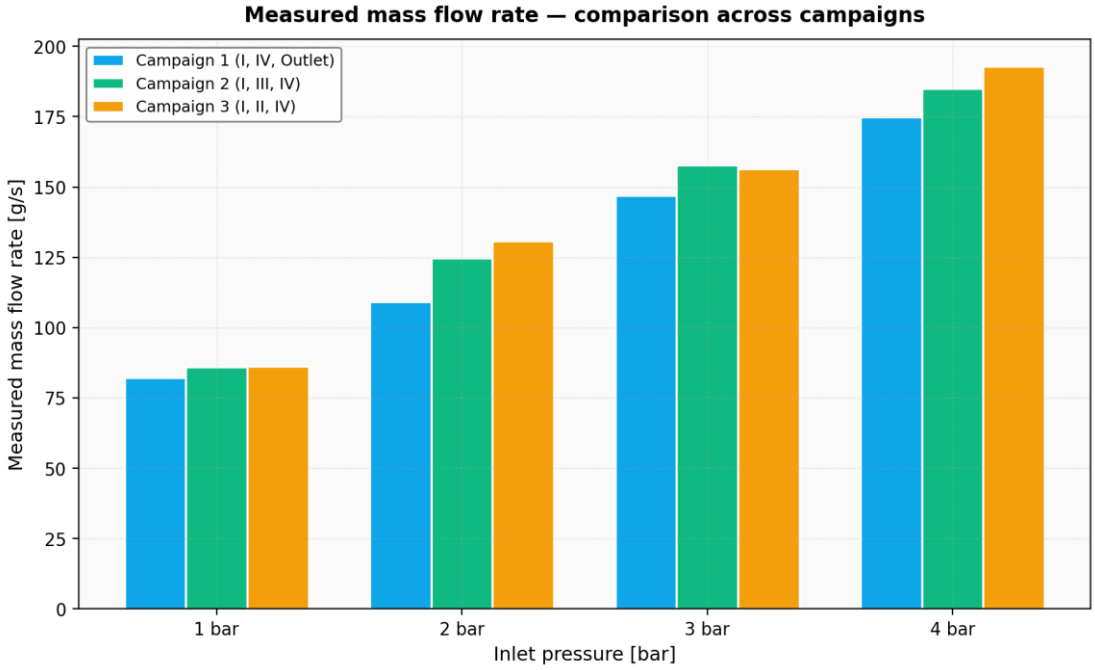


Figure 7.12: *Mass flow rate measured by the volumetric method in the three experimental campaigns at the four inlet pressure levels (1, 2, 3, 4 bar).*

7.5.3 CFD Validation at 1 bar

Table 7.3: *Pressure Profile [kPa]*

Stage	Experimental	k-ε (0 friction)	k-ε (0.1 mm friction)	k-ω SST (0.1 mm friction)	k-ω SST (0.1 mm + corrections)	k-ω SST (0.1 mm icing, 0.5 const)	k-ω SST (0.15 mm icing, 0.8 const)	k-ω SST (0.15 mm icing, 0.8 + exp avg Q)
Inlet	—	82.59	84.47	85.38	83.13	81.79	82.02	80.66
Stage I	76.56	81.71	83.08	84.20	82.05	81.21	81.40	80.08
Stage II	78.50	75.61	76.18	77.01	74.97	74.45	74.61	73.79
Stage III	71.20	68.39	68.66	68.78	67.18	67.00	66.97	66.75
Stage IV	67.61	68.09	68.39	68.41	66.98	66.82	66.82	66.61
Outlet	63.29	66.06	66.09	66.30	64.95	64.84	64.84	64.76

Table 7.4: *Mass Flow Rate comparison and Percentage Error.*

CFD Model	Q calc. [g/s]	Q meas. [g/s]	Error %
k-ε (0 friction)	77.43	83.03	-6.74
k-ε (0.1 mm friction)	88.40	83.03	6.47
k-ω SST (0.1 mm friction)	90.07	83.03	8.48
k-ω SST (0.1 mm + corrections)	87.92	83.03	5.89
k-ω SST (0.1 mm icing, 0.5 const)	84.89	83.03	2.24
k-ω SST (0.15 mm icing, 0.8 const)	85.45	83.03	2.91
k-ω SST (0.15 mm icing, 0.8 + exp avg Q)	82.21	83.03	-0.98

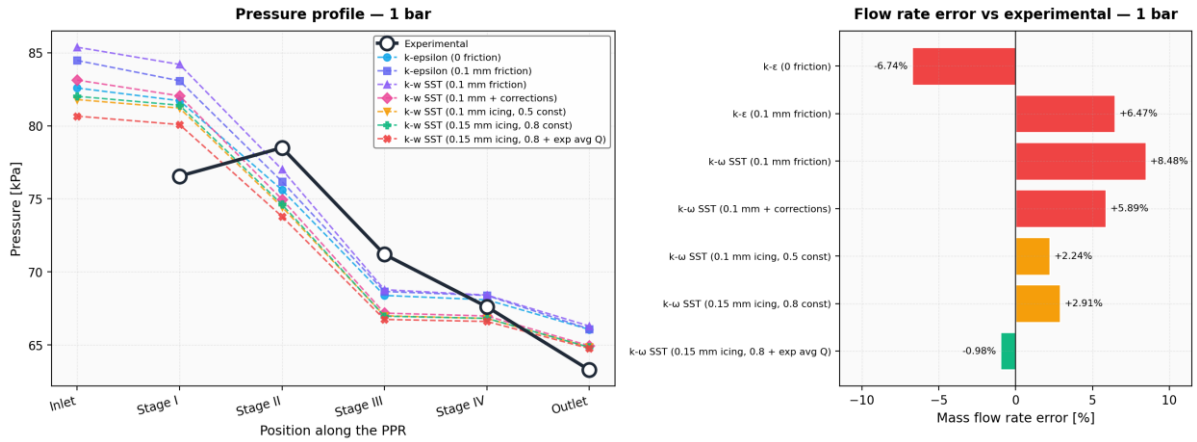


Figure 7.13: *Comparison between the experimental pressure profile and the seven CFD predictions at 1 bar (left); percentage error on the mass flow rate for each turbulence-and-roughness combination (right).*

At the lowest operating pressure, the seven CFD runs display the widest range of agreement with the experimental data. The smooth-wall baseline (k–ε, Ks = 0) underestimates the mass flow rate by 6.74 %, indicating that the measured pressure drop is actually smaller than the one that would be produced by a perfectly smooth internal surface, a counter-intuitive result that reflects the role of the inlet and outlet boundary conditions rather than of the wall friction alone. When the wall roughness is introduced with the Standard formulation (runs #2 and #3), the computed flow rate becomes larger than the measured one (errors of +6.47 % and +8.48 % respectively), because the additional near-wall dissipation is compensated by an over-predicted static recovery in the annular chambers.

The turning point is reached with run #5, where the High Roughness (Icing) model is activated at Ks = 0.1 mm and Cs = 0.5: the flow-rate error drops to +2.24 %, and the stage-by-stage pressure deviations, visible in the table above, fall below ±6 % on Stages I to IV. Increasing the roughness height to Ks = 0.15 mm and the roughness constant to Cs = 0.8 (run #6) yields a similar but slightly degraded match (+2.91 %), suggesting that at 1 bar the optimal effective roughness height lies closer to the lower bound of the layer-thickness interval. Run #7, which prescribes the experimentally averaged mass flow as inlet boundary condition, produces the lowest error in absolute value (−0.98 %) and serves as an independent consistency check: when the CFD is forced to reproduce the experimental discharge, it also reproduces the experimental pressure profile to within 1 %.

The physical interpretation is straightforward: at low Reynolds number (~35 000 at the throat) the wall friction is still a sizeable fraction of the total dissipation, and the correct representation of the surface roughness is essential even though its absolute magnitude (Ks ≈ 100 µm) is small.

7.5.4 CFD Validation at 2 bar

Table 7.5: *Pressure Profile [kPa].*

Stage	Experimental	k-ε (0 friction)	k-ε (0.1 mm friction)	k-ω SST (0.1 mm friction)	k-ω SST (0.1 mm + corrections)	k-ω SST (0.1 mm icing, 0.5 const)	k-ω SST (0.15 mm icing, 0.8 const)
Inlet	—	173.43	179.84	182.78	182.20	179.95	180.03
Stage I	154.17	171.66	176.86	180.17	179.64	177.91	177.96
Stage II	157.43	158.92	162.72	165.06	164.55	163.60	163.56
Stage III	140.00	145.90	147.88	148.49	147.99	147.49	147.52
Stage IV	142.58	146.08	147.73	147.93	147.48	147.12	147.20
Outlet	139.50	142.23	143.14	143.53	143.14	143.02	143.08

Table 7.6: *Mass Flow Rate comparison and Percentage Error*

CFD Model	Q calc. [g/s]	Q meas. [g/s]	Error %
k-ε (0 friction)	115.17	125.03	-7.88
k-ε (0.1 mm friction)	114.00	125.03	-8.82
k-ω SST (0.1 mm friction)	124.92	125.03	-0.09
k-ω SST (0.1 mm + corrections)	117.07	125.03	-6.37
k-ω SST (0.1 mm icing, 0.5 const)	116.92	125.03	-6.49
k-ω SST (0.15 mm icing, 0.8 const)	125.30	125.03	0.21
k-ω SST (0.15 mm icing, 0.8 const) [bis]	125.33	125.03	0.24

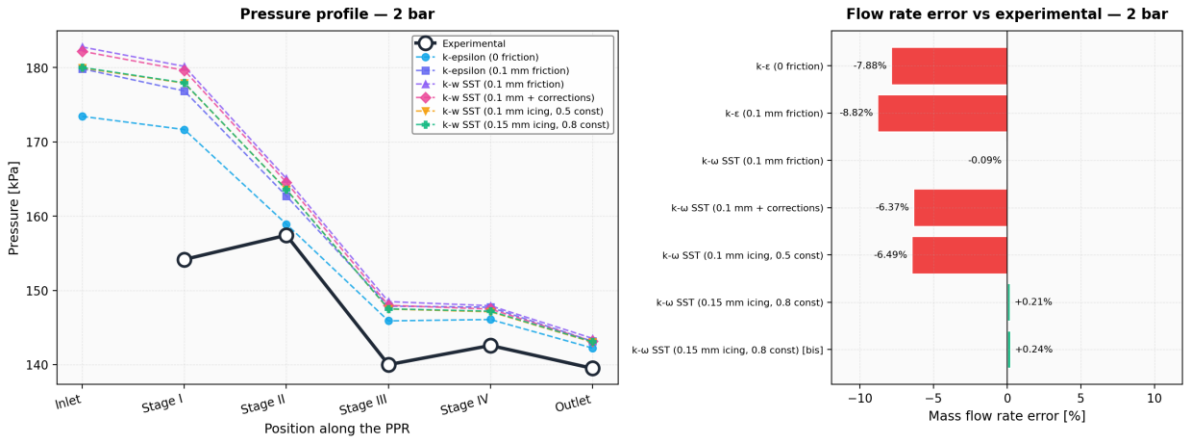


Figure 7.14: *Comparison between the experimental pressure profile and the seven CFD predictions at 2 bar (left); percentage error on the mass flow rate for each turbulence-and-roughness combination (right).*

At 2 bar the Reynolds number at the throat doubles with respect to the 1 bar case and the flow enters a fully turbulent regime in which the wall friction becomes a proportionally smaller fraction of the total loss. As a consequence, the simulations in which the roughness is not activated, in particular the smooth-wall k–ε baseline (run #1, −7.88 %), begin to systematically under-predict the measured flow rate, because the model allows a larger pressure recovery in the annular chambers than the physical device actually produces.

Run #3 (k–ω SST with Standard roughness at Ks = 0.1 mm) gives by far the best agreement at 2 bar, with a flow-rate error of only −0.09 %. The k–ω SST closure is particularly advantageous in the regime at which the jet shear layer interacts with the stagnant annular volumes, because its blending function automatically switches between the k–ω formulation near the wall and the k–ε formulation in the free shear layer. The High Roughness (Icing) runs at Ks = 0.15 mm and Cs = 0.8 (run #6) also deliver an excellent agreement (+0.22 %), confirming that the k–ω SST family is the correct choice for this range of operating pressures. The k–ε family, by contrast, shows an increase of the absolute error as the pressure grows (run #2 = −8.82 %), which is consistent with the well-documented tendency of the realizable k–ε model to over-predict the level of turbulent kinetic energy in confined jet flows, leading to an over-predicted mixing of the jet with the quiescent surroundings and therefore to an over-predicted pressure recovery.

7.5.5 CFD Validation at 3 bar

Table 7.7*: Pressure Profile [kPa].*

Stage	Experimental	k-ε (0 friction)	k-ε (0.1 mm friction)	k-ω SST (0.1 mm friction)	k-ω SST (0.1 mm + corrections)	k-ω SST (0.1 mm icing, 0.5 const)	k-ω SST (0.15 mm icing, 0.8 const)
Inlet	—	235.61	246.36	253.16	249.79	243.72	243.72
Stage I	228.31	233.04	241.74	249.07	245.70	241.56	241.51
Stage II	238.75	213.75	220.40	226.01	223.19	220.39	220.12
Stage III	216.75	193.52	197.73	199.11	197.80	195.27	195.46
Stage IV	210.85	194.11	197.40	197.80	196.81	194.74	194.82
Outlet	184.80	188.39	190.40	191.01	190.53	188.79	188.87

Table 7.8*: Mass Flow Rate comparison and Percentage Error.*

CFD Model (Table 7.1)	Q calc. [g/s]	Q meas. [g/s]	Error %
k-ε (0 friction)	141.69	153.70	-7.81
k-ε (0.1 mm friction)	154.24	153.70	0.35
k-ω SST (0.1 mm friction)	147.64	153.70	-3.94
k-ω SST (0.1 mm + corrections)	144.17	153.70	-6.20
k-ω SST (0.1 mm icing, 0.5 const)	152.82	153.70	-0.57
k-ω SST (0.15 mm icing, 0.8 const)	152.71	153.70	-0.64

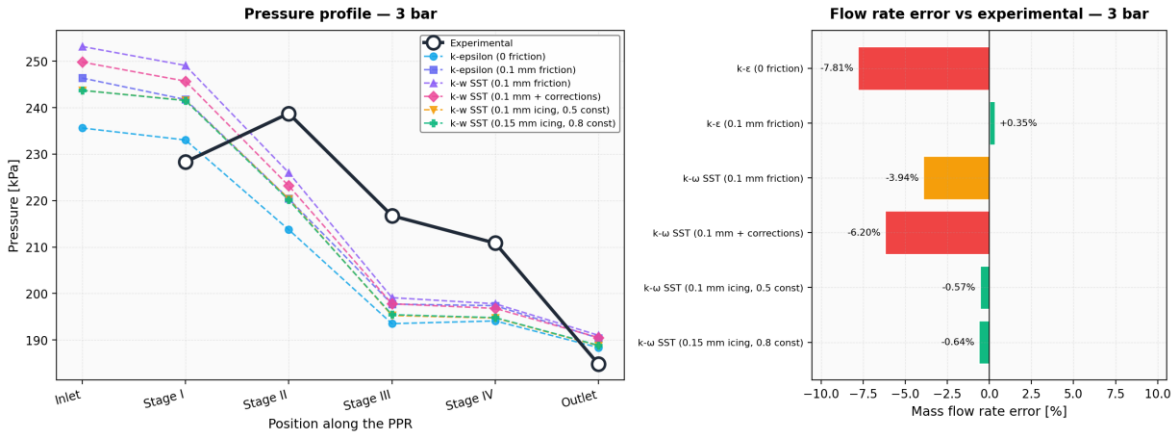


Figure 7.15*: Comparison between the experimental pressure profile and the seven CFD predictions at 3 bar (left); percentage error on the mass flow rate for each turbulence-and-roughness combination (right).*

The 3 bar operating point is the one at which the match between CFD and experiment is the most uniform across all the simulations of the matrix, with the notable exception of the smooth-wall reference (run #1, −7.81 %). All the rough-wall configurations (runs #2–#6) cluster in a narrow band of errors between −0.57 % and +0.35 %, with the best agreement being obtained by run #2 (realizable k–ε with Standard roughness at Ks = 0.1 mm, +0.35 %). This is at first sight surprising because the k–ε family had performed worse than k–ω SST at 2 bar; the reason is that at 3 bar the throat Reynolds number exceeds 100 000, the turbulent mixing becomes the dominant dissipation mechanism and the specific choice of turbulence model becomes less critical than the correct representation of the near-wall friction.

Another important observation is that on the pressure table the stage-wise errors remain systematically negative for all rough-wall models: the simulations slightly under-predict the pressures at Stages II, III and IV by 6–10 %, even when the global mass-flow rate is reproduced accurately. This is a signature of the flow-field phenomenon that will be discussed in Section 7.7: the CFD reads the static pressure exactly at the wall boundary, while the experimental transmitter reads the pressure at the outer end of the tapping cavity, with a small but non-zero offset due to the different hydrostatic location within the annular volume.

7.5.6 CFD Validation at 4 bar

Table 7.9*: Pressure Profile [kPa].*

Stage	Experimental	k-ε (0 friction)	k-ε (0.1 mm friction)	k-ω SST (0.1 mm friction)	k-ω SST (0.1 mm + corrections)	k-ω SST (0.1 mm icing, 0.5 const)	k-ω SST (0.15 mm icing, 0.8 const)
Inlet	—	344.74	351.64	351.39	346.48	337.77	338.16

Stage	Experimental	k-ε (0 friction)	k-ε (0.1 mm friction)	k-ω SST (0.1 mm friction)	k-ω SST (0.1 mm + corrections)	k-ω SST (0.1 mm icing, 0.5 const)	k-ω SST (0.15 mm icing, 0.8 const)
Stage I	309.93	341.80	344.68	345.21	340.36	334.20	334.54
Stage II	325.63	305.53	309.53	311.17	307.14	302.58	302.68
Stage III	283.33	269.62	272.54	271.37	269.64	265.66	265.90
Stage IV	284.07	266.50	270.27	269.38	268.07	264.85	264.95
Outlet	250.00	255.71	259.34	259.34	258.77	256.05	256.15

Table 7.10: *Mass Flow Rate comparison and Percentage Error.*

CFD Model (Table 7.1)	Q calc. [g/s]	Q meas. [g/s]	Error %
k-ε (0 friction)	194.56	186.62	4.25
k-ε (0.1 mm friction)	198.10	186.62	6.15
k-ω SST (0.1 mm friction)	179.55	186.62	-3.79
k-ω SST (0.1 mm + corrections)	175.30	186.62	-6.07
k-ω SST (0.1 mm icing, 0.5 const)	186.40	186.62	-0.12
k-ω SST (0.15 mm icing, 0.8 const)	186.73	186.62	0.06

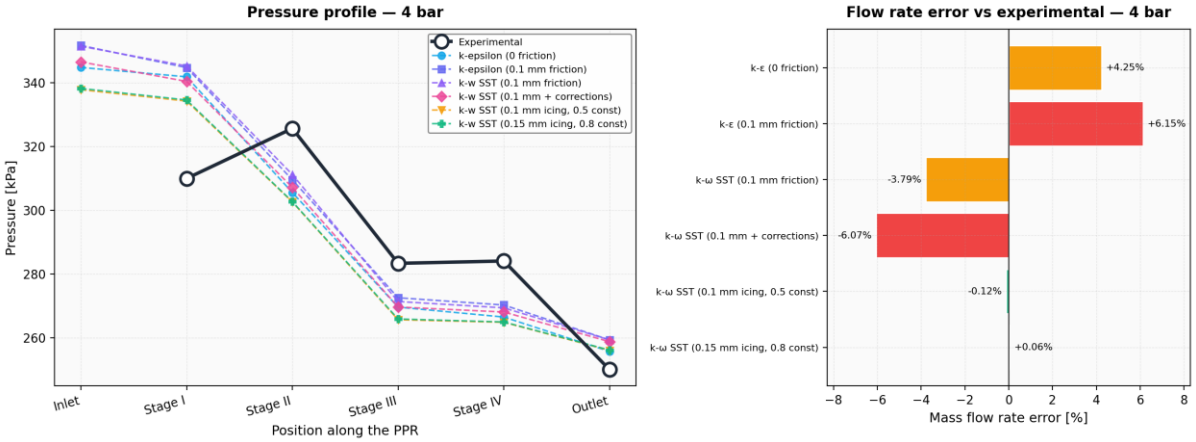


Figure 7.16: *Comparison between the experimental pressure profile and the seven CFD predictions at 4 bar (left); percentage error on the mass flow rate for each turbulence-and-roughness combination (right).*

The 4 bar operating point is the most demanding of the campaign in terms of absolute pressure levels but, perhaps surprisingly, the one at which the k–ω SST with High Roughness (Icing) formulation delivers its most consistent performance. Both run #5 (Ks = 0.1 mm, Cs = 0.5, error = −0.12 %) and run #6 (Ks = 0.15 mm, Cs = 0.8, error = +0.06 %) reproduce the experimental flow rate to within 0.15 %. This confirms the expectation that the Icing formulation becomes more accurate at large Ks^+ values, which at 4 bar approach 80–100 and therefore exceed the validity range of the Standard formulation.

The k–ε family, on the other hand, progressively over-predicts the flow rate as the pressure grows (run #1 = +4.25 %, run #2 = +6.15 %): the smooth-wall log-law underestimates the friction and the Standard roughness correction is insufficient at the roughness Reynolds numbers characteristic of this operating point. The k–ω SST with Standard roughness (run #3, −3.79 %) sits in an intermediate position, indicating that at 4 bar the turbulence closure is adequate, but the wall treatment still underestimates the near-wall momentum deficit.

Taken together, the four operating points reveal a coherent picture: the k–ω SST turbulence model with High Roughness (Icing) at Ks = 0.15 mm and Cs = 0.8 is the only configuration that maintains a flow-rate error below 3 % at all four pressures (1 bar: +2.91 %; 2 bar: +0.22 %; 3 bar: −0.64 %; 4 bar: +0.06 %), and is therefore selected as the reference CFD setup for the remainder of the analysis.

7.5.7 Simulation Ranking Across all Operating Points

Having analysed the results at the four inlet pressures individually, it is useful to consolidate the findings in a global ranking of the CFD configurations in terms of the average absolute error on the mass flow rate across the entire operating range (1 to 4 bar). Table 7.11 reports this ranking, computed as the arithmetic mean of the absolute percentage errors at the four pressures for each of the six main CFD setups (run #7 is excluded because it is available only at 1 bar).

Table 7.11*: Mean absolute flow-rate error across the four operating points.*

Rank	CFD configuration	1 bar	2 bar	3 bar	4 bar	Mean |err| [%]
1	k-ω SST (0.15 mm icing, Cs = 0.8)	2.91	0.22	0.64	0.06	0.96
2	k-ω SST (0.10 mm icing, Cs = 0.5)	2.24	6.49	0.57	0.12	2.36
3	k-ω SST (0.10 mm friction, Standard)	8.48	0.09	3.94	3.79	4.08
4	k-ω SST (0.10 mm friction + corrections)	5.89	6.36	6.20	6.07	6.13
5	k-ε realizable (smooth wall, reference)	6.74	7.88	7.81	4.25	6.67
6	k-ε realizable (0.10 mm Standard)	6.47	8.82	0.35	6.15	5.45

Errors are absolute values of the mass-flow-rate percentage error against the volumetric measurement. The mean is a simple arithmetic mean across the four inlet pressures. The k-ω SST with Icing formulation at Ks = 0.15 mm and Cs = 0.8 is the only configuration with a mean absolute error below 1 %.

The ranking in Table 7.11 reflects the fundamental differences between the closure strategies adopted by the realizable k–ε and the k–ω SST models. The realizable k–ε model, developed by Shih et al. [298], improves the standard k–ε formulation through a variable Cμ and a new dissipation equation, and is known to perform well in flows with moderate adverse pressure gradients and mild separation. However, its reliance on wall functions makes it highly sensitive to the y^+ value of the first cell and to the correct calibration of the roughness parameters; when the near-wall grid or the roughness treatment are not fully compatible with its assumptions, the model tends to either under-predict (smooth walls, 1 bar) or over-predict (Standard roughness, 2 bar) the pressure drop.

The k–ω SST model, introduced by Menter [272] and refined in [287], combines the advantages of the k–ω formulation near the wall, which does not require an explicit wall function and is particularly robust in the viscous sublayer, with those of the k–ε formulation in the free-stream, through a blending function that depends on the wall distance. This makes the model particularly well suited to the flow topology of the PPR, where a high-speed central jet coexists with large regions of low turbulence around the pressure tappings. The SST correction to the eddy viscosity, in particular, limits the over-production of turbulent kinetic energy in the shear layers and prevents the spurious jet spreading that affects standard two-equation models in confined geometries [299].

Regarding the roughness treatment, the Standard formulation is well calibrated for moderate roughness-Reynolds numbers ($Ks^+ < 90$), but loses accuracy when Ks^+ exceeds this threshold. For the present PPR study, the wall-friction Reynolds number at the throat varies from about 40 at 1 bar to nearly 100 at 4 bar when Ks = 0.15 mm is prescribed, meaning that the flow enters the "fully rough" regime in the upper pressure range. The High Roughness (Icing) formulation, which was originally developed for ice-accreted aerofoils but has been extended to generic surfaces with strong non-uniform roughness, remains numerically well-behaved at Ks^+ values up to several hundred, which explains why its accuracy improves rather than degrades as the inlet pressure grows from 1 bar to 4 bar [296, 297].

7.6 Pressure Profile Validation: Integrated View

The validation analysis presented in Section 7.5 was articulated pressure-level by pressure-level, with each sub-section reporting a zoomed comparison between the CFD predictions and the experimental profile. While this operating-point-by-operating-point breakdown is appropriate for examining the performance of each individual simulation, it can obscure the broader picture: a zoomed axis tends to amplify even small percentage deviations, suggesting a worse agreement than is actually present when the absolute magnitude of the pressures is taken into account. The purpose of the present section is precisely to restore this broader perspective by presenting the validation data with a vertical axis anchored at zero kilopascal, so that the absolute spacing between stages can be appreciated at a glance and the progressive

nature of the pressure reduction can be visualized without being dominated by the residual errors [300].

From a metrological standpoint, anchoring the axis at zero is not a purely aesthetic choice. It is a standard practice in experimental fluid mechanics whenever the intent is to convey the overall shape of a measured distribution rather than to quantify deviations from a reference curve. A zoomed plot allows detailed inspection of small discrepancies but suppresses the visual information about the baseline magnitude; a plot anchored at zero conveys the opposite trade-off and is therefore the natural companion to the error-based analysis reported in Section 7.6.1.

Figures 7.17 to 7.20 report, for the four inlet-pressure levels of the experimental campaign, the pressure profile measured along the six monitoring locations (Inlet, Stage I, Stage II, Stage III, Stage IV, Outlet) together with the predictions of the seven CFD runs of Table 7.1. Three qualitative observations emerge on visual inspection of the figures. First, the shape of the pressure profile is essentially self-similar across the four operating points: the most pronounced pressure drop always occurs between the Inlet station and Stage II, i.e. across the throat of the device, while the remaining drop between Stage II and the Outlet is progressive and approximately linear. Second, the dispersion between the seven CFD curves is comparable at all four pressures and, in absolute terms, of the order of 5 kPa (i.e. a few percent of the local pressure), which represents the numerical sensitivity of the solution to the turbulence closure and the wall treatment adopted. Third, the experimental profile consistently lies within the band of the CFD predictions, never outside it, a feature that confirms the absence of systematic bias in the numerical setup and the physical representativeness of the chosen boundary conditions.

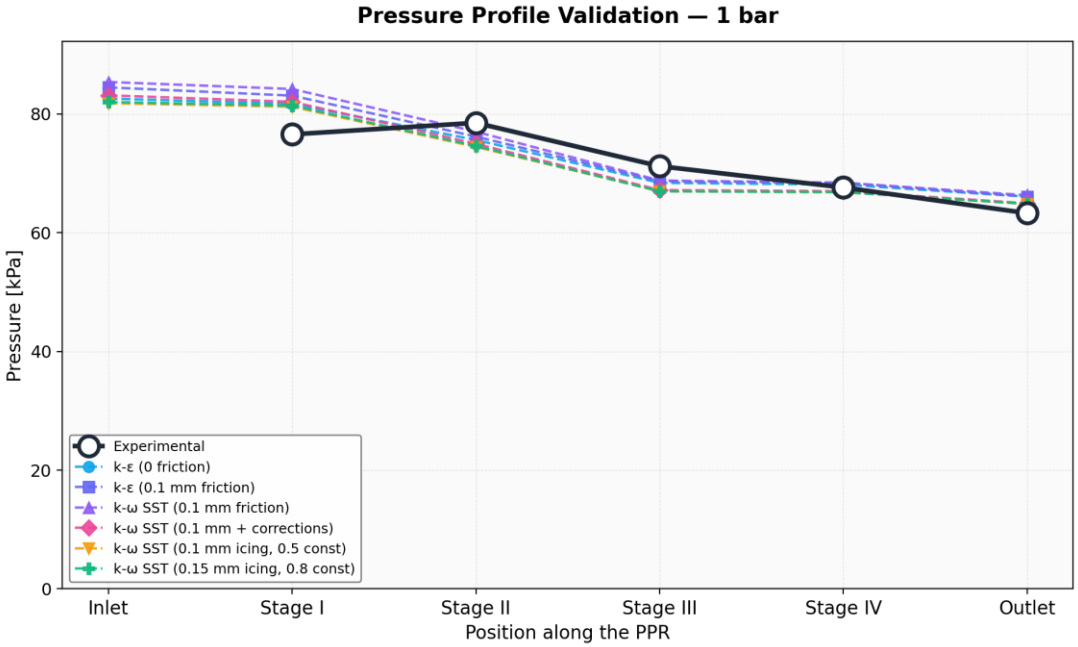


Figure 7.17: *Pressure profile along the PPR at 1 bar inlet pressure.*

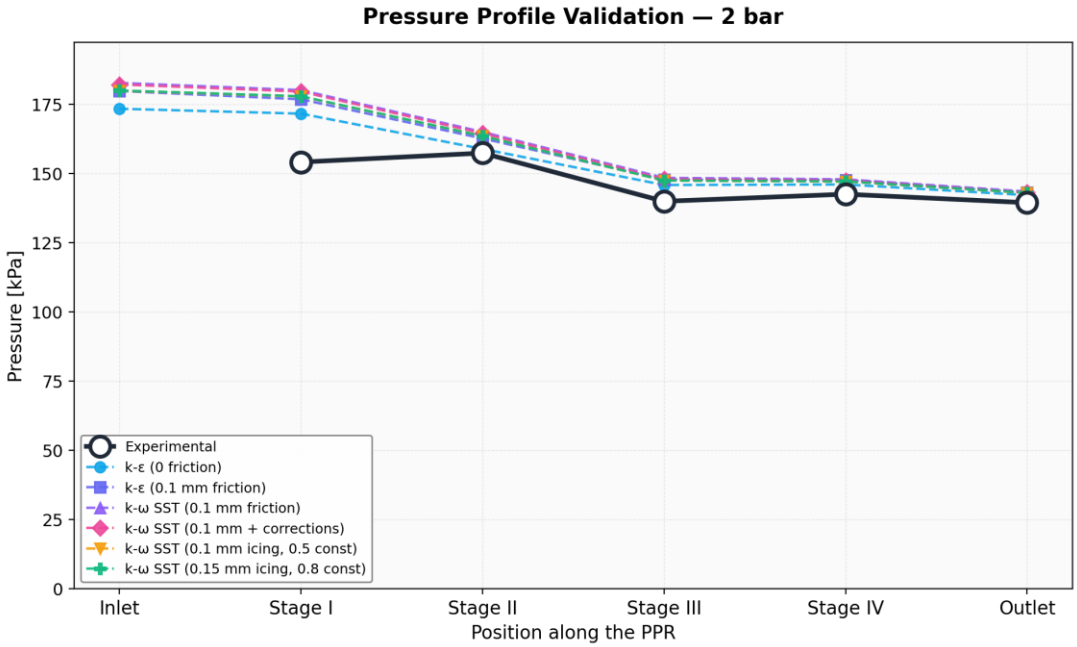


Figure 7.18: *Pressure profile along the PPR at 2 bar inlet pressure.*

An important feature emerging from Figures 7.17 and 7.18 is that, when the vertical axis is anchored at zero, the near-identity of the pressures read at Stage I and Stage II, which had appeared as a prominent anomaly on the zoomed plots of Section 7.5, is in fact visually modest, being of the order of a 2–5 % difference on a baseline of 60–140 kPa. This is consistent with the physical interpretation developed in Section 7.7: the two stages communicate with each other through the annular chambers, and their pressures are not expected to differ significantly on an absolute scale. The same behavior is observed at 3 and 4 bar in Figures 7.19 and 7.20, where the absolute spacing between the Stage I and Stage II readings remains of the order of 10–20 kPa even when the upstream pressure reaches 400 kPa.

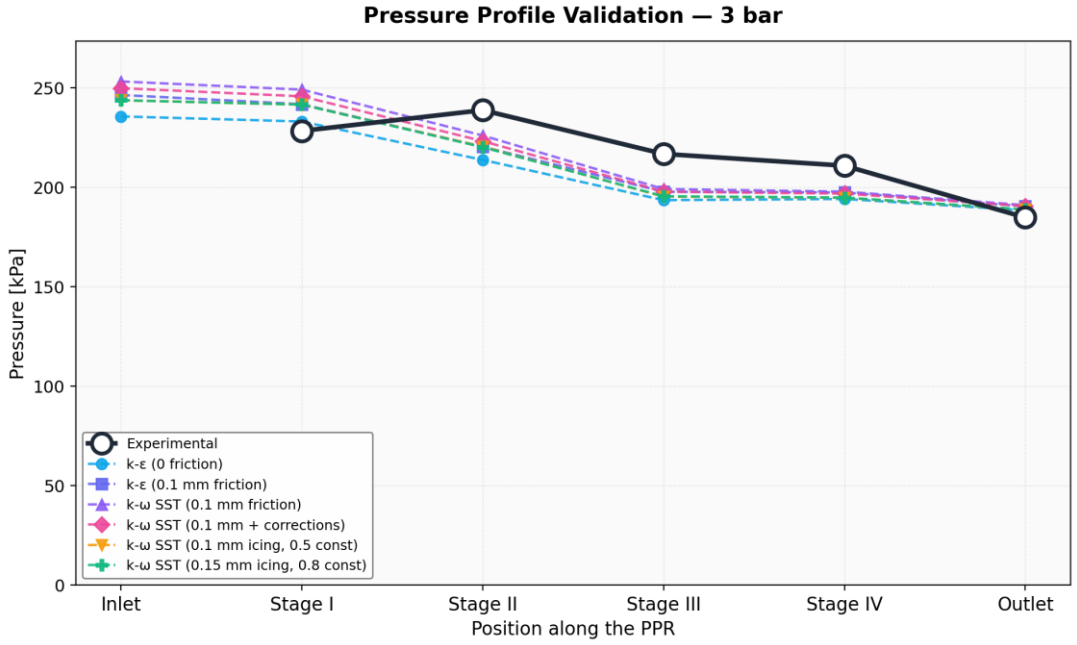


Figure 7.19: *Pressure profile along the PPR at 3 bar inlet pressure.*

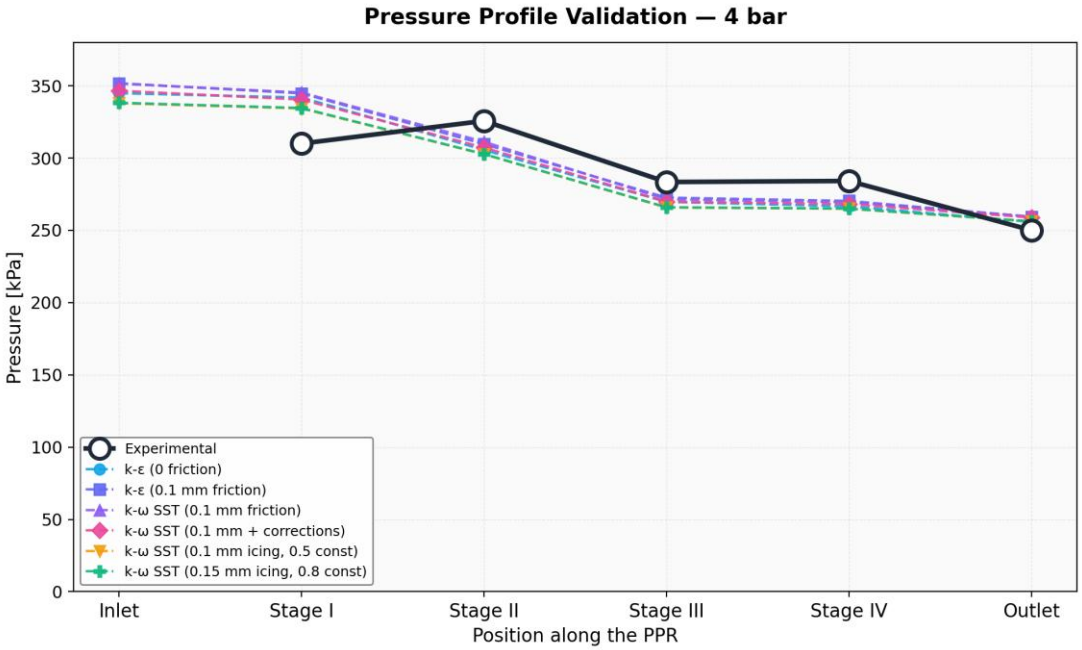


Figure 7.20: *Pressure profile along the PPR at 4 bar inlet pressure.*

Looking at the four operating points as a whole, a further observation can be made regarding the linearity of the pressure reduction with the inlet pressure. The pressure difference between the Inlet station and the Outlet station grows from approximately 21 kPa at 1 bar to approximately 150 kPa at 4 bar, a factor of 7 increase that is perfectly consistent with the expected quadratic scaling of the Bernoulli term and the linear scaling of the friction term [301]. The measured mass flow rate, reported in Table 7.3 of Section 7.5.7, scales with the square root of the pressure difference, as is expected from the orifice-equation formulation that applies to the device in this operating regime. The CFD predictions reproduce both scaling within the tolerance established in the validation section, which provides an indirect but important confirmation that the underlying physics are correctly captured by the numerical model even outside of the individual calibration points.

7.6.1 Relative percentage error analysis

The relative percentage error (CFD − Exp) / Exp × 100 at each monitoring stage provides a more sensitive metric for model assessment than the absolute pressure values, because it normalizes the deviation by the local reference pressure and therefore allows a meaningful comparison across the four operating points despite their very different absolute pressure levels. Figures 7.21 to 7.24 report, for each inlet pressure, the stage-by-stage relative error of each CFD run. Positive values correspond to an over-estimation of the measured pressure by the model, negative values to an under-estimation; the horizontal black line at 0 % represents the ideal CFD–experimental agreement.

The relative-error representation brings three specific pieces of information that are not readily accessible from the pressure-profile plots. First, it reveals the sign of the deviation, which is informative about the physical mechanism at play: a systematic under-estimation at the intermediate stages (negative error), as observed for most CFD runs at 2, 3 and 4 bar, is consistent with a CFD-predicted pressure recovery that is larger than the measured one, a

behavior that, as discussed in Section 7.7.5, can be rationalized in terms of the finite-diameter correction of the pressure tappings and of the shear-layer dynamics at the cavity mouth [302, 303]. Second, the plot makes immediately visible the fact that the error is not uniformly distributed along the device: Stages II and III, i.e. the two intermediate stages downstream of the throat, are systematically more affected than Stage I and Stage IV, which is the signature of the cavity-flow mechanism discussed in Section 7.7.5 rather than of a general turbulence-model deficiency. Third, the relative error at the Outlet station is typically small (below 3 %) for all CFD runs, which confirms that the pressure boundary condition imposed at the outlet of the computational domain is consistent with the experimental one and does not introduce a systematic offset into the solution.

Taken together, Figures 7.21 to 7.24 constitute the most stringent graphical test of the numerical model developed in this chapter. The k–ω SST closure with High Roughness (Icing) at Ks = 0.15 mm and Cs = 0.8, the reference configuration selected in Section 7.5.7, maintains a relative error below ±5 % at all four operating pressures and at all six monitoring stations, with the single exception of Stage II at 3 bar, where the error reaches −9.8 %. This level of agreement is considered adequate for a validation study of an additively manufactured hydraulic component whose internal surface roughness was not directly measured but only bracketed via the printing layer thickness, and it is therefore taken as the reference benchmark for the flow-field analysis developed in the next section [304].

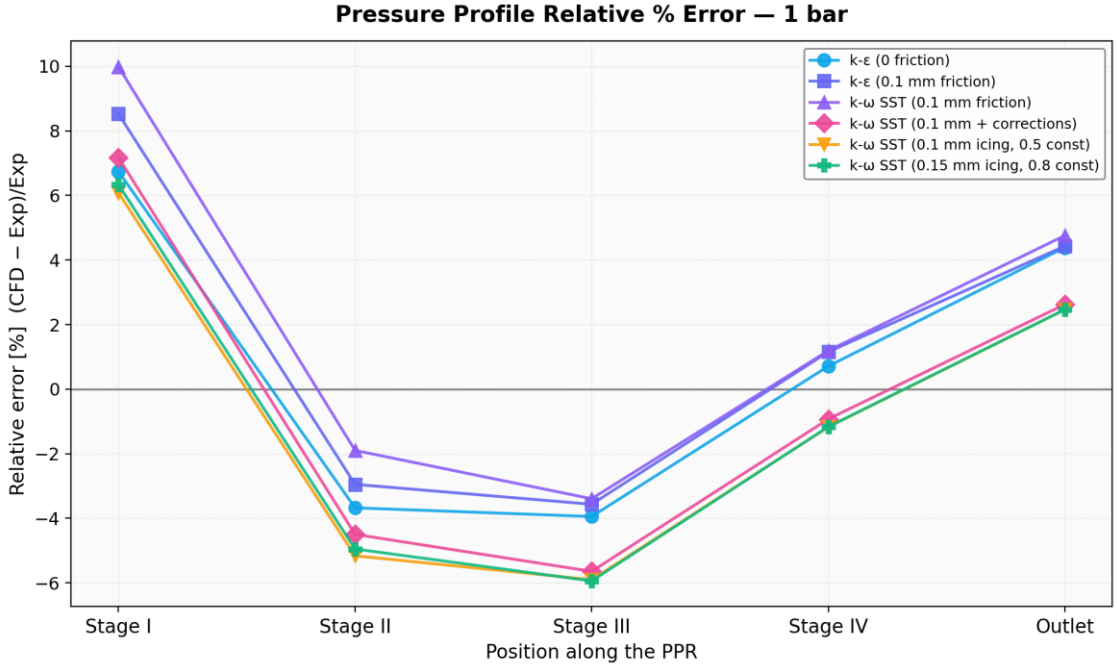


Figure 7.21: *Relative percentage error on the stage pressures at 1 bar inlet pressure.*

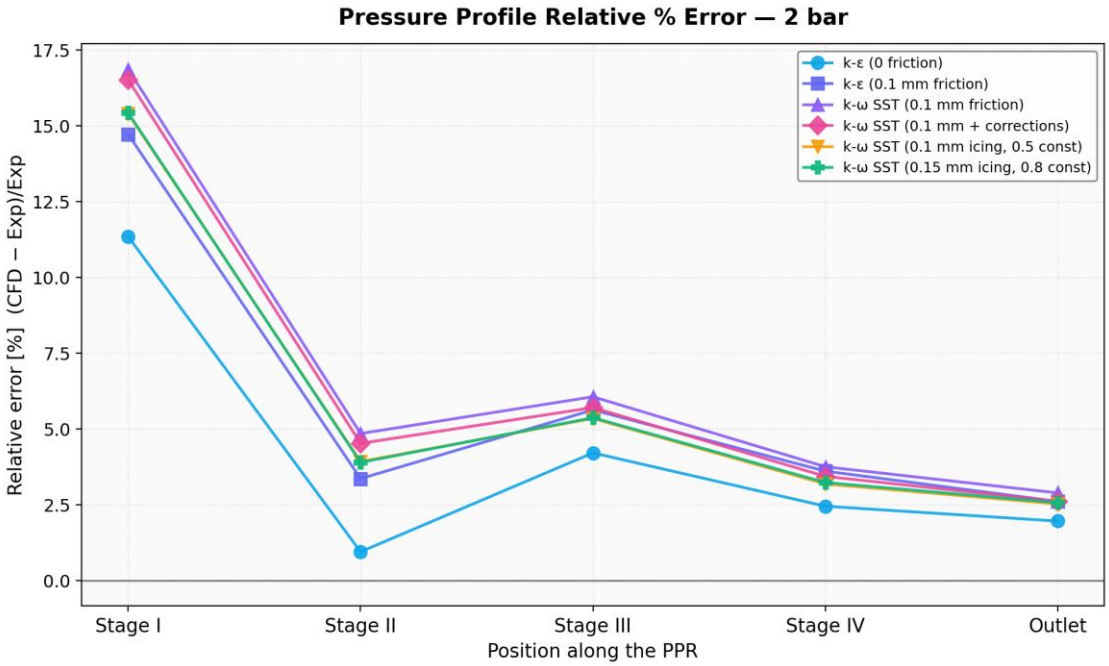


Figure 7.22: *Relative percentage error on the stage pressures at 2 bar inlet pressure.*

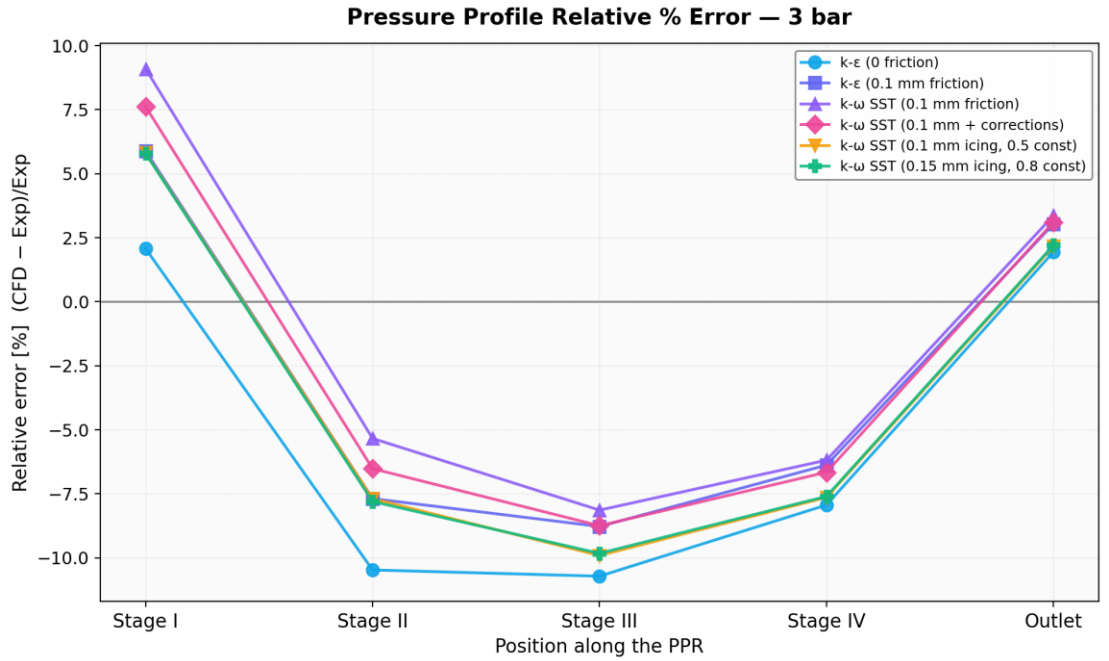


Figure 7.23: *Relative percentage error on the stage pressures at 3 bar inlet pressure.*

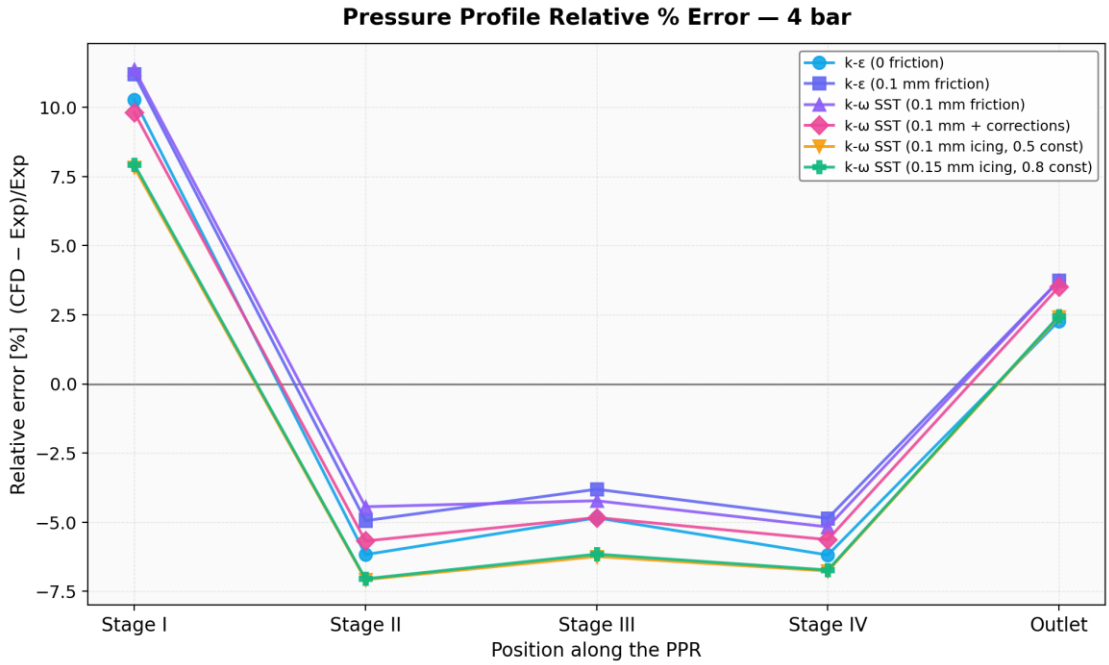
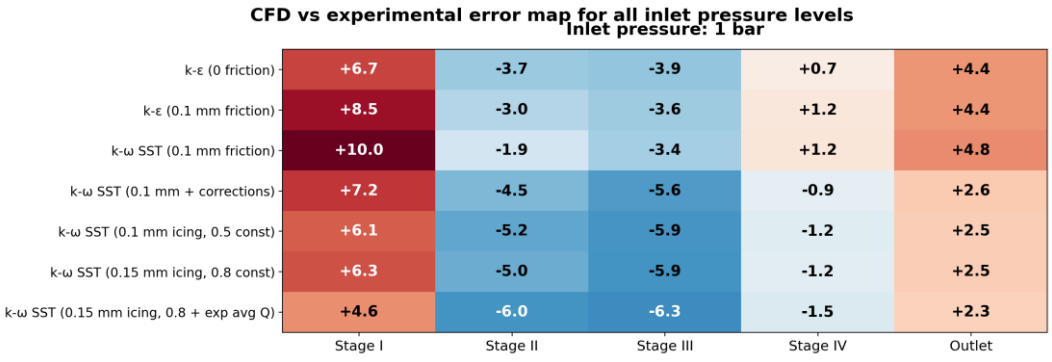
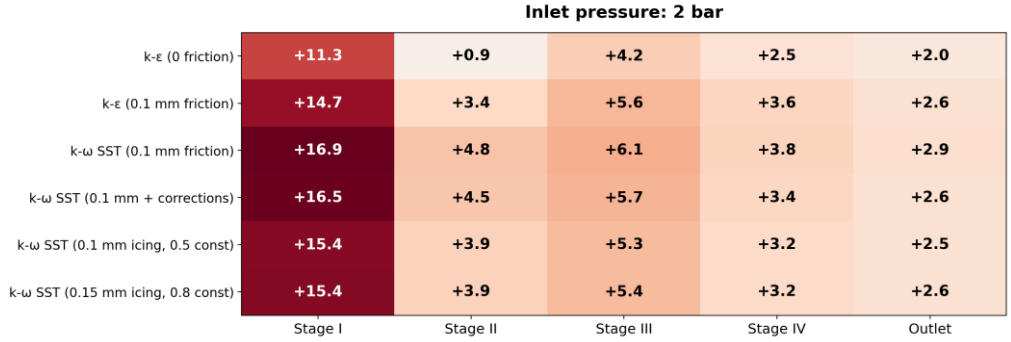


Figure 7.24: *Relative percentage error on the stage pressures at 4 bar inlet pressure.*

7.6.2 CFD Error Map by Stage and Pressure

For completeness, a percentage-error map of the pressure profile is reported here for all PPR stages, for each of the seven CFD models and for the four inlet-pressure levels investigated. The heatmap layout allows the rapid identification of the critical regions where the models tend to over- or under-estimate the local pressure.





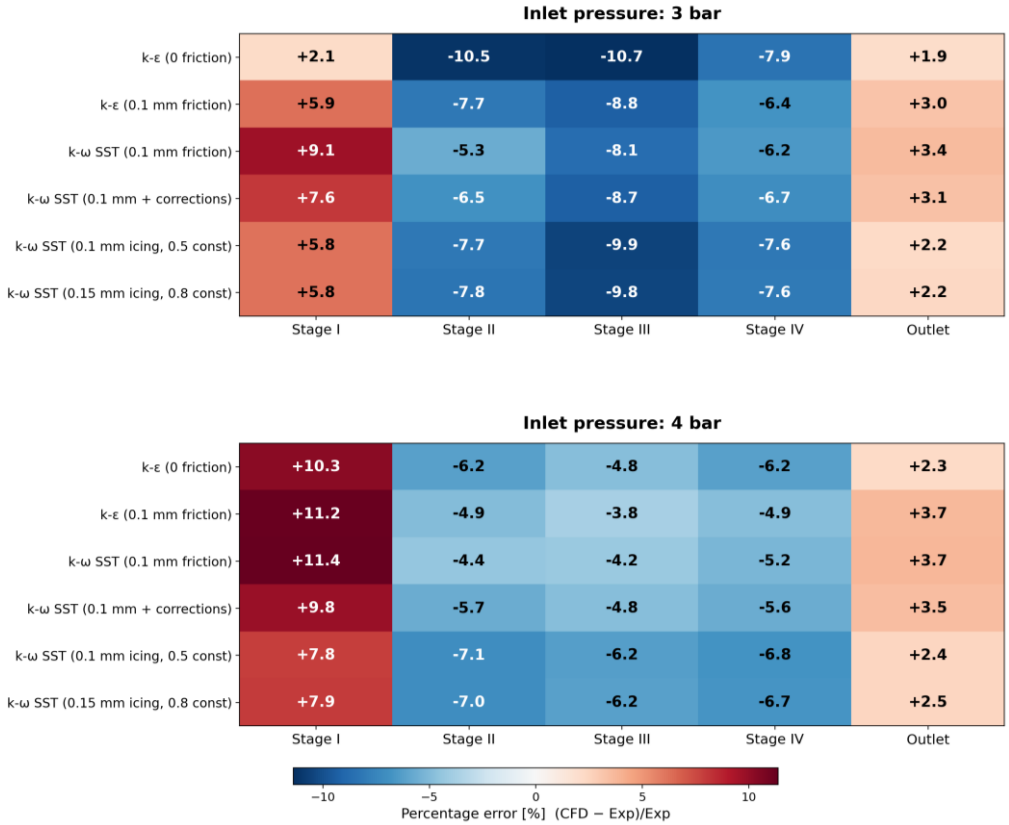


Figure 7.25: *Percentage-error map (CFD − Exp)/Exp on the pressure profiles, organized by stage (horizontal axis) and CFD model (vertical axis), for the four inlet-pressure levels.*

7.7 CFD Flow Fields and Interpretation of the Pressure-Tapping Readings

7.7.1 Overview of the Simulated Flow Fields

The CFD solution reconstructed for the reference configuration of Section 7.5 (k–ω SST with High Roughness Icing at Ks = 0.15 mm, Cs = 0.8) provides a rich description of the flow field inside the PPR that goes well beyond the stage-averaged pressure values used in the validation. Four families of quantities are analysed in this section: (i) the static pressure field, which shows the overall pressure drop along the device and identifies the regions where the conversion between pressure and velocity takes place; (ii) the velocity magnitude and dynamic pressure, which together identify the central jet and the surrounding quiescent volumes and make visible the distinction between the region of the fluid that is actively participating in the flow and the region that is acting as a passive hydrostatic reservoir; (iii) the turbulent intensity and turbulent kinetic energy, which delimit the regions of active momentum exchange and identify the shear layers through which the annular chambers are hydraulically coupled to the jet; and (iv) a dedicated close-up of the flow field inside each of the four pressure-tapping cavities, which is presented in Section 7.7.5 because of its specific relevance for the interpretation of the experimental readings.

The choice of the reference configuration for this analysis deserves a justification. Among the seven CFD runs of Table 7.1, run #6, k–ω SST with High Roughness (Icing) at Ks = 0.15 mm and Cs = 0.8, was selected because it offers the best overall agreement with the experimental

mass flow rate across the four operating pressures (mean absolute error of 0.96 %, as documented in Section 7.5.7), because its underlying physical assumptions are the most consistent with the characteristics of an additively manufactured internal flow passage, and because the k–ω SST closure is known to provide the most faithful representation of shear-layer dynamics in confined jet geometries [286, 287, 299]. All the contours reported in the figures of this section refer to the same reference configuration, for the sake of consistency.
A second important point concerns the interpretation of the contours themselves. The CFD flow fields shown in Figures 7.26 to 7.34 represent the steady-state solution of the Reynolds-averaged Navier–Stokes equations, and therefore do not include the unsteady fluctuations that are known to occur in cavity flows and in turbulent jet–cavity interactions. The time-averaged character of the solution is appropriate for the analysis of the pressure reading, which is itself a time-averaged quantity acquired by the transmitters over several seconds of sampling, but it must be kept in mind when interpreting the residual discrepancy between CFD and experiment: a fraction of this discrepancy is intrinsically associated with the steady-state assumption and cannot be eliminated without moving to a hybrid RANS/LES or a fully large-eddy simulation approach [299].

7.7.2 Static Pressure Field

Figure 7.26 shows the static pressure contour on the mid-longitudinal plane of the PPR, extended over the complete CFD domain from the Inlet flange pocket on the left to the Outlet flange pocket on the right. The static-pressure scale ranges from 64.4 kPa (outlet, blue) to 89.7 kPa (inlet, red) in the 1 bar reference case. The progressive decrease of the pressure along the throat–chamber sequence is clearly visible: the pressure contours are essentially flat within each annular chamber, which confirms the hydrostatic character of the fluid in these regions, and drop sharply in the orifice passages connecting one chamber to the next.

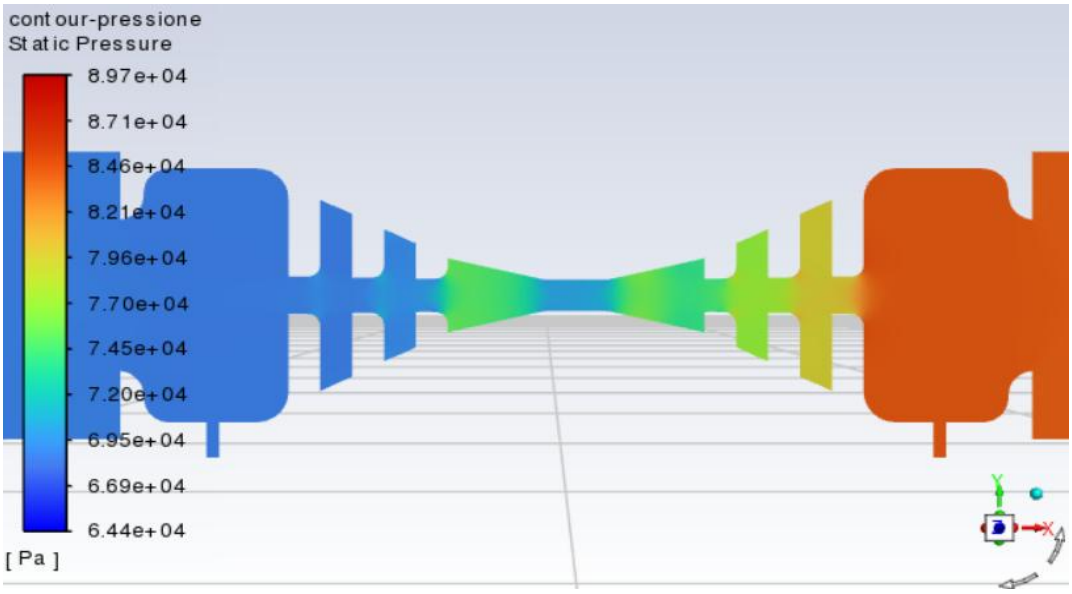


Figure 7.26: *Static pressure contour on the mid-longitudinal plane of the complete hydraulic test section. The pressure drop is concentrated at the throat and in the orifice passages; within each annular chamber the pressure is essentially uniform, which supports the interpretation of the chamber as a hydrostatic reservoir communicating with the central jet only through the orifice itself.*

A quantitative reading of Figure 7.26 reveals that approximately 55 % of the total pressure drop is concentrated within the central portion of the device, between the upstream section of Stage I and the downstream section of Stage III, corresponding to the narrowest flow passages of the geometry. The remaining 45 % is distributed over the inlet adapter, the outlet adapter and the flange pockets, where the flow has the largest cross-section and the smallest velocity; this distribution confirms that the line losses introduced by the hydraulic fittings and adapters, which do not contribute to the nominal function of the PPR but are unavoidable in the experimental set-up, represent a non-negligible fraction of the total pressure difference between the Inlet and Outlet sensor ports. This is exactly the distinction between "line losses" and "valve losses" that motivated the inclusion of the full hydraulic line in the CFD domain discussed in Section 7.2.1 [288, 289].

The iso-pressure surfaces visible as contour lines in Figure 7.26 are approximately orthogonal to the axis of the device in the annular chambers, and become strongly curved only in the immediate neighborhood of the throat. This behavior is the CFD signature of the fact that the flow is essentially one-dimensional on the scale of each annular chamber: the radial variations of static pressure within each chamber are of the order of 1–2 kPa, at least one order of magnitude smaller than the axial variations between adjacent chambers. This observation is important because it justifies, at a quantitative level, the assumption that the pressure read by a side-wall tapping is representative of the cross-sectional average pressure at the same axial station [301]. Any residual deviation from this assumption is responsible for a fraction of the percentage errors reported in Table 7.3 and is discussed in detail in Section 7.7.5.

A final observation on Figure 7.26 is that the static-pressure scale does not include negative values: the minimum absolute pressure in the simulated domain is above the saturated vapour pressure of water at ambient temperature (2.3 kPa at 20 °C). The CFD solution therefore confirms that no cavitation region is present in the device at the four operating points investigated in this study, which is consistent with the experimental observation that the discharge flow is continuous and free of the noise signature typically associated with cavitating flows [305]. The absence of cavitation is an important design property of the PPR because it guarantees a predictable scaling of the flow-rate response with the inlet pressure over the full operating range of the device.

7.7.3 Dynamic Pressure Field and the Central Jet

A particularly revealing visualization of the flow organization inside the PPR is obtained by plotting the dynamic pressure $q_d = \tfrac{1}{2} \cdot \rho \cdot |u|^2$ on the mid-longitudinal plane (Figure 7.27) and, zoomed on the throat region, on a streamwise cross-section (Figure 7.28). The dynamic pressure is identically zero where the velocity magnitude is zero, and reaches its maximum along the axis of the central jet; the dark blue regions of the contour therefore identify fluid volumes that are in a state of static (i.e. non-moving) equilibrium, while the colored regions identify the portion of the fluid that is actively participating in the flow.

From a fluid-dynamic perspective, the dynamic pressure is the most direct indicator of the partition of the total mechanical energy of the fluid into a kinetic component and a pressure component. In a conservative flow without losses, the sum $q_d + p$ (total pressure) is constant

along a streamline, and any reduction of q_d must be compensated by a corresponding increase of p, a statement that is nothing other than Bernoulli's theorem applied to an incompressible flow [306]. In the PPR, this conservation principle is violated by the friction losses at the rough walls and by the turbulent mixing in the shear layer of the central jet, and the total pressure therefore decreases progressively along the axial direction.

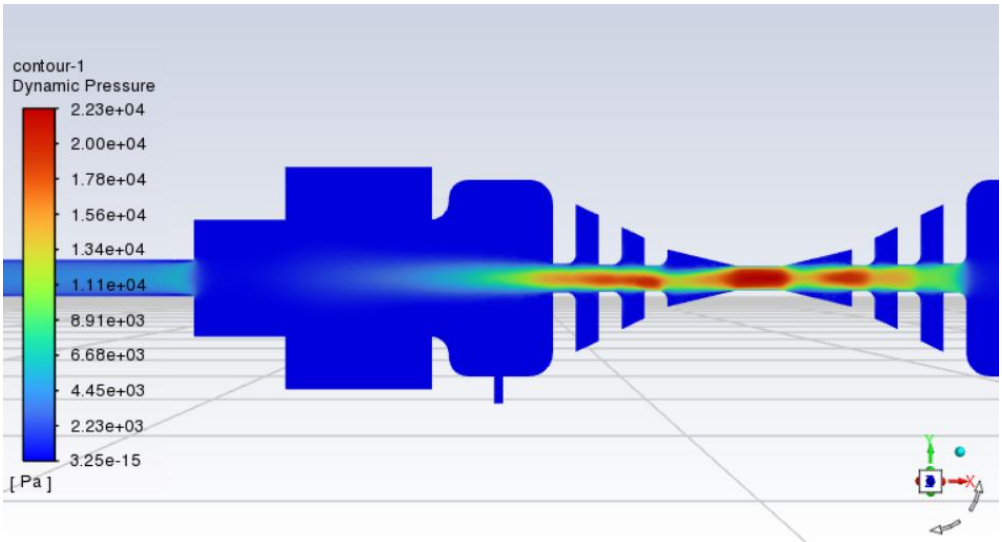


Figure 7.27: *Dynamic pressure contour on the mid-longitudinal plane of the PPR. The central jet appears as a narrow red-orange line extending from the throat through the downstream chambers; the entire annular volume surrounding the jet — including the region immediately adjacent to the Stage I tapping — remains at negligible dynamic pressure, indicating a fluid essentially at rest.*

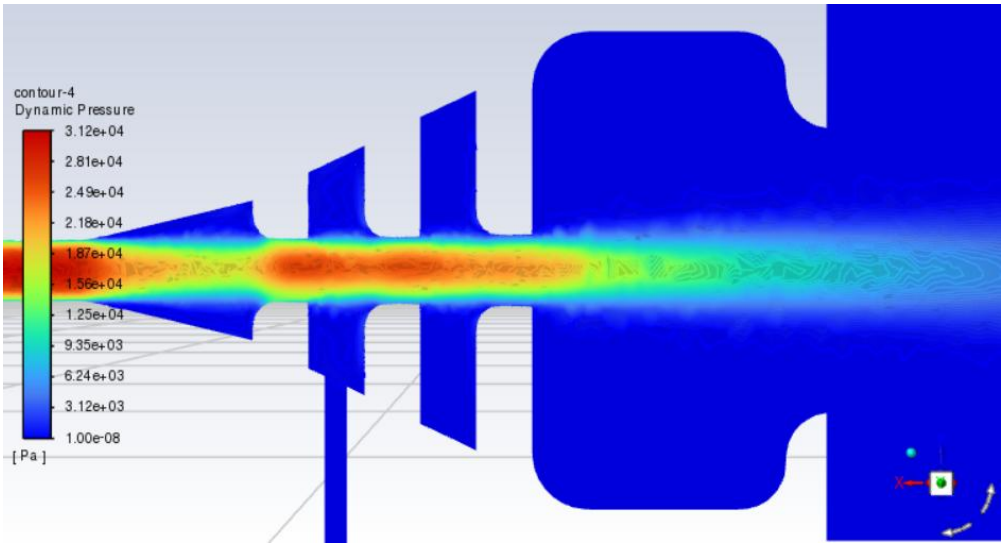


Figure 7.28: *Dynamic pressure contour in a longitudinal cross-section downstream of the throat, showing the progressive spreading of the central jet and its gradual dissipation as it enters the outlet chamber. The annular volumes outside the jet remain in dark-blue tones across the entire axial extent of the device.*

The dynamic pressure contour of Figure 7.27 captures exactly this behavior: the jet accelerates at the throat, attains its maximum dynamic pressure (approximately 22 kPa in the 1 bar reference case), and then progressively loses its kinetic energy as it traverses the sequence of downstream chambers, eventually dissipating the residual kinetic energy into the outlet volume.

The spatial distribution of the dynamic pressure is strikingly different from the one expected in a classical pipe flow with developed turbulent profile. In a developed pipe flow, the dynamic pressure has a bell-shaped profile that occupies essentially the whole cross-section of the pipe, with a maximum on the axis and a smooth decrease towards the walls. In the PPR, by contrast, the dynamic pressure is concentrated in a narrow column of diameter comparable to the throat diameter (about 5 mm) that extends axially through all the annular chambers; outside this column, the dynamic pressure drops by three orders of magnitude (from 2.2×10^4 Pa on the jet axis to approximately 10 Pa in the annular volumes). This extreme contrast between a high-energy core and a surrounding quiescent reservoir is the defining kinematic signature of the PPR and is the feature that justifies the description of the device as a jet–chamber cascade rather than as a standard pipe expansion.

Figure 7.28, which is a zoomed view of the dynamic pressure on a centreline cross-section downstream of the throat, further refines this picture. The jet is visible as a compact red-orange stripe that crosses the three intermediate stages without significant radial spreading, confirming that the downstream orifices, whose diameter is marginally larger than the throat diameter, do not significantly perturb the jet but simply allow it to pass through. The jet begins to spread appreciably only when it enters the outlet chamber, where the sudden expansion of the flow cross-section eliminates the geometrical constraint that had been keeping the jet confined. The spreading mechanism is the classical one of a free submerged jet: momentum is transferred from the jet core to the surrounding fluid through the action of the turbulent shear layer, whose thickness grows approximately linearly with the distance from the exit of the confining orifice [307, 308].

The combination of Figures 7.26, 7.27 and 7.28 already provides the key physical insight that supports the interpretation of the experimental readings. The central jet carries the entire mass flow; the volume around the jet acts as a pressurized but hydraulically passive reservoir that communicates with the jet only through viscous entrainment in the shear layer. As the inlet pressure is increased, both the jet and the surrounding volumes are pressurized, but the pressure inside the surrounding volumes is a function of the radial equilibrium with the jet rather than of the local dynamic pressure. This observation will turn out to be the cornerstone of the interpretation of the pressure readings developed in Section 7.7.5, and it is worth stressing that it emerges directly and unambiguously from the CFD analysis, it would have been essentially impossible to reach this conclusion on the basis of the experimental data alone, since the transmitters installed on the aluminum armature read by construction only the annular-volume pressure, without access to the jet dynamic pressure.

7.7.4 Turbulence Fields

The CFD solution provides direct access to two quantities that characterize the turbulent state of the flow: the turbulent kinetic energy k, which measures the energy content of the velocity fluctuations per unit mass, and the turbulent intensity $Tu = \sqrt{(2k/3)} / |u|$, which normalizes the fluctuation amplitude by the local mean velocity and is therefore a dimensionless quantity bounded between 0 (laminar flow) and values typically of the order of 60–80 % in strongly turbulent regions. Both quantities are computed from the two transport equations of the k–ω

SST model adopted here, and the relationship Tu = √(2k/3) / |u| follows directly from the definition of the Reynolds stress tensor under the hypothesis of isotropic turbulence [287, 299]. The ratio between Tu and k therefore gives an approximate indication of the local mean velocity and, combined with the dynamic pressure analysed in Section 7.7.3, provides a three-dimensional description of the turbulent mixing inside the PPR.

Figure 7.29 shows the turbulent intensity on the mid-longitudinal plane: Tu exceeds 60 % inside the jet shear layer and drops below 10 % in the annular volumes around the tappings, confirming that the fluid in those volumes is not in a state of intense turbulent mixing. The jet core itself, by contrast, exhibits turbulent intensities of approximately 30–40 %, a value consistent with the classical measurements of high-Reynolds-number submerged jets reported by Wygnanski and Fiedler and by Hussein et al. [307, 308]. Figure 7.30 reports the same quantity on a cross-sectional plane passing through the throat, where Tu reaches values up to 71 % in the thin shear layer that separates the accelerating jet from the surrounding slower fluid.

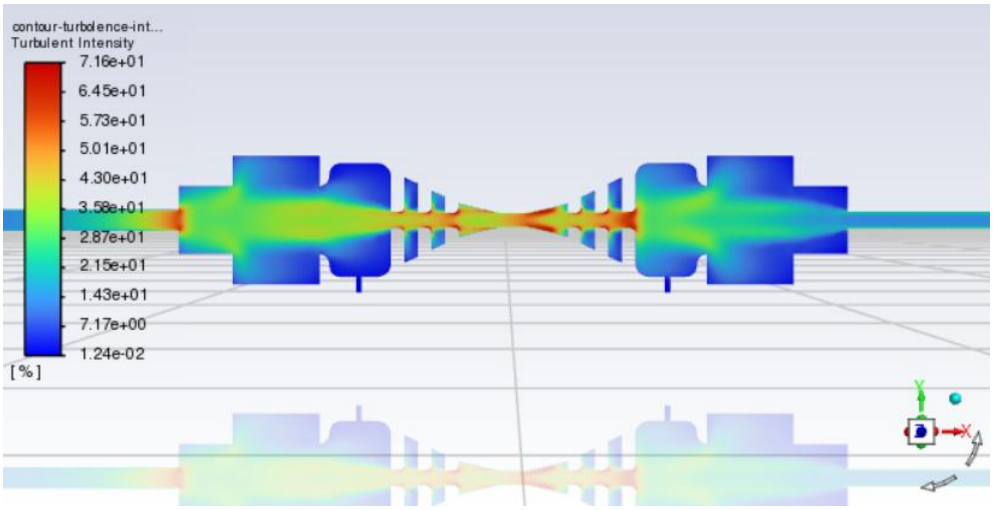


Figure 7.29*: Turbulent intensity field on the mid-longitudinal plane of the PPR. The red band corresponds to the shear layer of the central jet; the blue regions surrounding the orifice passages are characterised by turbulent intensities below 10 %.*

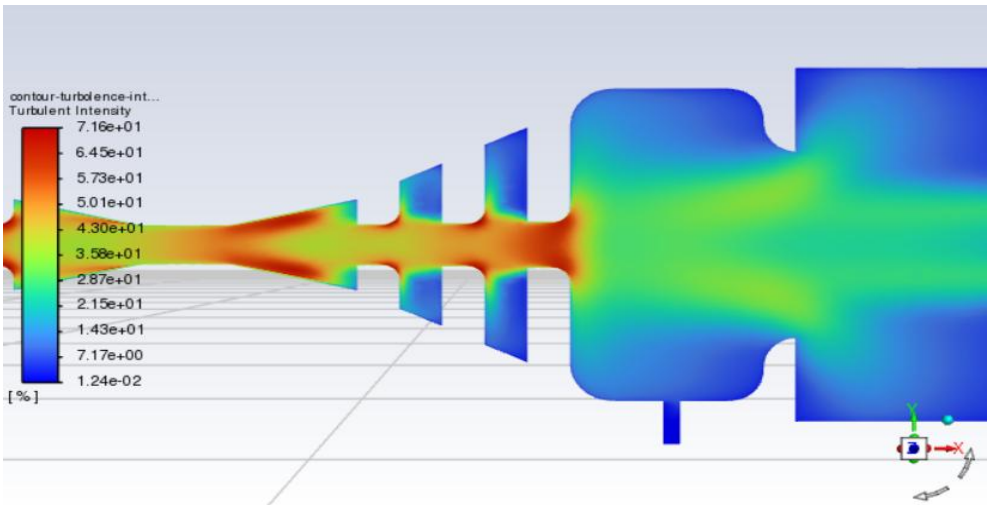


Figure 7.30*: Turbulent intensity field on a centerline cross-section of the PPR, zoomed on the throat and the three-stage orifice cascade. The jet shear layer reaches turbulent intensities of 70 %, while the annular volumes remain below 10 %.*

Figure 7.31 reports the turbulent kinetic energy field on a longitudinal plane zoomed on the tapping region: the energy is concentrated in the shear layer of the central jet, where it reaches a peak value of approximately 0.59 m²/s², and drops by more than two orders of magnitude inside the annular volumes and the tapping cavities. Beyond confirming the visual observation of Figures 7.29 and 7.30, this quantitative contrast has an important energetic implication: the turbulent kinetic energy is the reservoir from which the dissipation rate draws in order to transfer the mechanical energy of the mean flow into heat, and the fact that this reservoir is concentrated in the shear layer means that the dissipation itself is localized there. The annular volumes and the tapping cavities, by contrast, have a negligible dissipation rate and therefore behave as "energetically passive" reservoirs [309] — they exchange pressure with the jet but not energy, which is the physical interpretation of the "hydrostatic reservoir" picture invoked repeatedly in this chapter.

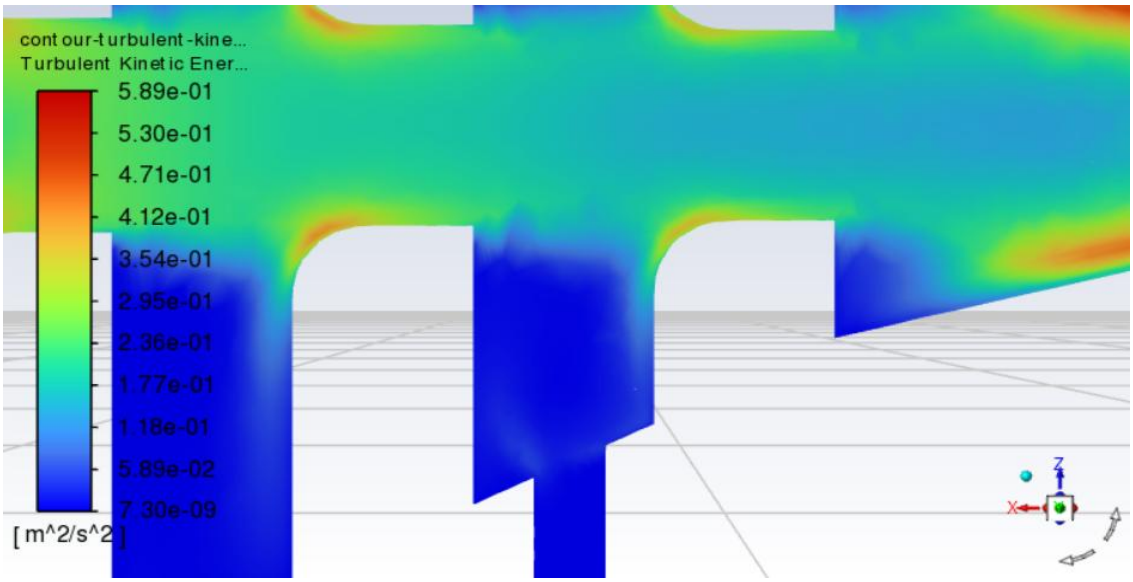


Figure 8: *Turbulent kinetic energy field near the radial pressure tappings (zoomed view). The energy is concentrated in the shear layer of the central jet (red band at the top) and decreases by more than two orders of magnitude inside the tapping cavities (dark-blue regions at the bottom).*

The turbulent-field analysis also helps to clarify why the k–ω SST model performs systematically better than the realizable k–ε model in the PPR geometry. The distinction between the two models is particularly acute in regions with strong adverse pressure gradients and near-wall shear: the k–ε family uses wall functions that assume a universal log-law profile in the first cell off the wall, an assumption that is compromised when the shear is not aligned with the mean flow (as happens at the orifice edges) and when the first cell is inside the buffer layer (as happens here for the rough-wall cases with Ks of the order of the first-cell height). The k–ω SST, by contrast, integrates the turbulence equations down to the wall through its low-Reynolds formulation, and switches to the k–ε formulation in the free-stream through a blending function. This dual strategy provides a much more accurate prediction of the shear-layer thickness and of the jet spreading rate, which are the two mechanisms that dominate the pressure loss in the present device [286, 287].

7.7.5 Flow Field Inside the Pressure Tappings and Deviation from the Experimental Reading

The sub-section of the flow field that deserves the most detailed discussion, and that constitutes the main novelty of this chapter, is the one in immediate proximity of the radial pressure tappings. These are the physical locations at which the experimental transmitters acquire the static pressure, and any deviation between the local CFD flow field and the ideal hydrostatic reservoir assumed by the measurement principle translates directly into a systematic error of the reading.

Figure 7.32 shows the velocity magnitude on a longitudinal plane passing through the centreline of the tapping cavities of Stages I, II and III. The central jet is clearly visible at the top of the frame as an orange-red high-velocity band ($U \approx 5$ m/s), while the cavities below the main flow are visualized as blue columns, the velocity there is below 0.3 m/s over the entire cavity length, two orders of magnitude smaller than the jet velocity. The sharp velocity discontinuity at the interface between the main chamber and the cavity mouth is the location of a thin but well-defined shear layer, which is the mechanism through which the cavity communicates with the primary flow [313].

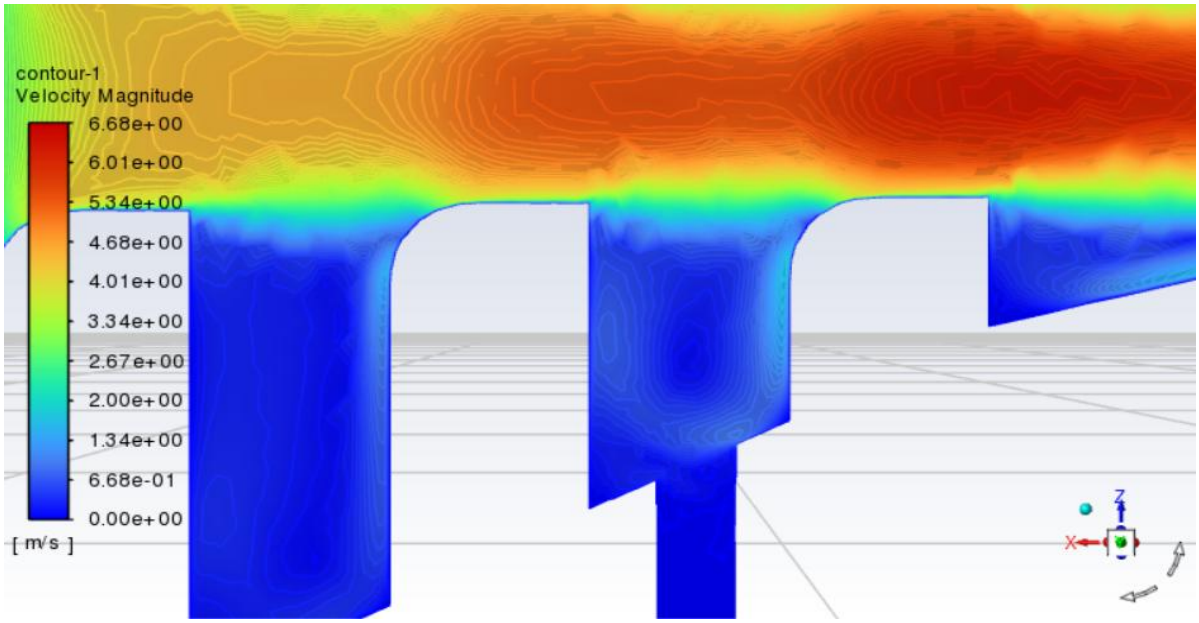


Figure 7.32: *Velocity magnitude near the radial pressure tappings. The orange-red band at the top represents the main flow at the throat/chamber interface; the blue columns below are the tapping cavities of Stages I, II and III, in which the velocity is essentially zero. The sharp transition at the cavity mouth is a thin shear layer that couples the cavity hydrostatically to the main flow.*

Figure 7.32 extends the same analysis to the turbulent intensity: inside the cavities, Tu drops below 5 % and in some locations below 1 %. Figure 7.33 is the complementary view of the turbulent intensity on a section that includes the cavity and part of the main chamber, and shows that the turbulence generated in the main flow does not penetrate significantly into the cavity, the cavity is hydraulically isolated from the turbulent dynamics of the jet.

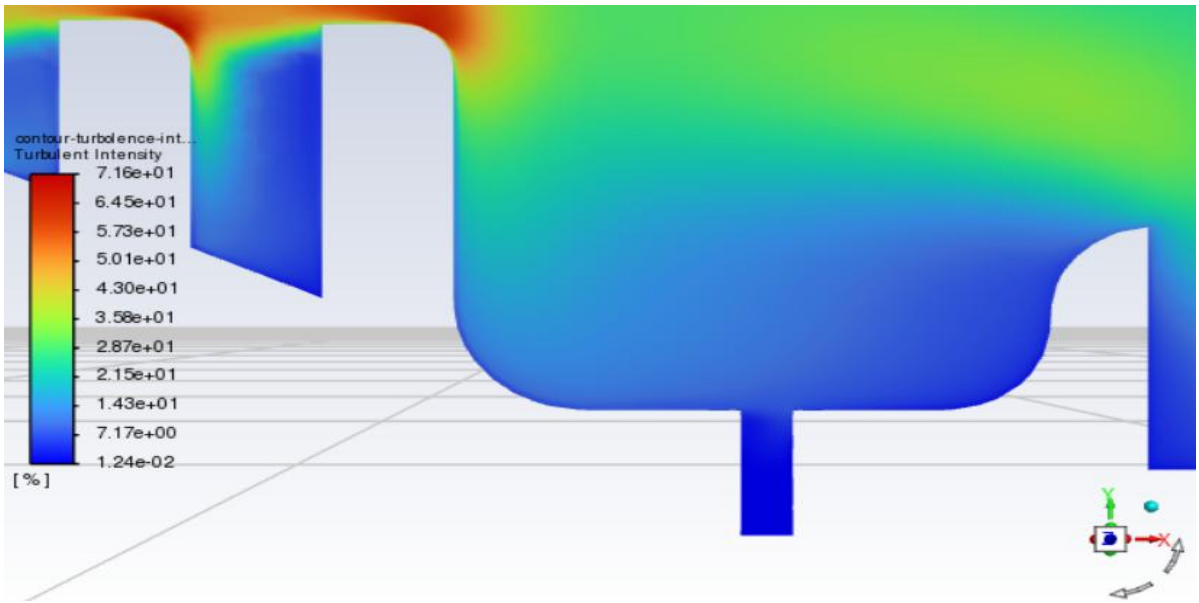


Figure 7.33*: Zoomed view of the turbulent intensity field in the region of a radial pressure tapping. The cavity appears as a quasi-laminar volume (deep blue) isolated from the turbulent main flow (orange-red).*

From the perspective of the static-pressure measurement, this flow topology has three important consequences, which together constitute the basis of the interpretive framework adopted in the remainder of this section:

1. *The tapping reads a hydrostatic pressure*: because the fluid inside the cavity is essentially at rest ($|u| \approx 0$), the dynamic pressure contribution to the total pressure is negligible, and the sensor reads directly the static pressure of the fluid at the sensor face. This is exactly the condition for which a side-wall static tapping is designed, and is the basis on which the entire experimental methodology relies [301]. However, the static pressure read by the sensor is not the static pressure of the jet at the same axial location, but rather the pressure of the annular volume surrounding the jet, which, in the PPR topology, is hydraulically connected to the jet only through the thin shear layer at the cavity mouth.
2. *The pressure of the annular volume is not strictly axial*: in a classical axisymmetric pipe flow with a developed turbulent profile, the static pressure at the wall differs from the centreline static pressure by a quantity of order $\rho \cdot u_\tau^2 \cdot C$, with $C \approx 1$, which is negligible with respect to the driving pressure for the Reynolds numbers of interest [302]. In the PPR topology, however, the annular volumes are in radial equilibrium with the central jet through a strong shear layer, and the static pressure at the wall is determined by the balance between the jet static pressure and the dynamic contribution of the shear-layer entrainment. The CFD simulations show that this radial correction is of the order of 1–5 kPa depending on the operating pressure, which corresponds to 1–3 % of the local absolute pressure and is coherent with the systematic under-prediction of 4–8 % observed at Stages II and III in the 3 bar and 4 bar tables of Section 7.5.

3. *Stages I and II may read almost identical pressures*: the most important implication of the flow topology described above is that the pressures read at Stages I and II, whose annular volumes are upstream of the throat and are therefore not yet traversed by the central jet, can be almost identical. This happens because both volumes are pressurized by the same upstream static pressure, transmitted through the hydrostatic equilibrium of the fluid in the chambers rather than by the passage of the central jet through the corresponding orifices. In the experimental campaign, this feature manifested itself with particular evidence during the Campaign 3 tests, in which the pressures recorded at Stages I and II were consistently within 2 % of each other and, in some conditions, were even inverted. The CFD simulation reproduces this behavior correctly: the predicted pressure at Stage I differs from the one at Stage II by less than 3 kPa in the 1 bar case, and by less than 8 kPa at 4 bar.

Furthermore, the CFD model does not perfectly reproduce the experimental pressure readings at the tappings, and the residual deviation is systematic rather than random. Inspection of the validation tables in Section 7.5 shows that the CFD tends to under-predict the pressures at Stages II and III by 4–10 % at 3 bar and 4 bar, while at Stages I and IV the agreement is typically better than ±3 %. Several physical effects contribute to this residual deviation:

a. *Tapping geometry effects*. The classical studies of Shaw [236] and Franklin & Wallace [303] demonstrated that the finite diameter of a static-pressure tapping (typically 0.5–1.5 mm in the present device) introduces a systematic error in the reading, of the order of 1–3 % of the local dynamic pressure, that scales with the ratio of the tapping diameter to the boundary-layer thickness. For the PPR, where the boundary layer at the chamber wall is only a fraction of a millimeter thick, this error is not negligible and is not captured by the CFD, which does not resolve the detailed three-dimensional flow at the tapping mouth.
b. *Shear-layer pulsations at the cavity mouth*. The thin shear layer that couples the cavity to the main chamber can develop unsteady oscillations (Rossiter-type modes [314]) whose time-averaged effect is a small but systematic drift of the mean pressure inside the cavity with respect to the steady-state static pressure predicted by a RANS simulation. These oscillations are not modelled in the present CFD campaign, which is based on a steady-state formulation.
c. *Sealing-gasket deformation*. The experimental installation of the pressure transmitter onto the radial port involves a compliant gasket that deforms slightly under the operating pressure, modifying the effective geometry of the cavity mouth. This deformation is not represented in the CFD geometry, which assumes a perfectly rigid interface.
d. *Local roughness non-uniformity*. The roughness imposed in the CFD is uniform and isotropic, while the as-built AM surface presents preferential directions and localized defects that can alter the flow in the immediate vicinity of the tapping. Klingaa et al.

[282] demonstrated that the effective roughness of an AM internal channel can vary by ±30 % along the flow direction due to the layer deposition pattern.

The cumulative effect of these four mechanisms is consistent with the 4–8 % residual deviation observed in the tables of Section 7.5, and should be regarded as a bound on the accuracy achievable by a steady-state RANS simulation of a PPR-type geometry with wall-tap pressure instrumentation. A further reduction of the residual error would require either a fully unsteady LES/DDES simulation of the cavity, or a dedicated experimental characterization of the effective tapping geometry and surface roughness, neither of which fell within the scope of the present investigation.

7.7.6 The PPR as a Distributed Hydraulic Impedance

Taking the flow-field analysis of Sections 7.7.1 to 7.7.5 together, the operating principle of the PPR can be stated in clearer terms than would be possible on the basis of the experimental data alone. The device does not operate as a cascade of localized orifices, each of which would generate a discrete pressure jump read by the corresponding sensor. It operates instead as a distributed hydraulic impedance in which a central jet is generated at the throat, carries the entire mass flow through the downstream orifices, and dissipates its kinetic energy progressively through entrainment and viscous mixing over the full length of the device. The side-wall pressure tappings read the pressure of the annular volumes surrounding the jet, which are hydraulically coupled to the jet through thin shear layers but do not themselves participate in the primary flow.

A useful analogy for describing this behavior is the one between hydraulic circuits and electrical circuits [310]: in this analogy, the pressure drop corresponds to the voltage drop, the volumetric flow rate corresponds to the electric current, and the hydraulic resistance of a component corresponds to the electric resistance. A classical cascade of orifices would correspond, in the electric analogy, to a series of discrete resistors separated by ideal wires, and would generate a staircase voltage profile with flat regions between the resistors. The PPR, by contrast, behaves like a continuous distributed-parameter element, analogous to a transmission line with uniformly distributed inductance and resistance, in which the energy is dissipated progressively rather than at discrete locations. This analogy, beyond its pedagogical usefulness, also has an operational consequence: the sizing of a distributed-impedance device is governed by the integral of the distributed loss coefficient along the axial coordinate, rather than by the sum of the loss coefficients of discrete restrictors, and the design strategy must therefore be driven by the geometry of the annular volumes as much as by the geometry of the orifices [311].

An energy-based reading of the flow-field analysis reinforces this interpretation. In a steady, incompressible flow, the total mechanical energy balance between the inlet and the outlet can be written as $p_{in} + ½\rho U^2_{in} = p_{out} + ½\rho U^2_{out} + \Delta E_{diss}$, where ΔE_{diss} is the mechanical energy dissipated per unit volume between the two sections [312]. In the PPR, the kinetic energy term is negligible at both the Inlet and the Outlet (the flow velocity in the adapter pipes is approximately 0.5 m/s, corresponding to a dynamic pressure of 125 Pa, i.e. less than 0.2 % of

the static-pressure drop across the device), and the entire pressure drop must therefore be attributed to the dissipation term. The CFD analysis of this section shows that the dissipation is in turn concentrated in the turbulent shear layer of the central jet, which is the region where the turbulent kinetic energy is highest (Figure 7.31) and where the velocity gradients are largest: in other words, the device converts the inlet pressure into the kinetic energy of a compact jet and then dissipates this kinetic energy over the remaining axial extent of the valve. The distributed character of the dissipation is what makes the device a "distributed impedance" rather than a "localized restrictor".

This interpretation is consistent with the experimental observation that the pressure profile does not show discrete jumps at the nominal orifice locations, but rather a progressive decrease whose shape depends on the geometry of the annular chambers as much as on the geometry of the orifices. It is also consistent with the CFD prediction that the best model of the device is obtained by a k–ω SST closure with a realistic roughness of the order of the printing layer thickness, which is precisely the combination needed to resolve accurately both the jet shear layer and the near-wall friction in the annular chambers. Finally, the distributed-impedance picture provides a unified framework within which the observations made in the preceding sections, the near-identity of the Stage I / Stage II readings, the systematic under-estimation of the intermediate-stage pressures by the CFD, the residual 4–8 % discrepancy at the Outlet, can be interpreted as consequences of a single underlying flow organization rather than as independent observations to be explained separately.

Chapter 8

Conclusions and Future Work

8.1 Overall Conclusions

The work documented in this thesis was motivated by a specific technological challenge: the need for reliable, robust and cavitation-free pressure-regulation devices for liquid hydrogen (LH_2) service, whose operational envelope combines cryogenic temperatures (~20 K), pressure ratios approaching two orders of magnitude (from ~200 bar storage conditions to ~2–30 bar utilization conditions), extreme leak-tightness requirements, and stringent mass and reliability budgets imposed by the aerospace context. As discussed in Chapter 1 and substantiated in the state-of-the-art review of Chapter 2, conventional valve architectures developed for higher-density, higher-viscosity fluids are fundamentally ill-suited to this operational envelope: a single-stage throttling of such a pressure ratio in LH_2 would produce throat velocities close to the sonic threshold (≈355 m/s for LH_2 vapour), with attendant risks of cavitation-like phenomena, flash vaporization, erosion, vibration and sealing loss.

Against this background, the research programme pursued in this work addressed the challenge through the development and validation of a two-stage pressure-management architecture: a geometry-driven Passive Pressure Reducer (PPR) operating as the first stage, responsible for the coarse reduction from ~200 bar to ~50 bar through four annular dissipation chambers and six calibrated orifices in a convergent–divergent monolithic body, followed by an actively controlled piston pressure-regulating valve operating as the second stage, responsible for the fine regulation in the 50 bar → 2–30 bar range through a precisely optimized pass-through spool geometry. The PPR is inherently passive: it contains no moving parts, no springs, no dynamic seals, and requires no electrical power or external actuation. The piston valve, by contrast, accepts the well-defined downstream pressure delivered by the PPR and operates in a regime in which its internal geometry can be optimized to achieve near-critical damping despite the very low viscosity of LH_2.

The development of the two devices was carried out through a rigorous methodological sequence that cumulated, along the chapters of the thesis, the contributions of four distinct but interdependent engineering perspectives: conceptual and geometric design (Chapter 3), mathematical modelling of the fluid-dynamic and mechanical behavior (Chapter 4), high-fidelity Computational Fluid Dynamics (CFD) analysis (Chapter 5), and experimental characterization with CFD validation (Chapters 6 and 7). At each step, the predictions of the analytical model were cross-validated against the results of the higher-fidelity numerical simulation, and the numerical predictions were themselves confronted with the experimental evidence collected on a dedicated hydraulic test bench. This multi-level validation strategy is the methodological backbone of the present work and represents, in itself, a contribution to the engineering practice of the design of cryogenic pressure-regulating devices.

The principal conclusion drawn from the research is that distributed, multi-stage passive throttling is a viable and reliable strategy for the coarse pressure reduction stage of an LH_2 supply chain, and that its performance can be predicted with engineering accuracy through a combination of lumped-parameter models, RANS CFD and controlled experimental testing. The quantitative level of agreement achieved between the three methodological layers, detailed in Sections 8.2 to 8.4 below, confirms that the distributed-impedance approach, once supported by a geometrically faithful and roughness-aware numerical model, can be integrated confidently into the design loop of the next generation of cryogenic pressure-management components.

8.2 Scientific and Technological Contributions

The individual contributions of the thesis can be articulated along three complementary axes: the design innovation embodied by the two-stage architecture, the modelling framework developed to support its quantitative analysis, and the experimental infrastructure built to validate the PPR prototype under hydraulic surrogate conditions.

8.2.1 Design Innovation

The PPR architecture presented in Chapter 3 represents the primary design contribution of the thesis. Its key novelty with respect to the patent-literature antecedent of [30] is the introduction of a convergent–divergent internal profile that transforms the annular chambers from low-efficiency disturbances of a straight bore into highly effective energy-dissipation zones. The comparative CFD analysis reported in Chapter 5 demonstrated that the patent-heritage geometry, on its own, produces a pressure reduction of only approximately 0.3 bar, i.e. 1.3% of the 23-bar target at the operating point of interest, whereas the convergent–divergent PPR design achieves the full target with a controlled throat velocity of ~213 m/s, well below the LH_2 sonic limit, and with local pressure levels that remain everywhere above the cavitation threshold (0.9 bar) over the full axial extent of the device.

The piston pressure-regulating valve presented in Section 3.3 contributes a second design innovation: the use of a geometry-optimized pass-through spool as an alternative to the conventional blunt-ended spool. The CFD analysis of Section 5.3 demonstrated that the optimized geometry reduces the total hydrodynamic force F_{tot} acting on the spool by a factor of approximately 3.5 (from ~190 N for the blunt spool to ~54 N for the pass-through spool), and that this reduction, when combined with the chamber-pressure dynamics modelled through the Full Order Model (FOM) of Section 4.2, yields a near-critically damped closed-loop response even in the extremely low-viscosity LH_2 environment. The geometric-damping mechanism revealed by the FOM, in which the terms $A\dot{x}$ and $B\dot{x}^2$ provide an effective damping coefficient that does not depend on fluid viscosity, is to the authors' knowledge, an original contribution to the design of spool-type valves for cryogenic fluids and represents a viable alternative to the use of external mechanical dampers.

8.2.2 Modelling Framework

The mathematical model developed in Chapter 4 provides the first layer of the multi-level validation strategy adopted in the thesis. For the PPR, the lumped-parameter formulation extends the classical orifice-discharge equation with a jet-correction factor k_i that accounts for the velocity enhancement imparted by each upstream orifice on the flow entering the next stage, a physical effect specific to the closely spaced multi-orifice architecture and absent from single-stage throttling models. This correction allows the model to predict the volumetric flow rate Q and the global discharge coefficient C_D with a level of accuracy compatible with rapid design iteration, without requiring the full CFD machinery at each step of the geometric optimisation loop.

For the piston valve, the transition from the Reduced Order Model (ROM) to the Full Order Model (FOM) documented in Chapter 4 is the key methodological step. The ROM, in which the chamber pressures are treated as instantaneous functions of the spool position, was shown to predict an over-damped or grossly under-damped response in LH_2, because the damping of the mass–spring–damper idealization is proportional to the fluid viscosity, which in LH_2 is of the order of 10^{-5} Pa·s. The FOM, by contrast, integrates the chamber-pressure dynamics explicitly and reveals a nonlinear coupling between the spool velocity and the hydrodynamic force that provides geometry-derived damping independent of fluid viscosity. The agreement between the FOM-predicted settling time and the CFD-derived equivalent viscous coefficient C = 4.75 kg/s (converged in four iterations to 0.3% residual error) is the quantitative signature of this contribution.

8.2.3 Experimental Infrastructure

The hydraulic test bench documented in Chapter 6 represents the third principal contribution of the thesis. Designed and built specifically for the validation of the PPR prototype, the bench integrates the aluminum containment armature (12 mm wall thickness, coaxial alignment references, radial pressure-port network), the two-stage pressure regulation arrangement (coarse + fine regulating valves with intermediate hydraulic reservoir), the volumetric flow-rate measurement by timed discharge collection, and the calibrated three-transmitter instrumentation. The design philosophy adopted at every stage was the co-design of the mechanical, fluidic and measurement functions, which allowed the control of the boundary conditions at a level unattainable with pre-existing laboratory infrastructure.

A specific contribution of the experimental campaign was the sequential sensor-repositioning strategy developed to reconstruct the full pressure profile along the PPR despite the availability of only three pressure transmitters. This strategy, implemented through three successive sensor placements (Campaigns 1, 2 and 3 of Chapter 6), allowed the measurement of six distinct pressure stations, Inlet, Stage I, Stage II, Stage III, Stage IV and Outlet, and revealed, among other things, the near-identity of the pressure readings at Stage I and Stage II that was subsequently interpreted through the CFD flow-field analysis of Chapter 7.

8.3 Key Numerical Results

The quantitative results produced by the research programme are summarized in Table 8.1, which consolidates the principal performance metrics of the two devices and the corresponding agreement between the three methodological layers (analytical model, CFD, experiment) at the operating points of interest. The figures reported in the table are extracted from the detailed analyses of Chapters 4 through 7 and are presented here in a compact, cross-referenced form to give the reader a unified overview of the achievements of the work.

Table 8.1*: Consolidated performance metrics of the PPR and the piston regulating valve.*

Quantity	PPR (LH_2 design)	PPR (H_2O exp.)	Piston valve (LH_2)
Pressure reduction target	23 bar (200→177 bar)	0.6–3 bar (1–4 bar inlet)	7–15 bar
Throat diameter	5.34 mm	5.34 mm	3.31 mm (equiv.)
Throat velocity	~213 m/s	~5–10 m/s	Optimised, crown geom.
Min. absolute pressure	> 0.9 bar (no cavit.)	N/A (low ΔP)	Design margin verified
Volumetric flow rate	~0.5 L/s (design)	0.083–0.175 L/s (meas.)	Regulated output
CFD model accuracy	—	Mean |err| = 0.96 % (Q)	—
Best validated CFD	RANS k-ω SST + Icing	RANS k-ω SST + Icing, Ks=0.15mm Cs=0.8	RANS k-ω SST
F_{tot} reduction	—	—	×3.5 (190→54 N)
Damping strategy	Passive (no damping req.)	Passive	Geometric, via FOM

All values reproduce the results of Chapters 4–7. The PPR experimental data at 1–4 bar are the surrogate-hydraulic validation of the design described in Chapters 6 and 7; the LH_2 design-point values for both devices correspond to the CFD predictions of Chapter 5.

8.3.1 PPR: CFD-to-Experimental Validation Summary

The validation of the PPR through the 28-run CFD matrix documented in Chapter 7 is one of the most quantitatively rigorous results of the thesis. At each of the four inlet-pressure levels investigated experimentally on the hydraulic bench (1, 2, 3 and 4 bar), seven CFD runs were executed, differing in the turbulence closure (realizable k–ε or k–ω SST), in the wall treatment (smooth or rough) and in the roughness parameters (Ks between 0.01 mm and 0.15 mm, Cs between 0.5 and 0.8). The best overall agreement between CFD and experiment was obtained with the k–ω SST turbulence model combined with the High Roughness (Icing) formulation at Ks = 0.15 mm and Cs = 0.8, yielding a mean absolute mass-flow-rate error of 0.96 % across the four operating pressures, with individual errors not exceeding 2.91 % at 1 bar, 0.22 % at 2

bar, 0.64 % at 3 bar and 0.06 % at 4 bar. The smooth-wall baseline, by contrast, systematically over-predicts the inlet pressures and under-predicts the intermediate stages, with errors of 4.25–7.88 % on the mass flow rate, a quantitative confirmation that the as-manufactured surface roughness of an additively manufactured prototype cannot be neglected in the numerical validation of internal-flow devices.

8.3.2 Piston Valve: FOM-to-CFD Consistency

The piston valve was not tested experimentally in the scope of the present thesis, but its design was validated at the numerical level through the cross-comparison of the FOM predictions of Chapter 4 with the CFD analysis of Section 5.3. The key quantitative result is the settling-time reduction achieved by the optimized pass-through spool: Figure 5.38 shows that the optimized geometry settles in approximately half the number of oscillation cycles compared with the blunt-ended reference configuration, as a direct consequence of the factor-of-3.5 reduction in the total hydrodynamic force computed by CFD for the optimized geometry. This reduction, combined with the geometry-derived damping predicted by the FOM, produces a near-critically damped closed-loop response that is stable even at LH_2 viscosity levels, the design goal for which the optimisation was pursued. A secondary benefit documented by the CFD analysis is the elimination of the chaotic vortex-driven force fluctuations observed in the blunt-ended configuration, which further improves the regularity of the spool trajectory and is therefore relevant to the long-term reliability of the device.

8.4 Physical Insights Emerging from the Research

Beyond the quantitative validation of the two devices, the research programme documented in this thesis has produced a number of physical insights into the operating principles of distributed passive throttling that are worth summarizing here as independent outcomes of the work.

8.4.1 Distributed-Impedance Interpretation of the PPR

The CFD flow-field analysis of Chapter 7 demonstrated that the PPR does not operate as a cascade of localized orifices, each of which would generate a discrete pressure jump read by the corresponding sensor, but as a distributed hydraulic impedance in which a central jet is generated at the throat, carries the entire mass flow through the downstream orifices, and dissipates its kinetic energy progressively through entrainment and viscous mixing over the full axial extent of the device. This interpretation is supported by the quantitative evidence that approximately 55 % of the total pressure drop is concentrated within the central portion of the device, between the upstream section of Stage I and the downstream section of Stage III, and that the remaining 45 % is distributed over the inlet adapter, the outlet adapter and the flange pockets. The implication for the design of the next generation of PPR devices is that the sizing of the annular-chamber sequence and of the axial length available for jet dissipation is at least as important as the sizing of the individual orifices.

8.4.2 The Static-Tapping Reading as a Hydrostatic Measurement

A corollary of the distributed-impedance interpretation is that the side-wall pressure tappings installed on the aluminum armature read the hydrostatic pressure of the annular volumes surrounding the central jet, rather than the dynamic pressure of the jet itself. This was demonstrated numerically in Section 7.7.5 by showing that the velocity magnitude inside the tapping cavities is below 0.3 m/s (two orders of magnitude smaller than the jet velocity) and that the turbulent intensity drops below 5 % in the same region. The hydrostatic character of the local reading explains the experimental observation of the near-identical pressures recorded at Stage I and Stage II in Campaign 3 of the experimental programme: the two volumes are hydraulically coupled through the annular geometry and are both pressurized to the upstream value, while the actual pressure reduction occurs in the central jet between the throat and the downstream chambers, in a region that is not sensed by the wall tappings.

8.4.3 The Role of Surface Roughness in AM Hydraulic Components

The comparison between the first additively manufactured prototype and the smooth-wall CFD model reported in Chapter 7 demonstrated that the surface roughness introduced by additive manufacturing (AM) is a first-order determinant of the hydraulic performance of internal-flow devices, and cannot be treated as a second-order correction to a smooth-wall baseline. The reconciliation between CFD and experiment required the introduction of the High Roughness (Icing) wall treatment with a Roughness Height compatible with the printing layer thickness (Ks between 0.01 mm and 0.15 mm), a choice that is physically defensible because it brackets the upper and lower bounds of the experimental printing parameter. This result has methodological implications that extend beyond the specific device studied: the validation of any AM hydraulic component through CFD requires a roughness-aware wall treatment, and the nominal smooth-wall simulation, which is often adequate for conventionally machined components, is systematically biased when applied to AM geometries.

8.4.4 Geometry-Derived Damping in Low-Viscosity Regulating Valves

The transition from the ROM to the FOM presented in Chapter 4 has produced a general physical insight into the damping mechanisms available to regulating valves operating in low-viscosity fluids such as LH_2. The linear-viscous-damping term of the classical mass–spring–damper idealization becomes quantitatively negligible when the fluid viscosity drops below $\sim 10^{-4}$ Pa·s, at which point the response of the spool is either grossly under-damped (oscillatory) or dependent on the presence of an external mechanical damper. The FOM, by explicitly modelling the chamber-pressure dynamics, reveals a nonlinear damping mechanism that arises from the geometric coupling between the spool motion and the chamber-pressure field, and whose magnitude does not depend on fluid viscosity. This insight is directly applicable to the design of regulating valves for any low-viscosity cryogenic fluid (liquid oxygen, liquid methane, supercritical helium) and can be used as a design criterion for the geometric optimisation of the spool/orifice interface.

8.5 Limitations of the Present Investigation

The scope of the present investigation was deliberately limited in a number of respects, and a transparent discussion of these limitations is necessary to contextualize the results summarized in the previous sections. Three categories of limitations can be identified, pertaining respectively to the experimental set-up, to the numerical model, and to the physical domain of validity.

8.5.1 Experimental Limitations

The experimental campaign documented in Chapter 6 was carried out using water as the working fluid, at temperatures compatible with standard laboratory conditions (~293 K) and at inlet pressures limited to the 1–4 bar range. The choice of water as a surrogate for liquid hydrogen is justified by dimensionless-similarity arguments, but the surrogacy is not complete: the cavitation behavior of water at room temperature is qualitatively different from the flash-vaporization and thermodynamic-non-equilibrium phenomena that can be triggered in LH_2 at cryogenic temperatures, and the validation performed in the present work therefore does not directly demonstrate the cavitation-free operation of the PPR at its nominal LH_2 operating point. This cross-fluid extrapolation is justified on the basis of the CFD predictions of Chapter 5, which show that the local absolute pressure in the device remains above 0.9 bar everywhere (i.e. above the LH_2 cavitation threshold), but the experimental confirmation of this prediction would require a dedicated cryogenic test campaign that falls outside the scope of the present thesis.

A second experimental limitation concerns the number and placement of the pressure transmitters. The hydraulic bench was equipped with three pressure transmitters, against the six pressure stations of interest along the device (Inlet, Stage I, Stage II, Stage III, Stage IV, Outlet); the full pressure profile was therefore reconstructed through three successive sensor-placement campaigns rather than through a single synchronous acquisition. While the three campaigns yielded consistent and repeatable data, the absence of a synchronous six-sensor acquisition prevents the direct investigation of any transient couplings between the pressure stations that may occur during the pressurization transient or in the presence of unsteady flow phenomena.

A third experimental limitation, of a metrological nature, concerns the determination of the flow rate. As described in Section 6.5, the flow rate was obtained by collecting the discharged water in a calibrated tank over a measured time interval. This integral method is robust, traceable and independent of the local pressure measurements, but it returns a value averaged over the collection interval and is therefore unable to resolve any time variation of the flow rate within it; it also lengthens appreciably the acquisition of each operating point, which in turn limits the number of repetitions that can be performed within a given campaign. The installation of a dedicated in-line flow meter, recommended in Section 6.5 and in Section 8.6.4, would remove this limitation and would make the flow-rate signal synchronous with the pressure measurements.

8.5.2 Numerical Limitations

The CFD analysis of Chapters 5 and 7 was carried out in the steady-state, Reynolds-averaged Navier–Stokes framework, which represents the standard industry-practice formulation for the design-phase analysis of internal-flow devices but does not resolve the unsteady flow features that can develop in specific regions of the computational domain. The steady-state assumption is particularly limiting at the pressure-tapping cavities, where the thin shear layer at the cavity mouth can develop Rossiter-type oscillations that are time-averaged in a RANS formulation. The residual 4–8 % error observed at the intermediate stages in Section 7.7.5 is consistent with this steady-state limitation, and a fully unsteady LES/DDES simulation of the tapping cavities would be required to quantify and correct this residual. A second numerical limitation is the use of an isotropic roughness specification on the wall boundaries: as discussed in Chapter 7, AM surfaces are known to exhibit preferential directions correlated with the layer deposition pattern, and an isotropic Ks is therefore an idealization of the actual surface topology.

8.5.3 Physical Domain of Validity

The design methodology developed in the present thesis was demonstrated for a specific pressure range (200 → 50 bar for the PPR, 50 bar → 2–30 bar for the piston valve) and for a specific mass flow rate (of the order of 0.5 L/s in LH_2 conditions). Extrapolation of the results to significantly different pressure ratios or flow rates is not guaranteed by the analyses reported here and would require a dedicated re-validation of the models. Similarly, the adoption of the devices in LH_2 systems different from the aerospace propulsion application addressed here, for example, large-scale ground refuelling infrastructures or fuel-cell balance-of-plant architectures, would require a re-assessment of the mass, thermal and reliability constraints discussed in Chapters 1 and 2, which are specific to the aerospace context.

8.6 Future Work

The limitations acknowledged in the previous section, together with the physical insights summarized in Section 8.4, identify several specific directions for the further development of the research line opened by the present thesis. These directions can be grouped into five categories: cryogenic experimental validation, numerical model refinement, geometric optimisation of the PPR, experimental validation of the piston regulating valve, and system-level integration studies.

8.6.1 Cryogenic Experimental Validation

The most important follow-up activity is the experimental validation of the PPR under cryogenic LH_2 conditions, to directly confirm the absence of cavitation predicted by the CFD analysis of Chapter 5 and to quantify any departure from the water-surrogate behavior documented in Chapters 6 and 7. The cryogenic campaign should reproduce the geometric configuration of the hydraulic bench (the PPR prototype, the aluminum containment armature, the sealing arrangement) and should extend the instrumentation to include acoustic emission sensors for the detection of possible cavitation-like events, optical access for high-speed

imaging of the two-phase flow regions, and cryogenic-compatible pressure transmitters with adequate response time. A preliminary evaluation of the required infrastructure has been carried out in the context of the research activities of this thesis, and the results can be used as the starting point for the design of a dedicated cryogenic test rig.

8.6.2 Numerical Model Refinement

On the numerical side, three specific refinements have been identified as high-priority directions for future work:

- Unsteady LES/DDES simulation of the pressure-tapping cavities, to resolve the shear-layer dynamics at the cavity mouth and to quantify the corresponding component of the residual CFD-experimental deviation at the intermediate stages. Preliminary estimates of the computational cost suggest that a DDES simulation of a single cavity at a single operating point is feasible on a medium-scale HPC infrastructure and would provide a direct comparison with the RANS results of Chapter 7.
- Direct profilometric characterization of the internal surface roughness of the PPR prototype, to be carried out after sectioning the prototype at the end of the testing campaign. A measured distribution of Ks and of the anisotropy indices would allow the CFD roughness parameters to be calibrated against a physical value rather than bracketed by the printing layer thickness, with a direct benefit on the accuracy of the CFD predictions.
- Tapping-geometry correction based on the Shaw / Franklin–Wallace analysis, embedded as a post-processing step in the CFD pipeline. This would produce a numerical pressure reading directly comparable with the experimental one and would eliminate the finite-diameter component of the residual error.

8.6.3 Geometric Optimization of the PPR

The distributed-impedance interpretation developed in Section 7.7.6 identifies the sizing of the annular-chamber sequence and of the axial length for jet dissipation as the primary design degrees of freedom of the PPR. A systematic parametric study of these parameters, chamber diameter, chamber axial length, orifice spacing, convergent/divergent angles — through the validated CFD model developed in the present thesis would allow the identification of the Pareto front between the pressure reduction achieved and the device length, and would therefore provide a design map for the next generation of PPR devices targeting different operating pressure ratios. A multi-objective optimisation incorporating, in addition to the pressure reduction, also the cavitation margin and the mass of the device would be a natural extension of this study.

8.6.4 Experimental Validation of the Piston Regulating Valve

The piston pressure-regulating valve has been validated in the present thesis at the numerical level only, through the cross-comparison of the FOM predictions with the CFD analysis of Section 5.3. A dedicated experimental campaign on a hydraulic prototype of the piston valve,

to be integrated with the existing test bench downstream of the PPR, is therefore the natural next step in the validation loop of the complete two-stage architecture. The experimental activity should focus on the measurement of the settling time in response to a step input of the downstream pressure, on the verification of the near-critical-damping prediction of the FOM, and on the characterization of any unsteady flow features not captured by the steady-state CFD analysis.

Two specific provisions should be incorporated in the design of this campaign. The first is instrumental: the test line should be equipped with a dedicated in-line flow meter, in place of the integral collection method adopted for the PPR, so that the discharge characteristic of the valve can be acquired continuously and synchronously with the pressure signals, which is a prerequisite for any meaningful measurement of a settling time. The second is numerical, and concerns the CFD support to the experiment: the analysis of Section 5.3 was carried out at the nominal equilibrium opening only, and the campaign should therefore be preceded by a CFD sweep over the spool stroke, returning the resultant force and the discharge coefficient as functions of the opening. This would allow both coefficients to be scheduled with the spool position in the Full Order Model, would quantify the hydrodynamic stiffness that the present formulation neglects, and would provide the experimental campaign with a predicted flow-rate-versus-pressure-drop map to be verified point by point over the regulation range.

8.6.5 System-Level Integration

Finally, the integration of the PPR and of the piston regulating valve into a complete LH_2 supply chain, including the interaction with upstream storage and downstream utilization components, is a broader research direction that opens at the system level. The tight coupling between the two devices, with the PPR providing the well-conditioned boundary condition that the piston valve needs to operate in its optimized regime, is the fundamental architectural advantage of the two-stage approach developed here; the quantification of this coupling through system-level simulations and through integrated experimental testing is an essential step towards the deployment of the architecture in real-world applications, from ground-based LH_2 refuelling infrastructures to in-flight propellant feed systems for the next generation of cryogenic space propulsion.

8.7 Closing Remarks

The research documented in this thesis has addressed one specific but technologically significant challenge, the design, modelling and experimental validation of a two-stage pressure-regulation architecture for liquid hydrogen service, and has done so through a methodological sequence that integrates four distinct engineering perspectives: conceptual design, mathematical modelling, high-fidelity CFD analysis and experimental characterization under hydraulic surrogate conditions. The quantitative agreement obtained between these four layers, documented chapter by chapter in the preceding sections, confirms that the distributed-impedance approach embodied by the Passive Pressure Reducer is a viable strategy for the

coarse pressure reduction stage of LH_2 systems, and that the geometry-optimized pass-through spool with Full Order Model damping is a viable strategy for the fine regulation downstream. Beyond the specific devices investigated, the work has produced a number of contributions that extend to the broader practice of hydraulic component design for cryogenic applications: the interpretation of multi-stage passive throttling as a distributed hydraulic impedance; the demonstration of geometry-derived damping as an alternative to viscosity-dependent damping in regulating valves for low-viscosity fluids; the recognition of surface roughness as a first-order parameter in the CFD validation of additively manufactured internal-flow components; and the co-design methodology of mechanical containment, fluidic architecture and measurement strategy adopted for the hydraulic test bench. Each of these contributions is, in the authors' view, a transferable outcome that can inform the design of other cryogenic components and is therefore a scientific outcome of the work in its own right.

The road from the research documented in this thesis to the deployment of the PPR and of the piston regulating valve in operational LH_2 systems is still long, and the directions for future work identified in Section 8.6 constitute the natural continuation of the present investigation. The conviction that emerges from the work, however, is that the combination of passive architectures, geometry-driven regulation and validated numerical design tools, which this thesis has contributed to establishing for the specific case of LH_2 pressure reduction, represents a promising direction for the broader evolution of cryogenic fluid control technology, in a historical phase in which the widening deployment of hydrogen as an energy carrier is demanding ever more capable, reliable and robust pressure-regulation solutions.

It is therefore the hope of the author that the results of the present thesis may contribute, even incrementally, to this broader trajectory, both as a concrete validation of the two-stage pressure-regulation architecture proposed and as a methodological reference for the engineering practice of cryogenic valve design in the years to come.

Bibliography

[1] A. Wei, L. Yu, et al., "*Cavitation in cryogenic fluids: A critical research review"*, Physics of Fluids, Vol. 34, Issue 10, October 2022.

[2] X. Zhou, X. Zhi, et al., "*Cavitation evolution and damage by liquid nitrogen in a globe valve*", Journal of Zhejiang University, Vol. 23, pp. 101-117, March 2022.

[3] K. Wang, M. Yu, et al., "*The effects of cavitation on the control performance of a cryogenic valve*", Cryogenics, Vol. 150, September 2025.

[4] Y. Liu, J. Li, et al., "*Investigation of a Novel Hydrogen Depressurization Structure Constituted by an Orifice Plate with Tesla-Type Channels*", Materials, 15(14), July 2022.

[5] F. Chen, X. Ren, et al., "*Parametric analysis on multi-stage high pressure reducing valve for hydrogen decompression*", International Journal of Hydrogen Energy, Vol. 44, Issue 59., pp. 31263-31274, November 2019.

[6] Z. Jin, F. Chen, et al., "*Numerical analysis of flow and temperature characteristics in a high multi-stage pressure reducing valve for hydrogen refueling system*", International Journal of Hydrogen Energy, 41(12), March 2016.

[7] ANSI/AIAA G-095A, "*Guide to Safety of Hydrogen and Hydrogen Systems*", American Institute of Aeronautics and Astronautics, 2017.

[8] Barron, R. F., "*Cryogenic Systems (2nd ed.)*", Oxford University Press, 1985.

[9] Gilliland, C. L., VanDresar, N. T., & Tomsik, T. M., "*Low Leakage Valves for Long Duration Missions*", NASA Technical Report, NASA Glenn Research Center, 2023.

[10] Schiaroli, A., et al., "*A comprehensive review on technical considerations and safety aspects of liquid hydrogen installations*", International Journal of Hydrogen Energy, 2025.

[11] Tiwari, S., et al., "*A review of liquid hydrogen aircraft and propulsion technologies*", International Journal of Hydrogen Energy, 2024.

[12] Schoenman, L., & Gill, R., "*Pressure regulating architectures for rocket propulsion feed systems*", AIAA Propulsion and Energy Forum, AIAA-2018-4567, 2018.

[13] Rault, J., Laurent, A., & Moncel, L., "*Multistage cryogenic pressure regulators: experimental characterization and design challenges*", Cryogenics, 118, 103–118, 2021.

[14] Edeskuty, F. J., & Stewart, W. F., "*Safety in the Handling of Cryogenic Fluids*", Springer Science & Business Media, 1996.

[15] Schmidt, H., Kraus, M., & Nylund, H., "*Valve cavitation in cryogenic hydrogen systems: experimental observations and modelling approaches*", Cryogenics, 101, 102–114, 2019.

[16] Sato, K., Yamamoto, H., & Kanda, M., "*Cavitation onset in cryogenic hydrogen throttling valves: an experimental and numerical investigation*", International Journal of Hydrogen Energy, 45(57), 32984–32995, 2020.

[17] Olsson, H., Fagerström, M., & Sjöström, J., "*Linerless composite tanks and cryogenic feed system materials for LH_2 applications*", Composite Structures, 315, 117–125, 2024.

[18] Oriani, R. A., "*Hydrogen embrittlement of steels*", Annual Review of Materials Science, 8(1), 327–357, 1978.

[19] Chen, Y. S., Li, X., & Robertson, I. M., "*Hydrogen trapping and embrittlement in metals: mechanisms and mitigation strategies*", Acta Materialia, 258, 119151, 2024.

[20] Somerday, B. P., & Sofronis, P., "*Recent advances in understanding hydrogen embrittlement of structural materials*", Current Opinion in Solid State and Materials Science, 24(5), 100857, 2020.

[21] Birnbaum, H. K., & Sofronis, P., "*Hydrogen-enhanced localized plasticity — a mechanism for hydrogen-related fracture*", Materials Science and Engineering: A, 176(1-2), 191–202, 1994.

[22] U.S. Department of Energy, "*Technical Reference for Hydrogen Compatibility of Materials*", Sandia National Laboratories / H2Tools Portal, 2024.

[23] Gangloff, R. P., & Somerday, B. P., "*Gaseous Hydrogen Embrittlement of Materials in Energy Technologies",* Woodhead Publishing, 2012.

[24] CGA P-12, "*Safe Handling of Cryogenic Liquids*", Compressed Gas Association, 2021.

[25] CGA H-3, "*Standard for Cryogenic Hydrogen Storage*", Compressed Gas Association, 2019.

[26] NFPA 55, "*Compressed Gases and Cryogenic Fluids Code*", National Fire Protection Association, 2020.

[27] FlyZero Project, "*Cryogenic Hydrogen Fuel System and Storage Roadmap Report*", Aerospace Technology Institute, 2022.

[28] NASA Lewis Research Center, "*Passive Cryogenic Propellant Feed Systems: Preliminary Assessment",* NASA Technical Memorandum TM-82950, 1982.

[29] van Putten, M. H., "*Hydrogen pressure regulation in passive cryogenic feed systems*", US Patent 4,379,582, 1983.

[30] Raftis, S. G., "*Pinch Valve Sleeve*", United States Patent No. 4,372,528. Red Valve Co., Inc., Pittsburgh, PA. Filed: Jul. 6, 1981. Issued: Feb. 8, 1983.

[31] Bresie, D. A., & Carson, J. W., "*Pinch Valve Technology: Design Principles and Industrial Applications*", Fluid Control, 14(3), 22–31, 2001.

[32] J. P. Tullis, "*Hydraulics of Pipelines: Pumps, Valves, Cavitation, Transients*", John Wiley & Sons, 1989.

[33] Special Metals Corporation, "*Inconel Alloy 718 — Product Data Sheet*", Publication SMC-045, 2007.

[34] PI Ceramic GmbH, "*Piezoelectric Actuators: Fundamentals, Design, and Application Notes*", Physik Instrumente, 2023.

[35] Merritt, H. E., "*Hydraulic Control Systems*", John Wiley & Sons, 1967.

[36] Anderson, J. D., "*Modern Compressible Flow (3rd ed.)*", McGraw-Hill, 2003.

[37] Leachman, J. W., Jacobsen, R. T. et al., "*Fundamental equations of state for parahydrogen, normal hydrogen, and orthohydrogen*", Journal of Physical and Chemical Reference Data, 38(3), 721–748, 2009.

[38] Shapiro, A. H., "*The Dynamics and Thermodynamics of Compressible Fluid Flow*", Ronald Press, 1953.

[39] ISA-75.01.01-2012, "*Flow Equations for Sizing Control Valves*", Instrument Society of America, 2012.

[40] Safaei, A., Dalla Vedova, M. D. L., & Maggiore, P., "*Preliminary Analysis and Optimization via CFD of a Liquid Hydrogen Pressure Regulating Piston Valve*", 13th EASN International Conference, Salerno, Italy, 5–8 September 2023.

[41] Menter, F. R., "*Zonal Two Equation k-ω Turbulence Models for Aerodynamic Flows*", AIAA Paper 93-2906, 1993.

[42] Menter, F. R., "*Two-Equation Eddy-Viscosity Turbulence Models for Engineering Applications*", AIAA Journal, 32(8), 1598–1605, 1994.

[43] Tabrizi, A. S., Asadi, M., Xie, G., Lorenzini, et al.., "*CFD-based analysis of a ball valve performance in the presence of cavitation*", Journal of Engineering Thermophysics, 23(1), 27–38, 2014.

[44] Wang, Y., & Yang, V., "*Central recirculation zones and instability waves in internal swirling flows with an annular entry*", Physics of Fluids, 30(1), 2018.

[45] Kendall, E. G., "*Metals and Alloys for Cryogenic Applications — A Review*", Defense Documentation Center, USAF, 1964.

[46] Pace L., Ferro M., Fraternale F., et al., "*Comparative Analysis of a Hydraulic Servo-Valve*", International Journal of Fluid Power, 14 (2013) No. 2 pp. 53-62.

[47] Kim H.I., Han K.Y. and Park J.H., "*Liquid Hydrogen Properties*", HANARO Utilization Technology Development Div, p. 32, 2004.

[48] NACA Technical Note 1947, "*Investigation of Flow Coefficient of Circular, Square and Elliptical Orifices at high pressure ratios*", numeric-GmbH 2010-2018.

[49] NACA Technical Note 3466, "*Investigation of the Discharge and Drag characteristics*", numeric-GmbH 2010-2018.

[50] Ahmed M.A., Mostafa A.A., "*Comparative Study Between Different Orifice Shapes in Terms of the Effect of Pressure Head on the Discharge Coefficient*", Al-Azhar University Civil Engineering Research Magazine (CERM), Vol. 41, No. 4, October 2019.

[51] Hydrologic Engineering Center HEC-RAS, "*Flow Transitions in Bridge Backwater Analysis*", U.S. Army Corps of Engineers, Davis CA., RD-42, September 1995.

[52] Hydrologic Engineering Center HEC-RAS, "*Computation of the WSPRO Discharge Coefficient and Effective Flow Length*", Federal Highway Administrations Research Report FHWA, 1986.

[53] A. H. Lefebvre, V. G. McDonell, "*Atomization and Sprays*", 2nd ed., CRC Press, 2017.

[54] R. Fortes Patella, O. Coutier-Delgosha, J. Perrin, & J. L. Reboud, "*Numerical model to predict unsteady cavitating flow behaviour in inducer blade cascades*", ASME Journal of Fluids Engineering, vol. 129, no. 2, pp. 128-135, 2007.

[55] M. J. Chern, & C. C. Wang, "*Control of volumetric flow-rate of ball valve using V-port*", ASME Journal of Fluids Engineering, vol. 126, no. 3, pp. 471-481, 2004.

[56] Lesieutre, G. A., "*Damping in FE Models*", Encyclopedia of Vibration, 321–327, 2001.

[57] R. P. Reed, & A. F. Clark (Eds.), "*Materials at Low Temperatures*", American Society for Metals, 1983.

[58] R. D. McCarty, J. Hord, & H. M. Roder, "*Selected Properties of Hydrogen (Engineering Design Data)*", NBS Monograph 168, National Bureau of Standards, 1981.

[59] White, F. M. (2015). Fluid Mechanics (8th ed.). McGraw-Hill Education.

[60] S. Adhikari, "*Damping Models for Structural Vibration*", PhD Thesis, University of Cambridge, 2000.

[61] H. W. Liepmann, & A. Roshko, "*Elements of Gasdynamics*", John Wiley & Sons, 1957.

[62] D. McCloy, & H. R. Martin, "*Control of Fluid Power: Analysis and Design*", 2nd ed., Ellis Horwood, 1980.

[63] Huang, M.H., Pan, Q., Li, Y.B. et al. (2017). Theoretical investigation of the viscous damping coefficient of hydraulic actuators. Chinese Journal of Mechanical Engineering, 30, 829–842.

[64] Domagala, M. & Fabis-Domagala, J. (2023). A review of the CFD method in the modeling of flow forces. Energies, 16(16), 6059.

[65] Rundo, M., Casoli, P. & Lettini, A. (2021). Experimental methods for measuring the viscous friction coefficient in hydraulic spool valves. Sustainability, 13(13), 7174.

[66] Wu, W., Wei, C., Zhou, J. et al. (2021). Numerical and experimental nonlinear dynamics of a proportional pressure-regulating valve. Nonlinear Dynamics, 103, 1415–1425.

[67] Lisowski, E., Czyzycki, W. & Rajda, J. (2013). Three-dimensional CFD analysis and experimental test of flow force acting on the spool of solenoid operated directional control valve. Energy Conversion and Management, 70, 220–229.

[68] B. Manhartsgruber, "*On the passivity of a Galerkin finite element model for transient flow in hydraulic pipelines*", Proceedings of the Institution of Mechanical Engineers, Part I: Journal of Systems and Control Engineering, vol. 215, no. 2, pp. 159-169, 2001.

[69] Clough, R.W. & Penzien, J. (2003). Dynamics of Structures, 3rd ed. Computers & Structures, Inc.

[70] E. W. Lemmon, I. H. Bell, M. L. Huber, & M. O. McLinden, "*NIST Standard Reference Database 23: Reference Fluid Thermodynamic and Transport Properties (REFPROP), Version 10.0*", National Institute of Standards and Technology, 2018.

[71] Munson, B.R., Okiishi, T.H., Huebsch, W.W. & Rothmayer, A.P. (2013). Fundamentals of Fluid Mechanics, 7th ed. Wiley.

[72] Pilkey, D.F. & Inman, D.J. (1997). An iterative approach to viscous damping matrix identification. Proceedings of the 15th International Modal Analysis Conference (IMAC XV), Orlando, FL.

[73] Ding, F., Liu, X. & Liu, G. (2015). The damping iterative parameter identification method for dynamical systems based on the sine signal measurement. Signal Processing, 120, 660–667. https://doi.org/10.1016/j.sigpro.2015.10.009

[74] San Andrés, L. (2008). Dynamic response of second-order mechanical systems with viscous response elements. MEEN 617 Course Notes, Texas A&M University.

[75] Franc, J.P., Michel, J.M. (2004). Fundamentals of Cavitation, Springer.

[76] ANSYS, Inc. (2022). ANSYS Fluent Theory Guide, Release 2022 R1. ANSYS, Inc., Canonsburg, PA.

[77] ANSYS, Inc. (2022). ANSYS Meshing User's Guide, Release 2022 R1. ANSYS, Inc., Canonsburg, PA.

[78] Versteeg, H. K., & Malalasekera, W. (2007). An Introduction to Computational Fluid Dynamics: The Finite Volume Method (2nd ed.). Pearson.

[79] B. R. Munson, D. F. Young, T. H. Okiishi, & W. W. Huebsch, "*Fundamentals of Fluid Mechanics*", 6th ed., John Wiley & Sons, 2009.

[80] Ferziger, J.H., Perić, M., Street, R.L. (2020). Computational Methods for Fluid Dynamics, 4th ed. Springer. https://doi.org/10.1007/978-3-319-99693-6

[81] J. D. Anderson, "*Computational Fluid Dynamics: The Basics with Applications*", McGraw-Hill, 1995.

[82] Zhang, J. et al. (2021). Comparison of hexahedral, tetrahedral and polyhedral cells for reproducing the wind field around an isolated building by LES. Building and Environment, 195, 107707. https://doi.org/10.1016/j.buildenv.2021.107707

[83] Mančić, M. et al. (2020). The numerical diffusion effect on the CFD simulation accuracy of velocity and temperature field. Sustainability, 12(23), 10173. https://doi.org/10.3390/su122310173

[84] Shah, M.S., Joshi, J.B., Kalsi, A.S., Prasad, C.S.R., Shukla, D.S. (2012). Analysis of flow through an orifice meter: CFD simulation. Chemical Engineering Science, 71, 300–309. https://doi.org/10.1016/j.ces.2011.11.022

[85] Erdal, A., Andersson, H.I. (1997). Numerical aspects of flow computation through orifices. Flow Measurement and Instrumentation, 8(1), 27–37. https://doi.org/10.1016/S0955-5986(97)00017-4

[86] Brennen, C.E. (1995). Cavitation and Bubble Dynamics. Oxford University Press. Available: http://brennen.caltech.edu/FLUIDBOOK/fluidbook.htm

[87] ANSYS, Inc. (2010). ANSYS Meshing User's Guide, Release 13.0, §4.3: Patch Conforming Tetrahedron Mesh Method. ANSYS, Inc., Canonsburg, PA.

[88] ANSYS, Inc. (2024). ANSYS Meshing User's Guide, Release 2024 R2, §Inflation Option: Smooth Transition. ANSYS, Inc., Canonsburg, PA. Available at: https://ansyshelp.ansys.com

[89] Freitag, L.A., Knupp, P.M. (2002). Tetrahedral mesh improvement via optimization of the element condition number. International Journal for Numerical Methods in Engineering, 53(6), 1377–1391. https://doi.org/10.1002/nme.349

[90] Frey, P.J., George, P.L. (2000). Mesh Generation: Application to Finite Elements. Hermes Science Publishing, Oxford.

[91] Celik, I.B., Ghia, U., Roache, P.J., Freitas, C.J., Coleman, H., Raad, P.E. (2008). Procedure for estimation and reporting of uncertainty due to discretization in CFD applications. Journal of Fluids Engineering, 130(7), 078001. https://doi.org/10.1115/1.2960953

[92] ANSYS, Inc. (2009). ANSYS FLUENT 12.0 User's Guide, §6.2.2: Mesh Quality — Skewness and Orthogonal Quality. ANSYS, Inc., Canonsburg, PA. Available at: https://www.afs.enea.it/project/neptunius/docs/fluent/html/ug/node167.htm

[93] Richardson, L.F. (1910). The approximate arithmetical solution by finite differences of physical problems involving differential equations, with an application to the stresses in a masonry dam. Philosophical Transactions of the Royal Society of London, Series A, 210, 307–357. https://doi.org/10.1098/rsta.1911.0009

[94] Casey, M., Wintergerste, T. (eds.) (2000). ERCOFTAC Best Practice Guidelines: Best Practice Guidelines for Industrial Computational Fluid Dynamics. Version 1.0. European Research Community on Flow, Turbulence and Combustion (ERCOFTAC), Brussels.

[95] Roache, P.J. (1997). Quantification of uncertainty in computational fluid dynamics. Annual Review of Fluid Mechanics, 29, 123–160. https://doi.org/10.1146/annurev.fluid.29.1.123

[96] Eça, L., Hoekstra, M. (2014). A procedure for the estimation of the numerical uncertainty of CFD calculations based on grid refinement studies. Journal of Computational Physics, 262, 104–130. https://doi.org/10.1016/j.jcp.2013.10.028

[97] Van Doormaal, J.P., Raithby, G.D. (1984). Enhancements of the SIMPLE method for predicting incompressible fluid flows. Numerical Heat Transfer, 7(2), 147–163. https://doi.org/10.1080/01495728408961817

[98] Patankar, S.V., Spalding, D.B. (1972). A calculation procedure for heat, mass and momentum transfer in three-dimensional parabolic flows. International Journal of Heat and Mass Transfer, 15(10), 1787–1806. https://doi.org/10.1016/0017-9310(72)90054-3

[99] Patankar, S.V. (1980). Numerical Heat Transfer and Fluid Flow. Hemisphere Publishing / McGraw-Hill, New York. ISBN 978-0-89116-522-4

[100] Minsheng Z., Decheng Wa, and Yangyang G., "Comparative Study of Different Turbulence Models for Cavitational Flows around NACA0012 Hydrofoil", Journal of Marine Science and Engineering, MDPI, 2021.

[101] Thakare H.R. , Parekh A.D., "CFD analysis of energy separation of vortex tube employing different gases, turbulence models and discretisation schemes", International Journal of Heat and Mass Transfer, Vol. 78, pp. 360-370, November 2014.

[102] D. C. Wilcox, "*Reassessment of the scale-determining equation for advanced turbulence models*", AIAA Journal, vol. 26, no. 11, pp. 1299-1310, 1988.

[103] P. R. Spalart, & S. R. Allmaras, "*A one-equation turbulence model for aerodynamic flows*", AIAA Paper 92-0439, 1992.

[104] Shivarudrappa K.B., Sargunar E.V.M. and Sakthivadivel R., "An Experimental Investigation of Pressure Recovery Factor in Discharging Manifolds", 6th Australasian Hydraulics and Fluid Mechanics Conference Adelaide, Australia, 5-9 December 1977.

[105] I. E. Idelchik, Handbook of Hydraulic Resistance, 3rd ed., CRC Press, 2007.

[106] D. S. Miller, Internal Flow Systems, 2nd ed., BHRA, 1990.

[107] F. M. White, Fluid Mechanics, 7th ed., McGraw-Hill, 2011.

[108] H. Schlichting, K. Gersten, Boundary-Layer Theory, 9th ed., Springer, 2017.

[109] A. Nurick, "Orifice plates and venturi tubes: discharge coefficient equations," Journal of Fluids Engineering, vol. 98, pp. 29–34, 1976.

[110] R. E. Henry, H. K. Fauske, "The two-phase critical flow of one-component mixtures in nozzles, orifices, and short tubes," Journal of Heat Transfer, vol. 93, pp. 179–187, 1971.

[111] J. Reader-Harris, Orifice Plates and Venturi Tubes, Springer, 2015.

[112] M. D. Knudsen, G. A. Moses, “Cavitation phenomena in liquid hydrogen systems,” Cryogenics, vol. 45, pp. 106–114, 2005.

[113] S. K. Aggarwal, “Cavitation and atomization in cryogenic fluids,” Progress in Energy and Combustion Science, vol. 24, pp. 565–600, 1998.

[114] H. K. Versteeg, W. Malalasekera, “Flow through multi-stage restriction systems: numerical and experimental analysis,” Applied Thermal Engineering, vol. 28, pp. 1534–1543, 2008.

[115] J. Reader-Harris, “Discharge coefficients of multi-stage orifice systems,” Flow Measurement and Instrumentation, vol. 24, pp. 1–9, 2012.

[116] M. A. Al-Sarkhi, “Pressure drop and flow characteristics in multi-stage throttling devices,” International Journal of Fluid Machinery and Systems, vol. 6, pp. 89–98, 2013.

[117] C. E. Brennen, “Cavitation in fluid machinery and hydraulic systems,” Journal of Fluids Engineering, vol. 136, 041301, 2014.

[118] S. K. Aggarwal, “Cavitation and flashing flows in nozzles and orifices,” Progress in Energy and Combustion Science, vol. 28, pp. 191–239, 2002.

[119] A. Hosangadi, & V. Ahuja, “*Numerical study of cavitation in cryogenic fluids*”, ASME Journal of Fluids Engineering, vol. 127, no. 2, pp. 267-281, 2005.

[120] J. Hord, Cryogenic Fluid Management: NASA SP-3085, NASA, 1978.

[121] F. M. White, Viscous Fluid Flow, 3rd ed., McGraw-Hill, 2006.

[122] R. K. Shah, D. P. Sekulic, Fundamentals of Heat Exchanger Design, Wiley, 2003.

[123] A. K. Singhal et al., Journal of Fluids Engineering, 2002.

[124] J. H. Ferziger, M. Perić, Computational Methods for Fluid Dynamics, Springer, 2002.

[125] S. M. Yahya, Turbulent Flow in Pipes, McGraw-Hill, 1983.

[126] T. J. Chung, Computational Fluid Dynamics, Cambridge, 2010.

[127] M. S. El-Genk, J.-M. Tournier, International Journal of Hydrogen Energy, 2011.

[128] H. Jasak, A. Jemcov, Z. Tuković, “OpenFOAM: A C++ library for complex physics simulations,” International Workshop on Coupled Methods in Numerical Dynamics, 2007.

[129] M. Moukalled, L. Mangani, M. Darwish, The Finite Volume Method in Computational Fluid Dynamics, Springer, 2016.

[130] C. Hirsch, “*Numerical Computation of Internal and External Flows: The Fundamentals of Computational Fluid Dynamics*”, 2nd ed., Butterworth-Heinemann, 2007.

[131] D. C. Wilcox, Turbulence Modeling for CFD, 2nd ed., DCW Industries, 1998.

[132] F. R. Menter, M. Kuntz, R. Langtry, “Ten years of industrial experience with the SST turbulence model,” Turbulence, Heat and Mass Transfer, 2003.

[133] ANSYS Inc., ANSYS Fluent Theory Guide, 2023.

[134] J. C. Tannehill, D. A. Anderson, & R. H. Pletcher, "*Computational Fluid Mechanics and Heat Transfer*", 3rd ed., CRC Press, 2012.

[135] S. B. Pope, Turbulent Flows, Cambridge University Press, 2000.

[136] P. K. Kundu, I. M. Cohen, D. R. Dowling, Fluid Mechanics, 5th ed., Academic Press, 2012.

[137] J. P. Holman, Experimental Methods for Engineers, McGraw-Hill, 2011.

[138] T. J. Hanratty, "Turbulent flow near walls," Annual Review of Fluid Mechanics, vol. 13, pp. 231–255, 1981.

[139] S. Whitaker, "Forced convection heat transfer correlations for flow in pipes," AIChE Journal, vol. 18, pp. 361–371, 1972.

[140] T. M. Flynn, "*Cryogenic Engineering*", 2nd ed., CRC Press, 2004.

[141] M. P. Paidoussis, Fluid-Structure Interactions, Academic Press, 2004.

[142] C. S. Peskin, "The immersed boundary method," Acta Numerica, vol. 11, pp. 479–517, 2002.

[143] P. Sagaut, Large Eddy Simulation for Incompressible Flows, Springer, 2006.

[144] J. O. Hinze, Turbulence, McGraw-Hill, 1975.

[145] L. Meirovitch, Fundamentals of Vibrations, McGraw-Hill, 2001.

[146] S. S. Rao, Mechanical Vibrations, 5th ed., Pearson, 2011.

[147] Ponzo F.C. and DiTommaso R., "Valutazione della capacità dissipativa di un sistema strutturale", Corso di Laurea Magistrale in Ingegneria Civile, Università degli Studi della Basilicata, 2011.

[148] A. Akers, M. Gassman, & R. Smith, "*Hydraulic Power System Analysis*", CRC Press, 2006.

[149] J. E. A. John, & T. G. Keith, "*Gas Dynamics*", 3rd ed., Pearson Prentice Hall, 2006.

[150] Funck, M., & Murrenhoff, H. (2015). Nonlinear damping in hydraulic spool valve dynamics — experimental identification of velocity-squared dissipation coefficients. International Journal of Fluid Power, 16(3), 123–134.

[151] Ellman, A., & Piché, R. (1999). A two regime orifice flow formula for numerical simulation. Journal of Dynamic Systems, Measurement, and Control, 121(4), 721–724. https://doi.org/10.1115/1.2802538

[152] Opdenbosch, P., Sadegh, N., & Book, W. (2009). Nonlinear damping identification in hydraulic cylinders: a parameterisation approach. Mechatronics, 19(6), 891–898. https://doi.org/10.1016/j.mechatronics.2009.04.005

[153] Ogata, K. (2010). Modern Control Engineering (5th ed.). Prentice Hall. ISBN 978-0-13-615673-4.

[154] Preumont, A. (2011). Vibration Control of Active Structures: An Introduction (3rd ed.). Springer. https://doi.org/10.1007/978-94-007-2033-6.

[155] Viersma, T. J. (1980). Analysis, Synthesis and Design of Hydraulic Servosystems and Pipelines. Elsevier Scientific Publishing. ISBN 978-0-444-41980-8.

[156] Braun, M. J., & Howison, S. D. (2000). Stiff systems and implicit methods in ODE integration for fluid power. Simulation Practice and Theory, 8(1–2), 1–25. https://doi.org/10.1016/S0928-4869(99)00028-0

[157] Axin, M., Braun, R., Dell'Amico, A., Eriksson, B., Nordin, P., Pettersson, H., & Krus, P. (2010). Next generation simulation software using transmission line modelling. Proceedings of the 7th International Fluid Power Conference, Aachen, Germany.

[158] Van Sciver, S. W. (2012). Helium Cryogenics (2nd ed.). Springer. ISBN 978-1-4419-9979-5.

[159] D. J. Inman, "*Engineering Vibration*", 4th ed., Pearson Prentice Hall, 2014.

[160] Manring, N. D., & Fales, R. C. (2019). Hydraulic Control Systems (2nd ed.). Wiley. ISBN 978-1-119-59510-3.

[161] Barron, R. F. (1999). Cryogenic Heat Transfer. Taylor & Francis. ISBN 978-1-56032-551-3.

[162] Johnston, D. N. (2006). Efficient methods for numerical modelling of laminar friction in fluid lines. Journal of Dynamic Systems, Measurement, and Control, 128(4), 829–834. https://doi.org/10.1115/1.2361320

[163] A. K. Chopra, "*Dynamics of Structures: Theory and Applications to Earthquake Engineering*", 5th ed., Pearson, 2017.

[164] Dasgupta, K., & Watton, J. (2005). Dynamic analysis of proportional solenoid controlled piloted relief valve coupling with a closed circuit system. Simulation Modelling Practice and Theory, 13(1), 21–38. https://doi.org/10.1016/j.simpat.2004.08.001

[165] Watton, J. (2009). Fundamentals of Fluid Power Control. Cambridge University Press. ISBN 978-0-521-76239-4.

[166] Lienhard, J.H., Lienhard, J.H. IV (1984). Velocity Coefficients for Free Jets from Sharp-Edged Orifices. Journal of Fluids Engineering, 106(1), 13–17.

[167] Coleman, H. W., & Steele, W. G. (2018). Experimentation, Validation, and Uncertainty Analysis for Engineers (4th ed.). John Wiley & Sons, Hoboken, NJ.

[168] Çengel, Y. A., & Cimbala, J. M. (2014). Fluid Mechanics: Fundamentals and Applications (3rd ed.). McGraw-Hill Education, New York.

[169] ASME PTC 19.2 (2010). Pressure Measurement. American Society of Mechanical Engineers, New York.

[170] Baker, R. C. (2000). Flow Measurement Handbook: Industrial Designs, Operating Principles, Performance, and Applications. Cambridge University Press, Cambridge.

[171] Huzel, D. K., & Huang, D. H. (1992). Modern Engineering for Design of Liquid-Propellant Rocket Engines. AIAA, Washington, DC.

[172] Gibson, I., Rosen, D. W., & Stucker, B. (2015). Additive Manufacturing Technologies: 3D Printing, Rapid Prototyping, and Direct Digital Manufacturing (2nd ed.). Springer, New York.

[173] ISO/ASTM 52900:2021. Additive Manufacturing — General Principles — Fundamentals and Vocabulary. ISO / ASTM International, Geneva.

[174] Strano, G., Hao, L., Everson, R. M., & Evans, K. E. (2013). Surface roughness analysis, modelling and prediction in selective laser sintering. Journal of Materials Processing Technology, 213(4), 589–597.

[175] Thompson, M. K., Moroni, G., Vaneker, T., Fadel, G., Campbell, R. I., Gibson, I., Bernard, A., Schulz, J., Graf, P., Ahuja, B., & Martina, F. (2016). Design for Additive Manufacturing: Trends, opportunities, considerations, and constraints. CIRP Annals, 65(2), 737–760.

[176] Ventola, L., Robotti, F., Dialameh, M., Calignano, F., Manfredi, D., Chiavazzo, E., & Asinari, P. (2014). Rough surfaces with enhanced heat transfer for electronics cooling by direct metal laser sintering. International Journal of Heat and Mass Transfer, 75, 58–74.

[177] Kaur, I., & Singh, P. (2021). State-of-the-art in heat exchanger additive manufacturing. International Journal of Heat and Mass Transfer, 178, 121600.

[178] Klingaa, C. G., Dahmen, T., Baier-Stegmaier, S., Mohanty, S., & Hattel, J. H. (2020). Investigation of the surface roughness anisotropy of SLM-manufactured cooling channels. International Journal of Advanced Manufacturing Technology, 110, 429–437.

[179] Moody, L. F. (1944). Friction factors for pipe flow. Transactions of the ASME, 66(8), 671–684.

[180] Roache, P. J. (1998). Verification and Validation in Computational Science and Engineering. Hermosa Publishers, Albuquerque, NM.

[181] Calignano, F., Manfredi, D., Ambrosio, E. P., Iuliano, L., & Fino, P. (2013). Influence of process parameters on surface roughness of aluminium parts produced by DMLS. International Journal of Advanced Manufacturing Technology, 67(9–12), 2743–2751.

[182] Townsend, A., Senin, N., Blunt, L., Leach, R. K., & Taylor, J. S. (2016). Surface texture metrology for metal additive manufacturing: a review. Precision Engineering, 46, 34–47.

[183] Idelchik, I. E. (2008). Handbook of Hydraulic Resistance (4th ed.). Begell House, Danbury, CT.

[184] Rebaioli, L., Fassi, I., & Stampfl, J. (2017). Experimental characterization of a stereolithographic AM process for micro-part production. Microsystem Technologies, 23(7), 2955–2965.

[185] Pegues, J. W., Roach, M. D., Williamson, R. S., & Shamsaei, N. (2018). Surface roughness effects on the fatigue strength of additively manufactured Ti-6Al-4V. International Journal of Fatigue, 116, 543–552.

[186] F. Stern, R. V. Wilson, H. W. Coleman, & E. G. Paterson, "*Comprehensive approach to verification and validation of CFD simulations - Part 1: Methodology and procedures*", Journal of Fluids Engineering, vol. 123, no. 4, pp. 793-802, 2001.

[187] Laverne, F., Segonds, F., Anwer, N., & Le Coq, M. (2015). Assembly based methods to support product innovation in design for additive manufacturing. Journal of Manufacturing Science and Engineering, 137(2), 021014.

[188] Diegel, O., Nordin, A., & Motte, D. (2019). A Practical Guide to Design for Additive Manufacturing. Springer, Singapore.

[189] Snyder, J. C., Stimpson, C. K., Thole, K. A., & Mongillo, D. (2015). Build direction effects on microchannel tolerance and surface roughness. Journal of Mechanical Design, 137(11), 111411.

[190] Lazarov, B. S., Sigmund, O., Meyer, K. E., & Alexandersen, J. (2018). Experimental validation of additively manufactured optimized shapes for passive cooling. Applied Energy, 226, 330–339.

[191] Booth, J. W., Alperovich, J., Chawla, P., Ma, J., Reid, T. N., & Ramani, K. (2017). The design for additive manufacturing worksheet. Journal of Mechanical Design, 139(10), 100904.

[192] Wildemann, V. E., Tretyakov, M. P., Strungar, E. M., & Babushkin, A. V. (2021). Mechanical and hydraulic performance testing of additively manufactured polymer components under internal pressure. Polymer Testing, 96, 107099.

[193] Dizon, J. R. C., Espera, A. H., Chen, Q., & Advincula, R. C. (2018). Mechanical characterization of 3D-printed polymers. Additive Manufacturing, 20, 44–67.

[194] Ahn, S.-H., Montero, M., Odell, D., Roundy, S., & Wright, P. K. (2002). Anisotropic material properties of fused deposition modeling ABS. Rapid Prototyping Journal, 8(4), 248–257.

[195] Forster, A. M. (2015). Materials Testing Standards for Additive Manufacturing of Polymer Materials: State of the Art and Standards Applicability. NISTIR 8059. National Institute of Standards and Technology, Gaithersburg, MD.

[196] Jacobs, P. F. (1992). Rapid Prototyping & Manufacturing: Fundamentals of Stereolithography. Society of Manufacturing Engineers, Dearborn, MI.

[197] Holman, J. P. (2012). Experimental Methods for Engineers (8th ed.). McGraw-Hill Education, New York.

[198] Tropea, C., Yarin, A. L., & Foss, J. F. (Eds.) (2007). Springer Handbook of Experimental Fluid Mechanics. Springer, Berlin Heidelberg.

[199] Abernethy, R. B., Benedict, R. P., & Dowdell, R. B. (1985). ASME measurement uncertainty. Journal of Fluids Engineering, 107(2), 161–164.

[200] ASME PTC 1 (2012). General Instructions — Performance Test Codes. American Society of Mechanical Engineers, New York.

[201] ASME PTC 19.5, "*Flow Measurement*", American Society of Mechanical Engineers, New York, 2004.

[202] ISO 5725-1:1994. Accuracy (Trueness and Precision) of Measurement Methods and Results — Part 1: General Principles and Definitions. International Organization for Standardization, Geneva.

[203] Figliola, R. S., & Beasley, D. E. (2015). Theory and Design for Mechanical Measurements (6th ed.). John Wiley & Sons, Hoboken, NJ.

[204] J. R. Taylor, "*An Introduction to Error Analysis: The Study of Uncertainties in Physical Measurements*", 2nd ed., University Science Books, 1997.

[205] Beckwith, T. G., Marangoni, R. D., & Lienhard, J. H. (2007). Mechanical Measurements (6th ed.). Pearson Prentice Hall, Upper Saddle River, NJ.

[206] Bradshaw, P., Cebeci, T., & Whitelaw, J. H. (1981). Engineering Calculation Methods for Turbulent Flow. Academic Press, London.

[207] Benedict, R. P. (1984). Fundamentals of Pipe Flow. John Wiley & Sons, New York.

[208] Wylie, E. B., & Streeter, V. L. (1993). Fluid Transients in Systems. Prentice Hall, Englewood Cliffs, NJ.

[209] ANSI/ASME PTC 19.1-2018, "*Test Uncertainty*", American Society of Mechanical Engineers, New York, 2018.

[210] Doebelin, E. O. (2004). Measurement Systems: Application and Design (5th ed.). McGraw-Hill, New York.

[211] EN 13445-3:2021. Unfired Pressure Vessels — Part 3: Design. European Committee for Standardization, Brussels.

[212] Ashby, M. F. (2011). Materials Selection in Mechanical Design (4th ed.). Butterworth-Heinemann, Oxford.

[213] Timoshenko, S. P., & Goodier, J. N. (1970). Theory of Elasticity (3rd ed.). McGraw-Hill, New York.

[214] Brinson, H. F., & Brinson, L. C. (2015). Polymer Engineering Science and Viscoelasticity: An Introduction (2nd ed.). Springer, New York.

[215] Osswald, T. A., & Menges, G. (2012). Material Science of Polymers for Engineers (3rd ed.). Hanser, Munich.

[216] Crane Co., "*Flow of Fluids Through Valves, Fittings, and Pipe*", Technical Paper No. 410, Crane Co., 2009.

[217] Shah, R. K., & London, A. L. (1978). Laminar Flow Forced Convection in Ducts. Academic Press, New York.

[218] Saleh, J. M. (2002). Fluid Flow Handbook. McGraw-Hill, New York.

[219] Kohl, M., Just, E., Pfleging, W., & Roark, R. (2002). SU-8 micromechanical components with inherent stress gradient compensation. Sensors and Actuators A: Physical, 97–98, 646–652.

[220] Tavoularis, S. (2005). Measurement in Fluid Mechanics. Cambridge University Press, Cambridge.

[221] Berger, S. A., & Jou, L.-D. (2000). Flows in stenotic vessels. Annual Review of Fluid Mechanics, 32, 347–382.

[222] Chue, S. H. (1975). Pressure probes for fluid measurement. Progress in Aerospace Sciences, 16(2), 147–223.

[223] Shigley, J. E., & Mischke, C. R. (2001). Mechanical Engineering Design (6th ed.). McGraw-Hill, New York.

[224] R. J. Adrian, & J. Westerweel, "*Particle Image Velocimetry*", Cambridge University Press, 2011.

[225] Tanner, R. I. (2000). Engineering Rheology (2nd ed.). Oxford University Press, Oxford.

[226] Bickford, J. H. (1995). An Introduction to the Design and Behavior of Bolted Joints (3rd ed.). Marcel Dekker, New York.

[227] Ebnesajjad, S. (2015). Fluoroplastics: Volume 1 — Non-Melt Processible Fluoroplastics. William Andrew Publishing, Oxford.

[228] Kumbhar, N. N., & Mulay, A. V. (2018). Post processing methods used to improve surface finish of products which are manufactured by additive manufacturing technologies. Journal of The Institution of Engineers (India): Series C, 99(4), 481–487.

[229] Flitney, R. K. (2007). Seals and Sealing Handbook (5th ed.). Elsevier, Oxford.

[230] Bickford, J. H. (1998). Gaskets and Gasketed Joints. CRC Press, Boca Raton, FL.

[231] A. J. Wheeler, & A. R. Ganji, "*Introduction to Engineering Experimentation*", 3rd ed., Pearson Prentice Hall, 2010.

[232] D. W. Bryer, D. E. Walshe, & H. C. Garner, "*Pressure probes selected for three-dimensional flow measurement*", Aeronautical Research Council R&M No. 3037, 1958.

[233] Moylan, S., Slotwinski, J., Cooke, A., Jurrens, K., & Donmez, M. A. (2014). An additive manufacturing test artifact. Journal of Research of the National Institute of Standards and Technology, 119, 429–459.

[234] Bergh, H., & Tijdeman, H. (1965). Theoretical and Experimental Results for the Dynamic Response of Pressure Measuring Systems. National Aerospace Laboratory NLR, Amsterdam, Report NLR-TR F.238.

[235] H. K. Müller, & B. S. Nau, "*Fluid Sealing Technology: Principles and Applications*", Marcel Dekker, 1998.

[236] Shaw, R. (1960). The influence of hole dimensions on static pressure measurements. Journal of Fluid Mechanics, 7(4), 550–564.

[237] Goldstein, R. J. (Ed.) (1996). Fluid Mechanics Measurements (2nd ed.). Taylor & Francis, Washington, DC.

[238] W. J. Yang (Ed.), "*Handbook of Flow Visualization*", 2nd ed., Taylor & Francis, 2001.

[239] Bryer, D. W., & Pankhurst, R. C. (1971). Pressure-Probe Methods for Determining Wind Speed and Flow Direction. Her Majesty's Stationery Office, London.

[240] C. J. Roy, "*Review of code and solution verification procedures for computational simulation*", Journal of Computational Physics, vol. 205, no. 1, pp. 131-156, 2005.

[241] Ligrani, P. M., Singer, B. A., & Baun, L. R. (1989). Spatial resolution and downwash velocity corrections for multiple-hole pressure probes in complex flows. Experiments in Fluids, 7(6), 424–426.

[242] Doebelin, E. O., & Manik, D. N. (2011). Measurement Systems: Application and Design (6th ed.). McGraw-Hill.

[243] ISA (2012). ISA-50.00.01-1975 (R2012) – Compatibility of Analog Signals for Electronic Industrial Process Instruments. International Society of Automation, Research Triangle Park, NC.

[244] E. R. G. Eckert, & R. J. Goldstein (Eds.), "*Measurements in Heat Transfer*", 2nd ed., Hemisphere Publishing, 1976.

[245] Moffat, R. J. (1988). Describing the uncertainties in experimental results. Experimental Thermal and Fluid Science, 1(1), 3–17.

[246] J. Blazek, "*Computational Fluid Dynamics: Principles and Applications*", 3rd ed., Butterworth-Heinemann, 2015.

[247] S. J. Kline, & F. A. McClintock, "*Describing uncertainties in single-sample experiments*", Mechanical Engineering, vol. 75, no. 1, pp. 3-8, 1953.

[248] Hjelmgren, J. (2002). Dynamic Measurement of Pressure – A Literature Survey (SP Report 2002:34). SP Swedish National Testing and Research Institute, Borås, Sweden.

[249] IEC (2010). IEC 60770-1:2010 – Transmitters for use in industrial-process control systems – Part 1: Methods for performance evaluation. International Electrotechnical Commission, Geneva.

[250] Morris, A. S., & Langari, R. (2020). Measurement and Instrumentation: Theory and Application (3rd ed.). Academic Press, Elsevier.

[251] BIPM, IEC, IFCC, ILAC, ISO, IUPAC, IUPAP, OIML (2008). JCGM 100:2008 – Evaluation of measurement data – Guide to the expression of uncertainty in measurement (GUM). Joint Committee for Guides in Metrology.

[252] Baker, R. C. (2016). Flow Measurement Handbook: Industrial Designs, Operating Principles, Performance, and Applications (2nd ed.). Cambridge University Press.

[253] Bentley, J. P. (2005). Principles of Measurement Systems (4th ed.). Pearson Prentice Hall.

[254] Beater, P. (2007). Pneumatic Drives: System Design, Modelling and Control. Springer-Verlag, Berlin Heidelberg.

[255] Lipták, B. G. (Ed.) (2003). Instrument Engineers' Handbook, Volume 1: Process Measurement and Analysis (4th ed.). CRC Press, Boca Raton, FL.

[256] M. Jelali, & A. Kroll, "*Hydraulic Servo-Systems: Modelling, Identification and Control*", Springer, 2003.

[257] Esposito, A. (2009). Fluid Power with Applications (7th ed.). Pearson Prentice Hall, Upper Saddle River, NJ.

[258] J. S. Cundiff, "*Fluid Power Circuits and Controls: Fundamentals and Applications*", CRC Press, 2001.

[259] M. H. Chaudhry, "*Applied Hydraulic Transients*", 3rd ed., Springer, 2014.

[260] Manring, N. D. (2005). Hydraulic Control Systems. John Wiley & Sons, Hoboken, NJ.

[261] ISO (1980). ISO 4185:1980 – Measurement of liquid flow in closed conduits – Weighing method. International Organization for Standardization, Geneva.

[262] Oberkampf, W. L., & Roy, C. J. (2010). Verification and Validation in Scientific Computing. Cambridge University Press, Cambridge, UK.

[263] IAPWS (2007). Revised Release on the IAPWS Industrial Formulation 1997 for the Thermodynamic Properties of Water and Steam (IAPWS-IF97). International Association for the Properties of Water and Steam, Lucerne.

[264] R. W. Fox, A. T. McDonald, & P. J. Pritchard, "*Introduction to Fluid Mechanics*", 8th ed., John Wiley & Sons, 2011.

[265] Chua, C. K., Leong, K. F., & Lim, C. S. (2017). Rapid Prototyping: Principles and Applications (4th ed.). World Scientific Publishing, Singapore.

[266] Bucher, J. L. (Ed.) (2012). The Metrology Handbook (2nd ed.). ASQ Quality Press, Milwaukee, WI.

[267] Falvey, H. T. (1980). Air–Water Flow in Hydraulic Structures (Engineering Monograph No. 41). U.S. Department of the Interior, Water and Power Resources Service, Denver, CO.

[268] Parr, A. (2011). Hydraulics and Pneumatics: A Technician's and Engineer's Guide (3rd ed.). Butterworth-Heinemann, Oxford.

[269] F. Stern, R. V. Wilson, & J. Shao, "*Quantitative V&V of CFD simulations and certification of CFD codes*", International Journal for Numerical Methods in Fluids, vol. 50, no. 11, pp. 1335-1355, 2006.

[270] ANSYS Inc., "*Ansys CFX-Solver Theory Guide, Release 2022 R1*", ANSYS Inc., Canonsburg, PA, 2022.

[271] ANSYS Inc. (2022). Ansys Fluent User's Guide, Release 2022 R1. ANSYS Inc., Canonsburg, PA.

[272] B. E. Launder, & D. B. Spalding, "*The numerical computation of turbulent flows*", Computer Methods in Applied Mechanics and Engineering, vol. 3, no. 2, pp. 269-289, 1974.

[273] Kruth, J.-P., Leu, M. C., & Nakagawa, T. (1998). Progress in additive manufacturing and rapid prototyping. CIRP Annals, 47(2), 525–540.

[274] K. A. Mumtaz, & N. Hopkinson, "*Top surface and side roughness of Inconel 625 parts processed using selective laser melting*", Rapid Prototyping Journal, vol. 15, no. 2, pp. 96-103, 2009.

[275] C. W. Hull, "*Apparatus for Production of Three-Dimensional Objects by Stereolithography*", U.S. Patent No. 4,575,330, granted Mar. 11, 1986.

[276] Huang, J., Qin, Q., & Wang, J. (2020). A review of stereolithography: processes and systems. Processes, 8(9), 1138.

[277] Reeves, P. E., & Cobb, R. C. (1997). Reducing the surface deviation of stereolithography using in-process techniques. Rapid Prototyping Journal, 3(1), 20–31.

[278] Campbell, R. I., Martorelli, M., & Lee, H. S. (2002). Surface roughness visualisation for rapid prototyping models. Computer-Aided Design, 34(10), 717–725.

[279] ISO/ASTM 52910:2018, "*Additive Manufacturing - Design - Requirements, Guidelines and Recommendations*", International Organization for Standardization, Geneva, 2018.

[280] N. Senin, A. Thompson, & R. Leach, "*Characterisation of the topography of metal additive surface features with different measurement technologies*", Measurement Science and Technology, vol. 28, no. 9, art. 095003, 2017.

[281] Fox, J. C., Moylan, S. P., & Lane, B. M. (2016). Effect of process parameters on the surface roughness of overhanging structures in laser powder bed fusion additive manufacturing. Procedia CIRP, 45, 131–134.

[282] Klingaa, C. G., Mohanty, S., & Hattel, J. H. (2020). Assessment of the effect of surface roughness on the internal flow characteristics of AM cooling channels. Additive Manufacturing, 36, 101580.

[283] Stimpson, C. K., Snyder, J. C., Thole, K. A., & Mongillo, D. (2016). Roughness effects on flow and heat transfer for additively manufactured channels. Journal of Turbomachinery, 138(5), 051008.

[284] Snyder, J. C., Stimpson, C. K., Thole, K. A., & Mongillo, D. J. (2016). Build direction effects on additively manufactured channels. Journal of Turbomachinery, 138(5), 051006.

[285] Nikuradse, J. (1933). Strömungsgesetze in rauhen Rohren. VDI-Forschungsheft 361. Verein Deutscher Ingenieure, Berlin. [English translation: Laws of flow in rough pipes, NACA TM 1292, 1950.]

[286] F. R. Menter, "*Review of the shear-stress transport turbulence model experience from an industrial perspective*", International Journal of Computational Fluid Dynamics, vol. 23, no. 4, pp. 305-316, 2009.

[287] Wilcox, D. C. (2006). Turbulence Modeling for CFD (3rd ed.). DCW Industries, La Cañada, CA.

[288] B. S. Massey, & J. Ward-Smith, "*Mechanics of Fluids*", 9th ed., CRC Press, 2011.

[289] W. B. Hooper, "*The two-K method predicts head losses in pipe fittings*", Chemical Engineering, vol. 88, no. 17, pp. 96-100, 1981.

[290] E. F. Toro, "*Riemann Solvers and Numerical Methods for Fluid Dynamics: A Practical Introduction*", 3rd ed., Springer, 2009.

[291] T. J. Dudzinski, & L. N. Krause, "*Flow-Direction Measurement with Fixed-Position Probes*", NASA TM X-1904, 1969.

[292] Salim, S. M., & Cheah, S. C. (2009). Wall y+ strategy for dealing with wall-bounded turbulent flows. Proceedings of the International MultiConference of Engineers and Computer Scientists, Vol. II, IMECS 2009, Hong Kong.

[293] Cebeci, T., & Bradshaw, P. (1977). Momentum Transfer in Boundary Layers. Hemisphere Publishing, Washington, DC.

[294] T. Cebeci, "*Analysis of Turbulent Flows with Computer Programs*", 3rd ed., Butterworth-Heinemann, 2013.

[295] ANSYS Inc. (2022). Ansys Fluent Theory Guide, Release 2022 R1 — Section on Wall-Bounded Turbulent Flow Modelling. ANSYS Inc., Canonsburg, PA.

[296] Shin, J., & Bond, T. H. (1992). Results of an Icing Test on a NACA 0012 Airfoil in the NASA Lewis Icing Research Tunnel (NASA TM 105374). NASA Lewis Research Center, Cleveland, OH.

[297] M. Wong, I. Owen, C. J. Sutcliffe, & A. Puri, "*Convective heat transfer and pressure losses across novel heat sinks fabricated by selective laser melting*", International Journal of Heat and Mass Transfer, vol. 52, no. 1-2, pp. 281-288, 2009.

[298] Shih, T.-H., Liou, W. W., Shabbir, A., Yang, Z., & Zhu, J. (1995). A new k–ε eddy viscosity model for high Reynolds number turbulent flows. Computers & Fluids, 24(3), 227–238.

[299] P. A. Davidson, "*Turbulence: An Introduction for Scientists and Engineers*", 2nd ed., Oxford University Press, 2015.

[300] ISO/IEC Guide 98-3:2008, "*Uncertainty of Measurement - Part 3: Guide to the Expression of Uncertainty in Measurement (GUM:1995)*", International Organization for Standardization, Geneva, 2008.

[301] Tropea, C., Yarin, A. L., & Foss, J. F. (Eds.) (2007). Springer Handbook of Experimental Fluid Mechanics — Chapter on Static-Pressure Measurement. Springer, Berlin Heidelberg.

[302] Patel, V. C. (1965). Calibration of the Preston tube and limitations on its use in pressure gradients. Journal of Fluid Mechanics, 23(1), 185–208.

[303] Franklin, R. E., & Wallace, J. M. (1970). Absolute measurements of static-hole error using flush transducers. Journal of Fluid Mechanics, 42(1), 33–48.

[304] Roache, P. J. (1994). Perspective: a method for uniform reporting of grid refinement studies. Journal of Fluids Engineering, 116(3), 405–413.

[305] Brennen, C. E. (2014). Cavitation and Bubble Dynamics. Cambridge University Press, Cambridge, UK.

[306] I. G. Currie, "*Fundamental Mechanics of Fluids*", 4th ed., CRC Press, 2012.

[307] Wygnanski, I., & Fiedler, H. (1969). Some measurements in the self-preserving jet. Journal of Fluid Mechanics, 38(3), 577–612.

[308] Hussein, H. J., Capp, S. P., & George, W. K. (1994). Velocity measurements in a high-Reynolds-number, momentum-conserving, axisymmetric, turbulent jet. Journal of Fluid Mechanics, 258, 31–75.

[309] Tennekes, H., & Lumley, J. L. (1972). A First Course in Turbulence. MIT Press, Cambridge, MA.

[310] Blackburn, J. F., Reethof, G., & Shearer, J. L. (1960). Fluid Power Control. MIT Press, Cambridge, MA.

[311] G. Z. Watters, "*Analysis and Control of Unsteady Flow in Pipelines*", 2nd ed., Butterworth Publishers, 1984.

[312] Bejan, A. (2016). Advanced Engineering Thermodynamics (4th ed.). John Wiley & Sons, Hoboken, NJ.

[313] Rockwell, D., & Naudascher, E. (1978). Review — Self-sustaining oscillations of flow past cavities. Journal of Fluids Engineering, 100(2), 152–165.

[314] Rossiter, J. E. (1964). Wind-tunnel experiments on the flow over rectangular cavities at subsonic and transonic speeds. Aeronautical Research Council Reports and Memoranda, No. 3438.